Nanosecond Sampling of Atmospheric Cherenkov Radiation Applied to TeV Gamma-Ray Observations of Blazars with VERITAS

Peter Cogan

Submitted to University College Dublin
for the degree of Ph.D. in the
College of Engineering, Mathematical and Physical Sciences

December 2006

School of Physics
Prof. Gerard O' Sullivan

Supervised by Dr John Quinn

Abstract

This thesis concerns a study to determine new methods of analysing data taken with VERITAS, a new array of atmospheric Cherenkov telescopes, and the application of these methods to astrophysical observations of blazars during the array-commissioning phase. The VERITAS array uses a data acquisition system which employs custom-built hardware to record the temporal development of the extensive air shower which occurs when a very high-energy gamma ray strikes the atmosphere. A suite of analysis tools are developed, investigated and optimised in order to determine the most suitable mechanism for analysing these data. Following this study, the new analysis tools are applied to observations of the Crab Nebula, a steady source of TeV gamma rays in the northern hemisphere. The Crab Nebula data are used to optimise and calibrate the analysis. This analysis is applied to very high-energy observations of the blazars 1ES 0647+250, 1ES 0806+524 and 1ES 2344+514. Although no emission is detected from any of these objects, constraining upper limits on the integral flux above 0.3 TeV are derived. The upper limit on TeV emission above 0.3 TeV from 1ES 0806+525 is less than that predicted by one of the emission models studied. Concurrent x-ray observations of the three blazars with the Rossi X-Ray Timing Explorer are used to find enhanced x-ray emission during one of the VERITAS exposures on 1ES 0647+250.

To my parents

Acknowledgements

It is often said that it takes a village to raise a child. The same, or at least something similar, can be said of a thesis dissertation. Without the help of the community around me, both professional and personal, I would not have been able to complete this work. I would like to take this opportunity to thank those people. My first thanks must go to my tireless supervisor Dr John Quinn. Dr Quinn always has time for his students and can often be found in his office after 6pm on a friday evening trying to find time to do his own work. Thank you John for all the interaction and encouragement ove the last few years. Thanks must also go to Professor David Fegan whose constant presence and experience was of great benefit to all who worked with him. I would also like to thank all the people with whom I have worked at the High Energy Astrophysics lab and have learned so much from- I would especially like to mention Stephen, Ray, Andrew, Michael, Conor, James, Alan and John E. That list would not be complete without a special mention for Catherine Casey who has been a constant companion for the last few years.

I would like to thank Professor Gerry O'Sullivan, Head of School for the School of Physics for making the facilities available to me. A very special note of thanks must be extended to Marion Hanson - a wonderful surrogate mother to all the graduate students in the School of Physics. I would like to thank the School of Physics Secretary Bairbre Fox for all her professional help and friendship. I would also like to thank Dennis Cusack for instilling a passion for physics in me, and thanks to Michael Grimley for showing me how to be an experimental physicist.

My time in UCD has been enriched by a number of extended visits to the Smithsonian Astrophysical Observatory in Arizona. I met a number of special people there - but I must start by thanking Dr Trevor Weekes. It was an enormous privilege to work with Dr Weekes and he must be acknowledged for the effort he makes to bring Irish students to Arizona to work at the Observatory. I was also fortunate to work alongside the likes of Ken Gibbs (and Bingo!), Steve Criswell (a true action man who brought me skiing and flying) and Gene Gardner (for keeping my tax returns honest). I have learned so much from all the people I have worked with in the VERITAS collaboration, and short (just about) of naming the entire group, I would like to especially mention Deirdre Horan, Andy Smith, Glenn Sembroski, Martin Schroedter, Jeremy Perkins, Brian Humensky, Liz Hays, Rob Atkins, Stephan Fegan, Richard White, Jamie Holder, Gernot Maier, John Kildea, Pascal Fortin, Mary Kertzman, Mark Quinn, Mark Lang, Gary Gillanders, John Toner, Gary Kenny, Pat Moriarty, David Hanna, Ken Ragan, Ana Mi-

lanovic, Jeffrey Grube, Alex Syson, Tulun Ergin, Michael Daniel, Rene Ong, Henric Krawczynksi, Alex Konopelko, Ozlem Celik, Vladimir Vasiliev and Abe Falcone.

The daily life in UCD ranges from slow to hectic on any given day, but certain constants are there to keep your sanity in check. I would like to thank all my friends who have ensured that sanity, with special mention for Paddy, Lynn, Michelle, Yurgos, Sean, Louise, and Colin. Outside of UCD I would like to thank Lloyd, Simon, Oisin and Brendan.

I would like to thank those that have provided funding for travel and fees - I have been extremely lucky to have visited Hong Kong, India, Canada, Germany, England, Spain and the US, with trips to Tucson, Chicago and LA (with an unplanned stop in Boston!) during my three years - not to mention meetings in Cork and Galway. I have the UCD Astrophysics group, IRCSET and the Smithsonian Institute to thank for that.

I would like to say a very special thank you to my parents John and Liz for their unwavering support over the last 4 years (indeed the last 26 years!). Thanks also to my sister Sue for always being there for me.

Finally the one person who has made all of this possible is Aislinn - who has been on this journey with me for the last 7 years. It is difficult to describe the impact you have had on my life in just a few sentences. I know that while in 20 or 40 or 60 years time, while this thesis gathers dust on a shelf, that we will remain as strong as ever together.

If I have missed anyone I thank you too.

Science is always wrong,
it never solves a problem without creating ten more

George Bernard Shaw

Contents

List of Figures

List of Tables

Figure 1: VERITAS telescopes 1 and 2 at the basecamp of the Fred Lawrence Whipple Observatory, Arizona.

Chapter 1

An Overview of Gamma-Ray Astronomy

1.1 Introduction

In his recent review, Weekes (2006) points out that a certain suggestion by Blackett (1948) ought to be the first reference in any high-energy astrophysics thesis, although it is only the second reference in this one. Blackett's suggestion was that the contribution to the night sky background by Cherenkov photons emitted by the atmospheric decay products of cosmic rays could amount to 1 part in 10000. This hypothesis was investigated by the physicists Bill Galbraith and John Jelley while working at the Harwell Air Shower Array. They assembled what must be regarded as the first atmospheric Cherenkov telescope, comprising a 5 cm photomultiplier tube and 25 cm parabolic mirror, coupled to an amplifier and oscilloscope. Every minute or so the decay products of a cosmic ray of sufficient energy produced enough Cherenkov light to trigger the oscilloscope (W. Galbraith, 1953). They were also able to use the Harwell Air Shower Array itself to find coincidences between cosmic-ray induced triggers from the array and light pulses from the photomultiplier tube. Subsequently, by studying the polarisation and directional properties of the detected light pulses at the Pic du Midi Observatory in France, Galbraith and Jelley proved that at least some if not all of the detected light pulses were indeed Cherenkov radiation (Galbraith and Jelley, 1955; Jelley and Galbraith, 1955).

It was clear that no useful astrometric information could be derived from the detection of charged cosmic rays, as their directional history is scrambled by galactic magnetic fields. However the technique could be used to locate point sources of very high-energy gamma rays. Subsequent experiments in

the Crimea and in the Dublin mountains in the early 1960's, failed to detect an excess of events from a variety of candidate sources, including the Crab Nebula. The primary reason for this, is that although they had the necessary equipment to detect gamma rays (albeit with a very-high energy threshold), they had no way to discriminate them from the huge background of cosmic rays. Progress towards that goal started in 1968, with the construction of the Whipple 10m gamma-ray observatory on Mount Hopkins which had a significantly lower energy threshold than previous experiments. However, it would be many years before the imaging technique arrived, and with it the first reliable detection of a source of very high-energy gamma rays. The imaging technique is discussed in detail in Section 2.4.

In the remaining sections of this chapter, an overview of the major gamma-ray projects is presented, with both space-based and ground-based detectors discussed. This is followed by a summary of the types of astrophysical objects which can be studied using ground-based gamma-ray astronomy. The chapter concludes with a guide to the thesis.

1.2 High-Energy Gamma-Ray Astronomy

High-energy gamma-ray astronomy is defined as astronomy in the energy range from 30 MeV to 100 GeV (Weekes, 2003). Such high-energy gamma rays are completely absorbed by the earth's atmosphere, meaning that detection of such photons must occur using space-based observatories. Fortunately, at these energies, the flux of gamma rays is adequately high that the small collection areas available to orbital observatories is sufficient to obtain a useful sensitivity. The first orbital gamma-ray telescope was Explorer XI in 1965. This tiny telescope merely established the existence of gamma rays in space, but could not discern their origin. The subsequent satellites SAS-2 and COS-B mapped the galactic plane and discovered point sources of gamma-ray radiation, thus pioneering the field of orbital gamma-ray astronomy.

The field of orbital gamma-ray astronomy truly came of age with the launch of the outstandingly successful Compton Gamma-Ray Observatory (CGRO). The CGRO will be succeeded by GLAST in 2007 which is expected to attain an order of magnitude increase in sensitivity at high energies, and will be co-operational with the VERITAS array of telescopes. The CGRO and GLAST telescopes are described further in Sections 1.2.1 and 1.2.2. Other orbital projects include Integral (International Gamma-Ray Astrophysics Laboratory) launched by the European Space Agency in 2002 (Winkler et al., 2003). Integral carries two main gamma-ray instruments which together are sensitive in the range 3 keV to 10 MeV. The Swift obser-

vatory, launched by NASA in November 2004, is primarily a GRB monitor. It is a multiwavelength observatory with gamma-ray, x-ray, UV and optical instruments onboard. The key strength of Swift is underlined by its wide field of view (2 steradians) gamma-ray telescope, coupled to its fast followup pointing with its x-ray and optical instruments allowing for redshift measurements. The Burst Alert Telescope (BAT) onboard Swift is sensitive from 15 keV to 150 keV. There are two further projects that are at an advanced stage of development, but have not yet been launched. One is Agile, whose gamma-ray telescope will be sensitive in the range 30 MeV to 50 GeV and the other is the Alpha Magnetic Spectrometer (AMS) which is primarily an anti-matter detector for the International Space Station, but will have EGRET-like sensitivity (Section 1.2.1) to high-energy gamma rays.

1.2.1 CGRO

The Compton Gamma-Ray Observatory was the second of NASA's Great Observatories (after the Hubble Space Telescope). It was launched in 1991 and operated until it was deorbited in 2000 (Figure 1.1(a)). The CGRO carried four instruments which covered an impressive six decades of the electromagnetic spectrum from 30 keV to 30 GeV. These were the Burst And Transient Source Experiment (BATSE), the Oriented Scintillation Spectrometer Experiment (OSSE), the Imaging Compton Telescope (COMPTEL), and the Energetic Gamma Ray Experiment Telescope (EGRET).

Most relevant to the study of high-energy sources was the EGRET detector which had an energy range from 20MeV to 30GeV and a collection area of $1400\mathrm{cm}^2$ at 3GeV. EGRET had a point-source sensitivity of $6\times10^{-8}\mathrm{cm}^{-2}\mathrm{s}^{-1}$ above 100MeV assuming a two week exposure. EGRET discovered many point-like sources, as displayed in the Third Egret Catalog (Figure 1.2). The Catalog consists of 271 sources, including 66 high-confidence blazar identifications, and a further 27 possible blazar identifications. The Catalog also contains a tantalising yet frustrating 170 unidentified sources. Many of these sources can not be assuredly identified because of the poor angular resolution of EGRET, but does hint that there could exist a population of dark accelerators (Section 1.4.3).

1.2.2 GLAST

The Gamma Ray Large Area Space Telescope (GLAST) (Mattox et al., 1996; Morselli, 2003) is the successor to EGRET that is expected to launch in 2007 (see Figure 1.1(b)). GLAST will carry two instruments, the Large Area Telescope (LAT) and GLAST Burst Module (GBM). The LAT will have a

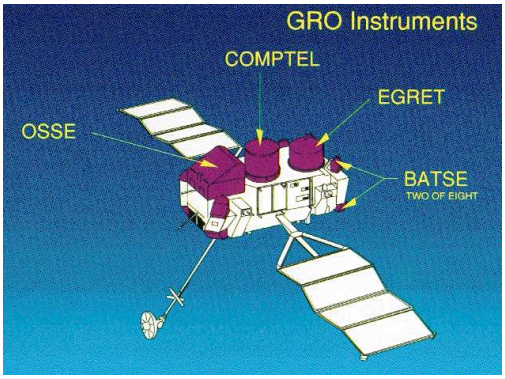

(a) CGRO

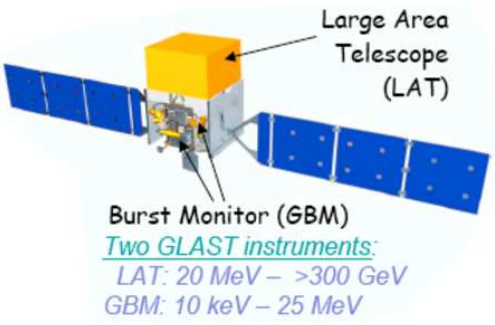

(b) GLAST

Figure 1.1: The high-energy orbital telescopes CGRO and GLAST.

field of view about twice as wide (more than 2.5 steradians) as EGRET, and sensitivity in the high-energy regime from 20 MeV to 300 GeV, with sensitivity about 50 times that of EGRET at 100 MeV. It will be able to locate sources with positional accuracies of 30 arc seconds to 5 arc minutes and will have a point source sensitivity of $6 \times 10^{-9}\,\mathrm{cm}^{-2}\,\mathrm{s}^{-1}$. The GBM is sensitive in the energy range 10 keV to 30 MeV with a field of view of $3\,\pi$ steradians.

GLAST will be the first space-based gamma-ray observatory whose energy range will overlap with that of ground-based Cherenkov detectors. This will provide a unique opportunity to cross-calibrate the instruments using the spectrum of a steady source such as the Crab Nebula. The key scientific objectives of the GLAST mission are to investigate high-energy sources such as AGN, pulsars and SNRs, to resolve the gamma-ray sky (particularly in relation to identifying the EGRET unidentified sources), and to probe GRBs.

1.3 Very High-Energy Gamma-Ray Astronomy

1.3.1 Imaging Cherenkov Telescopes

Perhaps the most significant advancement in ground-based gamma-ray astronomy was the introduction of arrays of phototubes at the focal plane. These phototubes allowed *imaging* of the extensive air shower to occur for

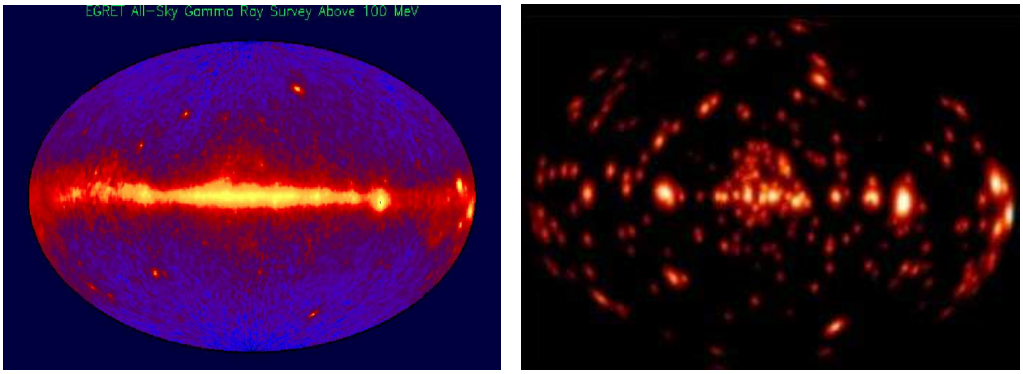

(a) All Sky Map

(b) Point Sources

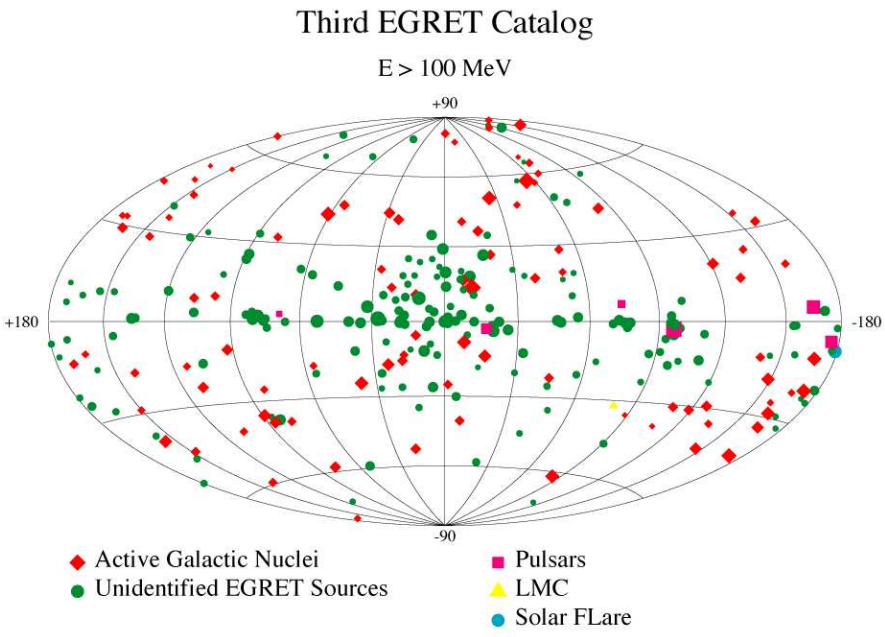

(c) Identification of Sources

Figure 1.2: The Third EGRET Catalog (Hartman et al., 1999). The top figure shows the raw gamma-ray counts recorded by the EGRET experiment. The map is characterised by many point sources against a backdrop of diffuse emission along the plane of the galaxy. The second figure subtracts the diffuse emission, leaving only the point sources (although some are in fact extended). The third figure identifies many of the point sources shown in the second figure.

the first time, enabling efficient cosmic-ray rejection schemes to be implemented. This technique was pioneered by the Whipple Collaboration, and led to the detection of VHE gamma radiation from the Crab Nebula in 1989. Following this important discovery, a series of ground-based gamma-ray astronomy projects commenced, with the intention of using this new technique to explore the universe in TeV gamma rays. These include HEGRA, the Telescope Array (Yamamoto et al., 1999), the Durham Mark 6 (Armstrong et al., 1999), CAT (Barrau et al., 1998), TACTIC (Yadav et al., 2004), the Crimean Astrophysical Observatory (Vladimirsky et al., 1989) and Shalon (Sinitsyna, 1993). Although these telescopes made important contributions, (notably the discovery of TeV emission from 1ES 1959+650 by the Telescope Array by Nishiyama et al. (1999)), only HEGRA and the Whipple 10m will be discussed in more detail given their importance in the context of this work as the major predecessors to VERITAS. A comparison of the sensitivity of a number of instruments is shown in Figure 1.3.

Whipple 10m

The Whipple 10m observatory (Kildea, 2006) is located on Mount Hopkins, Arizona, at an altitude of 2300 m (Figure 1.4(a)). It was built in 1968 following the Davies and Cotton (1957) solar-collector design. The primary mirror has a total surface area of 75 m^2, with an imaging camera that has undergone many upgrades, employing cameras with 37, 91, 109, 151, 331, 490 and 379 pixels. The Whipple 10m was the first Cherenkov Telescope to deploy an imaging camera, which lead to the first reliable detection of a very high-energy source. The two-level trigger chain comprises CFDs which determine whether a signal is present in a single photomultiplier tube by comparing the analog signal to a threshold, and a topological pattern trigger which determines whether a signal is present in the camera by determining whether adjacent photomultiplier tubes have a level 1 CFD trigger. Once a trigger occurs, the PMT signals are integrated and digitised over a 20 ns window and recorded with a GPS time stamp, and other ancillary information. Data are archived to disk for later analysis which typically invokes the moment analysis described by Hillas (1985). Notable detections by the Whipple 10m include the Crab Nebula (Weekes et al., 1989), the blazars Markarian 421 (Punch et al., 1992), Markarian 501 (Quinn et al., 1995), 1ES 2344+514 (Catanese et al., 1998), H 1426+428 (Horan et al., 2002) and the Galactic Center (Kosack et al., 2004).

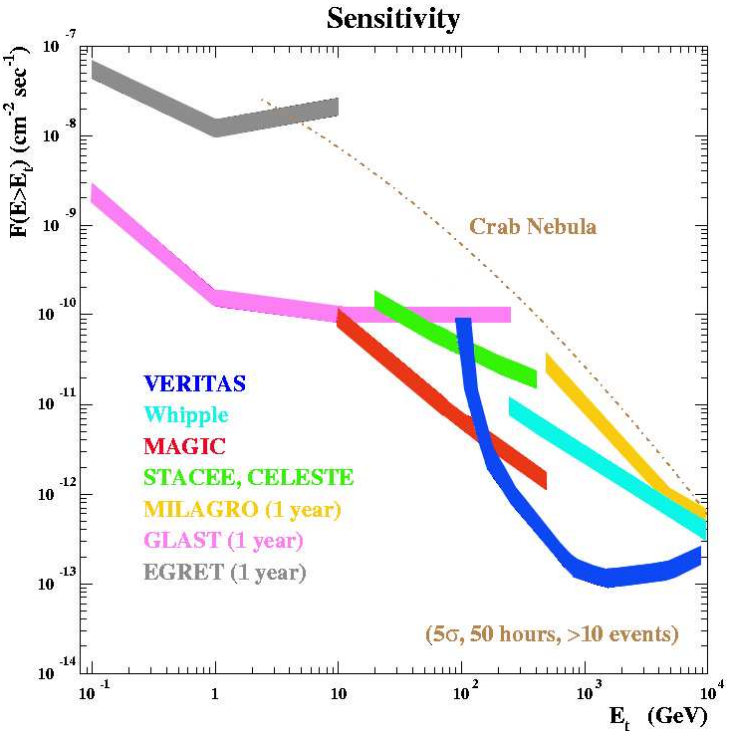

Figure 1.3: A comparison of the sensitivity of several high-energy observatories. The sensitivity curves are produced using Monte-Carlo simulations of high-energy gamma rays and appropriate detector simulations. Indicated sensitivities assume at least 50 hours of observations and a minimum 5 σ detection with at least ten excess events recorded (note that for certain instruments the integration time is much longer).

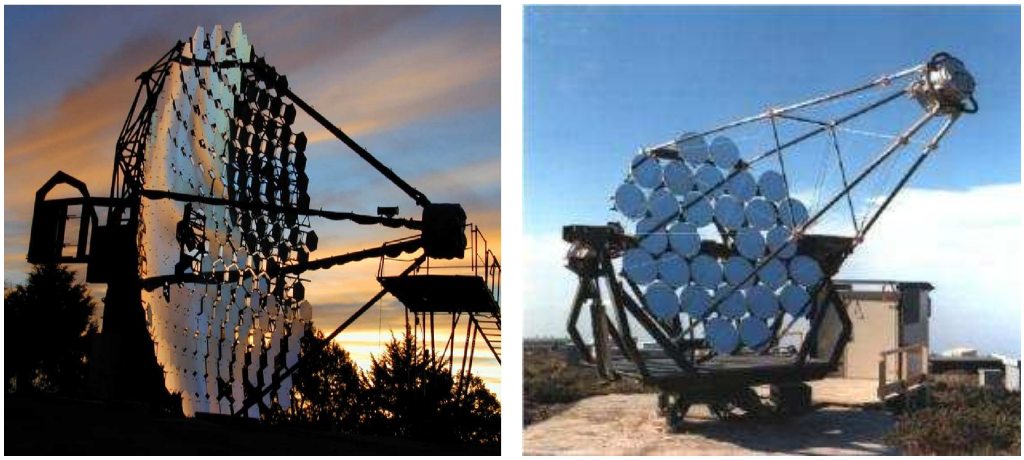

(a) Whipple 10m **(b)** HEGRA

Figure 1.4: The second generation very high-energy ground-based telescopes Whipple 10m and HEGRA.

HEGRA

The HEGRA (High Energy Gamma-Ray Astronomy) (Pühlhofer et al., 2003) system of telescopes was operated at Rocque de los Muchachos on La Palma from 1997 to 2002, at an altitude of 2200 m (Figure 1.4(b)). The array consisted of five relatively small Cherenkov telescopes of diameter 3.4 m, giving a mirror area of 8.5 m^2 each. The array operated in stereoscopic mode, thus pioneering the stereoscopic approach to ground-based gamma-ray astronomy. The focal plane cameras consisted of 271 pixels in a close packed hexagonal arrangement. The fast Cherenkov pulses were pulse shaped with a 12 ns time constant to match the time resolution of the 120 Mhz FADCs. The system had an energy threshold of 500 GeV. Notable detections by HEGRA include Cassiopeia A (Aharonian et al., 2001), TeV J2032+4130 (Aharonian et al., 2002) and M87 (Aharonian et al., 2003).

1.3.2 Third Generation Cherenkov Telescopes

The development of the Imaging Atmospheric Cherenkov Technique has culminated with the global deployment of arrays of large (> 10 m) aperture telescopes. There are four experiments that are currently operating or nearing completion which will be described in this section. Other planned exper-

iments include HAGAR (Chitnis, 2005) and MACE (Sapru, 2005).

CANGAROO-III

The CANGAROO-III (Collaboration of Australia and Nippon for a Gamma-Ray Observatory in the Outback) project (Enomoto et al., 2006; Kabuki, 2003) consists of four Cherenkov telescopes located near Woomera, South Australia, at an altitude of just 160 m (Figure 1.5(a)). Each telescope has a diameter of 10 m giving a total mirror area of 57 m^2. The mirrors are mounted on a parabolic reinforced plastic frame with a focal length of 8 m. The telescopes are arranged in a diamond formation of side 100 m. They are operated in pseudo-stereo mode, using software GPS time stamp matching to combine telescope events into array events.

MAGIC

The MAGIC (Major Atmospheric Gamma Imaging Cherenkov) Telescope is located at Rocque de los Muchachos on La Palma, at an altitude of 2200 m (Cortina, 2005). It comprises a large 17 m segmented parabolic mirror on a light weight carbon fibre frame with a fast-moving mount (Figure 1.5(b)). The parabolic mirror shape reduces the distribution of photon arrival times at the camera, which can help to identify muon induced air showers (Mirzoyan et al., 2006). Active mirror control is used to focus the mirrors with high accuracy (Mirzoyan et al., 2003). The camera has a 3.5° to 3.8° field of view with 397 inner 1 inch diameter photomultiplier tubes and 180 outer 1.5 inch diameter photomultiplier tubes. A special wavelength shifter coating extends the photocathode response to the UV, enhancing the signal by 30 % (Paneque et al., 2004). PMT signals are transmitted using an optical system over 162 m of fibre-optic cable to the counting room where they are split for the trigger and for acquisition. The analog signal is digitised using 300 MHz FADCs. The trigger system uses two levels, with a threshold discriminator as the first level and a topological trigger as the second. The trigger threshold is approximately 60 GeV, although the analysis threshold is > 100 GeV.

The MAGIC collaboration are currently constructing a second telescope that will be almost identical to the first (Baixeras, 2005). The second telescope will be located 80 m from the existing telescope and should more than double the sensitivity of the present system. The installation will include an upgrade of the FADC system to 2.5 Giga Samples/s (Bartko, 2005) which may permit new methods of background discrimination based on the temporal development of the electromagnetic cascade.

H.E.S.S.

H.E.S.S. (High Energy Stereoscopic System) is an array of Cherenkov Telescopes which have been operating in the Khomas Highland in Namibia at an altitude of 1800 m since 2003 (Figure 1.5(c)). The array comprises four telescopes of diameter 12 m giving an approximate mirror area of $100\,\mathrm{m}^2$ per telescope (Bernlöhr et al., 2003; Cornils et al., 2003). The telescopes are arranged in a simple square pattern of side 120m. The H.E.S.S. cameras contain 960 pixels arranged in 60 interchangeable drawers of 16 pixels each, which allows for easy replacement should parts of the camera become inoperable. This large camera offers a 5° field of view, which is optimal for sky surveys, and resulted in the first serendipitous detection of a VHE source in the same field of view as another source (Aharonian et al., 2005c). The camera triggers and readout electronics are located within the camera itself. Readout is achieved using a 1 GHz analog ring sampler, which is digitised using a 12-bit Analog to Digital Converter (ADC) when a trigger occurs (Vincent et al., 2003). A configurable array trigger (Funk et al., 2004) is used which allows subsets of the array to operate independently.

The H.E.S.S. collaboration are currently building a new telescope with a large rectangular segmented mirror 32 m high and 24 m wide giving a surface area of $596\mathrm{m}^2$ (Vincent, 2005). The telescope will use a fine pixellated camera with 2048 pixels. This telescope will be located at the center of the existing array of four telescopes and is expected to have an energy threshold in the $40 - 50$ GeV regime.

VERITAS

As the subject of this thesis, the VERITAS telescopes (Figure 1.5(d)) are discussed in great detail in Chapter 4 (with references therein), however a brief summary is given here for context and comparison. At the time of completion of this work, the VERITAS array consisted of two operating telescopes, with a third telescope in the commissioning phase and a fourth telescope under construction. The array is temporarily located at the Basecamp of the Fred Lawrence Whipple Observatory on Mount Hopkins in Arizona at an altitude of 1270 m. Each telescope has a mirror diameter of 12 m giving a total mirror area of over $100\,\mathrm{m}^2$. The focal plane cameras comprise 499 pixels in a close packed hexagonal array. The data acquisition consists of custom built 500 Mhz FADCs which sample the Cherenkov light pulse in the pixels every 2 ns. The two telescopes operate with an array trigger, which requires both telescopes to trigger within a 100 ns coincidence window. The energy threshold of the two telescope system is approximately 200 GeV.

(a) CANGAROO-III

(b) MAGIC

(c) H.E.S.S.

(d) VERITAS

Figure 1.5: The third generation very high-energy ground-based systems CANGAROO-III, MAGIC, H.E.S.S. and VERITAS.

1.3.3 Alternative Detectors

Third generation arrays of large imaging Cherenkov telescopes are currently the most sensitive instruments for gamma-ray astronomy in the TeV regime. However, there are instruments both planned and operating, which use different methods for detecting very high-energy gamma rays. These instruments are briefly summarised here.

Air-Shower Particle Detectors

Milagro (Smith, 2005) is a water Cherenkov air-shower detector located near Los Alamos, New Mexico, at an altitude of 2630 m (Figure 1.6(a)). It uses a 5000 m^2 pond surrounded by 175 outrigger tanks, which altogether spans an area of 40,000 m^2. The main tank contains 6 million gallons of water and has two layers of PMTs. The first layer is placed under 4 radiation lengths of water, and is used to detect Cherenkov light from the relativistic particles produced by the interaction of gamma rays with the atmosphere. A second layer of PMTs is placed under 16 radiation lengths of water and is used to aid background rejection of charged cosmic rays which have a more penetrating component. The 175 outrigger tanks each contain 500 gallons of water with a single PMT. The addition of these outrigger tanks constituted a significant improvement in sensitivity. Milagro has an energy threshold of approximately 250 GeV and will be operated until mid-2007. Planned projects include HAWC (Sinnis, 2005) which will use a 300 m $\times$ 300 m pond at a high altitude, but will be similar in operation to Milagro.

Another approach to detecting the extensive air shower produced by a very high-energy gamma ray involves the use of an array of particle detectors arranged over a large area. These experiments detect ultra high-energy gamma rays which have a penetrating particle component. Experiments that have used this approach include ARGO-YBJ (Bacci et al., 1999), GRAPES-III (Hayashi, 2005), Tibet (Amenomori et al., 1992), CASA-MIA (Borione, 1993) and HEGRA-AIROBICC (Aharonian, 1991).

Wavefront Sampling

An alternative approach to sampling the Cherenkov light in the atmosphere is to take advantage of otherwise defunct solar power stations. Such stations typically comprise an array of large reflecting heliostats which can be individually adjusted to reflect light from a point in the sky to an elevated collecting station. Although designed with power generation in mind, such a setup is intrinsically suited to detecting the faint flash of Cherenkov radiation produced when a very high-energy gamma ray strikes the atmosphere. This is a difficult

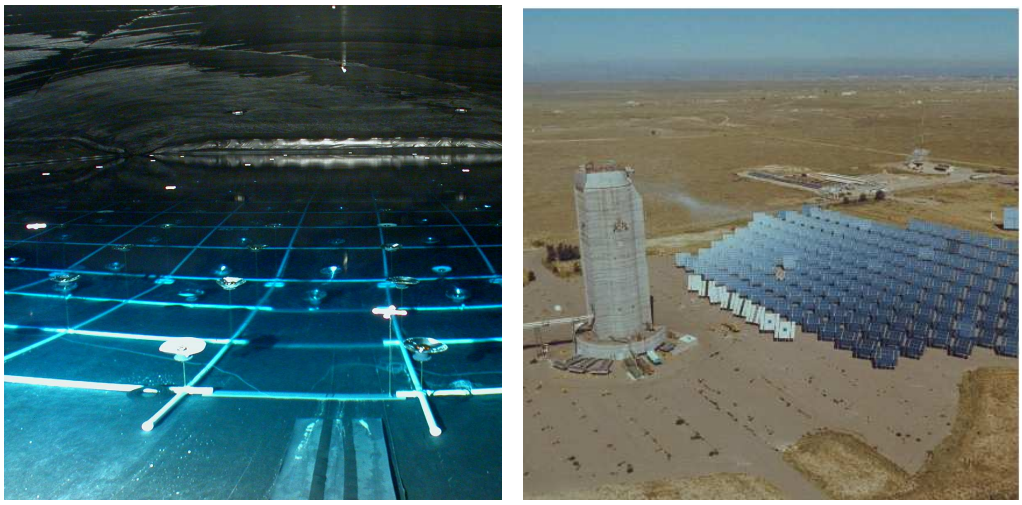

(a) Milagro **(b)** Stacee

Figure 1.6: The alternative ground-based very high-energy systems Milagro and Stacee.

technique to implement as each heliostat must be focused onto a single PMT. However, the very large mirror area allows an energy threshold below 100GeV which cannot be reached with single Cherenkov telescopes of the 10 m class. Currently, only the STACEE array (Bhattacharya et al., 1997) is operational, although previous experiments include CELSTE (Smith et al., 1997), Solar Two (Zweerink et al., 1999) and GRAAL (Arqueros et al., 2001). STACEE (Figure 1.6(b)) is the most advanced of these telescopes, using 1 GHz FADCs to help discriminate the hadronic background (Kildea, 2005).

1.4 Very High-Energy Gamma Rays Sources

There is a large range of objects that have been observed and detected at very high energies. The source types can be broken down into two main categories, namely galactic sources (Section 1.4.1) and extragalactic sources (Section 1.4.2). However there are three source families which by nature cannot be placed in either category - these are the unidentified sources (although these dark accelerators are more likely to be galactic in origin), dark matter which has not been detected, but can be sought from galactic or extragalactic observations and primordial black holes. These objects are discussed in Sec-

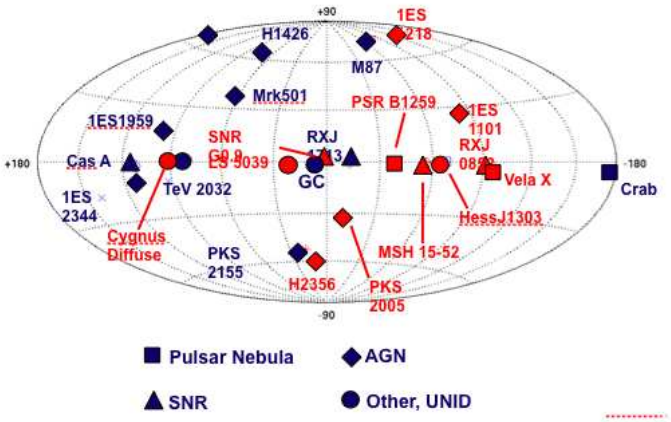

Figure 1.7: Map of the VHE sky in galactic coordinates in 2006. Many of the sources along the galactic plane shown in Figure 1.8 are excluded.

tion 1.4.3. Most of the sources that have been detected thus far at very-high energies are indicated in Figure 1.7.

1.4.1 Galactic Objects

The Milky Way galaxy is replete with objects that have the potential to be sources of high-energy non-thermal radiation. Indeed, the EGRET sky maps (Figure 1.2) indicate just how much non-thermal radiation is produced in the universe, and how much is produced in our own galaxy. In the last few years, the catalog of detected VHE galactic sources has expanded considerably, not least due to the galactic plane survey undertaken by H.E.S.S. (see Figure 1.8). The majority of point sources detected in our galaxy involve supernova remnants, however microquasars (including the one shown in Figure 1.9), diffuse emission and indeed the enigmatic galactic center have also been detected.

Supernova Remnants

There are a variety of forms that can follow a supernova explosion at the end of a large star's life. In some cases, the core of the star can remain as a compact object such as a neutron star, pulsar or black hole. This compact object is generally shrouded in material that was ejected during the explosion itself. This material, plus the compact object, is collectively known

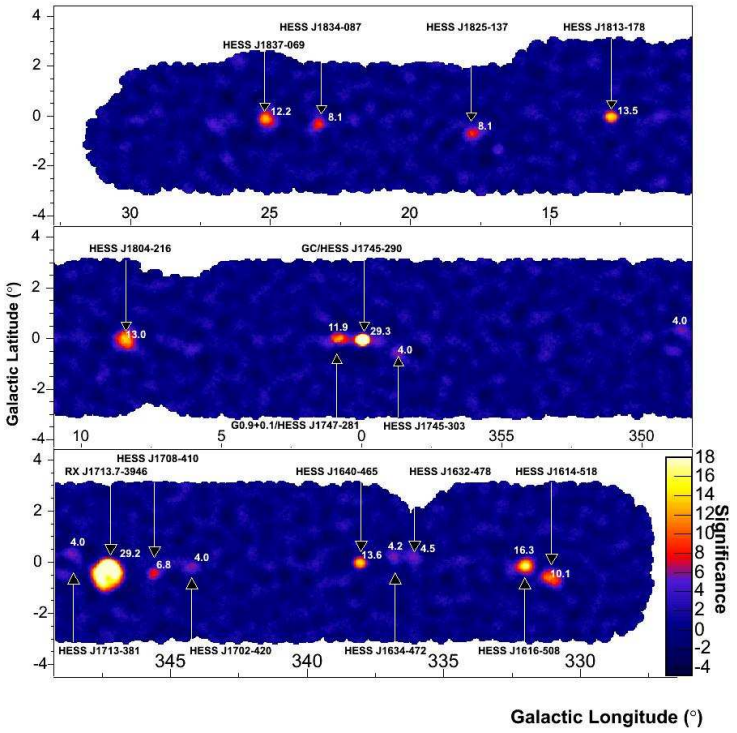

Figure 1.8: A deep scan of the central region of the galaxy ($\pm 30^\circ$ in latitude) along the plane ($\pm 3^\circ$ in longitude) (Aharonian, 2005b) revealed 14 new sources of VHE gamma-ray emission. Sensitivity reached 2% of the Crab Nebula flux above 200 GeV.

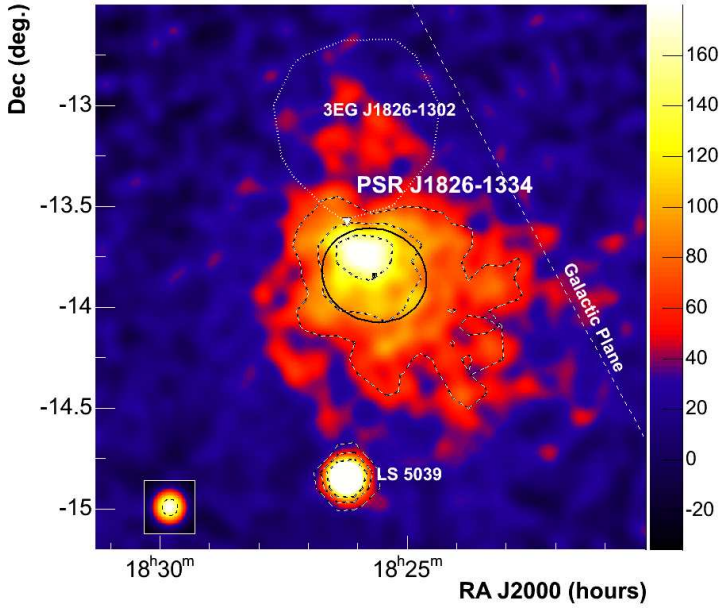

Figure 1.9: The pulsar wind nebula PSR J1826-1334 as observed by H.E.S.S. The field of view of this source harboured the source LS 5039 (Section 1.4.1). This was the first time two very high-energy sources were detected in a single field of view. Figure from Aharonian (2006c).

as a supernova remnant (SNR). Of most interest to high-energy astronomers is SNRs that contain pulsars - the rapidly rotating neutron stars the remain following the supernova explosion from a star of mass $3 - 5\,M_\odot$[1]. In cases where the pulsar is shrouded by stellar ejecta, the system is known as a *plerion*. A stream of energetic particles known as a pulsar wind is accelerated by the intense magnetic fields at the pulsar's surface. This wind interacts with the stellar ejecta resulting in the non-thermal emission of very high-energy gamma rays. This scattering to very high energies can take place as a result of synchrotron self-Compton processes.

Using the imaging atmospheric technique, the Crab Nebula (Figure 1.10), itself a plerion, was the first object to be reliably detected at very high energies (Weekes et al., 1989). The Crab Nebula has been independently detected by many high-energy experiments, and is regarded as a standard candle in the northern hemisphere given its steady emission and established flux and spectrum. Thus it is a primary target for many instruments both during the commissioning/engineering phase, and throughout regular observations in order to understand the instrument and to calibrate and optimise the analysis. A comparison of the measured Crab Nebula spectrum by many instruments is shown in Figure 1.11, indicating a relatively good cross calibration between independent experiments.

One of the primary motivations for studying SNRs is the connection to cosmic rays. Discovered in 1912, these enigmatic charged particles continuously strike the earth's atmosphere. Whereas their spectrum and composition can be measured, their origin is scrambled by galactic and extragalactic magnetic fields. SNRs is one of the favoured sources of high-energy cosmic rays by many theorists as supernovae contain both a tremendous source of energy, which is required for the acceleration of particles up to 10^{17}eV, and large quantities of matter available for acceleration. One of the most compelling pieces of evidence linking SNRs and the acceleration of charged particles is gamma-ray emission. Figure 1.12 shows gamma-ray emission from the shell type SNR RX J0852.0-4622. Overlayed are contours of smoothed x-ray data from the ROSAT All-Sky Survey with energies above 1.3 keV (Aharonian, 2005a). This correlation proves that particles are accelerated to multi-TeV energies in the shock waves of the supernova remnant. In the case of proton acceleration, high-energy gamma rays are produced via interactions with the gas, whereas in the case of electron acceleration, high-energy gamma rays are produced via synchrotron self-Compton emission. If the proton acceleration scenario is favoured, then such SNRs would be a primary candidate as the source of cosmic rays.

[1] $M_\odot$ refers to the mass of the sun

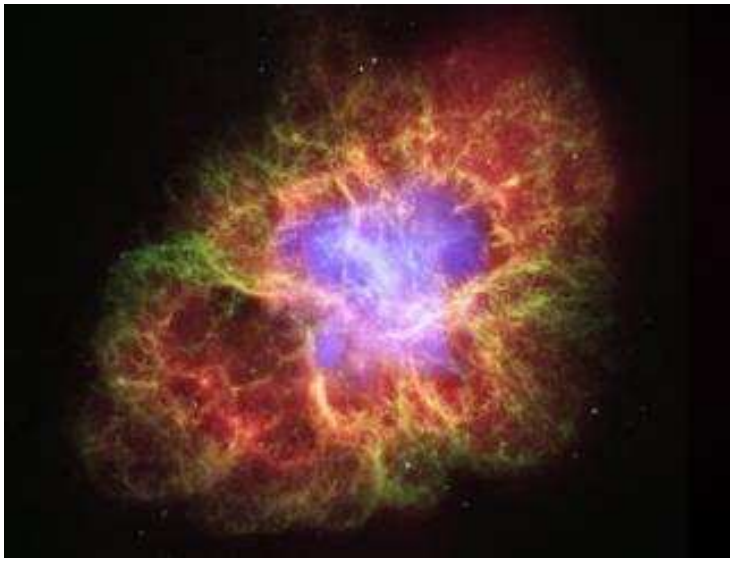

Figure 1.10: This composite image of the Crab Nebula combines data from Chandra, Hubble and Spitzer indicating emission in x-rays (blue-purple), optical (green) and infrared (red) wavebands.

Microquasars

A microquasar is a binary system comprising a dense compact object such as a black hole or neutron star, with a large star (eg a main sequence star) orbiting it. Matter is gravitationally removed from the surface of the large star and forms an accretion disk around the compact object. Radio observations indicate relativistic outflows, in which particles can be accelerated to extreme energies, similar to that observed in Active Galactic Nulcei (hence the name microquasar). The radio emission is attributed to synchrotron radiation of particles accelerated to high energies. VHE gamma-rays can be produced by inverse Compton scattering of the stellar photons by relativistic electrons, although hadronic processes may be more efficient, such as the neutral pion decay following interactions with non-relativistic stellar-wind ions. VHE photons can be attenuated via pair production on the stellar photon field in the environment of the donor star, redistributing the energy to lower frequencies. The first microquasar to be detected at very high energies was LS 5039 (Aharonian et al., 2005b), with a second microquasar LS I+61 303 discovered shortly thereafter (Albert et al., 2006a). Orbital modulation was found with both sources, indicating either that absorption or periodic emission could be taking place. This is explained in the case of LS 5039 (Figure 1.13) where gamma-ray emission peaks at inferior conjunction. The

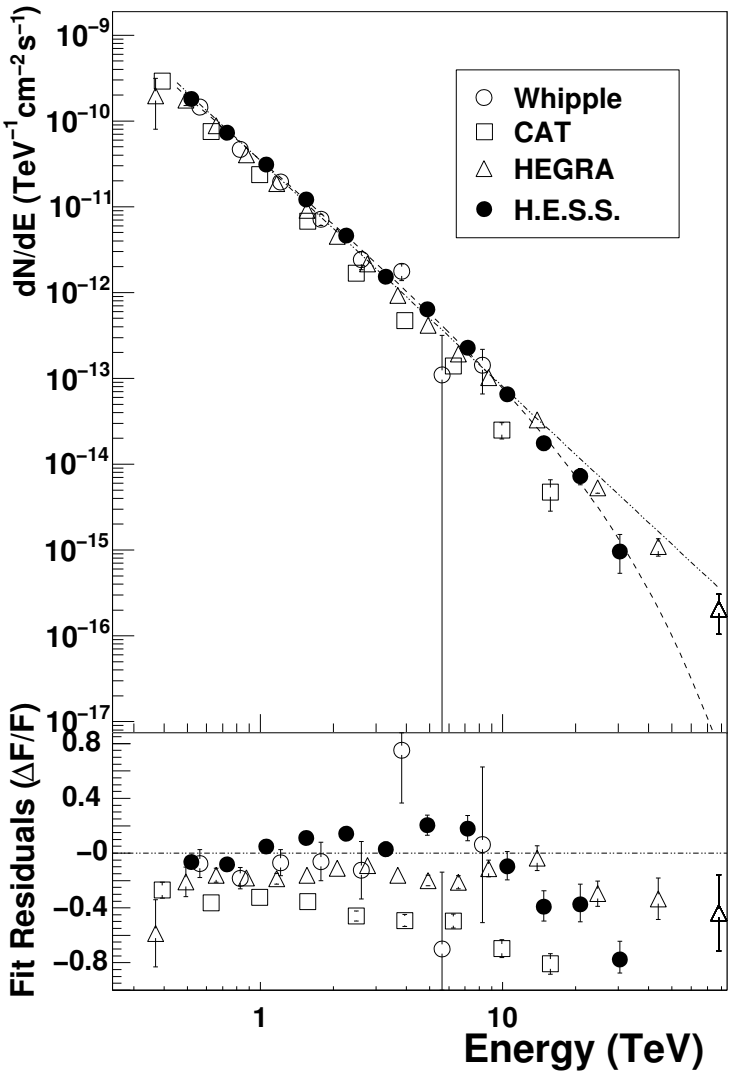

Figure 1.11: Cross comparison of measured spectrum of the Crab Nebula by four major ground-based instruments. All experiments are in good agreement, apart from the CAT telescope which shows some curvature at high energies. Figure from Aharonian (2006e).

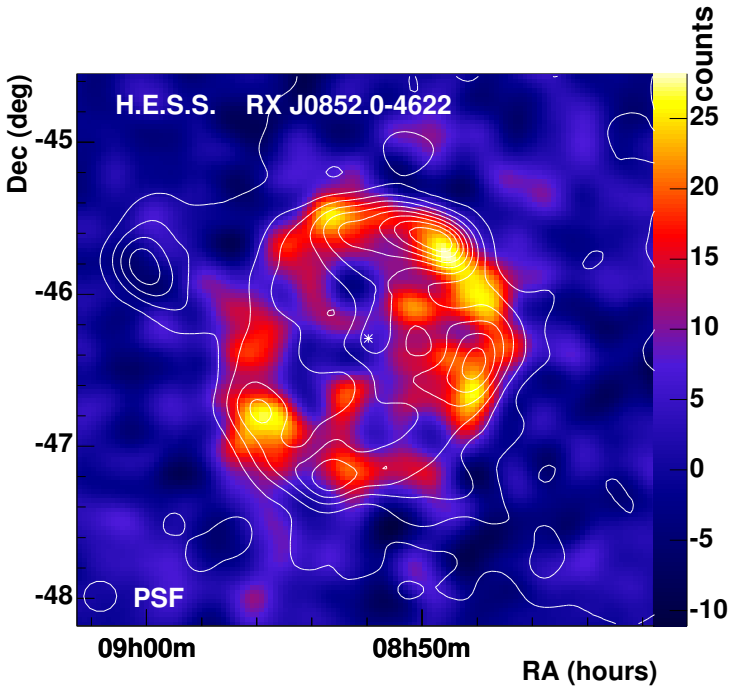

Figure 1.12: Map of very high-energy gamma-ray emission from the shell-type supernova remnant RX J0852.0-4622. Overlayed are the ROSAT All-Sky Survey x-ray contours, indicating a close correlation between gamma-ray and x-ray emission. Figure from Aharonian (2005a).

cross section for absorption varies with the angle θ as $1/(1-\cos\theta)$ between the VHE gamma rays and the optical photons. Thus the level of absorption depends on the geometrical arrangement between the VHE gamma-ray production region, the star and the observer. At inferior conjunction the VHE gamma rays are parallel to the stellar photons, minimising absorption. That this absorption has been observed implies that gamma-ray production takes place within the optical photon field of the star, and that the emission region is not significantly larger than the orbital size, or it would be smeared out over orbital phases. However, the absorption process is not fully understood as the flux at 0.2 TeV is quite stable, which is where the strongest absorption would be expected. The spectral hardening could be related to the change in magnetic field strength as the compact object approaches apastron, which happens to be close to inferior conjunction in this case. The flux is shown as a function in phase in Figure 1.14.

Diffuse and Extended Emission

Much of the high-energy gamma radiation detected by EGRET was diffuse, with EGRET skymaps indicating point sources against a backdrop of diffuse emission (Figure 1.2(a)). Diffuse emission can only be detected by a Cherenkov imaging telescope if the region of emission is larger than the point spread function of the telescope. Diffuse emission was first reported from observations of the Cygnus region (Aharonian et al., 2002), although gamma-ray emission from that region had already been reported by Neshpor et al. (1995). The source, designated TeV J2032+4130, was also detected at marginal significance in Whipple archival data (Lang et al., 2005). The final analysis of the HEGRA data (Aharonian et al., 2005a) indicates an extended source with a hard spectral index of 1.9 (Figure 1.15). The integral flux above 1 TeV amounts to 5% of the Crab Nebula flux, which is lower than the flux reported by the Whipple and Crimean observatories. There are no known counterparts in x-ray or radio data. Diffuse emission is also reported by Milagro (Smith, 2005), who indicate that the Cygnus region is the brightest part of the sky in TeV gamma rays (apart from the Crab Nebula). They argue that the Milagro detector, with its large field of view and high duty cycle, is better suited to searches for large areas of diffuse emission than pointed Cherenkov telescopes. Cherenkov telescopes are more suited to point source analysis as they rely on angular measurements of events to discriminate background, however their superior sensitivity makes them more suitable for searching for objects with variable or low flux.

Gamma-ray emission from TeV J2032+4130 may be associated with stellar winds from the member stars in Cygnus OB2. Such winds could pro-

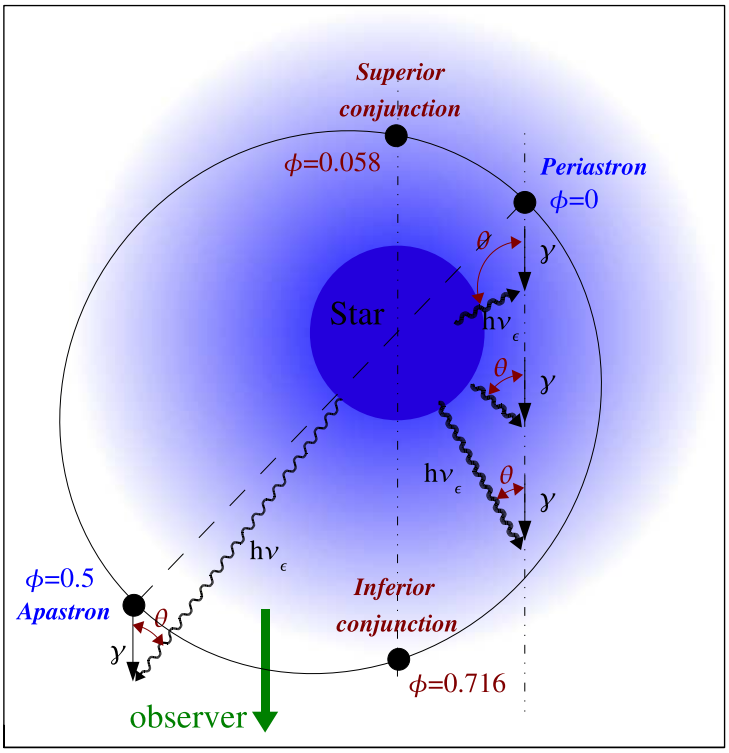

Figure 1.13: The orbital geometry of the VHE gamma-ray emitting microquasar LS 5039. The system consists of a main sequence star orbited by a compact object (assumed to be a neutron star or stellar mass black hole). Periastron and apastron are the points of closest and farthest approach of the elliptically orbiting compact object. Superior conjunction is the geometrical point (observer specific) where the star eclipses the microquasar (with the reverse for inferior conjunction). VHE gamma rays are produced in a region near the compact object and absorbed via pair production by photons produced by the star itself. At inferior conjunction, the angle between VHE gamma-ray emission and stellar photon emission becomes zero, which minimises the absorption. Thus for intrinsically steady emission, the observed gamma-ray rate is modulated by the orbital frequency. Figure from Aharonian (2006a).

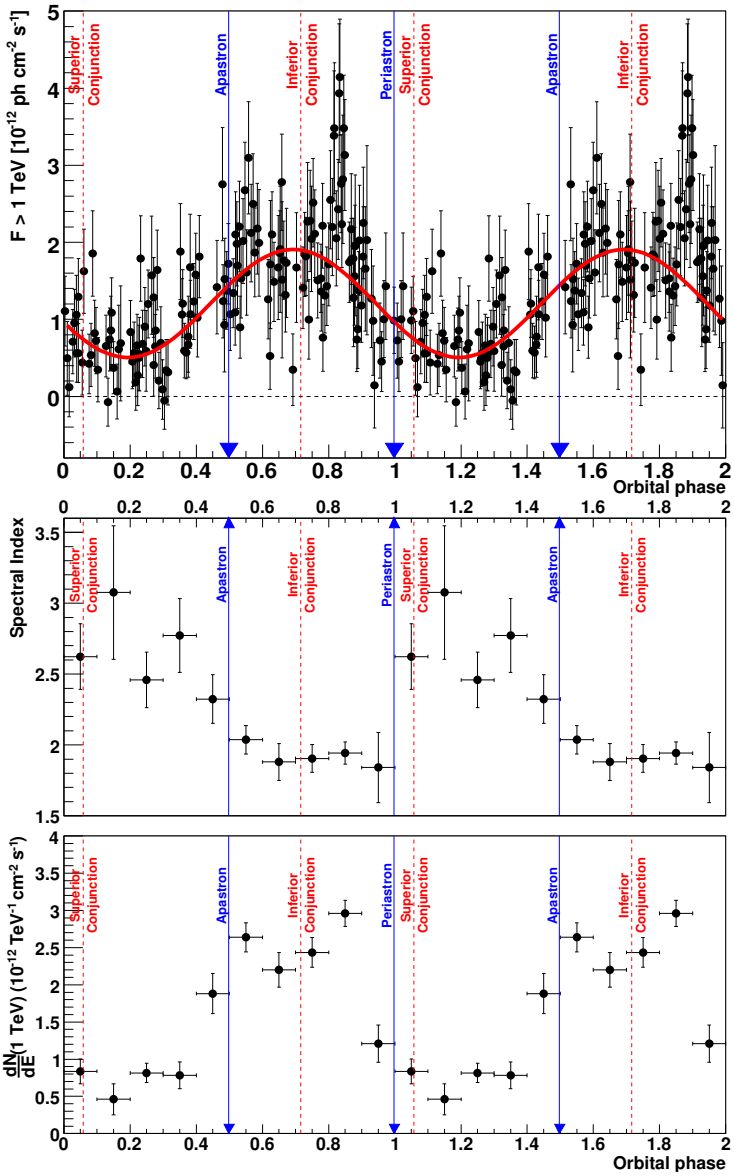

Figure 1.14: Top: Integral gamma-ray flux above 1 TeV for LS 5039 folded with an orbital ephemeris. Middle: Power law spectral index by phase, indicating a spectral hardening near periastron. Bottom: Power law normalisation (at 1 TeV) versus phase. Figure from Aharonian (2006a).

vide conditions conducive to stable or strong shock acceleration of particles to very high energies, with leptonic and hadronic gamma-ray emission channels available. An alternative scenario involves the nearby microquasar Cygnus X3, itself previously reported as a source of VHE gamma rays. In that model VHE gamma rays are produced at the termination shock between the microquasar jets and the interstellar medium, although it could merely be a cosmic coincidence that the northern jet lines up well with TeV J2032+4130. Upcoming observations with northern hemisphere third generation Cherenkov Telescopes such as VERITAS and MAGIC, may localise the source of emission, and solve the mystery of VHE gamma-ray emission from TeV J2032+4130.

Diffuse gamma-ray emission has also been detected from the galactic center ridge (Aharonian, 2006b). Wide field scanning exposures led to the detection of VHE gamma-ray emitting regions consistent with Sgr A* and the supernova remnant G 0.9+0.1, as well as apparent diffuse emission extending along the plane (Figure 1.16 upper). Subtracting these sources away indicates a large region of diffuse emission (Figure 1.16 lower). In the lower figure, the white contours trace CO emission indicating the presence of giant molecular clouds. This observed correlation is unique and constitutes a persuasive argument that the VHE emission is related to the molecular clouds. In this case, VHE emission could be produced by interactions with cosmic rays, where the cosmic rays are accelerated by a nearby supernova remnant or by some process related to Sgr A* itself.

Galactic Center

The Galactic Center is believed to harbour a supermassive black hole, referred to as Sgr A*, with a mass of 2.6×10^6 $M_\odot$ (Schödel et al., 2002), and has recently been identified as an emitter of x-rays and infrared radiation. Although the general environment of the galactic center was detected with EGRET, its poor angular resolution coupled with the diffuse glow of high-energy radiation from the region made it difficult to draw conclusions. Energy from the galactic center is generally attributed to the release of gravitational energy due to accretion of stellar winds onto the black hole. There are a variety of mechanisms by which very high-energy gamma rays can be produced in such a region, including electron or proton shock acceleration in the stellar winds, annihilation of dark matter particles (Section 1.4.3) or curvature radiation of protons near the singularity. Detection of VHE gamma-ray emission from the galactic center was reported by three experiments in 2004 (Aharonian et al. (2004b); Kosack et al. (2004); Tsuchiya et al. (2004)), although the H.E.S.S. data is by far the most sensitive, indicating a hard

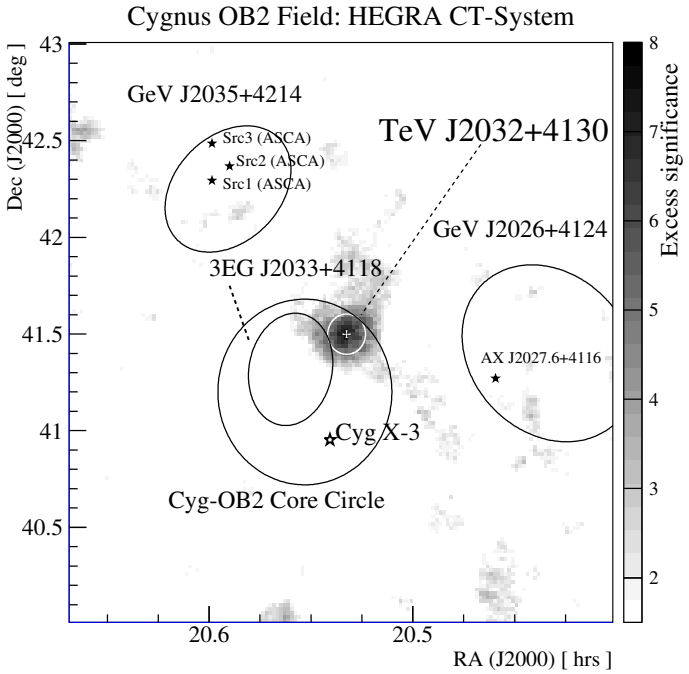

Figure 1.15: Distribution of significance as observed by HEGRA (Aharonian et al., 2005a) in the region of TeV 2032+4130. Also shown are various unidentified EGRET sources, whose large error circle makes firm identifications difficult. The OB2 region is also shown, as it may be related to the VHE gamma-ray emission (see text).

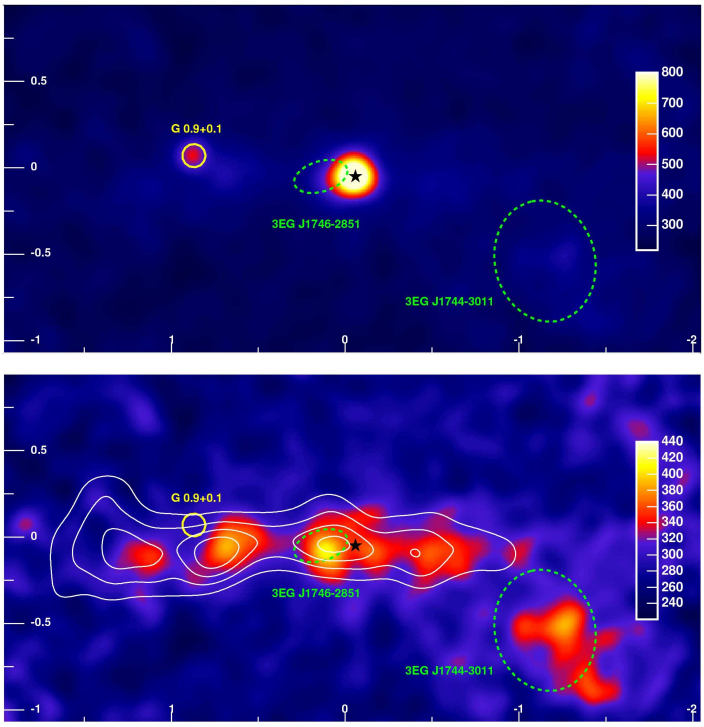

Figure 1.16: The Galactic Ridge. Top: H.E.S.S. view of the Galactic center. Evident are two strong sources, one coincident with Sgr A* and another coincident with G 0.9+0.1. Bottom: The same region with the two strong sources subtracted, indicating a pronounced and extended diffuse emission region. The white contours indicate CO emission, signalling the presence of giant molecular clouds, which are almost certainly related to the diffuse emission of VHE gamma rays. Image from Aharonian (2006b).

spectrum of 2.21 ± 0.09 with a flux of $(2.50 \pm 0.21) \times 10^{-8}\,\mathrm{m}^{-2}\,\mathrm{s}^{-1}$. Follow up observations in 2004 by the H.E.S.S. array extend the spectral measurements to 20 TeV which all but excludes dark matter annihilation as a source of VHE emission (Rolland, 2005). The source is also steady, on all timescales for which sufficient statistics are available, which generally rules out processes close to the black hole itself (such as curvature radiation). Rather, the location of the excess, considering errors, is consistent not only with Sgr A* itself, but also with the supernova remnant Sgr A East. The excess itself appears slightly diffuse, and an extraction of that excess (assuming it to be a point source) and another nearby point source associated with SNR G0.9+0.1 reveals a diffuse excess along a plane in the region of the galactic center.

1.4.2 Extragalactic Objects

Before the 1990's it was generally assumed that only galactic sources of very high-energy gamma rays could be detected. That changed however with the advent of the imaging technique which increased the sensitivity to a regime where such objects became detectable. Not surprisingly, the most powerful class of object, the blazar, was the first to be discovered. However this was soon followed by the detection of the radio galaxy M87. Searches are also currently being undertaken for very high-energy emission from starburst galaxies and gamma-ray bursts.

Blazars

As one of the major subjects of this thesis, blazars are discussed in detail in Chapter 3, however they are briefly mentioned here for context. Active Galactic Nuclei (AGN) are galaxies whose bright central cores outshine the rest of the host galaxy. The central engines of AGN are believed to harbour supermassive black holes, with gravitational energy released to an accretion disk feeding the prodigious output. In many cases, relativistic plasma jets emanate perpendicularly away from the planes of the galaxies. Those AGN whose jets are orientated with us are classified blazars, and can produce high and very high-energy emission which can be relativistically beamed towards us. The EGRET experiment detected 66 such blazars (Hartman et al., 1999) in the high-energy regime. The first detection of very high-energy gamma rays from a blazar was from Markarian 421 by the Whipple 10m (Punch et al., 1992). This exciting discovery heralded a new era in high-energy astrophysics, with the detection of very high-energy gamma radiation from a second extragalactic source Markarian 501 occurring shortly thereafter (Quinn et al., 1996). The investigation of AGN at very high energies

has the potential to shed light on one of the most violent and energetic regions of the universe, and can help to probe the infrared component of the extragalactic background light. Significant progress on this has already been made by Aharonian et al. (2006b), with initial results indicating the universe may be more transparent to VHE gamma rays than previously thought (this is expanded upon in Section 3.8).

Radio Galaxies

Radio galaxies are considered to be off-axis AGN, with the primary jet making an angle of perhaps $> 20^\circ$ with the observer. Radio galaxies exhibit jets with spectacular lobes far outside the visible part of the galaxy. The radio emission is thousands of times that of a normal galaxy, indicating the presence of relativistic particles. Nearby radio galaxies include Centaurus A and Cygnus A. These galaxies could potentially be significant sources of cosmic rays, if indeed cosmic rays have an extragalactic origin. Centaurus A was the only extragalactic object that all four of the CGRO instruments detected. High-energy gamma-ray radiation can be produced using the same mechanisms that produce high-energy gamma-ray radiation in blazars (Section 3.7), but at a much lower luminosity due to the line of sight. The nearby radio galaxy M87, which contains a supermassive black hole of mass $2 - 3 \times 10^9\,\mathrm{M}_\odot$ and with jet angle $30^\circ - 35^\circ$ has been detected at very high energies by the HEGRA collaboration (Aharonian et al., 2003) at a marginal significance of $4.1\,\sigma$. The limited number of excess events make it difficult to draw conclusions from the spectral analysis, however follow up observations with third generation Cherenkov telescopes should provide more information on the acceleration mechanisms.

Starburst Galaxies

Starburst galaxies are galaxies harbouring regions of intensive star formation, associated with a dense interstellar medium and an unusually high supernova rate. Such regions are expected to have extremely high levels of cosmic-ray production, given the theorised relation between supernova remnants and cosmic-ray acceleration. The cosmic-ray interaction rate may produce a detectable level of very high-energy gamma rays. Diffuse emission from the starburst galaxy NGC 253 was reported by the CANGAROO collaboration (Itoh et al., 2002) in excess of 500 GeV with a morphology matching the optical extent of the galaxy itself. However a far more sensitive search using the H.E.S.S. array (Aharonian et al., 2005e) reported upper limits far below the flux estimates of CANGAROO. Source variability seems unlikely, indicating

that one of the analyses may be erroneous. Further searches by the Whipple 10m telescope of the starburst galaxies IC342, M81, M82, and NGC3079 are reported in Nagai (2005) with upper limits placed on all four objects.

Galaxy Clusters

On very large scales, the universe is composed of clusters of galaxies. Often, the matter density in these regions can be relatively high, which could give rise to environments favourable to the acceleration of VHE gamma rays. In galaxy clusters, structure formation shocks are primary sources of the non-thermal energy of particle populations. Galactic winds may also be a source of particle acceleration. Already there is evidence for non-thermal electron populations in some clusters with the detection of diffuse synchrotron radio halos and radio relic sources. Also, an excess of hard x-ray radiation has been observed that could be attributed to inverse Compton scattering involving populations of relativistic electrons, with the jump to gamma-ray energies impossible to rule out from theoretical circumstances alone. Gamma-ray emission is also possible through hadronic channels (see Section 3.7.2 for a further explanation of this process), or dark matter annihilation (Section 1.4.3). Searches for VHE gamma-ray emission from such candidates as the Perseus and Abell 2029 galaxy clusters have been undertaken (Perkins et al., 2006) yielding null results, however there is as yet no deep exposures reported with third generation Cherenkov telescopes.

Gamma-Ray Bursts

The first Gamma-Ray Burst (GRB) was discovered quite accidentally in the 1960's by the VELA series of satellites. Although these satellites were almost perfectly matched to detecting gamma-ray bursts, their primary objective was to detect a burst of gamma-ray radiation indicative of a nuclear blast that would have signalled a breach of the nuclear test ban treaty between the United States and the Soviet Union. By design, the instruments were sensitive to gamma radiation, not only from the earth's surface, but also from space, in case a test was attempted behind the moon. It was some years after the detection of many such events, that it was realised that this was a new astrophysical phenomenon (Klebesadel et al., 1973). Over the following years, this discovery sparked heated debate between astrophysicists, who attempted to explain the origin of these powerful events. The CGRO instrument BATSE recorded 2704 gamma-ray bursts (Figure 1.17), and was able to determine from their distribution that the bursts could not originate in the galaxy (at least not in the galactic plane, although they could still have

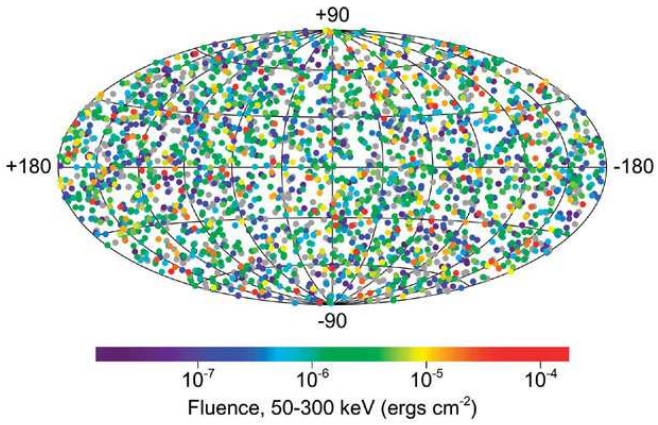

Figure 1.17: Distribution in galactic coordinates of gamma-ray bursts as recorded by BATSE. This map proved with almost complete certainty that GRBs did not originate in our galaxy.

originated in the galactic halo, if not indeed the Oort belt). In 1997, the multitasking BeppoSax satellite, which was equipped with a GRB monitor and narrow field x-ray telescopes, discovered a fading x-ray afterglow associated with a GRB (Costa et al., 1997). Interestingly, such an afterglow had been predicted by some cosmological GRB models. Within hours of the discovery, ground-based telescopes, connected via the BATSE Coordinate Distribution Network, recorded a slowly fading optical excess from the location of the burst. This location turned out to harbour what appeared to be a distant galaxy.

Accounting for the energy of these events, using simple inverse square laws indicated an intrinsic energy that was inconceivable. Modern theories however, describe a relativistic fireball, occuring perhaps due to the merger of two neutron stars, or the merger and/or production of a singularity, with the energy release beamed into symmetric jets. Some of these theories predict prompt or delayed emission in the very high-energy gamma-ray regime, although no such detections have yet been established. Search techniques for GRBs with ground-based gamma-ray telescopes require extremely rapid dissemination of the burst coordinates from space-based observatories, and fast reaction and slew times from the ground-based telescopes. With this in mind, all orbital observatories use the Galactic Coordinate Network to communicate with ground-based telescopes, and some gamma-ray telescopes employ extremely rapid slewing technology in an attempt to catch the burst (Bastieri et al., 2005).

1.4.3 Other Sources

There are some objects which can not necessarily be associated with either galactic or extragalactic objects. These are the already discovered unidentified sources, dark matter and primordial black holes.

Unidentifieds

In amassing an impressive catalog of gamma-ray sources, the EGRET experiment also left a legacy of unidentified sources. For the most part, this was due to the poor angular resolution of EGRET and the large error boxes it placed around many detections. Recently, ground-based telescopes have detected unexpected and otherwise unknown objects in their fields of view. The first of these was TeV J2032+4130, which has no confirmed counterpart at other wavelengths (although there is a strong suggestion that it has an OB association). This object has been detected by two independent telescopes, with the source most likely extended. Very recent radio observations with the Westbrook Synthesis Radio Telescope by Butt et al. (2006) and the Giant Meterwave Radio Telescope by Paredes et al. (2006) indicate regions of radio emission spatially coincident with TeV J2032+4130. The emission points to the existence of a jet-like, dual lobed non-thermal radio source, which could be either a microquasar, or an off-axis background blazar (analogous to M87). The latest TeV observations reported by the Whipple 10m observatory (Konopelko et al., 2006) and Milagro (Abdo et al., 2006) indicate the existence of a single strong source, with a potential source very nearby. Following the H.E.S.S. galactic plane survey, several unidentified sources were reported, although some of these were subsequently associated with other objects after follow up radio and x-ray observations. The question remains whether all these unidentified objects will at some point be associated with other more mundane objects, or whether there is a new class of dark accelerator that has been uncovered. A good argument could be made that the dark accelerators are galactic in nature, given their discovery along the galactic plane, however one must be cautious of reading too much into this given the selection effects.

Dark Matter

It is somewhat unsettling to know that we do not know what most of the universe is made of. At least 30 % of the universe is believed to be made of dark matter, a non-baryonic material whose existence can only be inferred by its gravitational influence on the baryonic matter around it. Ground-based gamma-ray observatories can in principle detect dark matter from its

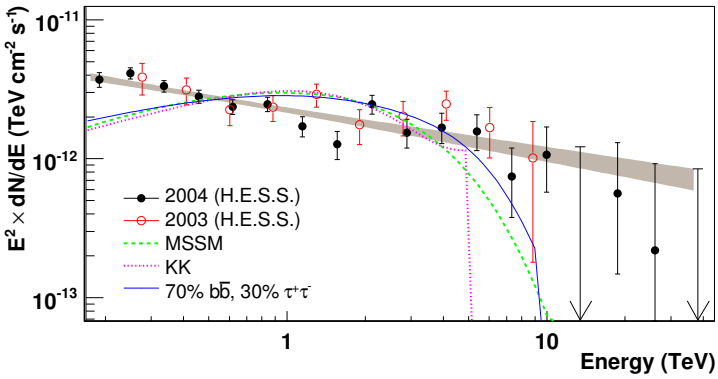

Figure 1.18: Attempt to understand the VHE gamma-ray emission from the galactic center using Dark Matter models. The models examined by Aharonian (2006d) are ruled out with these data (see text).

high-energy annihilation products. Such decay products can be sought from sources on many scales, from globular clusters in our own galaxy such as M3, M5 and M13, the galactic center, and in galaxy clusters such as the Coma Cluster.

One of the prime dark matter candidates that could be detected with this method is the neutralino, although most models do not indicate neutralinos generating spectra beyond 10TeV. Classical supersymmetric neutralino models predict strongly curved spectra, whereas Kaluza-Klein dark matter particles have flatter spectra (Bergström et al., 2005) - however neither model is consistent with the H.E.S.S. galactic center spectra (Aharonian, 2006d), which all but rules out neutralino annihilation as the dominant source of VHE gamma rays from the region (Figure 1.18).

Primordial Black Holes

Using classical (ie non-quantum) arguments, black holes are singularities that emit no radiation. They cannot emit radiation as their mass curves space time back in on itself so that no radiation can escape beyond a region known as the event horizon. However, Hawking (1974) applied quantum mechanical arguments to the region close to the event horizon, and predicted that black holes could loose energy. This energy loss occurs if a virtual particle-antiparticle pair is produced close to the event horizon. If one of the particles is captured by the singularity, mass from the singularity must be given to the other particle, allowing it to escape. By this process, the black hole *evaporates*, with the evaporation rate inversely proportional to

the square of the mass of the black hole. Stellar mass black holes radiate very slowly, with their radiation virtually impossible to detect. However, if miniature black holes were created in the early universe, then their mass could be small enough to produce significant radiation now. Radiation from such *primordial* black holes could be observable by detecting the burst of gamma rays associated with the final stages of evaporation. Reports and upper limits from such searches can be found at Porter and Weekes (1979); Connaughton et al. (1998); Linton et al. (2006).

1.5 Guide to Thesis

This thesis concerns the astrophysical observation of, and search for, very high-energy gamma-ray sources with the new VERITAS array of Cherenkov imaging telescopes. The sources that are observed and analysed are the Crab Nebula (primarily for the purposes of calibration and optimisation) and the blazars 1ES 0647+250, 1ES 0806+524 and 1ES 2344+514. The Cherenkov imaging technique is described in Chapter 2, with emphasis on the particle processes in the atmosphere and the production of Cherenkov radiation. In Chapter 3, the current understanding of AGN is described. This includes a description of the standard AGN unification model, and a comparison of leptonic and hadronic emission models. A detailed review of the VERITAS telescopes is given in Chapter 4. In Chapter 5, an outline of the standard analysis used by VERITAS is presented. Particular emphasis is placed on the early stages of analysis, especially regarding calibration and the treatment of FADC data, as this is core to the work done for the dissertation. Chapter 6 presents a more sophisticated analysis of the FADC data, invoking techniques that go beyond what is presently regarded as the standard analysis. In Chapter 7, an overview of how the Crab Nebula and blazar data were analysed is given, with a study of how the application of the extra FADC analysis techniques effect the results. Finally Chapter 8 presents the conclusions of this work.

Chapter 2

Detection of VHE Gamma Radiation

When Victor Hess discovered a population of cosmic charged particles striking the earth's atmosphere in 1912, it became clear there existed energetic sources in the universe that exceeded even our own sun's remarkable output. Since that time, many experiments have been built in an attempt to uncover the source of these cosmic rays, however such efforts are hampered by the intrinsic difficulties associated with determining the source of origin of a cosmic charged particle. Quite simply, the particle's trajectory through space is determined by the intervening magnetic fields, such that its arrival trajectory at the earth has no bearing on where it came from. The detection of high-energy photons is far more useful however, as having no charge they retain their source of origin in their trajectory when they arrive at the earth. Unfortunately for gamma-ray astronomers (but fortunately for human life), the atmosphere constitutes a shield against high-energy photons, and is virtually opaque above about 10 eV. The radiation depth of the atmosphere is $1030\,\mathrm{g\,cm^{-2}}$, and given a radiation length of $37.1\,\mathrm{g\,cm^{-2}}$ implies an atmospheric thickness of about 28 radiation lengths. Because of this, any astronomical instrument capable of detecting photons more energetic than 10 eV must be placed *above* the atmosphere. The cost of placing satellites in orbit is exorbitant, but manageable if the required telescope collection area is small. Most orbital observatories have collection areas of a few tens or hundreds of square centimeters. However, all cosmic sources of high-energy emission exhibit steeply falling spectra, with extremely low fluxes in the GeV/TeV regime. An orbital observatory with the aforementioned collection area would only detect a few TeV photons per year. This would not be sufficient to map the cosmos in TeV photons.

It is fortuitous that the photon energy at which it becomes impractical

to use an orbital observatory to detect high-energy photons, roughly coincides with the energy at which the reaction products of those photons in the atmosphere become detectable. Upon entering the atmosphere, a high-energy photon initiates an electromagnetic cascade resulting in a shower of relativistic leptons which emit Cherenkov radiation. Due to the brevity and relative intensity of the Cherenkov radiation, it can be detected against the background of night sky noise using a mirror, photomultiplier tube and fast counting electronics. An enhancement to this simple system is to use an array of photomultiplier tubes in the plane of the mirror to image the shower. Such imaging allows discrimination against the overwhelming background of extensive air showers caused by cosmic rays.

In this chapter, the principles involved in detecting very high-energy gamma rays are presented. A review of physical processes (Section 2.1) that are important in the development of extensive air showers are discussed, followed by a summary of the Cherenkov radiation phenomenon (Section 2.2). Once these important aspects are covered, the extensive air shower itself can be considered in the context of gamma-ray initiated showers (Section 2.3.1) and cosmic-ray initiated showers (Section 2.3.2). Finally an overview of the technique used to detect showers initiated by high-energy gamma rays is overviewed (Section 2.4).

2.1 Review of Physical Processes

There are a number of important reactions that will be used in considering the development of extensive air showers. These reactions are split into two simple categories, those concerning interactions between charged particles and matter, and those concerning interactions between photons and matter.

2.1.1 Charged Particle - Matter Processes

There are three matter-radiation processes that will be considered. These are Brehmstrahlung radiation, Coulomb scattering and ionisation.

Brehmstrahlung Radiation

Brehmstrahlung (or braking) radiation, can be considered classically as the emission of radiation by a charged particle such as an electron due to scattering in an electric field (see Figure 2.1(a)). The electric field can be highly localised, such as that due to an atomic nucleus, or that due to an atomic electron. The emission probability varies inversely as the square of the particle mass, thus for electrons the cross section for Brehmstrahlung radiation

is many orders of magnitude greater than for muons. The emission probability is also strongly determined by the strength of the electric field, thus screening by atomic electrons is significant, and Brehmstrahlung radiation is only likely to occur once the atomic electron barrier has been breached. Thus the cross section is not only effected by the electron's ability to breach the barrier (ie its incident energy) but also the strength of the barrier (ie the atom's atomic number Z).

Coulomb Scattering

Coulomb scattering is a simple electromagnetic effect between two charged bodies. In this case the important reaction is that between an electron and a nucleus, with the energy imparted to the nucleus being relatively small (see Figure 2.1(b)). There are three important scattering regimes determined by the number of times a given electron undergoes a scattering reaction within a medium. For a single reaction, the process is known as *single* scattering, for < 20 reactions, the process is known as *plural* scattering and for > 20 reactions the process is known as *multiple* scattering. This break is important since for multiple scattering, statistical processes can be used to determine the average final electron distribution (angular and energy), whereas plural scattering must be modelled as a series of single scatterings.

Ionisation

Ionisation is the removal of an electron from an atomic orbital due to an inelastic collision with an incoming electron (see Figure 2.1(c)). The primary ejected electron is sometimes called a δ-ray. This δ-ray can cause secondary ionisations if its energy is sufficiently high.

2.1.2 Photon - Matter Processes

There are three photon-matter processes that are important to consider. These are the photoelectric effect, Compton scattering and pair production. The cross section for each reaction is a strong function of the photon energy (see Figure 2.2), with the photoelectric effect dominating at low energies ($<$ 1MeV), Compton scattering dominating at intermediate energies ($<$ 10MeV) and pair production dominating at high energies ($>$ 20 MeV). One of the primary differences between charged particle - matter reactions and photon - matter reactions is that for a beam of photons, the photon energy is not attenuated by the matter, only the intensity is attenuated. If a reaction

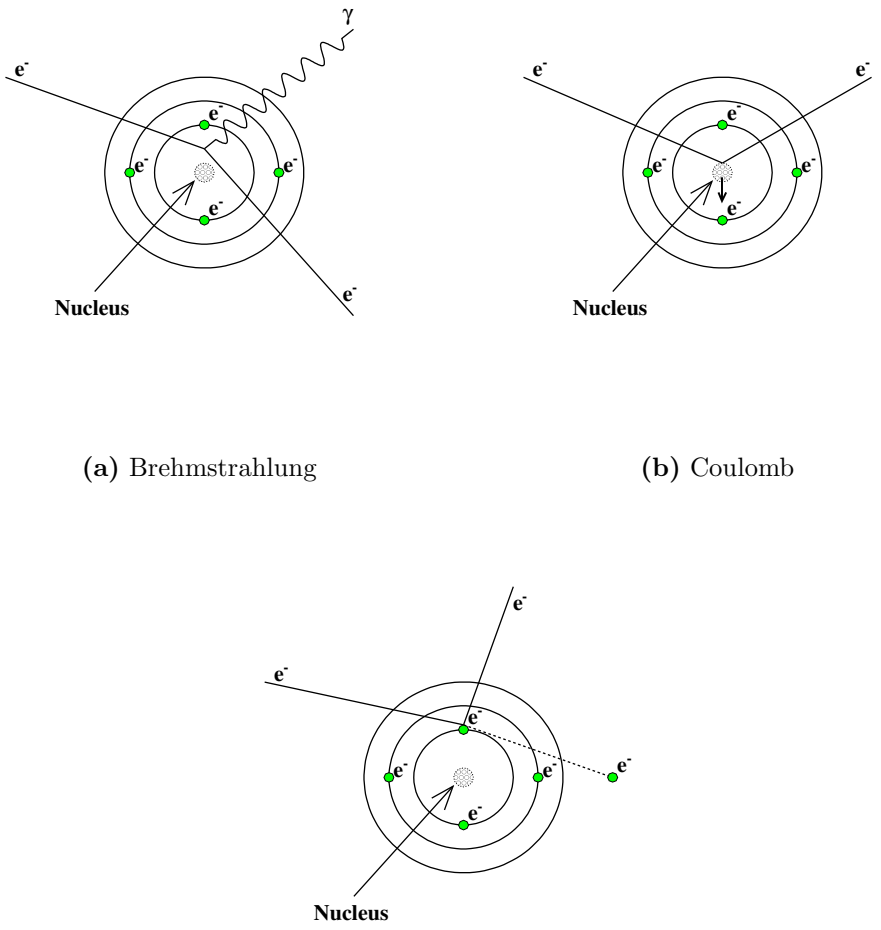

(a) Brehmstrahlung

(b) Coulomb

(c) Ionisation

Figure 2.1: Figure depicting Brehmstrahlung radiation, single Coulomb scattering and ionisation. In all cases an electron is incident on the atom from the left hand side of the diagram.

occurs (via absorption or scattering), the photon is completely removed from the beam.

Photoelectric Effect

The photoelectric effect is the total absorption of an incident photon by an atomic electron (see Figure 2.3(a)). This absorption results in the electron being ejected from the atom with energy E given by

$$E = h\nu - W \tag{2.1}$$

where h is Planck's constant, ν is the photon frequency and W is the binding energy of the electron. The recoil momentum of the reaction is absorbed by the nucleus (which is why the photoelectric effect only occurs with bound atomic electrons). The cross section for the photoelectric effect is low at high energies, but increases rapidly as the energy of the outermost binding electron is reached.

Compton Scattering

Compton scattering is the scattering of photons on free electrons (Figure 2.3(b)), as opposed to bound electrons in the case of the photoelectric effect. However if the photon energy is very high, the binding energy of an electron can be ignored and treated as a free electron. In low-energy reactions, Compton scattering is governed by the Thompson cross section, whereas for high-energy reactions, scattering is governed by the Klein-Nishina cross section. Compton scattering can also occur in the inverse case, where an electron up-scatters a photon (Section 3.7.1).

Pair Production

Pair production is the conversion of a high-energy photon into an electron-positron pair (see Figure 2.3(c)). The photon's energy must exceed a critical energy given by the sum of the electron and positron rest masses (1.022MeV) in order for pair production to occur. Also, the reaction must occur close to a third body such as a nucleus so that momentum can be conserved. As is the case with Brehmstrahlung radiation, screening by atomic electrons is important, as the incoming photon may undergo a Compton scattering with a bound electron.

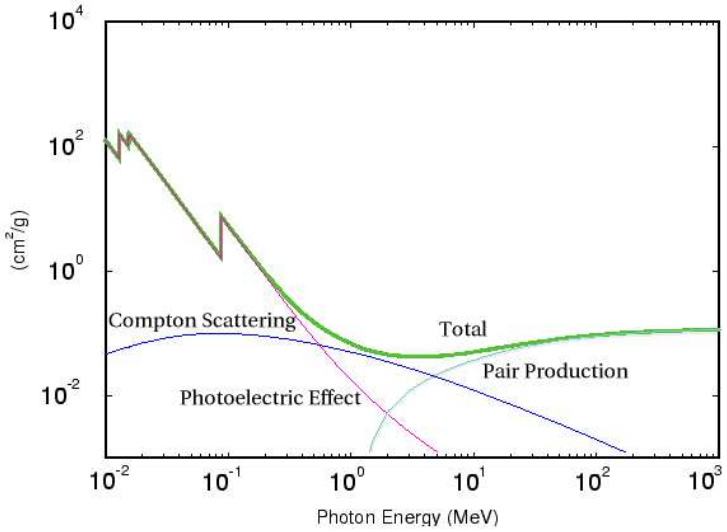

Figure 2.2: Contribution to the total cross section for photons interacting with electrons as a function of energy by the photoelectric effect, Coulomb scattering and pair production. Figure taken from Gammell (2004).

2.2 Cherenkov Radiation

When a charged particle travels through a dielectric medium, it has a polarising effect on the atoms or molecules around it causing them to briefly radiate as they relax to their original state (Jelley, 1958). As the polarisation is symmetric about the charged particle, the radiation emitted by the medium is incoherent and no significant radiative output is observed (Figure 2.4(a)). If the particle is travelling faster than the phase velocity of light in the medium, then its own electromagnetic field is travelling slower than it (Figure 2.4(b)). This results in an asymmetry in the ionisation and causes the radiation that is emitted in the forward direction to interfere constructively. This results in an observable burst of light which is called Cherenkov radiation.

Several properties of Cherenkov radiation, such as the emission angle, can be determined from simple geometric arguments. The phase velocity of light in a medium is given by

$$v = c/n \tag{2.2}$$

where c is the speed of light in a vacuum and n is the refractive index of the medium. Thus Cherenkov radiation will occur if

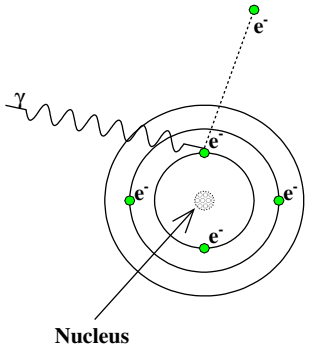

(a) Photoelectric Effect

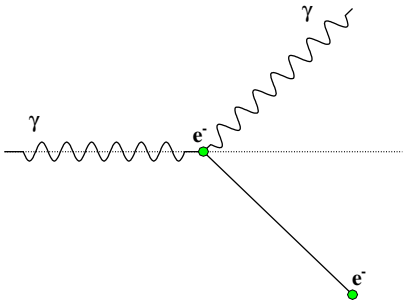

(b) Compton Scattering

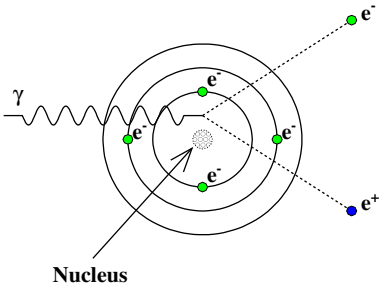

(c) Pair Production

Figure 2.3: Figure depicting the photoelectric effect, Compton scattering and pair production. In all cases, a photon is incident from the left hand side of the diagram.

$$v_{\mathrm{p}} > c/n \tag{2.3}$$

where v_{p} is the velocity of the particle in the medium. From Figure 2.5 it can be seen that the Cherenkov emission angle θ_c is given by

$$\cos\theta_c = \frac{c}{n v_{\mathrm{p}}} \tag{2.4}$$

Setting $\theta_c = 0$, it can be seen that there is a threshold velocity v_t below which no emission occurs given by

$$v_t = \frac{c}{n} \tag{2.5}$$

This corresponds to a threshold energy E_t below which Cherenkov emission does not occur given by

$$E_t = \frac{m_0\, c^2}{\sqrt{1 - (v_t/c)^2}} \tag{2.6}$$

For a solid medium the energy threshold is generally a few hundred MeV, however for a gas, which has a small refractive index, the energy threshold is much higher, in the GeV range. There exists a maximum Cherenkov emission angle given by the limit $\theta_{\mathrm{max}} \rightarrow \cos^{-1}(1/n)$ as $v/c \rightarrow 1$.

2.3 Extensive Air Showers

When a high-energy gamma ray or charged particle strikes the atmosphere, it interacts with molecules in a series of successive interactions generating a cascade of relativistic particles. These particles travel with sufficient velocity to emit Cherenkov radiation which penetrates to ground level. The detection and discrimination of these showers is based on physical differences in the development of the cascade in the case of gamma rays and charged cosmic rays. Thus a review of the development of these cascades will be given for both of these cases.

2.3.1 Gamma-Ray Induced Air Showers

The first interaction of a high-energy gamma-ray photon is almost always pair production as pair production dominates interactions above 20 MeV. The energy of the gamma-ray photon is converted into a highly relativistic electron-positron pair, which are emitted at a very narrow angle relative to the original gamma-ray trajectory. This is important because it means

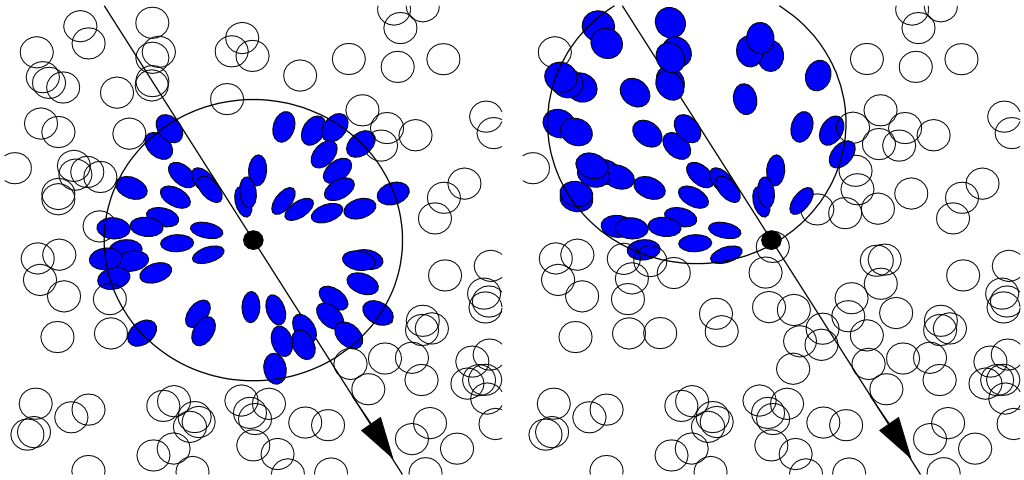

(a) Non-Relativistic **(b)** Relativistic

Figure 2.4: This figure shows a charged particle travelling through a medium, where the atoms are indicated by the black circles. The large black circle indicates the region of significant electromagnetic influence of the charged particle. Particles within the region of electromagnetic influence are polarised and oriented towards the charged particle. In the non-relativistic case, the region of influence is centered on the charged particle and the orientation of the polarised atoms results in destructive interference of any radiation induced by the charged particle passing through. In the relativistic case, the region of influence lags the charged particle, resulting in an alignment of the polarised atoms. This allows constructive interference of the emitted radiation to occur, and Cherenkov radiation is the result.

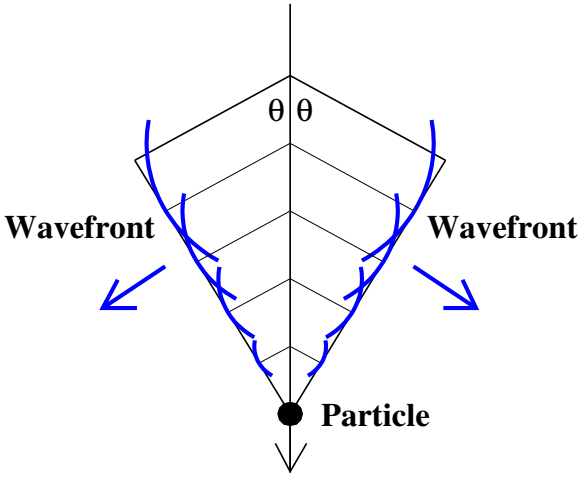

Figure 2.5: The Cherenkov radiation is emitted at an angle θ to the particle trajectory, where θ is determined by the particle velocity and the refractive index of the medium (Equation 2.4).

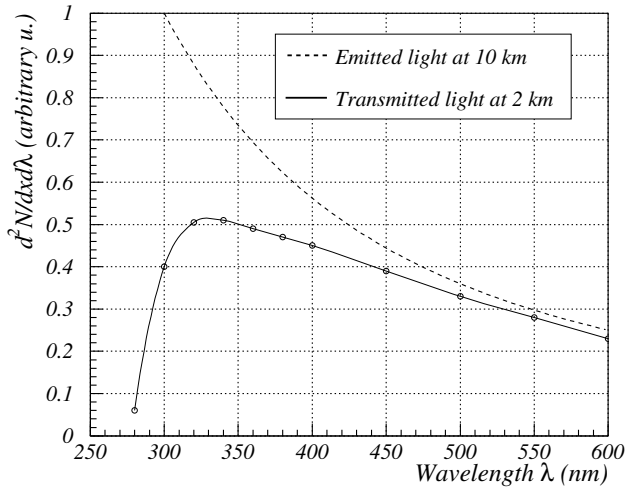

Figure 2.6: The intrinsic Cherenkov emission spectrum, compared to the spectrum after interacting with the atmosphere. This profoundly affects the observed Cherenkov radiation by telescopes on the ground. Figure taken from de la Calle Perez (2003).

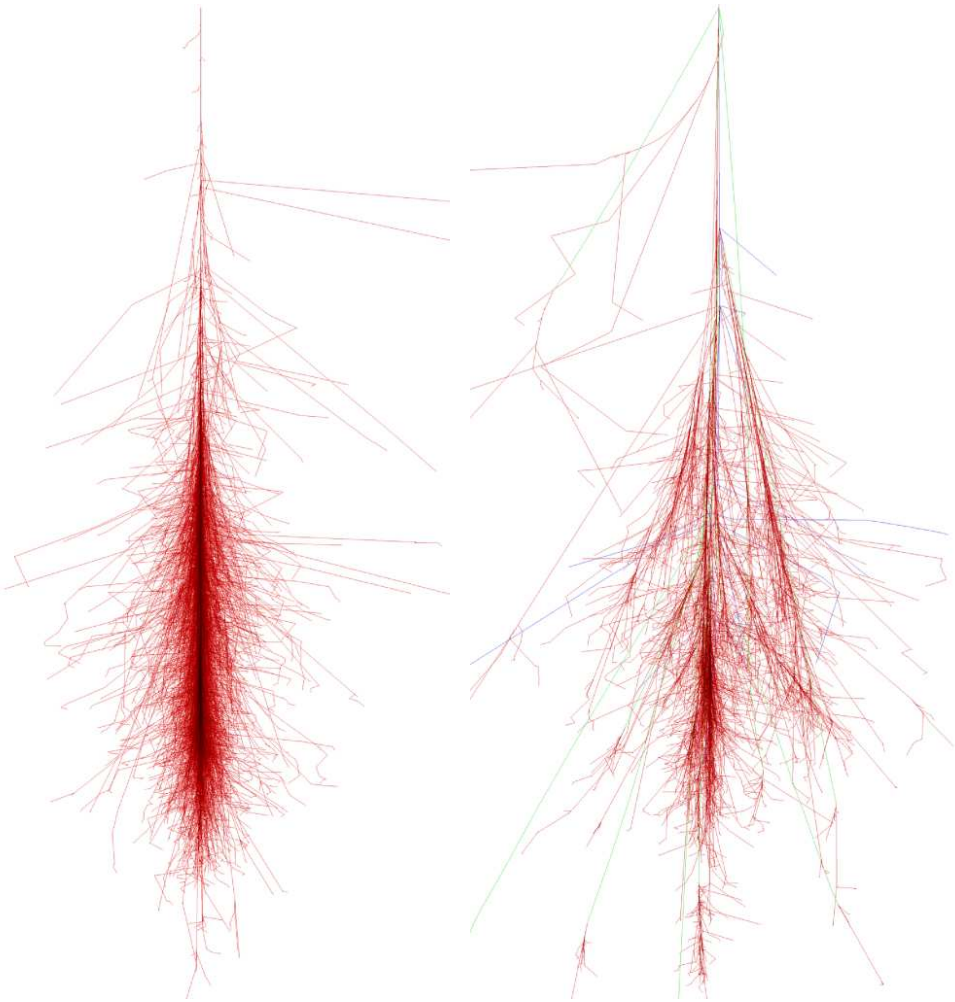

(a) Longitudinal view of 100 GeV photon.

(b) Longitudinal view of 100 GeV proton.

Figure 2.7: Monte-Carlo simulations of extensive air showers can be used to map the development of the cascade. Shown are the longitudinal developments of a cascade initiated by a single 100 GeV photon and a single 100 GeV proton. Red tracks are used to indicate electrons, positrons and gamma rays.

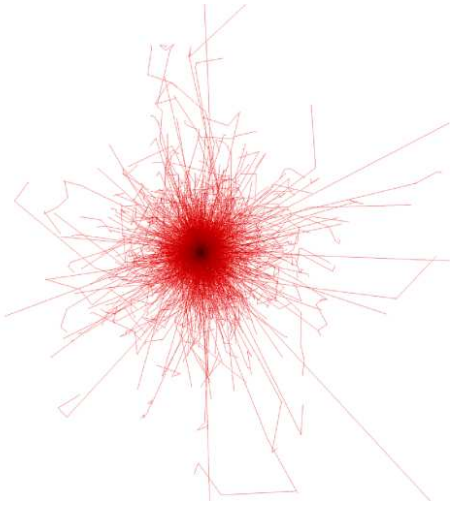

(a) Lateral view of 100 GeV photon.

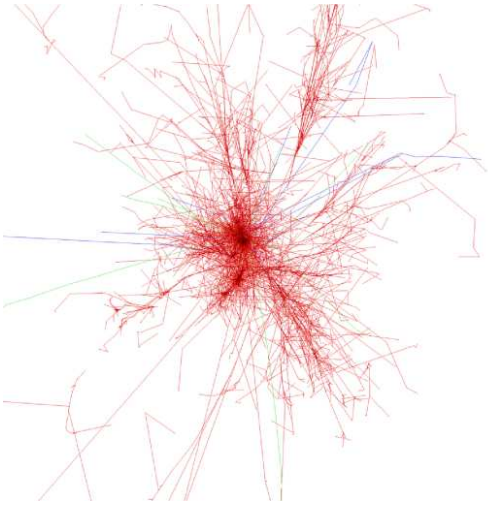

(b) Lateral view of 100 GeV proton.

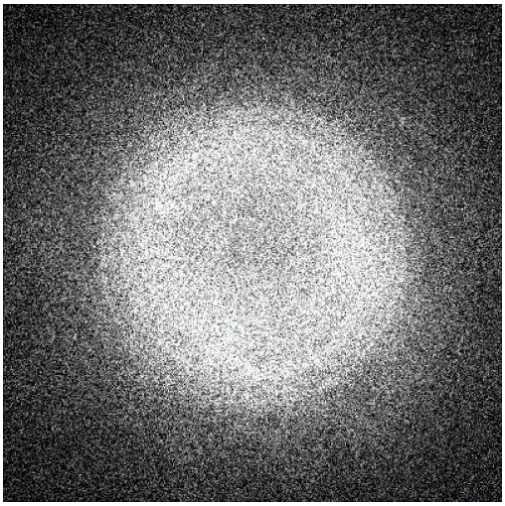

(c) Distribution of Cherenkov photons on the ground from 100 GeV photon.

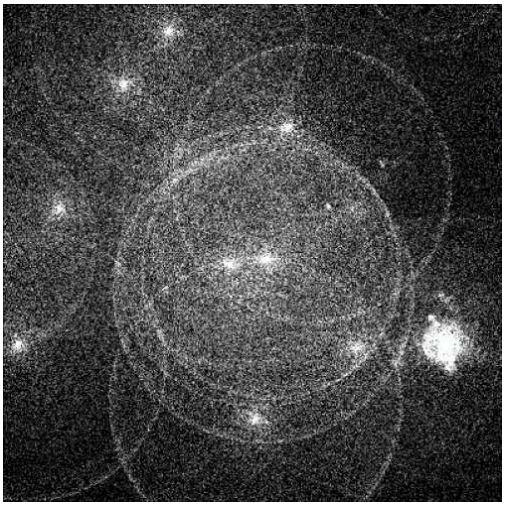

(d) Distribution of Cherenkov photons on the ground from 100 GeV proton.

Figure 2.8: Monte-Carlo simulations of extensive air showers can be used to map the development of the cascade. Shown are the lateral development initiated by a single 100 GeV photon and a 100 GeV proton. Red tracks are used to indicate electrons, positrons and gamma rays. The bottom figures shows the distribution of Cherenkov photons on the ground for the same showers.

that the trajectory of the initial gamma-ray photon is preserved in the products of its decay in the atmosphere. The relativistic electron and positron will emit more high-energy gamma rays via Brehmstrahlung radiation, which in turn undergo pair production to produce more relativistic electrons and positrons. The lateral spread in the shower development is dominated by Coulomb scattering of the electrons and positrons. This cascade process continues, with successively lower-energy particles being produced until electron-positron interactions are dominated by ionisation and photon interactions are dominated by Coulomb scattering. The narrow emission angles for these processes dictates that the resulting electromagnetic shower is rather narrow and beamed along the trajectory of the primary gamma ray (Figures 2.7(a),2.8(a)). The shower maximum occurs when the number of particles is a maximum - most of the Cherenkov radiation comes from this region. The height of shower maximum is dependant on the primary energy, with the shower resulting from higher energy gamma rays penetrating deeper into the atmosphere (although altidude of first interaction is also a factor). For showers from ultra high-energy gamma rays, the charged particle products can penetrate to ground level (note that this is the working premise for water based detectors such as Milagro - Section 1.3.3). For a 100 GeV photon, the height of shower maximum is approximately 10.3 km above sea level and the shower maximum contains $\sim$ 130 charged particles. These relativistic electrons and positrons are responsible for generating a pool of Cherenkov photons on the ground (Figure 2.8(c)), where the Cherenkov photon density is about 7.6 photons/m^2. This brief flash of Cherenkov photons is not strongly attenuated by the atmosphere in visible wavelengths (Figure 2.6). In some cases an electromagnetic cascade will produce a muonic component, however the cross section for such an interaction is small and the contribution to the overall intensity of Cherenkov photons is negligible. A schematic of the development of a gamma-ray initiated extensive air shower is shown in Figure 2.9.

2.3.2 Cosmic-Ray Induced Air Showers

The vast majority of cosmic-ray induced air showers are caused by protons, although there is significant contribution from helium nuclei. Heavier elements up to iron have been detected by cosmic-ray experiments, but do not contribute significantly to the cosmic-ray background suffered by Cherenkov telescopes. For protons, the initial reaction is typically with another proton, generating a charged/neutral pion pair and nucleonic debris.

The gamma-ray pair produced by the decay of the neutral pion is the most significant source of Cherenkov photons on the ground as they gener-

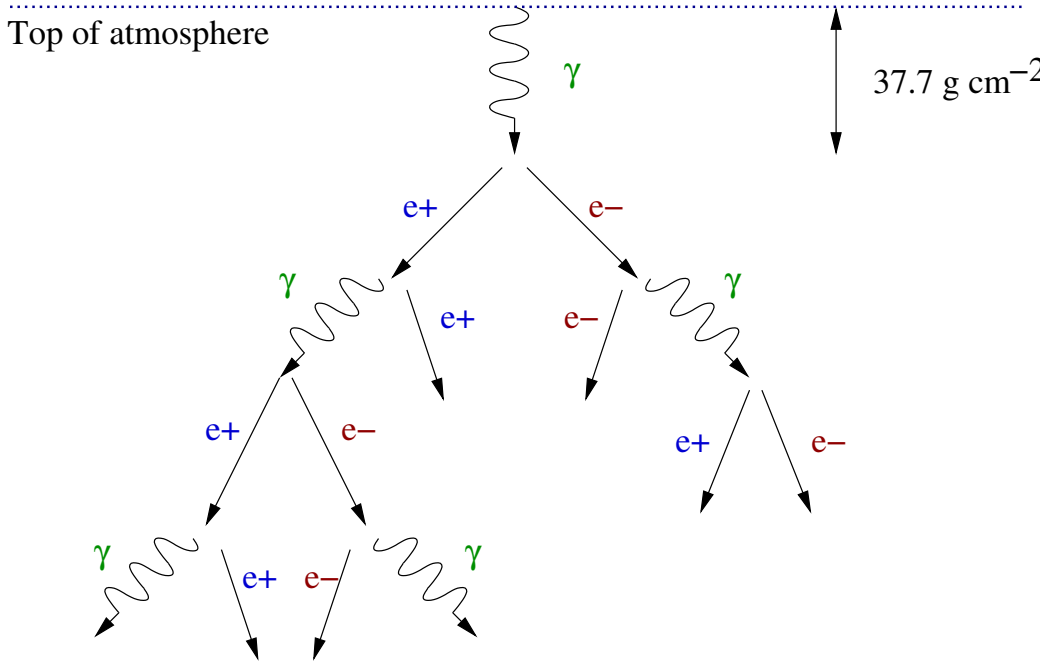

Figure 2.9: Diagrammatic view of the development of a gamma-ray initiated electromagnetic cascade. The primary photon produces an electron positron pair which quickly generate gamma-ray photons via Brehmstrahlung radiation. The ensuing electromagnetic cascade generates a brief pulse of Cherenkov photons. Figure from Gammell (2004).

ate an electromagnetic cascade similar to the one described in Section 2.3.1. Approximately one third of the primary energy is passed on to the electromagnetic component of the cascade. The muons can either decay to electrons and neutrinos (if they are low energy) or if they have sufficiently high energy may penetrate to ground level with the assistance of a Lorentz contraction. It is this penetrating muonic component that determines the limiting background at low energies (in the case of single telescope observations).

$$\begin{aligned} \pi^0 &\rightarrow \gamma + \gamma \\ \pi^+ &\rightarrow \mu^+ + \nu_\mu \\ \pi^- &\rightarrow \mu^- + \nu_\mu \end{aligned} \tag{2.7}$$

The transverse momentum imparted to the pion triplets is significantly larger in a hadronic shower than the transverse momentum imparted to an electron-positron pair in a gamma-ray shower. This means that hadronic showers have a greater lateral spread than gamma-ray showers. The multi-component nature of the hadronic shower also means that the hadronic shower is wider and more irregular than a gamma-ray shower. It is this simple characteristic which allows gamma-hadron separation to occur. A schematic of the development of a gamma-ray initiated extensive air shower is shown in Figure 2.10.

2.4 Imaging Atmospheric Cherenkov Technique

The IACT is unusual in that it uses a Cherenkov emitting dielectric medium that is not within the control of the experiment. The atmosphere is a dynamic environment, with variations in aerosol density, temperature, pressure etc occurring throughout the medium. Even the refractive index changes through the atmosphere. An accurate understanding of the emission of Cherenkov radiation in such a material is fraught with difficulty, nevertheless Jelley (1967) showed that the maximum emission angle in the atmosphere is given by

$$\theta_{max} = \sqrt{2\eta} \tag{2.8}$$

where η is a term used to model the refractive index n by $n = 1 + \eta$, with $\eta << 1$. Since the refractive index scales with the density, θ_{max} is higher in the high-density regions (ie lower in the atmosphere) and θ_{max} is lower in the low density regions (ie higher in the atmosphere). The threshold energy E_t for production of Cherenkov radiation is

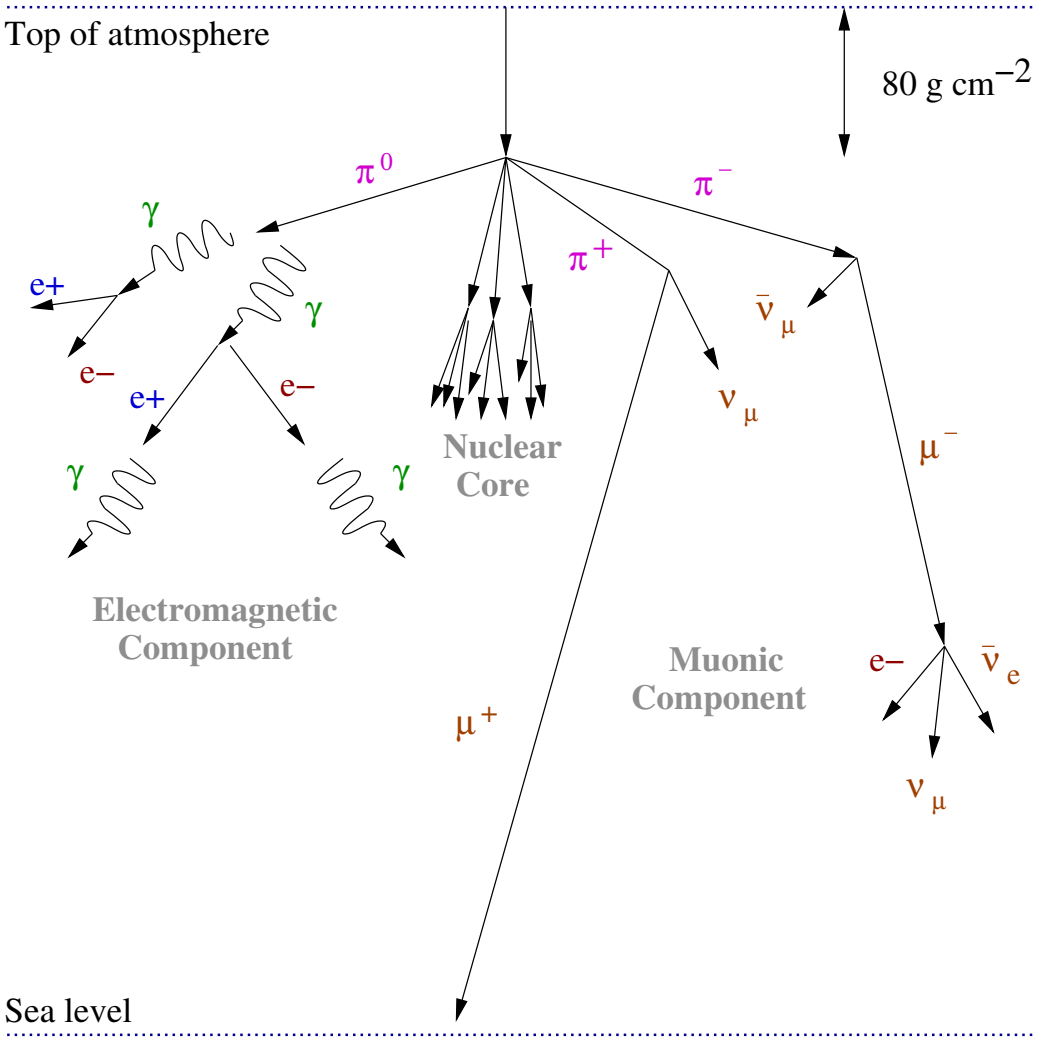

Figure 2.10: Diagrammatic view of the development of a hadron-initiated cascade. The primary hadron undergoes pion production producing a charged pion pair, a neutral pion and nucleonic debris. The neutral pion may initiate an electromagnetic cascade, whereas the charged pions decay to produce muons and neutrinos. Figure from Gammell (2004).

$$E_t = m_0 c^2 \left(\sqrt{2n} - 1\right) \tag{2.9}$$

This implies that the threshold energy increases with altitude. As the threshold energy is proportional to the particle mass, heavy particles such as muons and protons must be much more energetic than a light particle such as an electron or positron in order for Cherenkov emission to occur. The number of Cherenkov photons emitted by an electron (or positron) moving a distance l in a vacuum is given by

$$N = 2\pi\alpha l \left(\frac{1}{\lambda_2} - \frac{1}{\lambda_1}\right)\left(1 - \frac{1}{\beta^2 n^2}\right) \tag{2.10}$$

where α is the fine structure constant, λ_1 and λ_2 are the wavelength range. The spectrum of emitted photons is displayed in Figure 2.6. However, there are various atmospheric processes that can absorb Cherenkov photons. These processes include Rayleigh scattering, Mie scattering and ozone absorption, which combine to produce a Cherenkov spectrum peaking at UV wavelengths at typical observatory elevations. The spectrum of Cherenkov photons actually processed by the camera is further attenuated by the wavelength dependent reflectivity of the telescope mirrors (Figure 4.4) and quantum efficiency of the PMTs (Figure 4.6).

2.4.1 Cherenkov Telescopes

The detection of the flash of Cherenkov photons produced when a high-energy gamma ray or charged particle strikes the atmosphere is possible because of the relative intensity of the flash in a short timescale. Although the flux of night sky background photons is large ($\sim 10^{12}$ photons $\mathrm{m^{-2}s^{-1}sr^{-1}}$), given an integration time of $5 - 10$ ns a substantial signal-to-noise ratio can be achieved. The signal-to-noise ratio is maximised by selecting a field of view corresponding to the angular extent of the shower, and an integration gate corresponding to its duration.

Assuming an integration time greater than the Cherenkov flash time ($\sim$ 5 ns), the total number of photoelectrons registered by the camera is given by

$$S = \int_{\lambda_1}^{\lambda_2} C(\lambda)\, \eta(\lambda)\, A \, \mathrm{d}\lambda \tag{2.11}$$

where $C(\lambda)$ is the Cherenkov photon flux within the wavelength sensitivity range of the PMT ($\lambda_1 - \lambda_2$), A is the mirror collection area and $\eta(\lambda)$ is the

wavelength dependent quantum efficiency of the PMT. The Cherenkov flux can be written as

$$C(\lambda) = kE(\lambda)\,T(\lambda) \tag{2.12}$$

where $E(\lambda)$ is the Cherenkov emission spectrum from the extensive air shower, $T(\lambda)$ is the atmospheric transmission and k is a constant encompassing other factors such as the shower and detector geometry. The night sky noise is given by

$$B = \int_{\lambda_1}^{\lambda_2} B(\lambda)\,\eta(\lambda)\,\tau A\,\Omega\,\mathrm{d}\lambda \tag{2.13}$$

where $B(\lambda)$ is the emission spectrum of the night sky background, τ is the integration time and Ω is the solid angle. Thus the signal-to-noise ratio is given by

$$\frac{S}{N} = \frac{S}{\sqrt{B}} = \int_{\lambda_1}^{\lambda_2} C(\lambda) \sqrt{\frac{\eta(\lambda)\,A}{B(\lambda)\,\tau\,\Omega}}\,\mathrm{d}\lambda \tag{2.14}$$

$$E_t \propto \frac{1}{C(\lambda)} \sqrt{\frac{B(\lambda)\,\Omega\,\tau}{\eta(\lambda)\,A}} \tag{2.15}$$

The role of the integration time τ is interesting, in that it can be seen from equations 2.14 and 2.15 that the signal-to-noise ratio is inversely related to the integration time while the energy threshold is directly related to the integration time. Thus a minimisation of the integration time is desirable as it optimises the signal-to-noise ratio and reduces the energy threshold. Optimisation of this integration factor using fast digitisation of the PMT output is one of the goals of this thesis (Section 6.4).

2.4.2 Collection Area

One of the primary reasons high-energy gamma-ray astronomy is impractical from orbital observatories is the relatively low flux of gamma-ray photons at high energies. Orbital observatories, despite their enormous size (Comptel was as big as a bus), have collection areas comparable to an A4 sheet of paper. The reason the collection area is so small is because the primary photon must directly intersect the detecting device on the observatory. Conversely, with the IACT, the detecting device must merely lie within the lightpool of the extensive air shower. Given the relative enormity of the light pool, the collection area of a gamma-ray telescope is $\sim 5000\,\mathrm{m}^2$. It can be seen from Figure 2.8(c), which shows the distribution of Cherenkov photons on

the ground for a vertically incident 100 GeV photon, that a detector placed *anywhere* within that large light pool will be able to record the shower image. Thus the effective collection area is very large. The collection area is also effected by photon energy and the zenith angle of observations. A more energetic photon will produce a broader distribution of Cherenkov photons on the ground, producing a larger collection area. Similarly, photons with a large zenith angle will produce a larger distribution on the ground simply from geometric effects (imagine shining a light onto a table at an angle, the light pool gets larger as the angle gets larger). The trade-off with zenith angle is that the relative intensity of Cherenkov photons per square meter decreases as the zenith angle increases. This implies that large zenith angle observations are suitable for measuring photons in the high-energy range of the IACT band (> 5 TeV). The calculation of collection area is discussed in Section 5.6.1.

2.4.3 Photon Collection

Mirror technology has advanced to the point where highly accurate optical observations can be made with mirrors in the 10 m class. These mirrors rely on technologies such as adaptive optics which continuously adjust the mirror shape in order to account for atmospheric distortion during observations. Such ground-based mirrors are now capable of resolving power comparable with orbital observatories. This level of accuracy is not required for Cherenkov telescopes as the intrinsic amount of directional information present in the shower is limited to a few arc-minutes. Rather than requiring a large expensive mirror used at optical observatories, Cherenkov telescopes generally use a segmented design mirror consisting of hundreds of individual facets following the Davies and Cotton (1957) design. Cherenkov telescope mirrors are typically $50 - 80$ cm in size to aid handling, hexagonal or circular for close packing, anodised to prevent weathering and front aluminised to optimise reflectivity in the UV range (see Figure 4.4). Because they are usually left uncovered, the mirrors must be regularly washed (Badran and Weekes (2001)) and regular alignment (Section 4.1.4) ensures the telescope does not defocus. In order to detect Cherenkov photons from the extensive air shower, they are focused onto an array of photomultiplier tubes. The operation of these tubes and their characteristics is discussed further in Section 4.2.1

2.4.4 Imaging

In order to accurately record the development and distribution of an extensive air shower a technique to image the shower is required. This is required

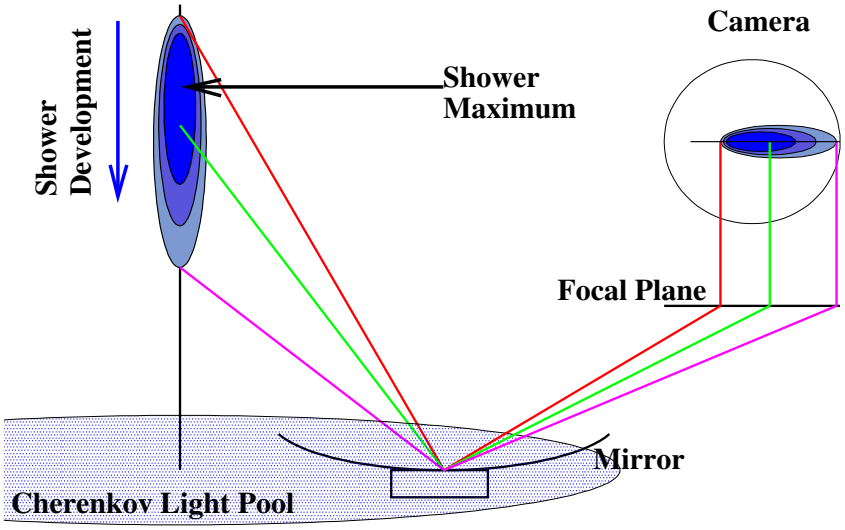

Figure 2.11: An incoming, vertically incident, gamma ray (or charged particle) initiates an extensive air shower on the left side of the figure. Shower maximum occurs at an altitude of approximately 10 km. A flash of Cherenkov photons is emitted, generating a light pool on the ground. The shower is imaged in the camera, generating a generally elliptical form, where the image *width* corresponds to the lateral development of the shower and image *length* corresponds to the longitudinal development of the shower. The image axis points to the region in the camera field of view where the shower originated.

if any effective discrimination (Section 2.4.5) is to be achieved. At the heart of the imaging technique is the array of photomultiplier tubes located in the focal plane of the segmented mirror. Each tube records a signal which is proportional to the number of photons which came from a small segment of the field of view. This signal is split, with one component used to trigger the camera, and another component digitised and read out if a trigger occurs. The digitised component is used to generate a 2 dimensional map of the extensive air shower (Figure 5.18), which allows the shape and orientation of the shower to be determined. Figure 2.11 displays the recording of the shower via reflection from the mirror on the focal plane. Simple geometry shows that the image axis points towards the location in the sky where the shower originated. It is this important piece of information, along with determination of shower shape which makes discrimination possible and paved the way to the first reliable detection of a source of very high-energy gamma rays (Weekes et al. (1989)).

2.4.5 Discrimination

Early efforts at detecting very high-energy gamma rays were confounded by the overwhelming flux of cosmic rays. The determination of whether an extensive air shower was caused by a cosmic ray or high-energy photon is impossible without an accurate representation of the shower - this representation is provided by imaging. Discrimination against cosmic-ray initiated air showers is based on the orientation and shape of the focal plane image. Due to the broad irregular development of cosmic-ray initiated extensive air showers, the images recorded in the camera tend to be broader and longer than those recorded by high-energy gamma-ray initiated air showers. A moment fitting technique developed by Hillas (1985) is used to determine the *width* and *length* of the image and can be used to *cut* events which do not possesses the required selection criteria. Due to the isotropic nature of cosmic rays, their arrival direction is evenly distributed in the camera plane. However, if there is a source of high-energy gamma rays in the center of the field of view, then there will be an excess of events which point back towards the center of the field of view. Thus by cutting on arrival direction, a further subset of cosmic-ray events can be removed. There are several techniques which use these basic principles of shower physics and geometry to effect background rejection. These are discussed in further detail in Section 5.4.

2.4.6 Sensitivity

In order to detect a source of cosmic high-energy photons, the statistical presence of a signal must be reliably estimated. The expected number of background events (from cosmic rays) is governed by the flux of cosmic rays and the detector sensitivity to them. The cosmic-ray spectrum is given by

$$F_{cr}\left(>E\right) \propto E^{-a} \tag{2.16}$$

where a is the cosmic-ray spectrum and is equal to about 1.7 in the relevant energy range. Gamma-ray spectra have a similar form, but the spectral index a_γ varies from about 1 to 3 depending on the source physics, absorption features etc. For an integration time τ and collection area A_γ for gamma rays and A_{cr} for cosmic rays, the number of detected gamma-ray events is given by $S = F_\gamma\left(E\right) A_\gamma t\tau$ and the number of detected background events is given by $B = F_{cr} A_{cr}\left(E\right) \Omega\tau$. Thus the significance of the signal in standard deviations is given by

$$\sigma \propto \frac{S}{\sqrt{B}} \propto E^{\frac{1.7}{2-a_\gamma}} \sqrt{\frac{A_\gamma}{A_{cr}}} \sqrt{\tau} \tag{2.17}$$

The number of standard deviations required to reliably claim detection of source has been the subject of much controversy in the field of gamma-ray astronomy. Given the sensitivity of the technique to bias induced by observing conditions, weather, stars, sky brightness etc, it is easy for a dataset to give a result of a few σ where no signal is actually present. With modern instruments and analysis methods, the required number of standard deviations is generally taken as 5 (Horan and Weekes, 2004), although some mature experiments have quoted 4 standard deviations to report the existence of marginal sources (Aharonian et al., 2006c). Other papers still have reported even lower significances (< 4) as confirmations of gamma-ray sources (Lang et al., 2005), and in one case of a detection of a source (Kosack et al., 2004).

The calculation of the absolute sensitivity of Cherenkov telescopes requires a large database of Monte-Carlo simulation of extensive air showers induced by protons and gamma rays. These simulations are then propagated through a detector simulation to determine the telescope response. A cross comparison of detector sensitivity for several gamma-ray instruments is shown in Figure 1.3.

2.4.7 Angular Resolution

Good angular resolution is achieved because of the very narrow emission angles associated with the electromagnetic interactions of the shower, and the relative weakness of the earth's magnetic field. This results in the shower axis being essentially parallel to the incident primary gamma ray. Using a single telescope, the shower axis can be reconstructed to an accuracy of about 0.1°, this can be reduced using an array of telescopes (Section 2.4.9) to about 0.05°. Using the statistics benefited from a few hundred gamma-ray events, the source location can be reconstructed to within a few arc-minutes. This remarkable angular resolution is superior to that of the orbital EGRET gamma-ray observatory, which left a litany of unidentified gamma-ray sources with large error boxes. Measurement of the angular resolution is achieved by propagating a set of Monte-Carlo simulations of gamma-ray induced extensive air showers through a detector simulation and measuring the RMS spread of the reconstructed source positions for all showers. Angular resolution tends to increase as a function of energy, as for larger air showers, a larger image is formed in the camera plane. This results in a more accurate determination of the image axis and thus the direction of the shower. This is also the case in stereoscopic observations where a high-energy shower is more likely to be imaged by more telescopes, allowing a superior reconstruction of the arrival direction.

2.4.8 Energy Resolution

One of the most significant problems in determining the energy of a given gamma-ray event, is overcoming the inherent ambiguity concerning image brightness and the distance/energy relation (ie if an object appear dim, is it weak or distant?). This ambiguity is solved using an array of Cherenkov telescopes (Section 2.4.9) which enables an accurate determination of the shower core location. Determination of energy from the light content of the image is possible because the number of Cherenkov photons recorded by the camera is proportional to the energy of the gamma ray. The energy resolution is measured in a similar way to the angular resolution. Again the energy resolution improves with energy as more light is available to more accurately determine the energy.

2.4.9 Stereoscopy

The use of multiple telescopes to view a single extensive air shower has had profound ramifications in the development of the IACT. This impact is sim-

ilar in magnitude to the use of an array of PMTs to image a shower.

The most significant barrier to reducing the energy threshold of the telescope to a regime below 200 GeV is the population of local muons which generate small compact images in the focal plane which are almost indiscernible from images of low energy gamma-ray induced extensive air showers. There are many reasons to want to push the threshold as low as possible. Many of the EGRET sources displayed no obvious cut-off in their spectra at high energies, implying there could be a large population of sources with significant flux above 20 GeV. Many of the models of high-energy emission predict a turnover in the high-energy spectrum in the multi-GeV range. The use of multiple telescopes allows the muon problem to be overcome, as the local light pool generated by these muons can typically only be seen by one telescope, so long as the telescopes are sufficiently far apart. Using a simple coincidence trigger between telescopes, the muon background can essentially be eliminated, pushing down the energy threshold (Section 4.3.3).

The use of multiple telescopes also has a profound effect on discrimination, angular resolution and energy resolution. The primary reason for these improvements is that the use of stereoscopy, along with simple geometry allows both the shower core position on the ground (Figure 5.20) and the shower source position in the sky (Figure 5.21) to be determined. Without stereoscopy, only the direction of the shower can be determined, however with stereoscopy the actual source location of the shower can be determined. This allows the use of a much more powerful orientation cut. With the information regarding the shower core location on the ground, the ambiguity regarding the distance/energy relationship can be overcome, resulting in a much more powerful energy-determination algorithm. Use of Monte-Carlo simulations of gamma-ray initiated extensive air showers allows discrimination by comparing parameters such as image *width* and *length* to expected parameters derived from Monte-Carlo simulations.

2.4.10 Observation Strategy

The observation strategy undertaken while making observations of candidate or known gamma-ray sources depends upon several factors including sky noise, duty cycle, variability, signal strength, weather and planned analysis. One of the most important factors is a recognition of the background dominated nature of IACT telescopes, requiring a reliable measurement of the background to be made. The simplest way to do this is using PAIRS observations. In this mode the target is tracked and data taken for a specified period of time (typically 28 sidereal minutes). The region of sky observed during this time is referred to as the ON source. In order to reliably assess

the background, a region of sky offset from the source by 30 minutes in right ascension is observed for 28 sidereal minutes (with a 2 sidereal minute gap between observations to allow for slewing and data run starting and stopping). This offset sky region is referred to as the OFF source. Thus calculating the number of excess gamma-ray candidate events is a simple matter of comparing the number of gamma-ray candidate events in the ON and OFF region. Thus the number of excess events is given by

$$N_\gamma = N_{on} - \alpha N_{off} \tag{2.18}$$

where α is a scaling factor tying up the ratio of the livetimes between the ON and OFF observation runs (this is discussed more formally in Section 5.5). The actual amount of time spent on the ON and OFF regions can be varied if required. For instance observations of the region around the unidentified source TeV J2032+4130 could be increased to 40 sidereal minutes to reduce bias induced by sky noise. One of the major drawbacks to the PAIRS method is the large sacrifice of observing time, with half of the allocated hours spent observing a supposedly empty piece of sky. This is especially frustrating given the relatively large exposures required to detect a source or place constraining upper limits, and the already low duty cycle of the instrument. Also, if observations are taking place in unfavourable conditions (eg slightly cloudy), then PAIRS are not useful as the atmospheric conditions may have changed substantially between the ON and OFF runs introducing a bias. One way of remedying these problems is to forgo the OFF run and instead use a scaling factor to estimate the background directly from the ON run. One of the largest drawbacks with this method, called TRACKING mode, is that the background is not as reliably estimated as with PAIRS mode, thus it is only suitable for monitoring the flux of existing sources, or searching for candidate sources in bad weather (where a follow up with PAIRS would be employed if a signal was found). TRACKING is not suitable for deep searches for weak sources or for spectral analysis where an accurate background estimate is paramount. In stereoscopic observations, where accurate shower core and shower source location lead to a more accurate background estimation, an offset tracking mode called WOBBLE can be used. In this mode, the target is offset from the center of the field of view by $+0.5^\circ$ in declination (or right ascension), and a data run is taken. Various regions within the field of view can be used as background (Sections 5.5.2, 5.5.3). Typically a second run is also taken with the target offset by -0.5° in declination (or right ascension) and the data are analysed together. One of the trade-offs with the WOBBLE mode versus PAIRS mode is that whereas for PAIRS mode half the observing time is spent not looking at the source, for WOBBLE mode the source is not at

the center of the field of view which is where the sensitivity is highest. Thus the WOBBLE offset must be carefully chosen using Monte-Carlo simulations of the detector response to maximise sensitivity in the context of the extra observing time available.

2.5 Summary

This chapter has provided an overview of the ground-based detection of very high-energy gamma-ray radiation. Arguments have been presented as to why orbital observatories are not suitable for high-energy sources with small fluxes. A review of the physical processes, including Cherenkov radiation, involved when a high-energy gamma ray or cosmic ray strikes the atmosphere is described. This leads to a comparison of the development of gamma-ray initiated and cosmic-ray initiated extensive air showers. The Imaging Atmospheric Cherenkov Technique is introduced with descriptions of the propagation of Cherenkov photons through the atmosphere and their collection with a pixellated camera in the plane of a large reflector. Basic methodologies behind background discrimination are reviewed in the context of differing hadronic and gamma-ray induced cascade development. Telescope sensitivity, energy and angular resolution is discussed. The advantage of using multiple telescopes in stereoscopic mode is described and finally the observing modes available to an IACT are discussed.

Chapter 3

Blazars

3.1 Introduction

Active Galactic Nuclei (AGN) are galaxies whose central cores greatly outshine the rest of the host galaxy. The central engines of AGN are believed to be powered by supermassive black holes which draw surrounding matter into a circulating accretion disk. Infalling matter loses angular momentum through viscous or turbulent forces and powers the accretion disk whose thermal emission peaks at UV wavelengths. Beyond the accretion disk lies a dusty region, commonly regarded as torus shaped, which absorbs visible and UV light along some lines of sight. Jets of energetic particles stream perpendicularly away from the plane of the host galaxy, along the axis of rotation of the accretion disk. These collimated relativistic plasma outflows harbour some of the most energetic processes in the universe and exhibit emission from radio to gamma ray. This unifying model of AGN implies that the observed emission from AGN is a strong function of the observation angle in relation to the relativistic jet, with the highest energy emission beamed along the direction of the jet. The unifying model describes blazars as those AGN whose collimated plasma jets are closely aligned with our galaxy. Such a chance orientation provides unique opportunities to study these jets and to understand the underlying emission mechanisms in AGN.

In this chapter, the many types of observed AGN are summarised and interpreted in terms of the unification model (Section 3.2). The emanating plasma jets are described (Section 3.3), along with a discussion of relativistic beaming (Section 3.4). The role of obscuration and jet angle relative to the observer is also discussed (Section 3.5) and the definition of blazars outlined (Section 3.6). Leptonic and hadronic emission models for very high-energy gamma radiation in blazar jets are described (Section 3.7). The contribution

to understanding AGN in terms of very high-energy gamma-ray observations is discussed (Section 3.8) along with implications for exploring the density of the extragalactic infrared background (Section 3.9).

3.2 Types of AGN

AGN comprise a small percentage of all galaxies which, in the most general terms, are defined as galaxies whose cores outshine the usual stellar thermal emission in the rest of the galaxy. That common component apart, AGN display an almost bewildering range of measurable properties. Some are radio quiet, some radio loud, many AGN display different absorption features - some are completely featureless. There is varying degrees of polarisation, there is rapid variability across the electromagnetic spectrum, some peak in emission at UV wavelength, some at radio and others still in gamma ray. It seems the only common component is the impressive core luminosity. This overwhelming list of properties led to the definition of many subclasses of AGN based on radio output and spectrum, resolvability, polarisation and variability. The subclasses and their characteristics are listed in Table 3.1.

3.3 Relativistic Jets

Many AGN appear to exhibit either one or two jets, although some exhibit none at all. It is believed that the jets are powered by the gravitational potential energy of the central black hole, although the exact mechanics of how they are formed is not known. The best studies of jet morphology come from VLBI studies which reveal milli-arcsecond detail. These studies show that jets are often inhomogeneous with regions of increased density called knots travelling along the length of the jet. These knots are especially interesting in the context of very high-energy emission as their existence may be related to the variability detected at TeV energies. The velocity of these knots is usually expressed in terms of the bulk Lorentz factor Γ as their velocity is often relativistic. The bulk Lorentz factor is defined as

$$\Gamma = \frac{1}{\sqrt{1 - \frac{v^2}{c^2}}} \tag{3.1}$$

where v is the velocity of the knot relative to the galaxy and c is the speed of light. That the knot speed is relativistic has important consequences for the observed parameters of jets which will be discussed in Section 3.4. An example of a jet from an AGN is shown in Figure 3.1.

Type	Abbr.	Properties
Active Galactic Nuclei	AGN	Extragalactic source with a variable bright nucleus
Seyfert 2	–	Resolvable spiral galaxy of low luminosity, brightest at infrared wavelengths with narrow emission lines
Narrow Emission Line Galaxy	NELG	Radio quiet x-ray galaxy with narrow emission lines
Narrow-Line Radio Galaxy	NLRG	Radio Galaxy that exhibits narrow optical emission lines
Fanaroff-Riley I	FR I	Low radio luminosity radio galaxy; emission peaked near central source
Fanaroff-Riley II	FR II	High radio luminosity radio galaxy; emission brightest at lobes or hot spots far from central source
Seyfert 1	–	Resolvable spiral galaxy of low luminosity, brightest at ultraviolet and x-ray wavelengths with broad emission lines
Quasi-Stellar Object	QSO	Unresolved radio quiet extragalactic source with broad spectral lines
Broad-Line Radio Galaxy	BLRG	Radio Galaxy that exhibits broad optical emission lines
Steep Spectrum Radio Quasar	SSRQ	Quasar with radio spectral index > 0.5
Flat Spectrum Radio Quasar	FSRQ	Quasar with radio spectral index ≤ 0.5
Blazar	–	AGN with strong optical polarisation, rapid optical variability, and flat spectrum radio emission
BL Lacertae Object	BL Lac	AGN with featureless optical continuum and weak emission lines
Optically Violent Variable	OVV	AGN with dramatic optical variability and highly polarised optical continuum
Highly Polarised Quasar	HPQ	Quasar with high degree ($> 3\%$) of polarisation

Table 3.1: AGN types, abbreviations, and descriptions of defining properties (adopted from Urry and Padovani (1995)).

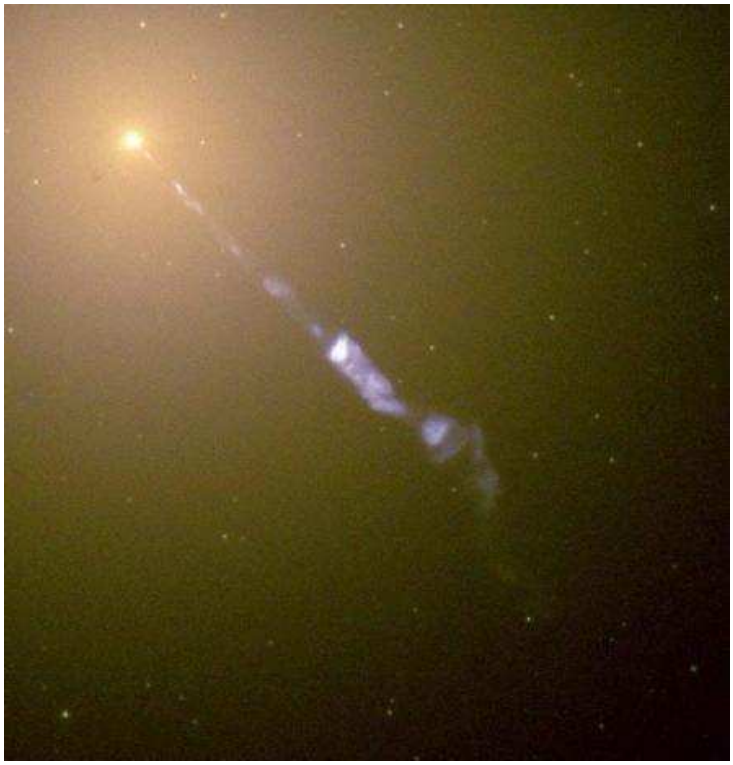

Figure 3.1: A spectacular example of a plasma jet emanating from the core of M87. Figure from Hubble Heritage Team(heritage.stsci.edu).

3.4 Relativistic Beaming

Many of the characteristics associated with high-energy emission from AGN jets can be explained by relativistic beaming in the jets. Such characteristics include apparent superluminal motion, rapid variability and high luminosity.

3.4.1 Superluminal Motion

Superluminal motion is the observed motion of a structure with apparent velocity v_a greater than the vacuum speed of light c. Such motion has been observed in the radio maps of jets, where knots or blobs of matter appear to move along the jet with $v_a > c$. Relativistic sources pursue the photons they emit, reducing the effective time interval between two events in the observers frame and giving the impression of superluminal motion.

When a radiative plasma is moving in the direction of the observer (assumed to be fixed) at bulk relativistic velocities, then its emission will be relativistically beamed towards the observer. The Doppler factor of a relativistically moving source is given by

$$\delta = \frac{1}{\gamma\left(1 - \beta\cos\theta\right)} \tag{3.2}$$

where β is the bulk velocity in units of c and the Lorentz factor γ is

$$\gamma = \frac{1}{\sqrt{1-\beta^2}} \tag{3.3}$$

and θ is the angle between the velocity vector of the source and the observer. Such a scenario is demonstrated in Figure 3.2 where a source at time $T = 0$ is travelling towards the observer at an angle θ. An observed time $T = t_{obs}$ later, the source has moved an apparent distance $\beta ct\cos\theta$ towards the observer and has moved an apparent transverse distance of $\beta ct\sin\theta$. Thus the observed time $T = t_{obs}$ is given by

$$T_{obs} = t - \beta t\cos\theta = t\left(1 - \beta\cos\theta\right) \tag{3.4}$$

The observed transverse velocity $v_\perp$ is just the ratio of the apparent transverse distance divided by the apparent time

$$v_\perp = \frac{\beta ct\sin\theta}{t\left(1-\beta\cos\theta\right)} = \frac{\beta c\sin\theta}{\left(1-\beta\cos\theta\right)} \tag{3.5}$$

In units of c this can be expressed as

$$\beta_{\perp} = \frac{\beta \sin\theta}{(1 - \beta\cos\theta)} \tag{3.6}$$

Differentiating $\beta_{\perp}$ with respect to θ reveals that the maximum value of $\beta_{\perp}$ is found for $\theta = \cos^{-1}\beta$. Inserting this back into equation 3.6, and solving for $\beta_{\perp} \geq 1$ requires $\beta \geq 1/\sqrt{2}$. Thus for certain angles of sight between the emitting source and the observer, and for relativistic bulk velocities, apparent superluminal motion can be observed. In fact if superluminal motion is observed, then it serves as evidence of relativistic velocities within jet structures, and therefore of relativistic beaming of radiation.

3.4.2 Effects of Relativistic Beaming

Relativistic beaming leads to Doppler enhancement which boosts the observed flux and reduces the apparent time scales in which flux changes. Even allowing for time dilation, the time intervals measured in the observed frame are shorter than in the emitting rest frame because the emitter is moving towards the source. Thus an apparent flux doubling time as measured by the observer may have intrinsically taken much longer. Also the total number of photons received in a short time period by the observer, may be the total number of photons emitted over a long period by the source, implying that the observer will measure a higher flux during that short period. The observed luminosity L_{obs} is related to the emitted luminosity in the source rest frame L_{em} by

$$L_{obs} = \delta^{p} L_{em} \tag{3.7}$$

where $p = 2 + \alpha$ in the case of a continuous jet and α is the spectral index of the source (Urry and Padovani (1995)).

In many EGRET detected blazars, the observed gamma-ray luminosity dominates the luminosity in other wavebands by a factor between 1 and 1000. Multiwavelength studies have shown that the ratio of gamma-ray to bolometric luminosity increases with overall luminosity. In many blazars, the high-energy emission (both at GeV and TeV energies) has been observed to increase and decrease by a factor of 2 or 3 on time scales of hours. This rapid flux variability can be regarded as emission model independent evidence of relativistic beaming in blazars, where the jets are too closely aligned to observe superluminal motion in knots in the jet.

Beaming is also generally attributed to the fact that many AGN appear to exhibit only a single jet. This single jet is always the one that is oriented in our direction, and thus undergoes Doppler boosting to increase its apparent

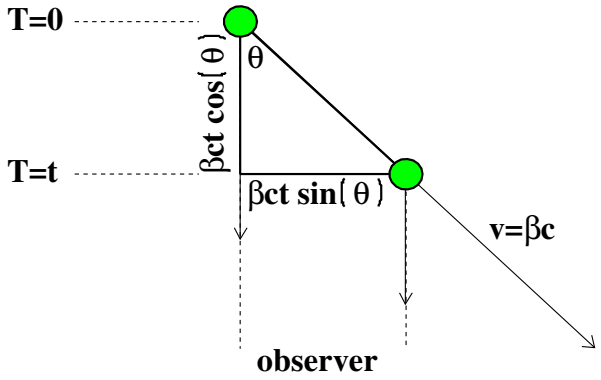

Figure 3.2: Apparent superluminal motion. The source is represented by the green circle and is moving towards the observer at an angle θ.

luminosity. Conversely, the counter-jet (if it exists) is beamed away from us, thus decreasing its apparent luminosity. Using a toy AGN model with bipolar jet axis oriented 10° from us, there would be a luminosity ratio between the knots in the jets of 10^{-4} if the bulk relative velocity of the knots was 0.95 c (Robson, 1996).

3.5 Unification

From the chaos of the multitude of AGN subclasses listed in Table 3.1, a surprisingly simple unification scheme has emerged. In this scheme, a prototype AGN is constructed with the following principle components

- The core contains a supermassive black hole up to 10^{10} $M_{\odot}$.
- The supermassive black hole is surrounded by an accretion disk which is heated by magnetic and/or viscous forces generating high-energy thermal radiation from optical to x-ray.
- A population of energetic electrons above and below the accretion disk radiates x-rays.
- Close to the supermassive black hole, clouds of high-velocity gas rapidly circulate emitting broad optical radiation lines.

- The accretion disk is surrounded by a cloud of gas and dust that is often regarded to be torus shaped, although there is little evidence to support this particular geometry.
- Beyond the torus lie clouds of narrow-line emitting relatively low velocity gas.
- Radio loud AGN exhibit a bipolar relativistic plasma jet originating within a few 100 Schwarzschild radii of the supermassive black hole and extending up to a megaparsec. Radio quiet AGN appear not to have such jets.

Apart from local variations in supermassive back hole mass, accretion disk density etc, the unification model simply holds that the observational properties of the various AGN types are determined not by intrinsic phenomenological differences, but rather is a simple case of power and orientation relative to the observer, with obscuration dominating optical features and relativistic beaming dominating radio and gamma-ray features.

The unification scheme can be regarded from an optical or radio viewpoint (Urry and Padovani, 1995; Urry, 2004). The optical scheme explains the absence of the broad-line emission region by the orientation of the obscuring torus whereas the radio scheme explains the core dominated versus lobe dominated radio-loud AGN by orientation relative to the jet axis. Due to the common rotational axes of jet and torus, the two schemes can be regarded to be identical. However the viewing angle dependencies are quite different as one is defined by the density and structure of the torus, whereas the other is defined by the beaming pattern and Doppler factor of the jet.

Using this common AGN prototype, all the AGN subclasses can be split into one of just three types named Type 0, Type 1, and Type 2 (see Figure 3.3 for graphical examples). Type 0 AGN are those AGN whose spectra are dominated by non-thermal emission as they are viewed directly along the axis of the jet. The non-thermal emission of those AGN is described in sections 3.7.1 and 3.7.2. It is these AGN that can be detected by the IACT owing to the relativistic beaming of high-energy photons along the jet axis. Type 1 AGN are viewed at an angle to the jet, and have a clear view of the accretion disk resulting in strong broadline optical emission. Finally Type 2 AGN view the galaxy edge on, resulting in obscuration of the broadline region by the torus. These AGN mainly exhibit narrow-line emission from the low velocity gas. The breakdown of the list of AGN subclasses in Table 3.1 is re-categorised in Figure 3.4. As this work is concerned with observations and understanding of very high-energy gamma-ray emission of blazars, the spectral energy distribution of blazars is discussed in the next section.

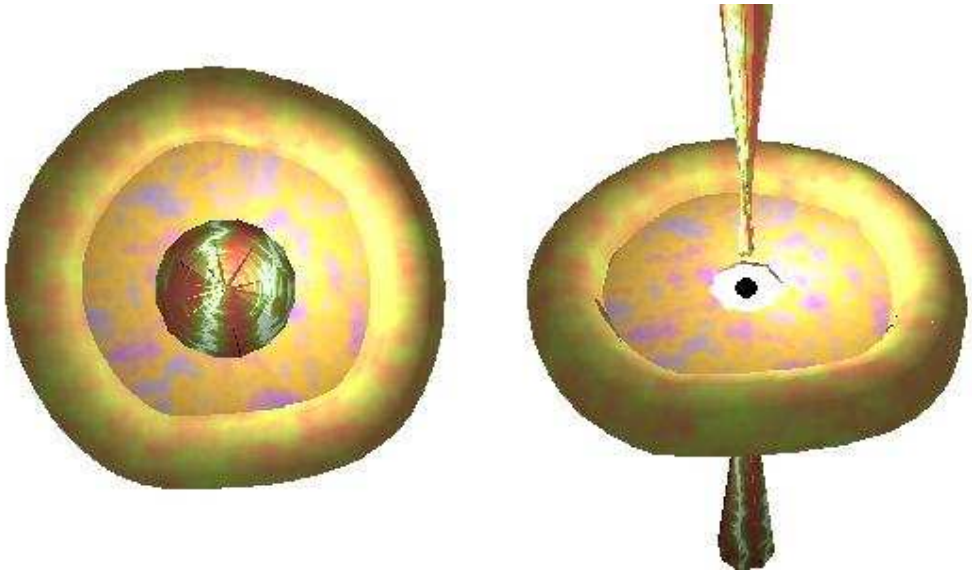

(a) Type 0 AGN

(b) Type 1 AGN

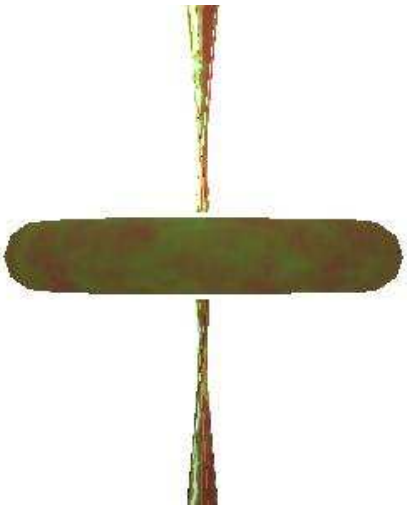

(c) Type 2 AGN

Figure 3.3: Graphic examples of the types of Active Galactic Nuclei inferred by the unification model, showing how viewing angle can profoundly effect observed radiation. The viewing angle determines category, with Types 0, 1 and 2 indicated.

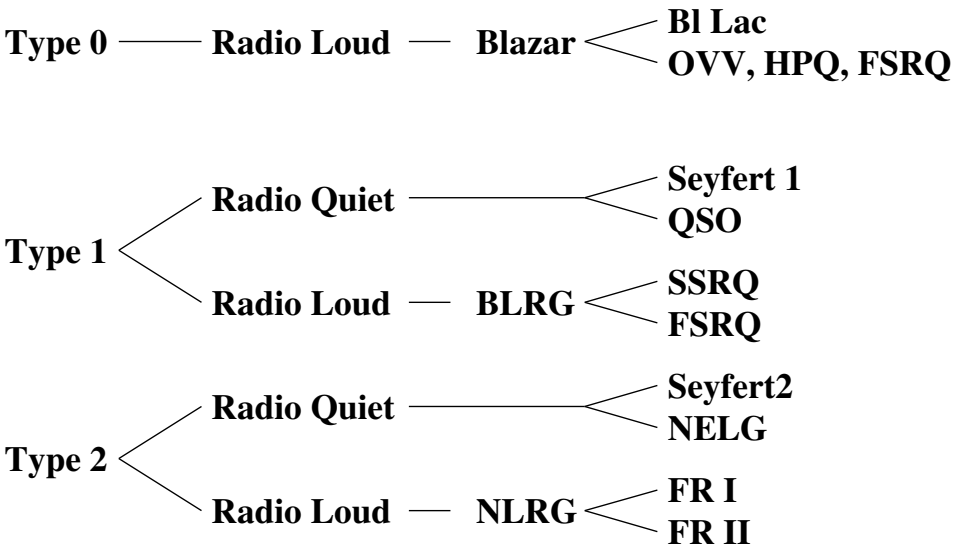

Figure 3.4: Outline of AGN taxonomy.

3.6 Blazars

Blazars are the class of AGN whose jets are oriented directly toward our galaxy. With the relativistic plasma jet pointing directly at us, such AGN are always radio-loud. It also means that any radiation emitted from AGN that is only beamed forwards within the jet can only be observed in blazars. Blazars can be studied by many instruments as their emission spectra stretch across the electromagnetic spectrum. Due to the jet orientation, the observed emission is dominated by the non-thermal processes and exhibit rapid variability on short time scales.

An example of the spectral energy distribution of a blazar is shown in Figure 3.5. Evident is the double humped nature of the distribution, and given the energies involved, the non-thermal nature of the emission. The first spectral peak spans radio to x-ray, with the second peak in the Gev-TeV range. There are several theoretical models to account for the double humped SED of blazars. These models fall into two primary categories of leptonic and hadronic models which are discussed in Sections 3.7.1 and 3.7.2.

Thus far, all the blazars detected by ground-based very high-energy gamma-ray telescopes have been High-frequency peaked Bl-Lacertae (HBL) objects. For these objects, the lower energy peak lies at x-ray wavelengths and the higher energy peak is in the TeV range. There is also a population of well studied Low-frequency peaked Bl-Lacertae (LBL) objects which cannot be detected by ground-based instruments as the upper energy peak lies in the MeV range. The EGRET orbital gamma-ray observatory detected over 60 such blazars (Hartman et al. (1999)). The detection of LBLs by orbital observatories and HBLs by ground-based observatories is determined by the range of energy sensitives of these instruments (ie they are dominated by selection effects). However with the instruments concerned (EGRET/Whipple/HEGRA), there was no overlap in energy regime, implying that there may yet exist a population of Intermediate-frequency peaked Bl-Lacertae (IBL) objects which have not been detected at high energy. In fact there is no reason to believe that there is not a continuous distribution of peak energies among blazars, with some authors Padovani (2006) suggesting that the classification is dominated by selection effects. It is hoped that the upcoming GLAST observatory, which has a design sensitivity up to $\sim 300\,\mathrm{GeV}$, in conjunction with the current generation of Cherenkov Telescopes such as VERITAS, H.E.S.S. and MAGIC, which have sensitivity down to $\sim 50 - 100\,\mathrm{GeV}$, will bridge the gap between orbital and ground-based observatories. This will close the electromagnetic window providing the first opportunity to search for IBLs (and to hopefully remove the selection effects) in the $100\,\mathrm{keV} - 100\,\mathrm{GeV}$ range. The reason for the distribution of peak fre-

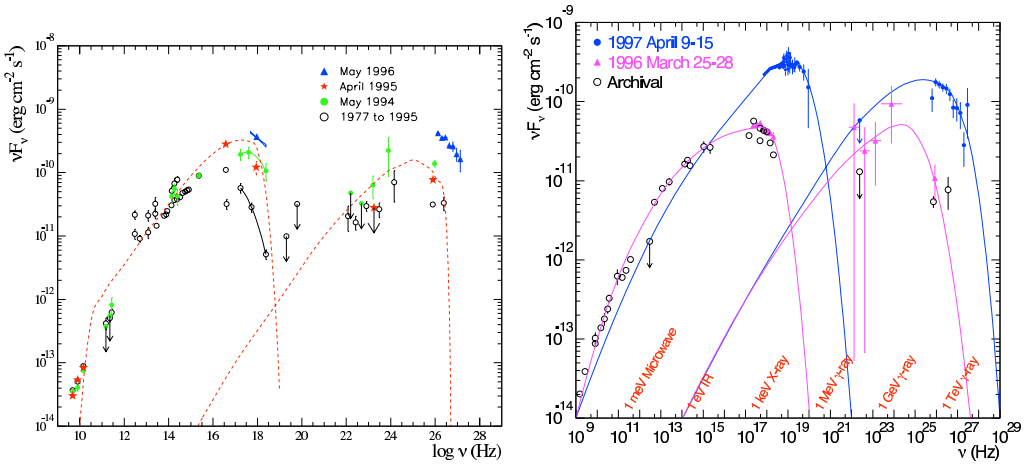

(a) Markarian 421 **(b)** Markarian 501

Figure 3.5: Broadband spectra of the blazars Markarian 421 and Markarian 501 in a $\nu F\nu$ representation. Data from the Rossi X-Ray Timing Explorer are used to cover the x-ray region, while data from the Whipple 10m Telescope cover the TeV region. The data are fit with a one zone Synchrotron Self Compton model. Figure from Buckley (1998).

quencies is not known but it is hoped that revealing the remainder of the population (if it exists) will shed new light on the underlying cause.

One of the characteristics that is revealed in blazar population studies is the existence of the so-called 'blazar sequence'. This essentially holds that the blazar luminosity depends on the location of the synchrotron peak. Thus LBLs are found to be less luminous than IBLs, and less luminous again than HBLs. This trend was initially reported by Fossati et al. (1998), but tellingly the dataset was limited to $\log \nu_{\rm peak} = 15 - 19$. A more extensive study by Nieppola et al. (2006) covered $\log \nu_{\rm peak} = 13 - 21$ and introduced a significant amount of scatter into the plot of $\log \nu_{\rm peak}$, and invalidating the overall trend of decreasing luminosity with increasing $\log \nu_{\rm peak}$. The authors go so far as to say that their results invalidate the blazar sequence. One of the interesting implications for observations in the TeV regime is that the synchrotron luminosity in the HBL waveband is not actually the lowest luminosity, and that some IBLs and even some LBLs have a lower synchrotron luminosity than most HBLs.

3.7 Models of High-Energy Emission in Blazars

As it is the high-energy emissions from blazars that is the subject of this thesis, a review of the most popular emission models will be reviewed here. In the context of the double humped νF_ν distribution, the high-energy peak is of course the second peak. However many high-energy emission models directly link the low-energy and high-energy peaks, thus the low-energy peak will also be discussed.

3.7.1 Leptonic Models

The common element of the leptonic models is that the non-thermal emission is sourced from a population of electrons (or positrons) within the plasma jet. These electrons are shock accelerated to relativistic energies within the jet due to multiple crossings with bulk matter fields travelling at different velocities (Maraschi et al., 1992).

First Spectral Peak

Relativistic electrons encountering a magnetic field in the plasma jet are forced to follow a helical path (Figure 3.6). The acceleration of the electron as it follows the curved helical trajectory results in the forward beamed emission of synchrotron radiation (where the beaming is a result of the relativistic electron velocity). The synchrotron radiation is beamed in a cone with width $1/\gamma$ where γ is the Lorentz factor of the relativistic electrons. The first spectral speak in the blazar spectral energy distribution is attributed to the polarised power-law spectrum of the synchrotron radiation.

Second spectral peak

In the leptonic model, the same accelerated relativistic electrons that produce synchrotron radiation in the plasma jet interact with photon fields via inverse-Compton emission (Figure 3.7) to boost those photons to GeV/TeV energies. In Compton scattering, the electron initial energy is negligible, thus any scattering between the electron and photon will result in the transfer of energy from the photon to the electron. The final energy of the photon can be calculated using the laws of conservation of energy and momentum and is given by

$$\epsilon_1 = \frac{\epsilon}{1 + \frac{\epsilon}{mc^2}\left(1 - \cos\theta\right)} \tag{3.8}$$

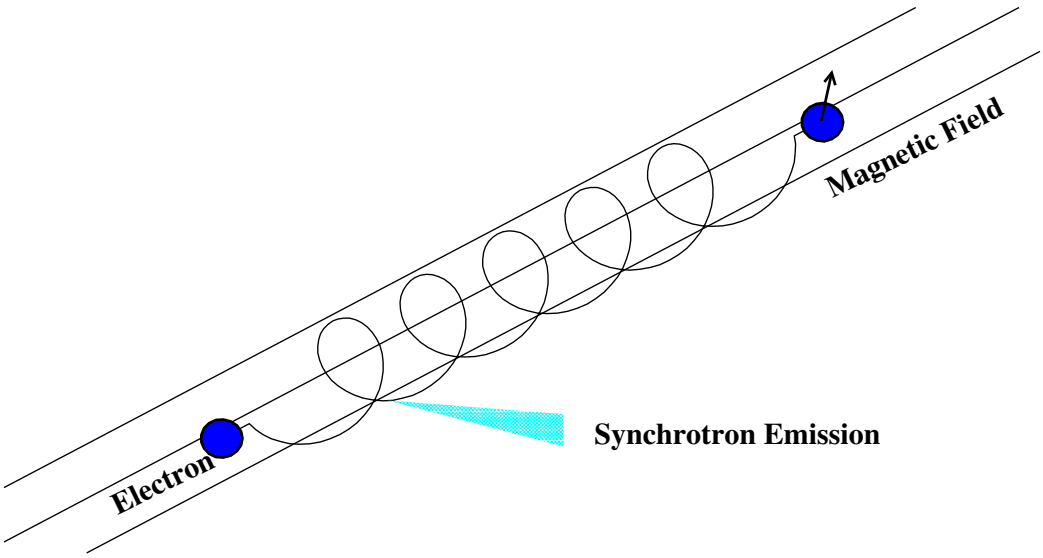

Figure 3.6: Synchrotron emission. An electron is accelerated in a magnetic field, forcing it to follow a helical path. The acceleration results in the forward beamed emission of synchrotron photons, which in leptonic emission models are the source of the first spectral peak in the spectral energy distribution of blazars.

where ϵ is the initial energy, m is the electron mass and $\cos\theta$ is the angle between the scattered photon and its original trajectory. Inverse-Compton scattering treats the case where the electron's kinetic energy is comparable to the photon energy. In this case, the electron can transfer energy to the photon. Such an interaction can be seen either from the rest frame of the electron or the observer (Rybicki and Lightman (2004)). In order to change to the electron rest frame coordinate system, the following Doppler shift formulae can be used

$$\begin{aligned} \epsilon' &= \epsilon\gamma\left(1-\beta\cos\theta\right) \\ \epsilon_1 &= \epsilon_1'\gamma\left(1+\beta\cos\theta_1'\right) \end{aligned} \tag{3.9}$$

where γ is the Doppler factor. Applying this transformation to Equation 3.8 gives

$$\epsilon_1' \simeq \epsilon'\left(1-\frac{\epsilon'}{mc^2}\left(1-\cos\Theta\right)\right) \tag{3.10}$$

where

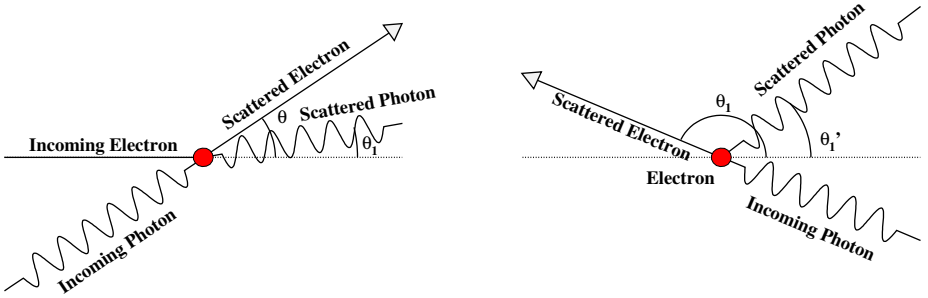

(a) Observer's Rest Frame **(b)** Electron Rest Frame

Figure 3.7: Inverse Compton scattering. A low-energy photon interacts with a high-energy electron resulting in the photon acquiring some of the electron's energy, up-shifting it to higher energies. According to leptonic models of gamma-ray emission, this process is responsible for the high-energy component of the spectral energy distribution of blazars.

$$\cos\Theta = \cos\theta_1' \cos\theta' + \sin\theta' \sin\theta_1' \cos\left(\phi' - \phi_1'\right) \tag{3.11}$$

where ϕ_1' and ϕ' are the azimuthal angles of the scattered and incoming photon in the electron rest frame. Thus the boost in energy received by the photon is of order γ^2. The cross section for this process is determined by the energy regime, with classical Thompson scattering governing low-energy interactions and Klein-Nishina scattering governing high-energy processes.

The mechanism with which the scattering environment is seeded with soft target photons is not known, although there are several possibilities. Bloom and Marscher (1996) further the attempt by Jones (1979) and Ghisellini et al. (1985) to explain the presence of the soft target photons as being those same photons that were produced via synchrotron emission by the relativistic electrons in the jet plasma (Figure 3.8(a)). The synchrotron self Compton model can be validated by multiwavelength observations since changes to the magnetic field in the jet will lead to well correlated fluctuations in the fluxes of the first and second peak, although the second peak is more sensitive to fluctuations in the electron density than the first.

This is in contrast to external photon sources which would result in weaker correlations between the two peaks. Such external models include UV to soft x-ray emission from the accretion disk itself (Dermer et al., 1992; Dermer and Schlickeiser, 1993), where using simple assumptions such as an

axially symmetric soft photon field lead to accurate fitting of boadband spectra. Another family of external models use photons from the broad-line region, which pervade the jet environment (Figure 3.8(b)). Sikora et al. (1994) use a single population of electrons shock accelerated in the jet to produce a model for variable gamma-ray emission, whereas Blandford and Levinson (1995) propose a model where the spectral output of the jet is a function of jet radius. The high-energy emission is produced by inverse Compton scattering of ambient soft photons by relativistic pairs accelerated to high energies in the jet. At small values of the jet radius, the gamma rays are strongly attenuated by pair production, thus the observed gamma-ray emission must come from further out in the jet.

A third family of seed photon models involves synchrotron radiation produced in the jet reflected back into the jet by the broad-line clouds (Figure 3.8(c)). Ghisellini and Madau (1996) use a double jet structure consisting of an inner and an outer jet. A relativistic blob moving through the jet illuminates the broad-line region with synchrotron photons, resulting in reprocessed softer x-ray photons being reflected back into the jet. This model suggests a natural scenario for flare generation when the relativistic blob in the jet crosses the broad-line region. However, this model is challenged by Bednarek (1998) who shows that the reflecting region would have to be inside the jet. Furthermore, that paper shows that the time-scale and shape of a flare should be indicative of the blob morphology, which, given flare observations, would require an exponential increase in relativistic electron density through the blob. Such an electron distribution is difficult to explain given the standard model of a relativistic shock propagating through the jet. However, Bottcher and Dermer (1998) use a small localised segment of the broad-line region which is Thomson-thick, located close to the jet axis, which can provide an efficient source of soft photons for Compton scattering for a short time. Again such a model naturally leads to flaring behaviour. They argue that this localised segment of a Thomson-thick cloud in the broad-line region is more realistic than the uniform spherically distributed clouds used in previous models as it is indicative of the probable clumpy nature of the cloud.

Although currently favoured by many authors, Leptonic models are not without their problems. For example, there is the possibility that populations of high-energy electrons in an optically thick jet environment should cool quickly before TeV gamma rays can be produced. Furthermore some of the Leptonic models predict jet magnetic fields that seem rather low ($\sim 10^{-4}$ G), and may not be sufficient to confine the jet. One of the more worrying problems is the requirement of a cut-off in the electron spectrum to reproduce the shape of the lower energy peak. This cut-off is somewhat

ad-hoc and as yet there is no valid interpretation to explain it. Interestingly Sikora and Madejski (2001) argue that x-ray observations of jets imply that electron/positron pairs dominate over protons (which has consequences for hadronic models), but that protons still dominate the jet dynamically. They go on to show that pure e^+/e^- jets overproduce soft x-ray radiation, instead favouring a proton/electron plasma. A recent study by Lindfors et al. (2005) describes a model with synchrotron emission in the plasma jet using a multi-component approach. In this model, synchrotron emission from both the jet and the shocks propagate through the jet. Using archival multiwavelength data they link EGRET gamma-ray flare observations of 3C 279 to radio shocks occurring within the jet to indicate that the flaring region is well beyond the broad-line region which casts doubt on certain external-Compton models. Furthermore, their model indicates that the high-energy emission is not consistent with the SSC model.

Perhaps a more significant problem with SSC models relates to unification. SSC models typically require a bulk Lorentz factor of $\Gamma > 25$ (Krawczynski et al. (2001); Konopelko et al. (2003)) in order to produce sufficient IR-UV synchrotron seed photons to produce the TeV peak of the spectral energy distribution. However such Lorentz factors require high Doppler factors of 10-20 if the spectrum is not de-absorbed and $\delta \geq 50$ if it is. This is in conflict both with plasma jet observations of FR I galaxies and with observations of sub-parsec regions of Markarian 421 (Marscher (1999)). The FR I observations are troubling in the context of unification as these galaxies are misaligned blazars in that scheme.

Georganopoulos and Kazanas (2003); Kazanas and Georganopoulos (2006) explore an alternative approach to the seed photon problem. In this model the seed photons come from synchrotron emission of downstream electrons which have decelerated in the jet from bulk Lorentz factors of ~ 15 to ~ 4. These photons undergo inverse-Compton scattering with fast up-stream electrons. One of the primary motivations for this model is that it overcomes the unification problem whereby standard SSC models predict jet Doppler factors which are far greater than those observed in the jets of supposed mis-aligned blazars. A similar reliance on jet morphology is studied by Laing et al. (1999) and Ghisellini et al. (2005) who use a fast central spine within the jet surrounded by a slow moving envelope. This model essentially uses a radial structure rather than a transverse structure as the Georganopoulos and Kazanas model does. Such radial morphology is supported by detailed VLBI radio maps of Markarian 501 (Giroletti et al. (2004)), where each part sees extra seed photons coming from the other part resulting in an enhancement in inverse-Compton emission from *both* parts.

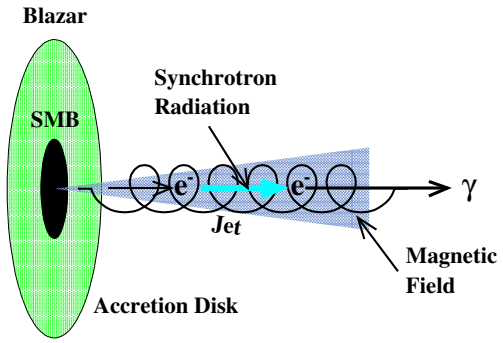

(a) Synchrotron Self Compton

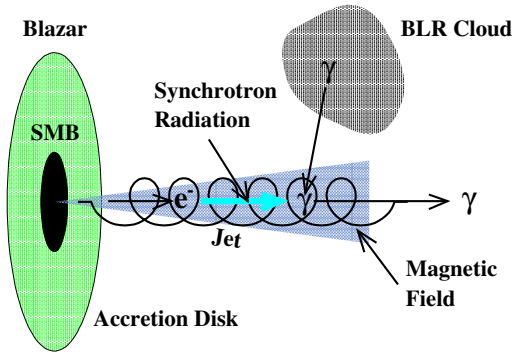

(b) External Compton with seed photons from the Broad-Line Region

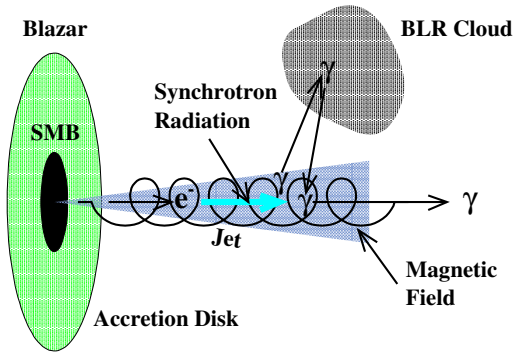

(c) External Compton with reprocessed jet photons from the Broad-Line Region

Figure 3.8: Leptonic Interactions. Three variants of the leptonic emission models are shown, and are discussed in the text.

3.7.2 Hadronic Models

Energetic hadrons in jets not only provide an opportunity to generate very high-energy gamma rays, but also involve acceleration of very high-energy protons up to 10^{20} eV. This is an attractive acceleration location for the extragalactic component of the flux of cosmic rays which strike the earth. The general form of gamma-ray production from energetic hadrons involves either the interaction of a proton with some target producing neutral pions (and other nucleonic debris), or direct synchrotron radiation. The neutral pions decay into a gamma-ray pair, whose energy is determined by the neutral pion energy.

$$\begin{aligned} p + p &\rightarrow \pi^0 + \text{debris} \\ \pi^0 &\rightarrow 2\,\gamma \end{aligned} \tag{3.12}$$

Production of TeV gamma rays is accompanied by simultaneous production of neutrinos, electrons and positrons via

$$\begin{aligned} p + p &\rightarrow \pi^{\pm} + \text{debris} \\ \pi^{\pm} &\rightarrow \mu^{\pm}\nu_{\mu} \\ \mu^{\pm} &\rightarrow e^{\pm}\nu_e\nu_{\mu} \end{aligned} \tag{3.13}$$

Various methods of TeV gamma-ray emission have been suggested using energetic protons, with two main families considered, the first involve high-energy ($E > 10^{16}$eV) proton beams, and the second involve ultra high-energy proton beams ($E > 10^{19}$ eV).

Pohl and Schlickeiser (2000) suggest a strong electron-proton beam that sweeps up and energises ambient matter which becomes isotropised by jet instabilities. This model is analogous to expanding fireball models for gamma-ray bursts, where most of the explosion energy is converted into the kinetic energy of a blast wave of relativistic baryons, and channeled by the collimating effect of the magnetic field. Upon interacting with the interstellar medium, low frequency Alfven waves are generated which isotropise the interstellar protons and electrons. Interactions between these protons and the blastwave protons generate neutral and charged pions which decay into gamma rays, electrons, positrons and neutrinos (Figure 3.9(a)). Alternatively Dar and Laor (1997) use the clouds of gas with high column density crossing the jet as a target for the accelerated protons, proposing the broad-line region of AGN as a natural candidate (Figure 3.9(b)). They imply that the electrons and positrons produced by the charged-pion decay undergo

cooling via synchrotron radiation and inverse Compton scattering producing delayed radiation from optical to x-ray, GeV and TeV.

The second family of hadronic models requires a beam of ultra high-energy proton beams ($E > 10^{19}\,\mathrm{eV}$) to interact with either ambient photons, the jet magnetic field, or both (Figure 3.9(c)). In the proton blazar model Mannheim (1993) uses protons and electrons co-accelerated in the jet due to multiple crossing of shock fronts propagating through it. Protons can be accelerated in this manner to hundreds of TeV, and can lose energy through adiabatic expansion, direct synchrotron cooling or by reacting with nearby photons according to the following mechanisms

$$\begin{aligned} p + \gamma &\rightarrow \pi^{\circ} + p \\ p + \gamma &\rightarrow e^{+} + e^{-} + p \end{aligned} \tag{3.14}$$

The pion decays into a gamma-ray pair, however this is scattered in the optically thick jet producing an electromagnetic cascade (referred to as the Proton Induced Cascade). The source of the target photons in the above interaction is not clear, however close to the supermassive black hole the target photons most likely comes from the accretion disk, whereas far from the supermassive black hole the target photons could come from broad-line clouds. The proton interaction with the seed photons initiates a pair-synchrotron cascade, comprising π^0 cascades, $\pi^{\pm}$ cascades, proton-synchrotron cascades, $\mu^{\pm}-$ synchrotron cascades and Bethe-Heitler cascades. Both the lower and higher energy peak in the blazar spectral energy distribution are attributed to these cascades, with the proton-synchrotron cascades and the $\mu^{\pm}$ synchrotron radiation accounting for the high-energy emission and the electron synchrotron radiation accounting for the lower energy emission.

An alternative model involving ultra high-energy protons proposed by Aharonian (2000) involve synchrotron radiation of $10^{19}\,\mathrm{eV}$ protons in a compact highly magnetised ($B \sim 30 - 100\,\mathrm{G}$) region of the jet. Assuming synchrotron cooling at the maximum allowed rate, this emission channel is shown to dominate other channels and provide good fits to the data for Markarian 421 and Markarian 501, and explains the consistency of the spectral shape during flaring activity.

Mücke et al. (2003) use both proton synchrotron and pair cascade hadronic models to explain the blazar spectral energy distribution, however they show that for low-frequency peaked blazars, the higher energy peak is explained by pion photoproduction and subsequent cascading (ie the proton blazar model), whereas in high-frequency peaked blazars, the higher energy peak is dominated by proton synchrotron emission with the magnetic field in the jet.

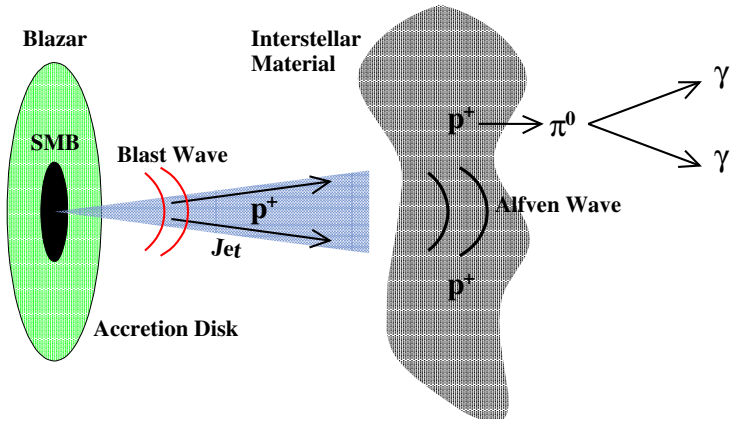

(a) Interstellar Medium Interaction

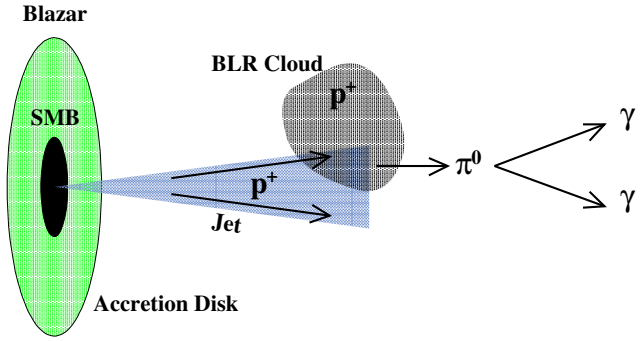

(b) Broad-Line Region Interaction

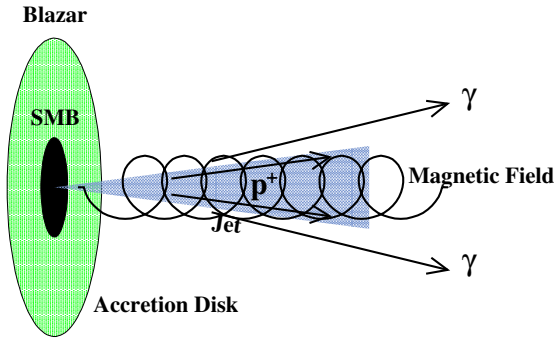

(c) Magnetic Field Interaction

Figure 3.9: Hadronic Interactions. Three variants of the hadronic emission models are shown, and are discussed in the text.

Just as there are problems with the leptonic models, the hadronic models also experience various difficulties. For instance some models have difficulty producing rapid variability on short time scales as it places extreme constraints on the magnetic field strength since the proton gyroradius has to be much smaller than the system itself. Models involving the broad-line region clouds suffer inefficiencies due to the optically thick nature of the clouds.

3.8 Extragalactic Infrared Background

Nikishov (1962) considered the absorption of high-energy gamma rays on the infrared radiation field from galactic stars and dust. The absorption of a high energy photon on a background photon can be simply represented by

$$\gamma + \gamma_{background} \rightarrow e^+ + e^- \tag{3.15}$$

The threshold energy required to produce the electron-positron pair is simply the sum of their rest energies. For gamma rays in the TeV range, the absorption cross section is a maximum when the background photon is in the infrared range. Thus for a high-energy gamma ray of energy E, the cross section peaks at energy $\epsilon\,(E)$.

$$\epsilon\,(E) \simeq 0.5 \left(\frac{1\ \mathrm{TeV}}{E}\right)\ \mathrm{eV} \tag{3.16}$$

For a 1 TeV photon, the cross section peaks at 0.5 eV or about 2 μm.

Following the discovery by Penzias and Wilson (1965) of the all-pervading photon field, which is a relic of the decoupling of matter and photons approximately 300,000 years after the big bang, it was noted by Gould and Schréder (1966) and Jelley (1966) that the universe would be opaque above 100 TeV due to absorption on this field. The degree of absorption is determined by the intensity of the field and the distance to the source.

It was proposed by Stecker et al. (1992) that pair production absorption features in the spectra of AGN could be used to determine the density of the infrared component of the EBL. Subsequent observations of a cut-off (Krennrich et al. (2002); Aharonian et al. (2005d)) in the spectrum of the nearby blazar Markarian 421 around 4 TeV and no detections (at that time) of blazars at a redshift greater than 0.129 seemed to confirm that absorption played a critical role in detecting extragalactic sources, and that the region of space visible in TeV gamma rays was restricted to z $\sim$ 0.2.

Rather than using knowledge of the infrared background to correct observed AGN spectra to produce intrinsic spectra, spectral measurements of AGN can be used to constrain the infrared background. In order to do this,

a selection of AGN spectra at several redshifts are required. Then using these spectra, a set of test models of the infrared background are used to calculate the intrinsic source spectra. Assuming that the intrinsic spectra are falling in the TeV regime, and that the infrared background spectrum is greater than the lower limit implied by galaxy counts, new constraints can be placed on the infrared background spectrum Dwek and Krennrich (2005); Aharonian et al. (2006b)).

A direct measurement of the infrared component of the EBL is not possible due to the overwhelming foreground radiation such as that due to diffuse dust in the Milky Way, night sky glow and the zodiacal light. Until recently, the most significant lower limit on the intensity of the infrared component of the EBL was set by integrating galaxy counts. A measurement of the infrared component of the extragalactic background light is needed by cosmologists attempting to reconstruct galaxy formation. Observation of the attenuation of very high-energy gamma rays from AGN is one of the most promising new techniques for probing this background.

3.9 Importance of TeV Observations

Coppi and Aharonian (1999) show a method to distinguish between synchrotron self-Compton and external-Compton leptonic models by examining the time lag between x-ray and gamma-ray flares (assuming there is any correlation present at all). A time lag is expected in the external-Compton case as the synchrotron photons from newly accelerated electrons need time to propagate through the source. Such lags are reported in Błażejowski et al. (2005) by correlating multiwavelength observations of the blazar Markarian 421. X-ray data with the RXTE satellite measuring the lower spectral peak and TeV data with the Whipple 10m measuring the upper spectral peak are compared. The results are confusing at best, with one season's data showing an apparent x-ray lag, and another season showing an apparent gamma-ray lag. However the statistical significance in either case is not compelling, especially given the sparse sampling of the data. The work further suggests that, given the 'evidence' of the Markarian 421 x-ray flare lags, the orphan flares (Figure 3.10) reported by Krawczynski et al. (2004) for the blazar 1ES 1959+650 may not be orphaned at all, but may merely be lagged. However, if the existence of x-ray lags can be confirmed, it could provide compelling evidence for the Dar and Laor (1997) hadronic emission model.

Various Monte-Carlo simulation codes have been used to attempt to model the broadband spectra of blazars. Tavecchio et al. (2001) use relatively simpler Monte-Carlo simulation codes using one-zone homogeneous emission

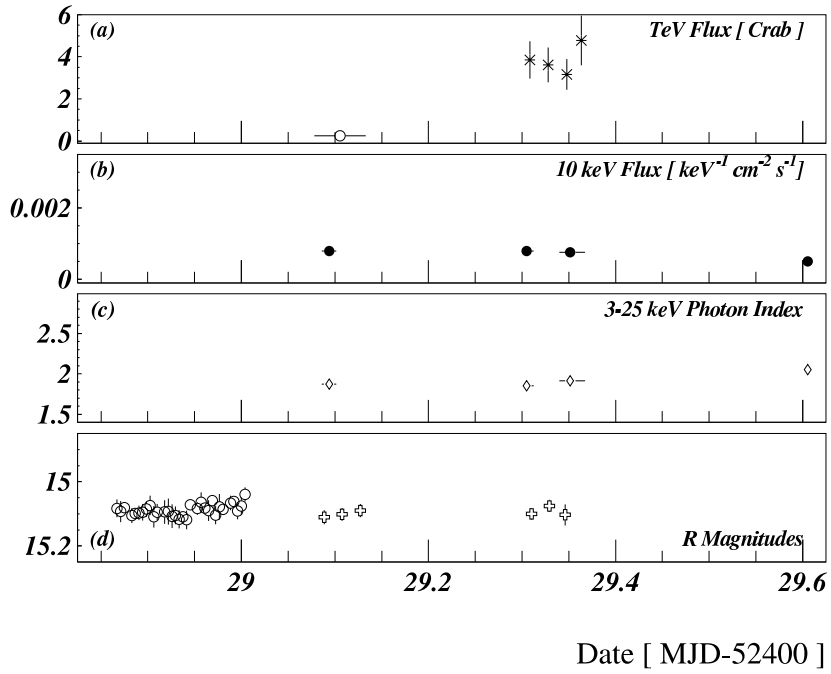

Figure 3.10: The detection of an orphan flare from the blazar 1ES 1959+650 from multiwavelength observations. The flare can be seen as the excess flux in TeV measurements in the top panel, where no coincident flare is detected at other wavelengths. This important result presents a challenge to all emission models. Figure from Krawczynski et al. (2004).

volumes. However more sophisticated codes by (for example) Krawczynski et al. (2002) use time dependent modelling to examine flaring activity. The conclusions drawn from much of this work indicates that relatively simple one-component and two-component models are consistent with most multi-wavelength data (except for instance the orphan flares reported by Krawczynski et al. (2004)). Most of the codes must take extragalactic absorption on the infrared background into account (even for nearby blazars) in order to explain the observed cutoff in several blazar spectra around $2-4$TeV. However recent observations of a selection of blazars at several redshifts by Aharonian et al. (2006b) indicate that extragalactic absorption may not be as significant as previously thought and that the observed cutoff in some blazars may be due to intrinsic processes (whether it is an emission effect or local absorption effect is not clear). Modelling has also indicated that relativistic beaming is extremely important to explain the flux of TeV photons, with Doppler factors of between 50 and 100 required (Krawczynski et al., 2001).

Studies of Fermi energy gains and radiative energy losses by Kirk and Mastichiadis (1999) predict correlations between hardness intensity for the low energy and high-energy spectral peaks. Multiwavelength observations in the x-ray and TeV bands appear to show the expected behaviour (Horns, 2003), with the x-ray and TeV spectral indices going through clockwise and anticlockwise loops during flaring activity. However the same source shows other signatures also, casting doubts on whether this hysteresis has actually been observed.

Studies of how the supermassive black hole and jet properties are connected have not progressed far. Models involving magnetohydrodynamic or relativistic-magnetohydrodynamic jet formation are at odds with observations as they imply the bulk relativistic Lorentz factor $\Gamma < 10$ (Krawczynski et al. (2004)), whereas observations fit to synchrotron-Compton models show $\Gamma >> 10$ (Koide et al. (1999)). Studies of galactic stellar velocity measurements have provided the first reliable estimates of black hole mass. No correlations between mass and peak location or luminosity have been found, despite measured black hole mass differences of an order of magnitude among blazars. However other jet parameters such as viewing angle, magnetic field and photon field could wash out any correlations that are present.

It is argued by Mannheim (1993) that proton-matter interactions can not be the radiation mechanism responsible for the production of very high-energy gamma-ray emission. This argument follows since unrealistically large amounts of target matter would be required in the blazar jets, and would result in an over abundance of light elements generated by the spallation of heavy nuclei (Baldwin et al., 1977).

In recent years, hadronic models have fallen out of favour because of the correlated x-ray and gamma-ray flaring observed in Markarian 421 and

Markarian 501. In the case of hadronic models involving interactions with ambient photons, rapid flaring observed in Markarian 421 (Gaidos et al. (1996); Albert et al. (2006b)), with doubling times of 15 minutes, places extreme constraints on the magnetic field and Doppler factor, with $B >>$ 10gauss and a Doppler factor $>> 100$ required to explain the flare (Pohl and Schlickeiser (2000)). The hadronic model involving collisions of a collimated proton jet with the broad-line clouds is also problematic as such clouds are optically thick. However, the reported detection of an orphan TeV flare from the blazar 1ES 1959+650 by Krawczynski et al. (2004) indicated that hadronic acceleration may still be an important component, as orphan TeV flares would naturally be expected from hadronic accelerators. However the authors stop short of claiming this as proof of hadronic acceleration, as correlated x-ray and gamma-ray flares had been observed from this source. Instead, various permutations of the synchrotron self-Compton and external-Compton models are suggested, with the primary conclusion merely being that a simple one-zone synchrotron self-Compton model is not sufficient. Interestingly, the Amanda neutrino detector reported the detection of two neutrinos (Halzen and Hooper (2005)) from the direction of 1ES 1959+650 coincident with a TeV flare. The detection of neutrinos requires nucleonic rather than photonic interactions with accelerated protons, and requires a TeV spectrum of approximately 2.8. Given the observation by Whipple of an orphan flare from 1ES 1959+650 and the HEGRA and Whipple spectral index measurements of ~ 2.83 (Daniel et al. (2005)), the possibility of hadronic related emission seems strong. However, it should be noted that the statistical significance of the neutrino 'burst' could not be calculated given the lack of statistics and the difficulty in accounting for trials. Still if further bursts are detected as larger neutrino detectors come online, it could prove to be a major discovery.

The discovery of the orphan flare from 1ES 1959+650 motivated new studies of high-energy emission models, with both leptonic and hadronic schemes revisited. A new leptonic model proposed by Kusunose and Takahara (2006) uses an inhomogeneous jet model whereby an x-ray flare occurs within the jet but encounters a dense region of highly relativistic electrons and/or positrons in the jet. This region upscatters the x-ray photons to TeV gamma-ray energies, thus absorbing the x-ray flare and producing a TeV gamma-ray flare instead. Such an event would be preceded by a correlated flare, which is exactly what happened with the 1ES 1959+650 orphan flare. A new hadronic model (Böttcher, 2005, 2006; Reimer et al., 2005) employs a hadronic-synchrotron mirror effect whereby electron-synchrotron radiation from a precursor SSC flare are reflected from clouds a few parsecs above the accretion disk back into the jet where they can interact with relativistic protons via a $\Delta\,(1232)$

resonance

$$p + \gamma \rightarrow \Delta\,(1232) \rightarrow p + \pi^0 \tag{3.17}$$

The neutral pions decay to very high-energy gamma rays producing the TeV gamma-ray flare. Although this model is attractive as it also predicts neutrino emission, the predicted emission requires unreasonably large values for the proton density (Böttcher (2006)).

3.10 Summary and Future Outlook

This chapter has summarised the current state of theory and observations of AGN, and in particular, the very high energy component of blazars. Topics such as unification, plasma jets, relativistic beaming and absorption on the extragalactic infrared background have been covered.

With the discovery of TeV emission from the blazar Markarian 421 came the realisation that TeV measurements of blazars provided an entirely new tool for studying blazar jet properties and emission mechanisms. As the TeV observations are at the extreme end of the electromagnetic spectrum, they are highly sensitive to the tuning of jet parameters in a given model, and thus provide excellent measurements of jet Doppler factors, magnetic field strengths, particle densities etc. It is unfortunate however, that actual values for these factors are not well known. This gives authors free reign to adjust these parameters until their models fit the data. It is no wonder that almost every theoretical paper quotes 'remarkable' or 'impressive' agreement between the model studied and the observed data given the number of free parameters available.

Nevertheless, TeV observations in concert with observations at other wavelengths, constitute an important tool in differentiating emission mechanisms. As the energy threshold for Cherenkov telescopes falls, and the sensitivity and resolution increases, the contribution of these telescopes becomes increasingly important. In that context, this thesis represents efforts to improve the sensitivity of VERITAS with applications to observations of two candidate TeV blazars and one established TeV blazar.

Chapter 4

The VERITAS Array

The VERITAS array of 12 m telescopes is located at the basecamp of the Fred Lawrence Whipple Observatory at an elevation of 1270 m. The first two telescopes were operated in array mode from March 2006 with data from those telescopes used in the analysis for this thesis. Telescopes 3 and 4 were partially installed in the summer of 2006, with commissioning of these telescopes planned for late 2006/early 2007. Observations with the full 4-Telescope array is expected to commence in spring 2007. Telescopes 1 and 2 are shown in Figure 1.5(d). A close up view of Telescope 2 is shown in Figure 4.1.

This chapter offers a detailed description of the VERITAS telescopes, commencing with the optical-mechanical elements of the telescope structure(Section 4.1). This is followed by a description of the cameras (Section 4.2), multi-level trigger system (Section 4.3), data-acquisition systems (Section 4.4) and calibration systems (Section 4.5). Finally the monitoring (Section 4.6) systems and online/offline control software (Section 4.7) are reviewed.

4.1 Telescope Structure

The VERITAS telescopes have the same essential design as the Whipple 10 m Cherenkov Telescope (Kildea, 2006). This design consists of an alt-azimuth mount supporting a tubular-steel space-frame Optical Support Structure (OSS). Hexagonal mirrors are mounted on the OSS following the segmented Davies and Cotton (1957) design. The camera is mounted on a quadrapod arm structure which uses a mechanical bypass to direct the camera load directly onto a set of counterweights at the back of the OSS. The VERITAS telescopes have a focal length and diameter of 12 m, giving an f number of

Figure 4.1: VERITAS Telescope 2. Evident is the tessellated mirror structure, quadrapod arms and camera (with access platform). The electronics room is located beneath the access platform and contains the Level 1, Level 2 and Level 3 triggers and data acquisition systems.

f/1.

4.1.1 Optical Support Structure

The OSS is a custom designed tubular-steel space-frame structure of approximately 12m diameter. It was designed by M3 engineering (Tucson, Arizona) and manufactured by Amber Steel (Chandler, Arizona). The OSS is delivered in three welded segments which can be bolted or welded at the telescope construction site. The weight of the camera, quadrapod arms, mirrors and the OSS structure itself causes varying degrees of flexure depending on the telescope elevation. The OSS is designed to minimise this flexure at the expense of weight and cost. Even so, flexure at typical observing elevations causes a spread in the Point Spread Function (PSF) which can be corrected using a bias alignment (Section 4.1.4). The PSF is defined as the width of a Gaussian fit to an image of bright star on the focal plane recorded by a CCD. A narrow PSF is desired as it leads to tight well defined images which aids gamma-hadron separation and improves angular resolution. The main factors affecting the PSF are mirror alignment and OSS flexure, which means the PSF can vary as a function of elevation. The VERITAS telescopes have a PSF corresponding to less than the diameter of a pixel (Figure 4.2). Camera

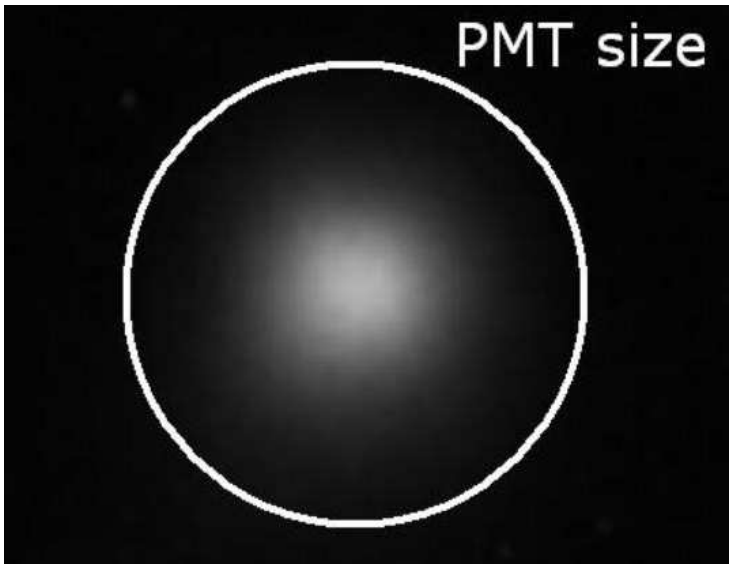

Figure 4.2: The image of a star reflected onto the focal plane. The diameter of a VERITAS PMT, which is 0.15° is indicated by the white circle. The PSF is the width of a 3-D Gaussian fit to the image of the star.

slumping due to OSS flexure results in the observed target not corresponding to the center of the field of view of the camera. Offsets can be applied to the drive system pointing software to account for this (Section 4.1.3).

4.1.2 Positioner

The telescope positioner is a commercially built Rotating Precision Mechanisms RPM-PSI model PG-4003 (Figure 4.3). This positioner is capable of position accuracies of better than 0.005°, and uses Proportional-Integral-Derivative motion control, brushless dual-opposed drive, and 26-bit absolute encoders. The selection of a commercial positioner ensures a relatively low cost and guarantees long term maintenance, support and parts availability. Although the positioner has a design slew speed of 1°/s in elevation and azimuth, it is driven at $0.3° - 0.5°$/s for safety reasons. It has a tracking accuracy of $< 0.005°/$ s and is controlled via serial or ethernet interface to a tracking computer, which logs the telescope pointing location to the VERITAS database (Section 4.7.2) at a rate of ~ 4 Hz. The positioner is designed to be safe to operate at wind speeds up to 20 MPH and has a design survival speed of 100 MPH at the parked position with azimuth and elevation stow pins engaged.

Figure 4.3: The VERITAS Positioner and OSS. This photograph was taken during construction of Telescope 1 before all the mirrors had been installed.

4.1.3 Optical Corrections

OSS flexure and imperfections in the mechanics of the drive system lead to telescope mis-alignment. This mis-alignment can be corrected by applying a series of adjustments to the azimuth and elevation drives which are listed below. The adjustments are a series of spherical rotations, similar to T-Point[1] corrections, which are designed to re-center the source on the center of the camera. The adjustments are calculated by pointing the telescope at a star whose exact location in the sky is known. A CCD camera is used to record an image of the star reflected onto a screen at the focal plane. The pointing of the telescope is adjusted, and further images recorded in an iterative procedure until the image of the star is coincident with the center of the camera. This process is repeated for several stars at a range of elevations and azimuths and used to construct a ten parameter model of the OSS and drive system. These parameters are then used to correct the telescope's pointing during observing.

4.1.4 Mirrors

The Davies-Cotton design specifies a large set of individual mirrors which combine to simulate a single large spherical reflector. The use of many small mirrors has several advantages over a single large mirror. A single large mirror would be extremely heavy and require an ultra strong OSS and steering mount. Such a heavy object would also suffer from gravitational slumping which would result in blurred images on the focal plane. Alternatively, small single mirrors are light, can be easily adjusted, cleaned and replaced if they become damaged. The most significant disadvantage to the Davies-Cotton design is its anachronicity. Mirrors at the edge of the reflector are farther from the camera than those in the central region. This spreads the Cherenkov light arrival time, which can hinder attempts to study the temporal evolution of EAS. However, analytic and simulated studies by White (2005) show that 90 % of the light received by a VERITAS reflector reaches the camera within 2 ns - this corresponds to the FADC (Section 4.4.1) digitisation timescale.

The mirror glass is ground at Displays & Optical Technologies Inc. Round Rock, Texas before delivery to the Fred Lawrence Whipple Observatory. There, the glass is cleaned before being placed into a large vacuum chamber which is evacuated to 10^{-4} atm. An aluminium layer is evaporated onto the glass to attain a thickness of approximately 1350 Å. Once the layer is set, a current is passed through the aluminium producing aluminium oxide. This adjusts the peak of the mirror reflectivity response curve to coincide with the

[1] http://en.wikipedia.org/wiki/Tpoint

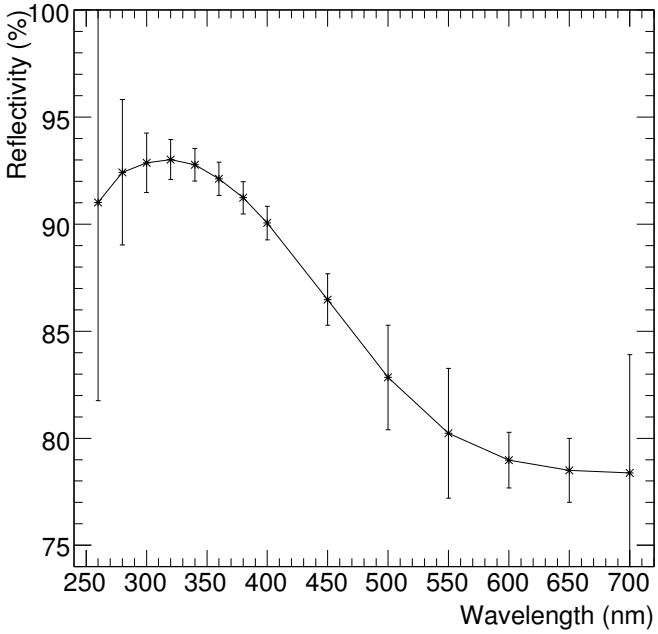

Figure 4.4: VERITAS Mirror Reflectivity Curve. The reflectivity is optimised to match the peak intensity of Cherenkov radiation at observing altitude.

peak in the Cherenkov spectrum from air showers at observing level (Figure 2.6). The mirrors are tested and are required to have a radius of curvature of $24\,\mathrm{m} \pm 1\,\%$. The reflectivity exceeds the design specifications, with reflectivity $> 90\,\%$ at 320 nm (Figure 4.4) and $> 85\,\%$ between 280 and 450 nm (Gibbs, 2003).

Each telescope is fitted with 350 hexagonal mirrors facets each with a surface area of approximately $0.333\,\mathrm{m}^2$ providing a total mirror area of $\sim 110\,\mathrm{m}^2$. A hexagonal design is preferable over a circular design as it allows close packing of the mirrors leading to a maximisation of total mirror area. The mirrors are attached to the OSS using a triangular mounting structure which isolates the mirrors from OSS flexure. Each mirror is attached to its mount using three screws which can be adjusted to correct the exact pointing of the individual mirror to within $< 0.02°$.

Alignment

Mirror alignment is achieved using a laser-based alignment tool which is placed at the 2F point of the telescope (see Figure 4.5). A helium-neon

laser is reflected from each individual mirror, and the mirror is adjusted until the return beam coincides with the outgoing beam. This is achieved by redirecting the beams via a prism onto a screen where an image of the two beam spots is recorded using a CCD camera. The system measures the relative locations of the beam spots and produces a series of corrections to be applied to the mirror-adjustment screws which brings the mirror into alignment.

OSS flexure causes a spread in the PSF at observing elevations. To correct for this, the mirrors are bias-aligned. This requires intentionally mis-aligning the mirrors in the stow position, such that the OSS flexure causes them to return to alignment at observing elevations. This is done by clamping a laser pointer to each mirror and recording its position on the focal plane using a CCD camera while the telescope is elevated. The correction required is computed and applied once the telescope is stowed with the aid of the mirror alignment system described earlier.

4.2 Camera

The VERITAS cameras are located 12 meters from the central mirrors of the telescope and have a field of view of 3.5°. Each camera is installed inside a focus box which is a sturdy light-tight, water-tight structure. The plane of the focus box is 1.8 m^2 allowing room for a larger field of view camera if a future upgrade is desired. The focus box is equipped with a remote control operated garage-style shutter which is opened during observing and closed during daytime to protect the PMTs from UV exposure. The primary component of the camera is the array of PMTs (Section 4.2.1) which detect Cherenkov light reflected from the mirrors. It also houses the preamplifiers (Section 4.2.3), Current Monitor boards (Section 4.2.4), Charge Injection boards (Section 4.2.5), environmental sensors (Section 4.2.6) and light cones (Section 4.2.7). Given that the focus box, camera and all its components are a major contributor to OSS flexure, the combined focal plane instrumentation weighs less than 350 kg.

4.2.1 Photomultiplier Tubes

In order to detect the extremely faint and brief flash of Cherenkov photons, a low noise, high gain, linear photon counting device with a fast (~ 2 ns) rise-time is required. The temporal evolution of the Cherenkov wavefront occurs over a period of $3 - 4$ ns necessitating a fast PMT risetime if this temporal behaviour is to be studied. The fast risetime also ensures a minimisation of

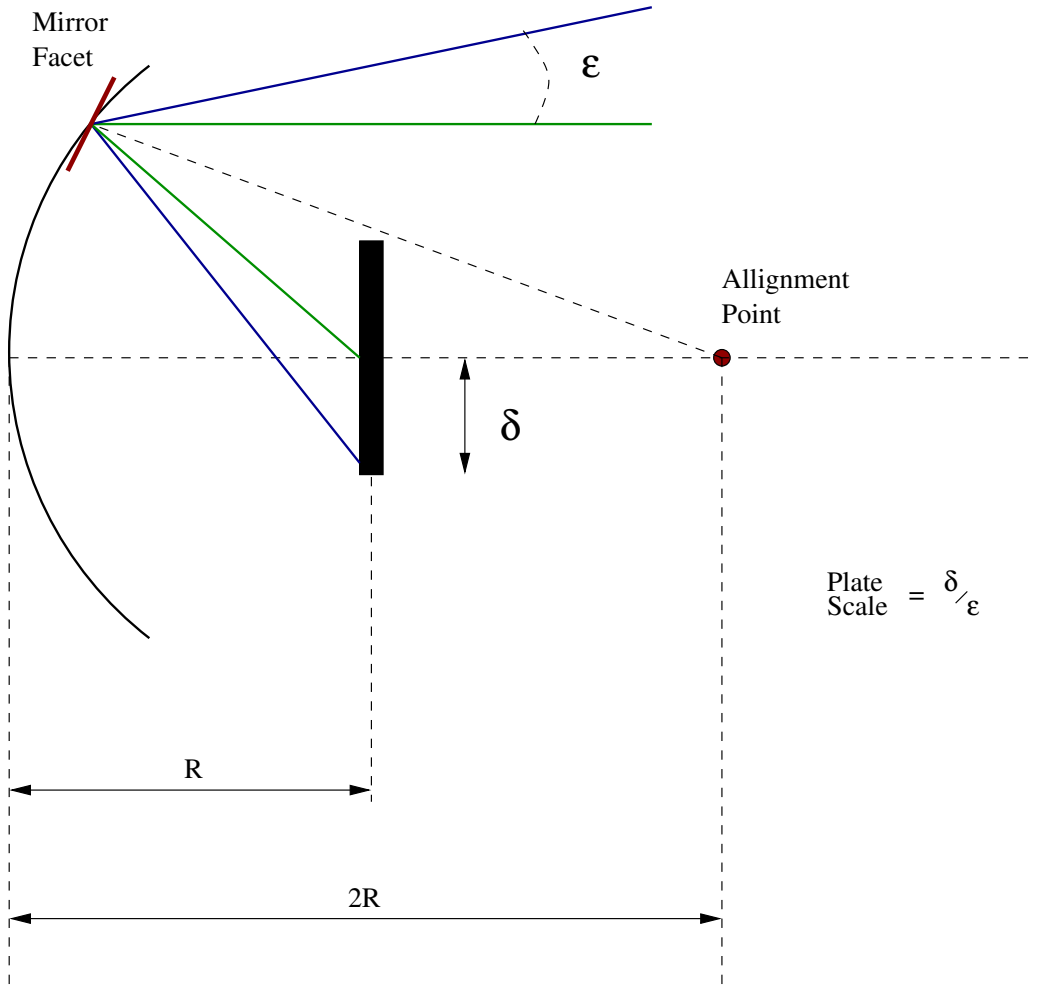

Figure 4.5: Definition of the alignment point for a focal plane camera located a distance R from the reflector. Each facet is located on an imaginary sphere of radius $2R$. When each fact is aligned with the $2R$ point, the telescope is focused onto the focal plane. The plate scale relates the amount of sky seen to the pixel size.

the charge integration gate which leads to a maximisation of the signal-to-noise ratio (Section 6.4). Despite steady advances in the field of solid state detectors, only PMTs currently meet these requirements. PMTs comprise a photocathode followed by a series of dynodes held at sequentially increasing potential and finally an anode. An incoming photon passes through a glass window at the front of the PMT and strikes the photocathode. When photons strike a metal surface with an appropriate work function, an electron (referred to here as a photoelectron) is released from the surface of the metal. This phenomenon is known as the photoelectric effect and is the basis of PMT operation. The Quantum Efficiency (QE) of the PMT is a measure of the probability of a photoelectron being released if the photocathode is struck by an electron, and is dependent on the wavelength of the original photon (Figure 4.6) and the material of the photocathode. Once released, the photoelectron is accelerated by a strong potential and strikes the first dynode which is coated with a secondary emissive material which releases electrons when struck by an electron. The number of electrons released depends on the kinetic energy of the incoming electron, which is directly proportional to the applied potential, and the material from which the dynode is made. These electrons travel to the next dynode which is held at a higher potential than the first, releasing more electrons in a cascading effect from dynode to dynode. Eventually the electrons are collected at the anode where a current is registered. The gain of the PMT is the average number of electrons produced at the final dynode by a single photoelectron and is related to the applied potential by a power law of the order of the number of dynodes.

The VERITAS PMTs are Photonis XP 2970/02 which are fast UV-sensitive, ten-dynode devices with a bi-alkali photocathode. The dynodes employ a linear focused geometry which ensures progressive focusing of the electron paths through the photomultiplier. This reduces the variation in transit times between the stages resulting in a fast response ((PHILIPS, 1994)). This model has a diameter of 2.86 cm with an effective radius of 1.2 cm corresponding to an angular spacing of 0.15°. The PMTs have a QE of 20 % at 300 nm and a maximum QE of 25 % at 400 nm. Each VERITAS camera houses 499 hexagonally packed PMTs with an average gain of 2×10^5.

The PMTs (Figure 4.7) are connected to the FADCs via 50 m of coaxial cable. The choice of cable (Kieda, 2003b) is driven by electrical and mechanical considerations. Electrical tests on several cable candidates were performed by passing a short pulse through 50 m of cable and measuring the performance in terms of the signal-to-noise ratio. An optimal signal-to-noise ratio is desirable as optimising this parameter is equivalent to adding or subtracting mirror area to the telescope. Cable candidates were compared to a normalised number of mirrors of 300, with some candidates having an equiv-

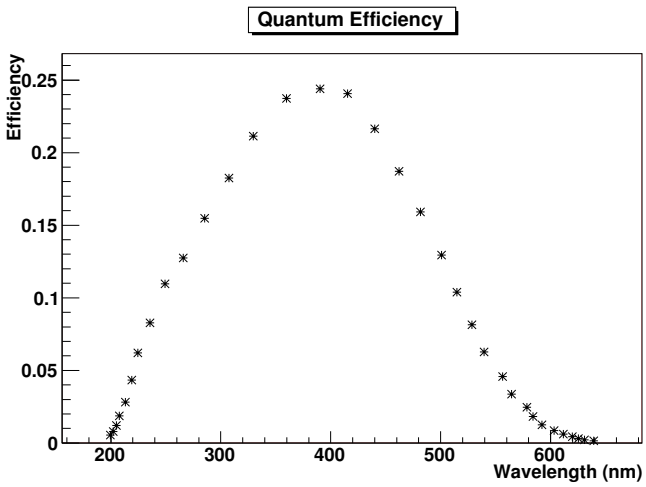

Figure 4.6: The quantum efficiency as a function of wavelength for the VERITAS PMTs. The quantum efficiency is measured using a specially designed laboratory test stand.

alent mirror area as low as 196 mirrors, and some as many as 361 mirrors. The cables were also subjected to mechanical stress tests which simulate rotation of the mount. The cables were twisted 270° back and forth at a fixed acceleration rate, and their integrity tested after millions of cycles. These tests corresponded to 10 years of VERITAS operations and took 3 months to complete. It was found that the stranded core candidates are more durable than the solid core candidates. The cable weight is also an important consideration in the context of OSS flexure as approximately 6 km of cable is routed through the quadrapod arms. Using these factors, and also considering cable diameter and cost, stranded core RG59(9803C) cable was chosen.

4.2.2 High Voltage

The HV of each telescope is controlled by a pair of CAEN multi-channel HV crates. The larger crate is CAEN Model 1527 and holds eight modules, whereas the small crate is CAEN Model 2527 and holds three modules. Each module controls six sectors of eight channels each. The voltage of each channel can be individually set over a specific range. Each channel has a current limit of 0.5 mA, which coupled with the 3MΩ resistance in the dynode chain, puts an upper limit on the channel voltage of 1500 V. The voltage in each channel can be fine-tuned to within one Volt allowing a precise gain setting.

Each PMT's HV is set using a custom designed ethernet interface con-

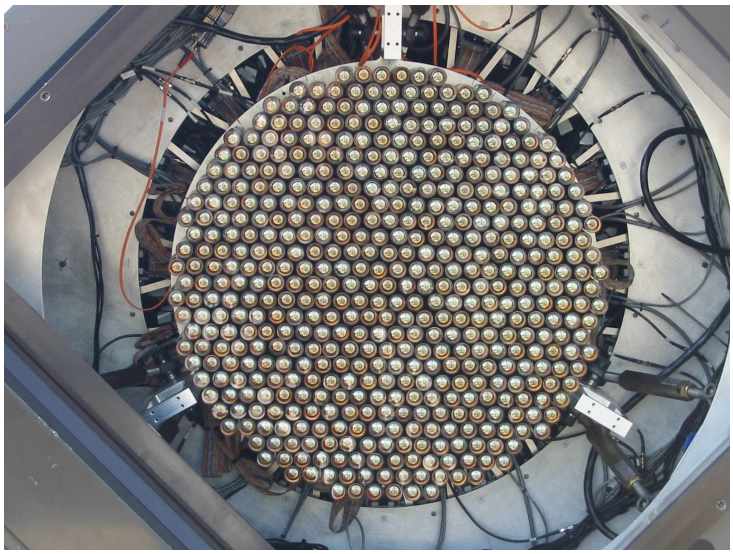

Figure 4.7: The 499 pixel camera on VERITAS Telescope 2. The PMTs are mounted on specially designed bases that fit into an aluminium frame. The charge injection and preamplifiers are located immediately behind the PMTs. The camera has a 3.5° field of view.

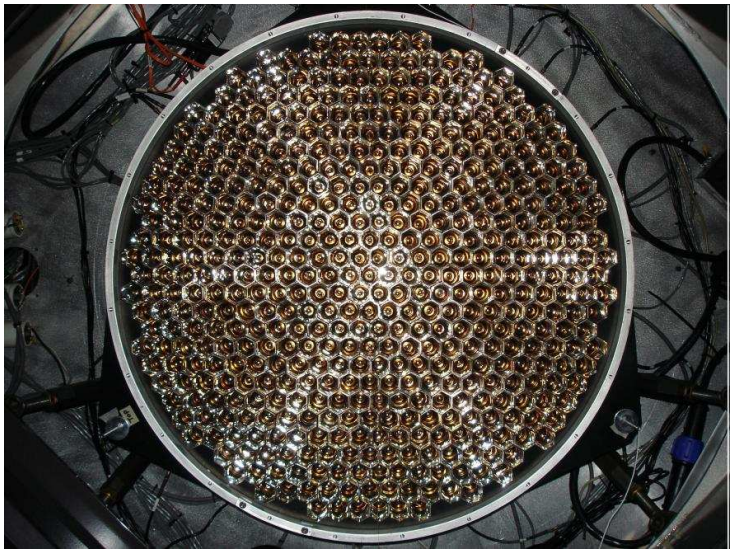

Figure 4.8: The same camera as Figure 4.7 but with the light cones added.

trol program. This program allows the voltage of individual tubes to be set manually or by reading them from the VERITAS database. The program also has the ability to automatically switch tubes off if the anode current exceeds a preset threshold. Such a situation can arise from stars or aircraft passing through the field of view, or from errant light sources in the vicinity of the telescope. A builtin safety feature automatically switches off the entire camera if a large number of tubes register a high current at the same time. Such a scenario would arise if a car passed by with headlights on or if somebody inadvertently flashed a torch on the camera. The program logs both measured HV values and anode currents to the VERITAS database once per minute, and any changes to the set HV are logged immediately.

There are various parameters with respect to which the camera can be flat-fielded; among these are the CFD trigger rate, the anode current and the integrated FADC charge. The latter is chosen as it incorporates uneven cable losses, preamplifier gain, onboard FADC gain and digitisation nonlinearities. The flat-fielding is accomplished by illuminating the camera with fixed intensity laser flashes in a series of runs with incrementing HV. For each pixel a response curve of integrated FADC charge versus applied HV is generated (See Figure 4.9). This is used to choose specific voltage values to ensure an even response across the camera. A typical distribution of the HV values for VERITAS Telescope 1 is shown in Figure 4.10.

For the VERITAS PMTs, the gain G is related to the Voltage V by the following relation[2]

$$G \sim V^{7.5} \tag{4.1}$$

thus the relative gain rg of a channel can be expressed as

$$rg = \frac{G_{abs}}{\langle G_{abs} \rangle} \sim \frac{V^7.5}{\langle V^7.5 \rangle} = A \frac{V^7.5}{\langle V^7.5 \rangle} \tag{4.2}$$

where G_{abs} is the absolute gain of that channel, $\langle G_{abs} \rangle$ is the mean of the absolute gains across the camera and $\langle V \rangle$ is the average voltage across the camera. Assuming rg is to be reassigned some rg_{new}, then the ratio of those gains is given by

$$\frac{rg_{new}}{rg} = \frac{\frac{hv_{new}}{\langle hv \rangle}^7.5}{\frac{hv}{\langle hv \rangle}^7.5} \tag{4.3}$$

which reduces to

[2]Photonis product specification data sheet

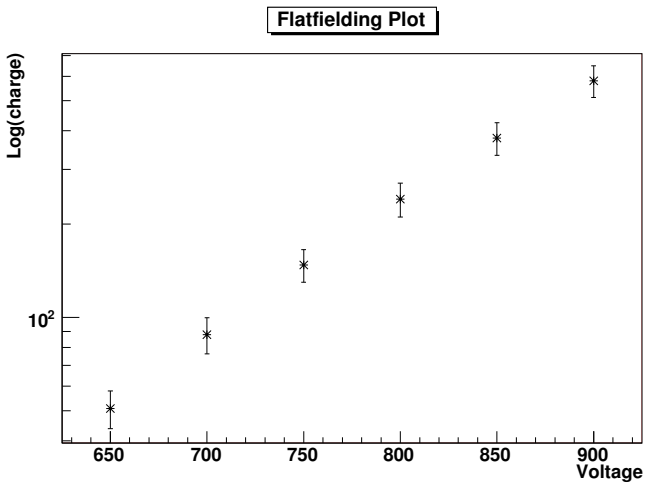

Figure 4.9: Integrated FADC charge for a single channel plotted against the High Voltage applied to that PMT. A similar plot is produced for each pixel and interpolation between points used to select the correct voltage.

$$\frac{rg_{new}}{rg} = \left(\frac{hv_{new}}{hv}\right)^{7}.5 \tag{4.4}$$

thus setting $rg_{new} = 1$ and solving for hv_{new} gives

$$hv_{new} = hv\left(\frac{1}{rg}\right)^{\frac{1}{7.5}} \tag{4.5}$$

In this way a flat trigger response in each camera can be assured.

4.2.3 Preamplifiers

Despite the huge gain afforded by the PMTs, the electric signal they deliver is still very small. This signal must be amplified in order to trigger on signals produced by 4 or 5 photoelectrons. Each PMT is supplemented with a preamplifier which implements a gain of 6.66 with a dynamic range of 700 photoelectrons. The voltage delivered to the front end of the FADCs should range from 0 V to −1.65 V. The 50 m of cable length from the camera to the FADCs attenuates the pulse by 25 %, implying the preamplifiers should have an output dynamic range of 0 V to −2.2 V. This gives a ratio of 3.14mV per photoelectron. Power to the preamplifiers is supplied by the Current Monitor distribution boards (Section 4.2.4).

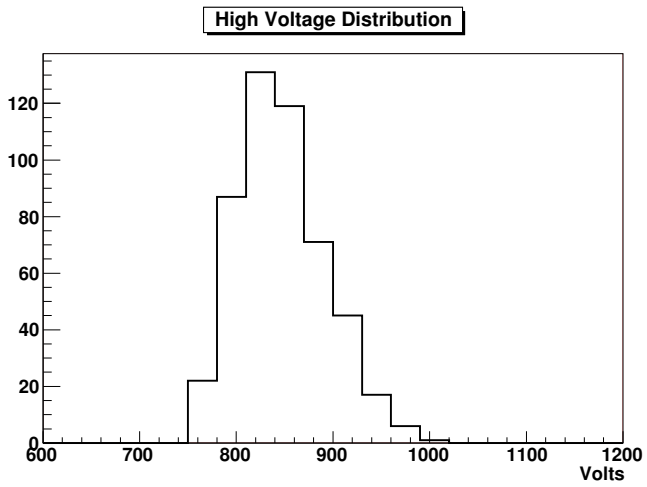

Figure 4.10: Distribution of High Voltages for VERITAS Camera 2.

4.2.4 Current Monitor

Each camera is fitted with a custom built system for monitoring the DC anode currents in the PMTs. The design specifies a 10 Hz readout with an accuracy of 0.5 μA. The Current Monitor system also provides power to the preamplifiers and provides power and readout channels for the environmental sensors (Section 4.2.6). There are two current monitor power supplies in each camera, with each supply capable of providing power to 300 preamplifiers. Each camera carries 16 current monitor boards with 32 channels per board. The boards are 'daisy-chainable', allowing for future expansion. Communication between the camera and the control room is via optical fiber with optoverters at both ends converting the data to/from optical/electrical signal.

As the light falling on a powered PMT increases, the anode current increases accordingly, however there is a limit to how much instantaneous current a PMT can tolerate, and permanent damage can be caused if this limit is exceeded. The lifetime of a PMT is dictated by the total charge deposited on it - e.g. a PMT will last twice as long if it is typically subjected to half the current. Apart from Cherenkov showers, the main sources of light that fall on a PMT during observing are the night sky background and starlight. Starlight can cause the PMT anode current to increase suddenly during normal operations. The current monitor reports the anode current to the observer and to the HV program which can automatically switch off the HV to that PMT. Average PMT anode currents range from 3 μA for dark fields to

6 μA for bright fields which corresponds to a $100 - 200$ MHz photoelectron background rate per PMT.

In order to obtain an accurate measurement of the current in each PMT, the current is initially recorded *prior* to the activation of the high voltage system. This provides a stable baseline, with respect to which the currents can be measured. However this baseline measurement does not of course exclude dark current. Dark current can come from leakage, thermionic emission, field emission and background radiation. Leakage currents contribute a continuous component of the dark current and are due to the surface conductivity of the PMT components. Leakage current varies linearly with high voltage but is not effected by temperature. Thermionic emission is the loss of an electron from a surface due to heating (eg from the photocathode). Such an electron will be accelerated through the dynode chain resulting in a current spike. Although there are not significant electric fields in a PMT, some emission can be expected due to the roughness of the electrodes. The final cause of dark current is background radiation - cosmic rays or radioactive decay products can give rise to Cherenkov radiation in the tube window. A muon passing through the camera can generate sufficient photons in several adjacent PMTs to trigger the telescope.

4.2.5 Charge Injection

The VERITAS cameras are fitted with a system for sending pulses directly into the PMT base (Kieda, 2003a). These pulses simulate the Cherenkov-light-induced signal produced by the PMT, and are used for testing and calibration. The charge injection system consists of a Programmable Pulse Generator (PPG) board with 16 fanout/mask boards. The PPG can produce frequencies from 1 Hz to 1 MHz using an internal crystal oscillator. The clock can also be triggered with an external optical signal which allows precise timing of injected pulses between telescopes. The PPG board carries two pulse generators which can be used to set the pulse width from 1 ns to 10 ms and adjust the pulse height over 85 dB.

The Charge Injection system is useful as a diagnostic/calibration instrument as it provides known calibrated pulses into the electronics/data stream. It can be used to test the Level 2 trigger patterns (Section 4.3.2), check for cross-talk, identify swapped channels and measure deadtime.

4.2.6 Environmental Sensors

Cherenkov telescopes are delicate instruments which are sensitive to environmental conditions such as temperature and humidity. The temperature

reduces PMT gain typically on the order of 1 %/C°, and PMT noise increases with temperature due increased thermionic emission. Safety is also a factor, as running the camera at high temperatures is detrimental to many electronic components. This is predominantly a factor during daytime testing where camera temperatures can exceed 50° C in the Arizona summer heat, mostly due to the $\sim$ 160 W dissipated by the preamplifiers. Camera fans provide extra circulation, however this generally only permits camera operation for a few hours during daytime. Humidity monitoring is very important in the case of PMTs as moist air can become sufficiently conductive that arcing occurs between PMTs.

4.2.7 Light Cones

The effective collecting area of a PMT is less than the diameter of the entire component because of the PMT housing surrounding the photocathode. This results in a significant amount of light reflected from the mirrors onto the camera plane not reaching the photocathodes.

This can be remedied by placing light concentrators in front of the PMTs (Figure 4.8 and 4.11). This light concentrator, known as a lightcone, reflects almost all incident Cherenkov light downward towards the photocathode. The light cones increase collection efficiency by $\sim$ 40% which has a significant impact on the energy threshold of the instrument. The light cones have the added bonus of excluding stray light from striking the photocathodes, as they effectively close the solid opening angle to match the profile of the mirror.

The lightcones follow the Winston design and are made of Aluminium with a Silicon Dioxide coating. This configuration gives a reflectivity greater than 85 % for wavelengths above 350 nm. The light cones are mounted on a machined aluminium plate which sits 1 cm in front of the plane of the PMTs. The focal plane of the camera lies on the surface of the lightcones.

4.3 Trigger

The night sky is a sea of fluctuations from such sources as starlight, ambient light, airglow etc. Since the EAS produces an extremely brief and faint flash of Cherenkov photons, a trigger scheme must be used which efficiently differentiates between random sky noise and showers of Cherenkov photons caused by very high-energy gamma rays. In principle, a very low threshold trigger could be used which could trigger continuously, but the data rate is limited by the readout limitations of the data acquisition system.

Each VERITAS telescope contains two trigger levels. Both triggers are

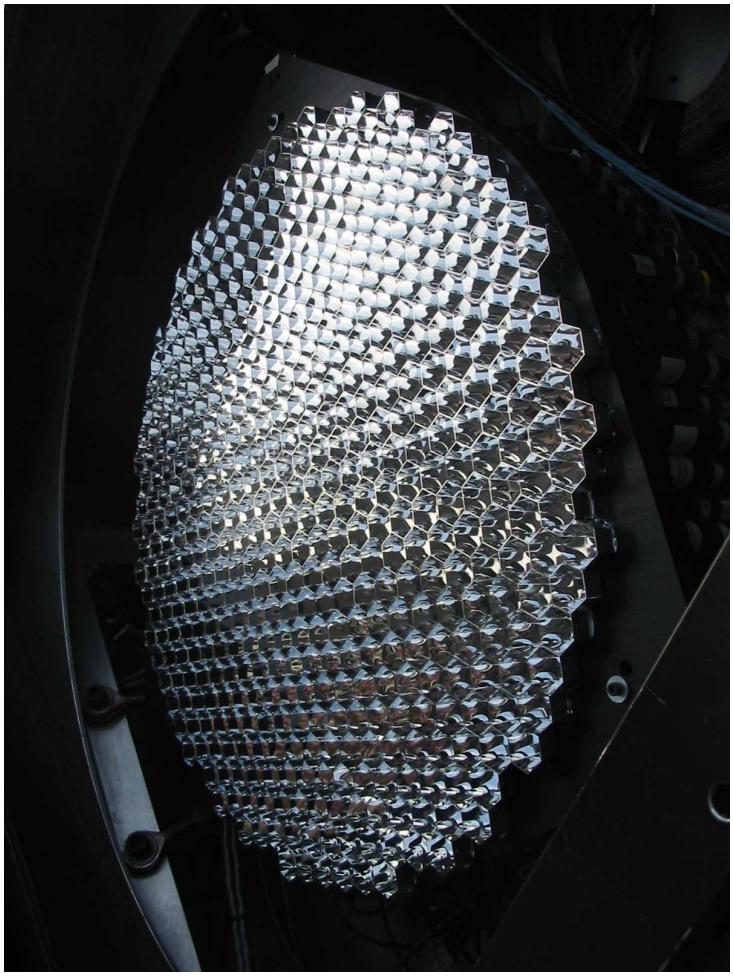

Figure 4.11: Lightcones mounted on the 499 Pixel Camera on VERITAS Telescope 1. The lightcones concentrate light from the full field of view onto the photocathodes. This can effectively increase the collection efficiency of the camera by up to 40% while shielding the PMTs from external light pollution (due to their baffling effect). The front face of the light cones is the focal plane of the camera.

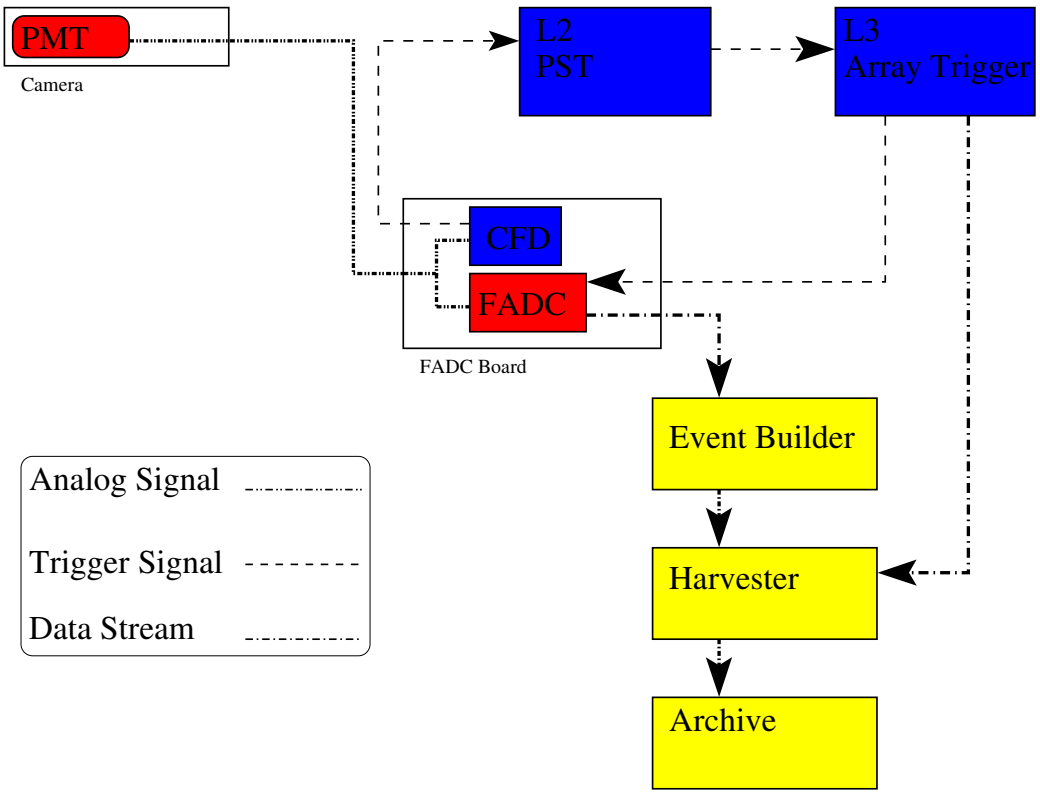

Figure 4.12: Simplified data/trigger schematic for the VERITAS Telescopes and Array. The schematic is described in the text.

designed to differentiate between photons from random night sky fluctuations and photons from extensive air showers. The signal from each PMT is routed through a CFD (Section 4.3.1) - this is the Level 1 trigger. The output from each CFD is routed to a PST (Section 4.3.2) - this is the Level 2 telescope trigger (Figure 4.12).

The Level 2 trigger from each telescope is routed into a Level 3 Array trigger. This trigger determines how many telescopes have produced a Level 2 trigger within a programmable coincidence window. This trigger is highly efficient at rejecting telescope triggers caused by local muons which typically only trigger a single telescope, and are a major source of background at low energies.

4.3.1 Level 1 Trigger

The Level 1 trigger comprises CFDs which work by initially splitting the analog PMT signal into three components. The first component goes into a simple threshold discriminator which generates a trigger signal if the input voltage exceeds a programmable threshold. The second signal component is inverted, delayed and fed into a Zero Crossing Discriminator (ZCD). The third component is attenuated and also passed into the ZCD. The ZCD combines the two pulses and selects the time at which the two pulses exactly cancel by checking for the point of zero crossing. It is at this time that the CFD will trigger. The output of the ZCD is routed into a flip-flop along with the output of the threshold discriminator. The output of the flip-flop is the actual CFD trigger which is routed into the PST.

Tight control of the timing in the CFD is desirable as a reduction in the coincidence resolving time of the PST can be used to lower the energy threshold of the telescope array. There are several factors which cause a deterioration in timing resolution. Jitter in the arrival time of the trigger can be caused by noise on the ZCD which is typically reduced by adding a small DC offset to the ZCD which prevents it from triggering on small distorted pulses. However this approach is not desirable as the primary source of noise is the night sky background (NSB) which can vary by as much as a factor of four depending on the sky field being surveyed. Also the rejection of small pulses is counter-productive as this increases the energy threshold of the telescope. In order to balance the requirements of triggering on small pulses and jitter minimisation, a novel circuit was designed by Vassiliev (2003) which automatically increases the ZCD offset as the ZCD trigger rate increases. This Rate Feed-Back (RFB) loop effectively increases the ability of the ZCD to eliminate small noisy pulses as the background noise increases. The RFB circuit responds to changes in the noise on a timescale of $\sim$ 1s. The VERITAS CFDs nominally operate with a RFB of 14 mV/MHz. This leads to an approximately 10 % reduction in timing jitter of pulses near the threshold.

In order to further minimise the coincidence window, programmable delays can be added to the incoming signal to account for small differences in cable length. A total of up to 6 ns can be added with a dynamic range of six bits.

4.3.2 Level 2 Trigger

In order to reduce the telescope energy threshold, it is desirable to set the CFD threshold as low as possible. However the trigger rate quickly increases as a high-order power low with decreasing CFD trigger threshold as one en-

ters the region dominated by sky noise. To account for this, a multiplicity trigger can be used which requires more than one CFD to trigger within some coincidence window. A further refinement to the trigger condition can be made by requiring that several *adjacent* CFD channels trigger within the coincidence window. It is found that the CFD threshold can be substantially lowered, while still maintaining a manageable telescope trigger rate, by requiring that three or four adjacent pixels must trigger.

The PST (Bradbury, 1999) is a topological hardware trigger which works because of the compact nature of gamma-ray induced Cherenkov showers. By contrast, pulses caused by the NSB tend to be confined to one or two PMTs. The PST has the added benefit of discriminating against ion-induced afterpulsing in the PMTs, which can significantly increase the trigger rate at low CFD thresholds.

The camera is divided into 19 overlapping patches of 59 pixels. Some of the outermost CFDs are not part of any patch and do not contribute to the Level 2 trigger (although the CFD trigger flags are still recorded to the data stream). Level 1 trigger pulses from 463 of the 499 CFDs are fed into a signal splitter via 24 input cards. Each input card card takes 20 channels, with the 24^{th} card taking only 3 channels. The signal splitter copies and organises the signals into the 19 overlapping patches of 59 pixels. These signals are directed to the 19 output cards of the signal splitter. Each signal splitter output card is connected to a PST module via a pair of 30 way ribbon cables, which carry the signals of the 59 channels in the patch. Each patch consists of 5 overlapping sub-patches of 19 pixels. Each sub-patch contains 2^{19} patterns, which are loaded into the memory of the PST module. If a pattern corresponding to one of the loaded patterns occurs within a sub-patch, a Level 2 trigger is produced using a custom built OR module. This Level 2 trigger is then passed to the Level 3 array trigger (Section 4.3.3). The PST modules are housed in a CAMAC crate and were designed and built by HyTEC.

In order to choose the CFD threshold and number of adjacent pixels required to initiate a telescope trigger, a special type of run is used whereby the system steps through a range of CFD thresholds, and the Level 2 (Section 4.3.2) trigger rate recorded. The data are characterised by a trigger rate which gradually increases from a high CFD threshold to a low CFD threshold. In this regime the trigger rate is dominated by cosmic rays. As the threshold gets lower, the trigger rate increases rapidly. In this regime the trigger rate is dominated by random fluctuations in the night sky. The CFD trigger is chosen to be as low as possible without being in the regime dominated by the night sky background. Figure 4.13 shows the data from such a run. This *bias curve* was run with PST multiplicities of 3 and 4 adjacent pixels. An

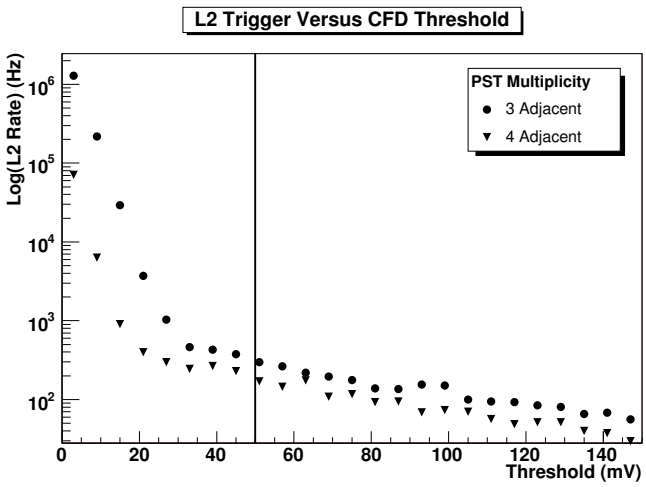

Figure 4.13: Telescope trigger rate versus CFD threshold. The CFD threshold is set close to the inflection point to a achieve as low an energy threshold as possible without operating in the noise.

operational threshold of 50 mV was chosen for the September-December 2006 observing period, with 3 adjacent pixels required to trigger.

4.3.3 Level 3 Trigger

At low energies the background is dominated by Cherenkov light from local muons. Cherenkov light from muons with a large impact parameter form images in the camera plane which are virtually identical to images formed by the Cherenkov light from VHE gamma-ray air showers. The most successful way of discriminating against muons is to use two or more telescopes with a coincidence trigger. In general local muons only produce Cherenkov light over a large enough area to trigger a single telescope, therefore if there is an array of telescopes with a coincidence trigger then the local muons can be removed from the datastream. This has the added advantage of enabling a reduction of the CFD thresholds into a domain where the telescope trigger would be otherwise swamped by muons and fluctuations in the night sky background. This significantly reduces the energy threshold of the array and substantially increases its sensitivity.

The VERITAS array trigger combines Level 2 trigger outputs from individual telescopes and produces a Level 3 trigger if a programmable number of telescopes trigger within a coincidence window which can be programmed from $10 - 250$ ns. The array trigger can operate up to 1kHz with a 10 %

deadtime at that rate, given a decision time of 1 μs. Apart from providing the Level 3 trigger, the array trigger system provides event numbers, event masks and logs rates, timing and diagnostic information to disk.

The array trigger is capable of running any subset or combinations of subsets of telescopes as independent subarrays - although any one telescope cannot be a member of more than one subarray.

Communication between the telescopes and the array trigger is carried over matched pairs of Digital Asynchronous Transceivers (DATs). Each telescope has two DATs, one for transmitting data and one for receiving data. The DATs send signals by xor'ing them with a 25MHz clock. Both the clock signal and the xor'd signal are sent via optical fiber to the receiving DAT where the signal is again xor'd with the clock to recover the original signal (Table 4.1). The DATs convert the incoming -5.2 V negative ECL signal to a 2.5 V positive ECL signal. This is input to a Field Programmable Gate Array (FPGA) which combines the ECL signal with the 25 MHz clock and converts it to a Low Voltage Differential Signal. The signal is then converted to an optical signal using a Gbps Vertical Cavity Surface Emitting Laser (VCSEL) and is transmitted to the receiving DAT using a Parallel Optical Link (PAROLI). At the receiving end, essentially the same components perform the conversion and xor'ing in reverse to recover the original signal.

Signal	Binary
25MHz Clock	10101010
Example Signal	10011101
Example Signal XOR 25 Mhz Clock	00110111
Example Signal XOR 25 Mhz Clock XOR 25 MHz Clock	10011101

Table 4.1: DAT Signal Conversion

There are a number of delays which are required by the array trigger system. The Level 2 signals are delayed to compensate for the different cable lengths associated with the physical geometry of the array. This equalises the Level 2 pulse arrival time from each telescope. However, the profile of the Cherenkov shower is such that the wavefront does not reach each telescope isochronously. To compensate for this, shower delays, which are dependent on the elevation and azimuth of the telescopes are required. These delays are corrected approximately every ten seconds. The telescope tracking software writes the tracking data to the VERITAS database, from where the array trigger can read the telescope tracking positions.

In order to minimise the readout deadtime, it is necessary to minimise the size of the FADC readout window. To do this without loosing shower

information, the timing edge of the Level 3 trigger which is sent to each telescope must be precise to within 2 ns. The array trigger achieves this low level of jitter by using the incoming Level 2 signal itself to generate the timing edge. The incoming Level 2 trigger signal is split in two, with one copy going to the array trigger coincidence logic, and the other being delayed for use as a timing edge. This delay, along with the compensating and shower delays, is done using custom built Pulse Delay Modules.

4.4 Data Acquisition

When an array trigger occurs, a Level 3 trigger is sent to each telescope. This halts the digitisation of PMT signals while the FADC memory is read into the VME-DACQ buffer. These buffers contain fragments of events and are sent to an event building computer which combines the data into telescope events. Buffered telescope events from the event building computer are then passed to the Harvester (Section 4.4.2) which builds array events.

4.4.1 Telescope Data Acquisition

FADCs

The front end of the VERITAS data acquisition chain consists of 50 custom built FADC boards (Figure 4.14) distributed across 4 VME crates. Each FADC board has 10 data channels, with the PMT signal cables connected directly to the front end of the FADC boards. There the PMT signal is split, with one copy going to the Level 1 trigger and another copy digitised (see Figure 4.15). Digitisation is carried out by 500 Mega-Samples-Per-Second(MSPS) FADCs. The digitised signal is written to a ring memory buffer with a depth of 32 μs. When an array trigger occurs the FADCs are stopped and the contents of the memory buffer are readout. In order to read out the correct part of the memory buffer, a specific lookback time must be set. This lookback roughly corresponds to the time between signal digitisation and trigger decision plus trigger signal propagation time. The lookback time can be chosen by taking a special laser (Section 4.5) run with the lookback time of each FADC board set differently. This essentially scans the circular memory buffer and the data can be analysed to select, and further fine-tune, the global lookback time for each telescope.

The FADCs have an eight bit dynamic range corresponding to 0-255 digital counts. By default, the signal is passed through an on-board amplifier which provides a gain of 6. If the dynamic range is exceeded, a delayed copy of the analog signal which follows a different gain channel can be digitised

instead. The lookback time is dynamically adjusted and a HiLo bit is set in the datastream so that these events may be analysed appropriately offline. This dual channel facility on the FADC board gives an effective dynamic range of ~ 1200 digital counts.

For a readout window of 24 samples, each telescope produces 12 KB per event. Running at 250 Hz this implies nearly 5 GB of data per 28 minute run per telescope, corresponding to 20 GB per run for the array. This data rate has a detrimental effect on the telescope deadtime and has implications for analysis, data transfer and data storage. In order to compensate these problems a zero suppression scheme has been implemented. Under this scheme, only those FADC traces whose maximum value exceeds a programmable threshold are read out. This has the effect of cutting the data size by a factor of four and keeps the deadtime at a manageable 10 %. The zero suppression threshold must be carefully selected so as to discard FADC information that does not contain useful information while retaining FADC information which does. This threshold can be selected on a channel by channel basis and is best chosen as a function of the pedestal.

Each of the four crates carries custom built clock-trigger boards which provide synchronous distribution of clock and trigger signals and provide scalars for latching the event time and livetime. A master clock-trigger board provides a 500 MHz clock used to phase lock the other three clock-trigger boards to within 200picoseconds. The clock-trigger boards also form a wired-OR to generate the telescope busy flag when the buffered FADC memory is being read out.

The four FADC crates each dissipate over 2 KW in a tightly confined space. Such a large heat output must be carefully managed to prevent permanent damage to the equipment. This is accomplished using a pumped chilled water system. Monitoring of the FADC temperatures is accomplished using thermometers mounted directly on the boards which are read out using a multi-channel Kiethly voltmeter which in turn is readout via serial interface and reported to array control (Section 4.7.1).

VME-DACQ

The Level 3 trigger and event number are received by the master clock-trigger board in each telescope's FADC system. The trigger and event number are fanned out to each FADC crate's clock-trigger board and to the auxiliary crate. Once a crate receives the trigger, it engages the wired-OR bus (ie sets it high) to indicate that it is busy. If any of the crates engage the wired-OR, the telescope busy is set, indicating that it is incapable of receiving further Level 3 triggers. The VME-DACQ reads out the data from the clock-trigger

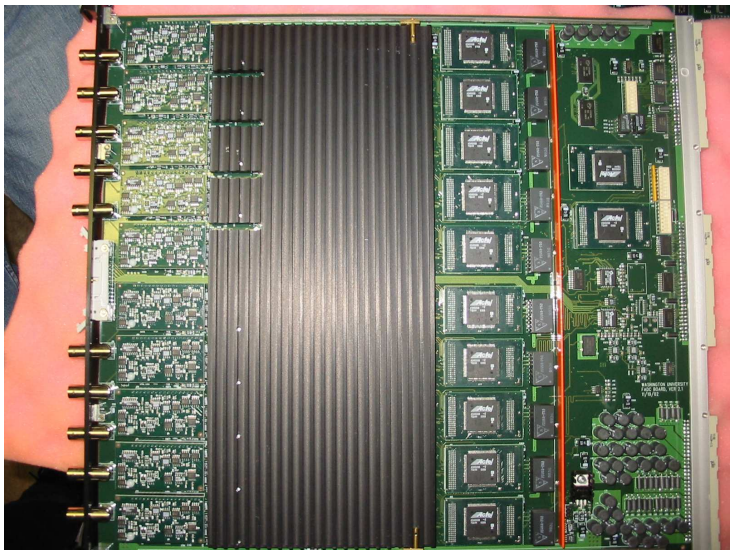

Figure 4.14: A VERITAS FADC board. Coaxial cables from the preamplifiers are connected directly into the ten BNC connectors on the left hand side. The CFDs can be seen immediately to the right of the BNC connectors. The FADCs themselves are located underneath the large heat sinc, with the FPGAs mounted to the right of the heat sinc. The right hand side of the board holds the interface to the VME backplane, including addressing switches and associated electronics.

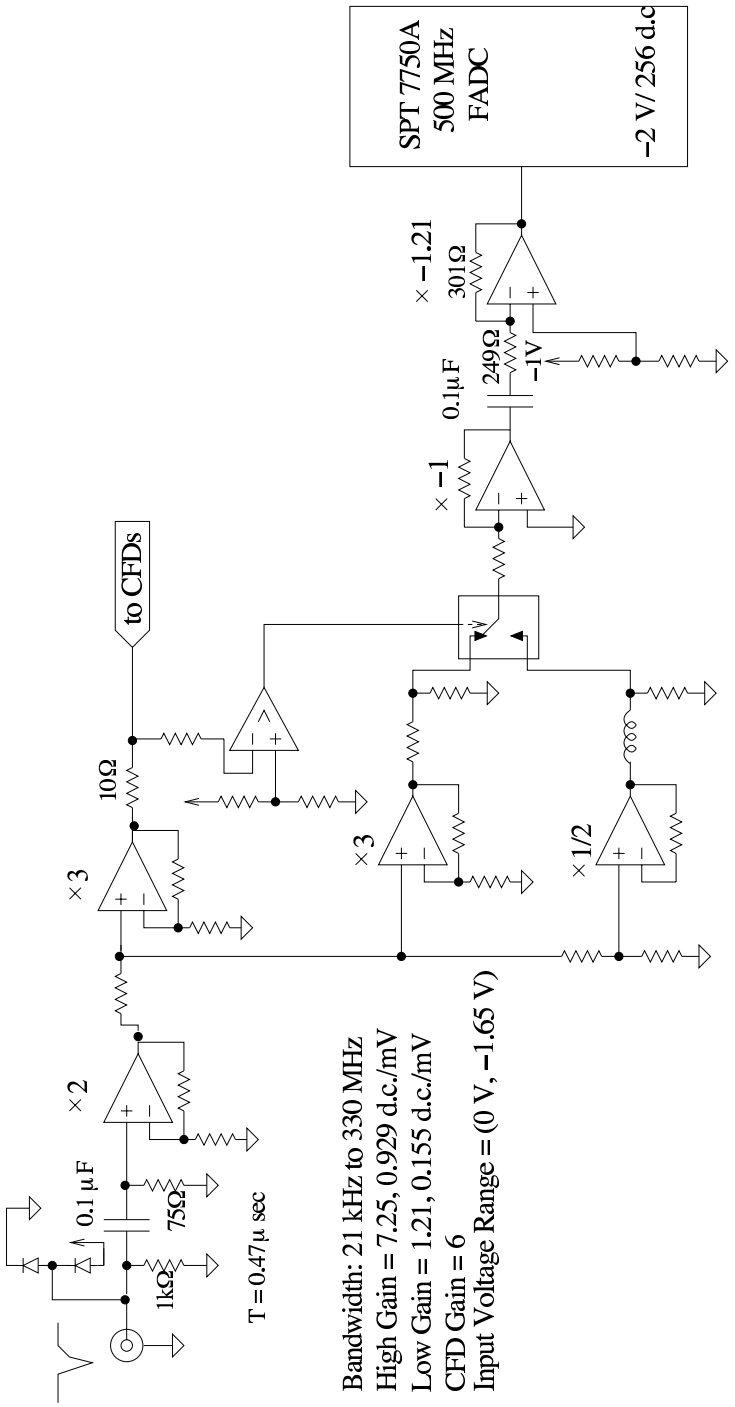

Figure 4.15: FADC schematic (Figure courtesy of Jim Buckley).

boards and the contents of the FADC ring buffer memory using a Chain Block Transfer(CBLT) and stores them in the VME-DACQ buffer. When the CBLT is complete, the wired-OR for that crate is disengaged. Once all the wired-ORs are disengaged, the telescope busy is unset and the telescope is ready to receive the next L3 trigger. Event fragments are buffered by the VME-DACQ until they are passed to the Event Builder via Scaleable Coherent Interface (SCI). The SCI is a high-speed computer bus commonly used in high-performance computing. It is similar to GigaBit ethernet but has less protocol overhead and is implemented on a PCI card. The VME-DACQ buffer contains a header indicating the number of events and data size, followed by data fragments.

The VME-DACQ also handles the front end interface to the FADC boards and controls such settings as the readout window size, lookback offset and zero suppression threshold. It also controls the CFD settings such as threshold, output width, delays and rate feedback settings. The VME-DACQ is responsible for reprogramming the FADC when a pedestal trigger occurs to override zero-suppression.

Event Builder

The telescope data acquisition is handled by the Event Builder. This multi-threaded C++ program runs on a Dual Xeon server with RAID storage and is connected to the VME-DACQ via the SCI interface. The program has seven threads which operate buffer acquisition, event building, harvester communications, disk writing, CORBA control, data monitoring, and main().

- The buffer acquisition thread polls the VME-DACQ system for new buffers. If a buffer is available it is transferred via SCI to local memory on the event building machine. The buffer is parsed and event fragments organised into a structure which indexes the data by event number. Once fragments from all crates for an event have arrived, all data up to and including that event are flushed to the event building thread.

- The event building thread pieces together buffer fragments to produce telescope events and stores them in a memory buffer whose size is optimised for network transfer. Once the buffer is filled, it is closed and sent to the harvester communications, disk writing and diagnostics threads.

- Three of the threads are consumer threads which receive buffers of built telescope events.

1. The harvester communications thread sends the data over GigaBit ethernet to the array level data acquisition system.
2. The disk writing thread saves a local copy of the data to the RAID disk for redundancy.
3. The data monitor thread performs some preliminary diagnostics on the data such as checking for corrupt or incomplete events. Diagnostics are displayed on a local display and reported to array control via the communications thread.

- The communications thread interacts with the global array CORBA environment to control starting and stopping of runs, monitor status, examine events and transfer diagnostic information and CFD scalar values.

4.4.2 Array Data Acquisition

The array level data acquisition is handled by the Harvester software. This program receives buffered telescope events from the Event Builder at each telescope. The Harvester combines these data with data from the array trigger to produce array level events. Once the array level events are generated, they are buffered and saved to a local RAID. Data are saved in a custom designed binary format named VERITAS Bank Format (VBF). Once the data run is complete, the files are compressed and transferred to local and remote archival machines.

In order to further reduce the data size a custom compression scheme has been implemented. The dynamic range of each FADC sample is 8 bits, however a channel that does not contain a significant signal beyond the pedestal baseline may have a much smaller dynamic range requirement. As an example, consider the set of eight samples

16 17 15 18 16 15 17 19

The dynamic range of each sample is 8 bits, or 0-255 in digital counts. Therefore storage of this set of samples requires 64 bits (8 samples $\times$ 8 bits per sample). However the range covered between maximum and minimum values is 5 - which requires only 3 bits to store. Therefore the above set of samples can be rewritten as

1 2 0 3 1 0 2 4

with an extra two bytes of information to store the minimum value and the number of bits required. Given that the above set of samples has a dynamic range of 3, the total storage requirement is 40 bits (8 samples $\times$ 3 bits per sample + 16 bits to store the minimum sample and new dynamic range). The

compression scheme is optimised further by limiting the allowed minimum value and dynamic range which allows both quantities to be stored in a single byte. For the given example, this would result in a storage requirement of 32 bits. As well as reducing the amount of disk space required, this compression scheme also speeds up analysis as the time saved in disk I/O is greater than the extra time required to decompress the data. This compression scheme is most effective on channels which contain no significant signal. However, the scheme is not as effective in conjunction with zero suppression, as zero suppression actually excludes those channels for which sample compression is most effective.

4.4.3 GPS Clocks

Each telescope is equipped with a GPS (Global Positioning System) clock mounted on a 6U crate. The clock provides a timestamp for each event which is accurate to within 1 μs. This timestamp is routed via the auxiliary crate and the VME-DACQ software to the Event Builder software where it is combined with the other telescope data to form telescope events. The array trigger also has an independent GPS clock mounted in a separate 6U crate. This clock provides timestamps for each array trigger - these timestamps are combined with the telescope events by the Harvester when the array events are built.

Accurate event timestamps are needed both for astrophysical studies and for data integrity checks and organisation of the offline analysis. It is expected that studies of pulsars such as the Crab Nebula at low energies ($< 100\,\mathrm{GeV}$) will reveal pulsed emission due to rotation of the neutron star. These pulsations occur at milli-second timescales which requires accurate clocks to study. In terms of diagnostics, a distribution of the exact time between events, known as a Delta-T distribution (see Figure 4.16 and Figure 4.17), can reveal periodic noise events or deadtime problems. This is an important tool when debugging and understanding a new telescope system. In the offline analysis, the data run is divided into fragments to ensure correct calculation and application of time dependent calibration data such as HV status and pointing information. It is also important to know exactly how long a run was active so that livetimes and deadtimes can be accurately calculated.

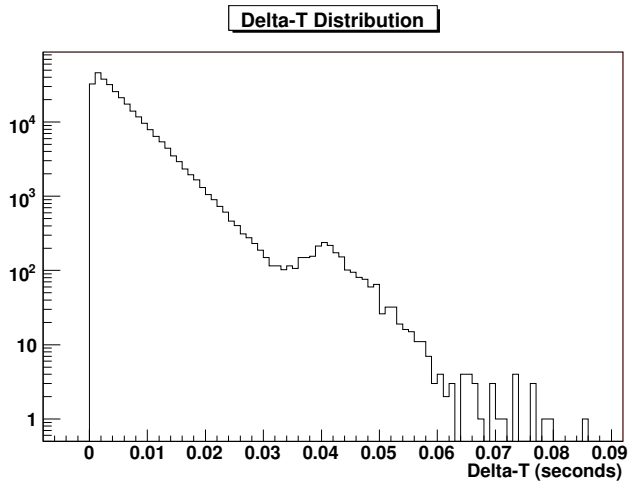

Figure 4.16: Distribution of the time difference between events. The excess at ~ 0.04 sec is caused by extra deadtime associated with buffer transfers in the data acquisition system. Note the log scale on the y-axis.

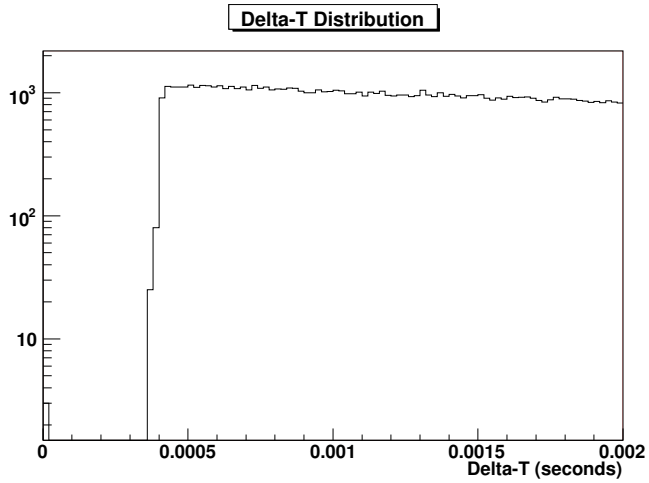

Figure 4.17: Same as Figure 4.16, with the x-axis scaled down to a few milliseconds. The sharp cut-off at ~ 0.4 milliseconds indicates the system deadtime.

4.5 Optical Calibration

Relative calibration between pixels in a single camera is performed using a laser-based flat-fielding technique. The laser illuminates the entire camera with a single flash causing the telescope to trigger. The integrated charge in each pixel, relative to the average charge across the image, is used to calculate relative gains. Relative calibration between telescopes is achieved by flashing each camera with the same laser source and measuring the laser intensity using an energy meter. Alternatively, local muons can be used as they are readily identifiable and produce a known spectrum of Cherenkov light. In fact this can be used both for an inter-telescope relative calibration and for an absolute calibration (Humensky, 2005).

Primary illumination is produced by a nitrogen dye laser which has a wavelength of 337 nm. This beam is directed into a dye which fluoresces at 400 nm. The light produced is carried via optical fiber to a diffuser located at the crossbeams of the telescope approximately 3 m from the focal plane. The diffuser produces a uniformly spread beam such that pixels at the edge of the camera receive the same amount of light as those at the center. In order to monitor the laser amplitude, it is passed through a beam splitter with at least one copy connected to a photodiode. This allows direct monitoring of the beam intensity either on an oscilloscope or by connecting the photodiode output to a spare FADC channel which records the intensity directly into the datastream. The laser system also provides an output which generates a trigger signal each time the laser system flashes which can be used to trigger the telescope. This allows triggering of the telescope at light levels which would not normally generate a trigger - and can be used to remove external trigger sources (eg NSB and Cherenkov showers). This is useful especially when measuring the single photoelectron response of the camera. The laser system has a series of filters which can be used to adjust the light intensity, but the most useful filter is the continuous filter wheel. This wheel is coated such that the transmission varies from 1 % to 100 % over 3/4 of the surface and remains at 100 % for the final 1/4. This enables illumination of the camera at steadily increasing amplitudes which is useful for linearity studies and for calibrating the HiLo gain switch on the FADC.

4.6 Monitoring

Cherenkov telescopes are sensitive to real time weather effects such as haze, cloud, wind, humidity and temperature. These external parameters must be monitored to ensure correct treatment of the data and safe operation of the

telescope.

4.6.1 Weather Station

A weather station is deployed close to the central control building. It is equipped with a rotating cup wind sensor, humidity sensor and rain sensor. Data are relayed to the central control building where future upgrades will allow these data to be stored in the VERITAS database.

4.6.2 Far-Infrared Pyrometer

A Far-Infrared (FIR) Pyrometer can be used to detect cloud cover. The Pyrometer measures the temperature of the night sky and is very sensitive to fluctuations greater than 1° C. The temperature of cloud is typically in the range −5° C to −10° C whereas a clear sky typically has a temperature of −50° C. The goal of the FIR Pyrometer would be to detect high thin wispy cloud that is difficult to see at night and would not be otherwise discarded by quality control. This type of cloud can have subtle affects on the data which are poorly understood, and could have detrimental results on the analysis of source flux. The presence of significant cloud cover is evidenced by strong fluctuations in the trigger rate, such data would be discarded by quality control. An example of such data is shown in Figure 4.18, note the sky temperature is in negative degrees Celsius. In order to appreciate the correlation, the data sets are averaged over 25 s periods. A correlation plot is shown in Figure 4.18(c), with the correlation peaking at ~ 90 % with a delay of 0 s.

4.6.3 Charged-Coupled Device Camera

Each telescope has a CCD (Charged-Coupled Device) camera mounted on the OSS. The CCD records images of the star field around the region where the telescope is pointing. This enables the observer to verify the pointing of the telescope, monitor cloud cover and monitor the optical transparency of the atmosphere.

4.7 Control Software

The VERITAS telescope array is a highly sophisticated system with many software and hardware components. In order to operate the array in an efficient and coherent manner, an Array Control (Section 4.7.1) program is

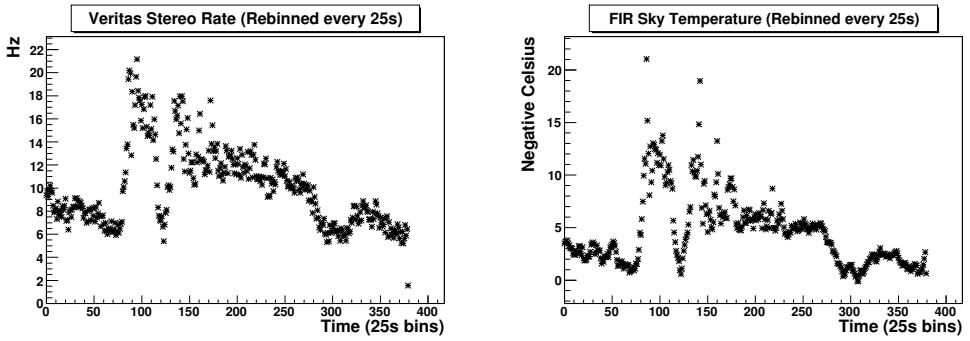

(a) VERITAS Trigger Rate

(b) FIR Sky Temperature

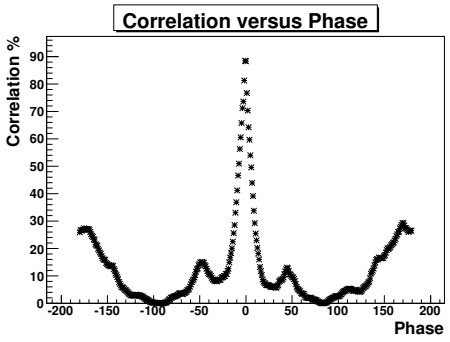

(c) Correlation

Figure 4.18: VERITAS Two telescope stereo rate compared to FIR Sky temperature. A VERITAS trigger rate, and correspondingly high negative value of the sky temperature corresponds to a gap in the cloud. The rates have been averaged over 25 s periods. A correlation plot of the two rate plots is also shown. The correlation peaks strongly at $\sim 90\,\%$ at a phase difference of 0° corresponding to 0 s.

used to facilitate the stopping and starting of runs and the interface with various subsystems. The VERITAS database (Section 4.7.2) is used to store a table of run information such as source identification, start time, participating telescopes etc. It also stores slow control run time information such as telescope pointing, HV data and PMT currents.

4.7.1 Array Control

The Array Control has interfaces to the following sub-systems

- L3
    1. Start night, End night
    2. Run Management
    3. Trigger Counts
    4. Diagnostics
- Event Builder
    1. Run Management
    2. Status Reporting
    3. Interface to VME-DACQ
- Harvester
    1. Start night, End night
    2. Run Management
- VERITAS Database
    1. Source Information
    2. Participating Telescopes and Configuration
    3. Run Information

Each of these sub-systems is controlled by a graphical interface window. The array control program also reports diagnostic information such as trigger rates, data size, number of corrupt events, deadtime and available hard disk space.

4.7.2 VERITAS Database

The VERITAS database is an archive of run information which is required for both online data taking and for offline analysis. The VERITAS database consists of a series of entry tables which can be accessed by a specially designed suite of interface tools. The VERITAS database is implemented in C++ and MySQL, and is backed up regularly to a remote machine. Many programs interface with the VERITAS database; this is summarised in Table 4.2.

Sub-System	VERITAS Database Interaction
HV	Reads and Writes High Voltage settings
HV	Writes Anode Current
Tracking	Writes telescope positions every 4 s
L3	Reads telescope positions every 10 s
VME-DACQ	Reads and Writes CFD and FADC settings
Array Control	Writes Run Information
Quicklook	Writes Quicklook Analysis Results

Table 4.2: Summary of software which interacts with the VERITAS Database.

There is also a large set of configuration data which should only change on the timescale of dark run or season. This includes location of Level 2 Trigger channels in the FADC data stream, pixel identifications and neighbour lists, telescope locations, certain CFD settings and Quicklook default cutting values.

4.7.3 Realtime QuickLook

There are some astronomical objects, such as AGN and gamma-ray bursts, whose flux can change on very short time-scales. It is for this reason that it is important that the telescope operator has reduced data promptly available so that a decision can be made regarding the usefulness of the run being taken. To accommodate this requirement, a Realtime Quicklook package has been developed which provides realtime information about the trigger rates, performs Hillas parametrisation and cutting, and gives rates and significances as the run develops. An example of the Realtime Quicklook output is shown in Figure 4.19. Early diagnostics information is also important to identify any problems in the run such as noisy PMTs.

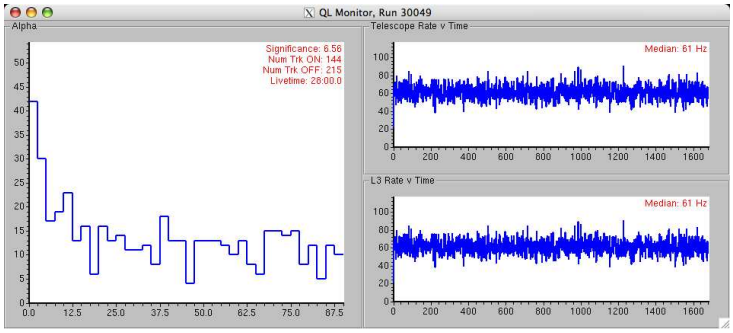

Figure 4.19: Quicklook output showing the Level 2 and Level 3 trigger rates and an alpha plot indicating the gamma-ray rate and significance.

4.8 Summary

An in-depth introduction to the VERITAS array has been provided in this chapter. All major physical elements including the telescope structure, drive system, optics, camera, trigger and associated electronics have been described. The major software components related to the acquisition, real-time monitoring, array control and VERITAS database have also been described.

Chapter 5

Data Calibration and Parameterisation

It is the requirement of the analysis procedure to determine the spectrum, flux, morphology and evolution of a gamma-ray source, or to place upper limits on the source emission in the case of a null detection. Analysis of Cherenkov telescope observations starts with the calibration (Section 5.1) of the dataset. The calibration procedure involves flat-fielding and correction for timing offsets between FADCs. A cleaning procedure is used in image reconstruction (Section 5.2) to identify those pixels containing a significant Cherenkov light component. Images are parameterised using a second-moment analysis to determine the shape and orientation of the image. Shower reconstruction (Section 5.3) is performed using a simple intersection of lines to determine the shower origin in the field of view and the core position on the ground. Due to the presence of the huge hadronic background, both background rejection (Section 5.4) and background estimation (Section 5.5) methods are required. Once the signal is established, the distribution of gamma-ray arrival directions in the sky can be plotted to map extended sources and search for serendipitous sources. Finally an overview of the calculation of event energies and array collection area is given (Section 5.6).

5.1 Telescope Calibration

Calibration of each telescope is required to ensure a uniform telescope response. This uniformity is required so that no camera bias is introduced which would could lead to a false-positive or false-negative result, and ensures an accurate measurement of the EAS. The first step in calibrating each

telescope is to remove the FADC injected pedestal. This is followed by equalising each PMT in terms of the integrated charge and FADC trace arrival time using a dedicated laser-calibration run. These steps are described in the following sections. Finally, to ensure a correct understanding of the telescope, a method to determine the combined camera and electronics response to a single photoelectron is described.

5.1.1 Pedestal Calculation

The main source of background noise in PMTs in the absence of Cherenkov emission is due to fluctuations in the NSB. In order to determine whether a PMT contained a Cherenkov signal, it is necessary to measure these fluctuations on a run by run basis. The PMT output is AC coupled, however any positive voltage fluctuations cannot be digitised. To cope with this, an injected *pedestal*, corresponding to approximately 16 digital counts, is added to the AC coupled PMT output - this allows both positive and negative fluctuations relative to the AC coupled mean to be measured. In order to correctly calculate the charge deposited, and its statistical significance relative to the NSB, both the pedestal and its standard deviation referred to as the *pedvar* must be calculated. This is done by artificially triggering the telescope during the run and integrating the FADC charge on an event by event basis to generate pedestal statistics for each data channel. The artificial trigger is generated within the array trigger system, and a special FADC readout mode is required to record these pedestal events. This mode disables the zero suppression system (if it is active) which would otherwise prevent the readout of channels with no significant Cherenkov component. In order to generate reliable statistics for the pedestal measurement, a high pedestal event rate is desirable, however switching the FADCs in and out of zero suppression mode at a high rate is detrimental as it inflates the deadtime. A trade-off between the benefit of high pedestal statistics and the cost of high dead-time is achieved with a pedestal rate of $1 - 3$ Hz.

The pedvar for a single channel can be calculated for multiple FADC integration window sizes. A given FADC trace may be large enough to accommodate multiple integration windows, eg if the integration window size is seven samples, and the readout is 24 samples then four windows can be readout with wrap-around for the fourth window (see Figure 5.1), although it should be noted that in this particular example the fourth window is not statistically independent from the first.

The effect of the NSB on the pedestal distribution is shown in Figure 5.2. Exposure to the NSB can be understood in terms of a random stream of photoelectrons in the data. This increases the average PMT output, however the

AC coupling resets that average to zero. Thus, after injection of the pedestal, the mean FADC charge (ie the pedestal) is the same with and without exposure to the NSB. However, the charge distribution is much wider with NSB exposure. In a given FADC readout, if it contains *less* than the average number of photoelectrons, then it will have a charge which is noticeably less than the average charge. However, if it contains *more* than the average number of photoelectrons, then it will have a charge which is noticeably larger than the average charge. For an observation field such as the Crab Nebula, the NSB is significantly greater than the extra-galactic source Markarian 421 resulting in a wider pedestal distribution - this is demonstrated in Figure 5.2.

The pedvar is dependant on the NSB in the region of observation and is a measure of the background noise from which the Cherenkov signals must be discerned. It cannot be assumed to be constant during an observing run as the NSB conditions can change. This arises due to rotation of the field of view and changing atmospheric conditions. To ensure a reliable measure of the pedvar, it is measured for every three minutes of the data run. Three minutes is long enough to accumulate sufficient statistics to give a reliable measure of the pedvar, while being short enough to be sensitive to changes in the level of NSB. The pedvar is also measured for many integration window sizes (2-10 samples by default), since the charge integration procedure may use variable size windows when calculating the Cherenkov light component in air-shower triggered events. It is assumed that the pedestal value does not change during the run - in order to minimise the statistical uncertainty in measuring the pedestal, the average of all window integration sizes, over all time windows is combined for a given channel to give the pedestal measurement per FADC sample. It is this pedestal value which is used when the pedestal-corrected charge is calculated. The pedestal is different when the FADC is in low-gain readout mode (Section 4.4.1) - the calculation of the low-gain pedestal is discussed in Section 6.7.

The FADCs implement clocking at 125 MHz which writes four bytes into the pipeline burst RAM for every channel. This clocking adds a periodic noise to the FADC data which can be clearly seen when the FFT of a large number of traces are summed for a single channel (see Figure 5.3). Such a periodic noise could bias the pedestal calculation, depending on the location of the integration window and the phase of the noise. In order to minimise systematic error caused by this noise, the start of the first integration window is chosen randomly on a trace by trace basis.

To evaluate the extent of the clocking noise problem, and to compare the noise between telescopes, a histogram of the power at 125 Mhz to the average of the powers in neighbouring frequencies(146 Mhz and 104 Mhz) is shown in Figure 5.4. While this figure indicates that the telescopes exhibit similar

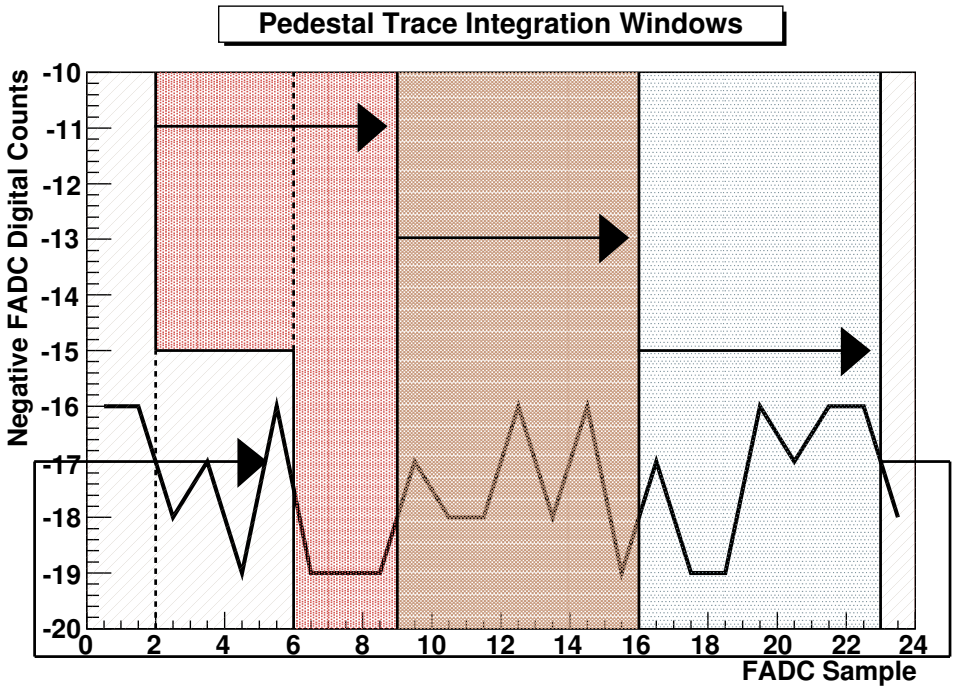

Figure 5.1: This FADC trace has 24 samples, and the integration window is seven samples. The start of the first window starts randomly at the second sample, covering samples 2 to 8. The second window covers 9 to 15 and the third window covers samples 16 to 22. The fourth window starts at sample 23 and wraps around to the beginning and includes samples 0 to 5.

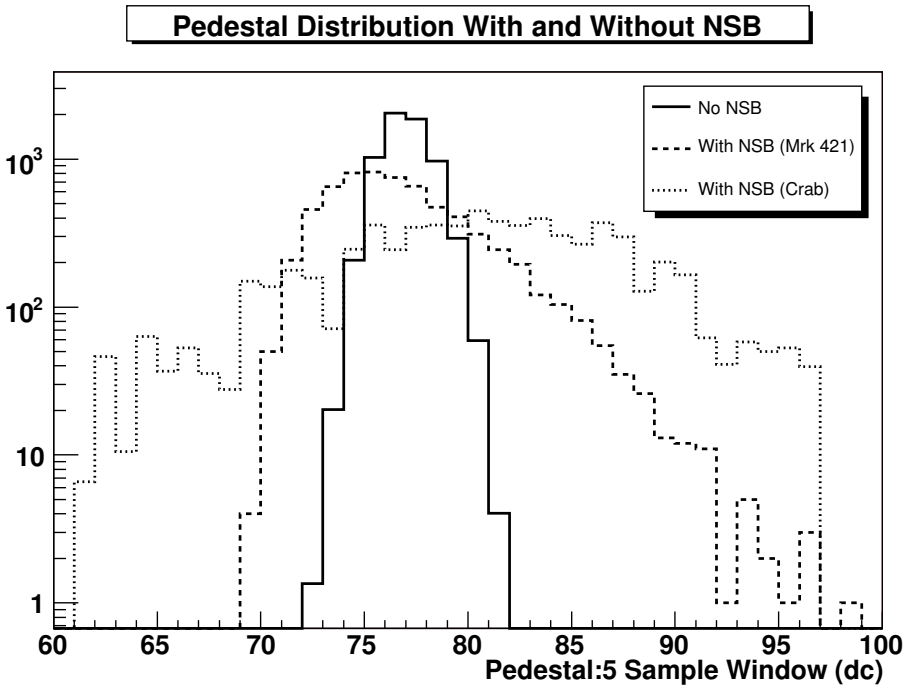

Figure 5.2: Comparison of the pedestal distribution with and without exposure to the NSB. The data set without NSB exposure was taken as a normal data run, but with the camera shutter closed. Two datasets are shown with exposure to the NSB, one is the from the Crab Nebula, a galactic source with a relatively bright NSB. The other is from Mrk421, an extra-galactic source with a relatively dark NSB.

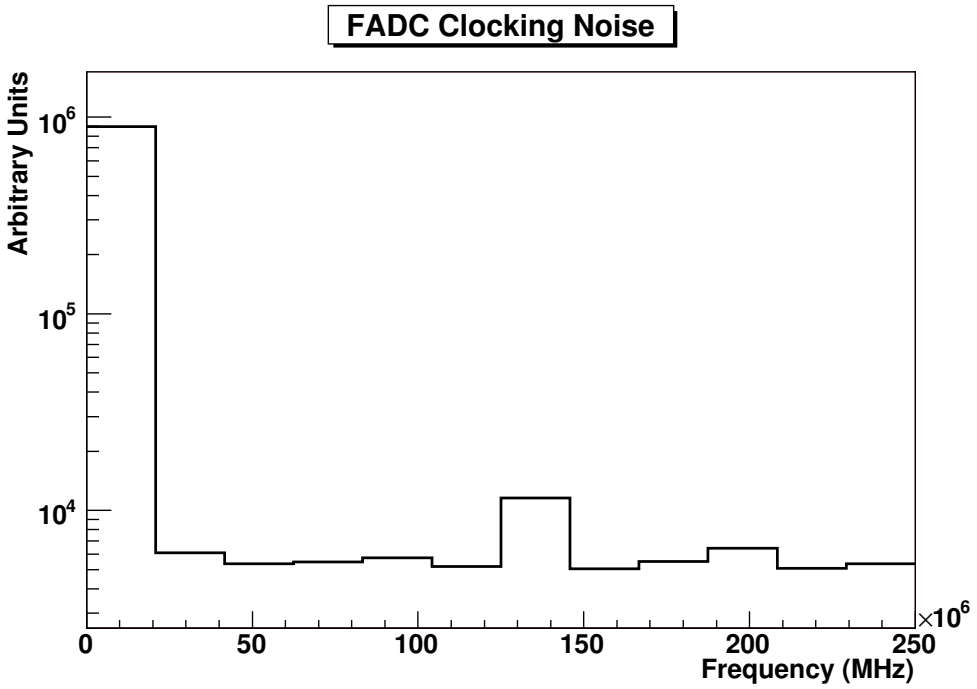

Figure 5.3: Summed FFT for a large number of raw FADC traces for a single channel. The large peak at 0 Mhz is the pedestal, or DC component. The second peak at 125 Mhz is a manifestation of the clocking noise.

degrees of clocking noise, there is clearly a spread which makes the problem difficult to deal with. Cogan (2004) investigated various methods of removing this noise including interpolation over affected samples and frequency damping, however no corrective measures are currently taken.

5.1.2 FADC Timing Calibration

In order to minimise the FADC integration window, and to accurately determine the arrival time of a recorded FADC trace, it is necessary to properly measure the average arrival time of the FADC trace. The arrival time of a single FADC trace, referred to as T_{zero} , is defined as the time on the falling edge at which the trace reaches half of its maximum value after subtraction of the pedestal baseline (see Figure 5.5). The average arrival time of each FADC trace is different, and for a uniform FADC look-back time, is dependent on cable length, HV and any electronic delays on the FADC boards. The correlation between average arrival time and HV is shown in Figure 5.6. Relative timing between channels is given by the T_{offset} calculation. For a

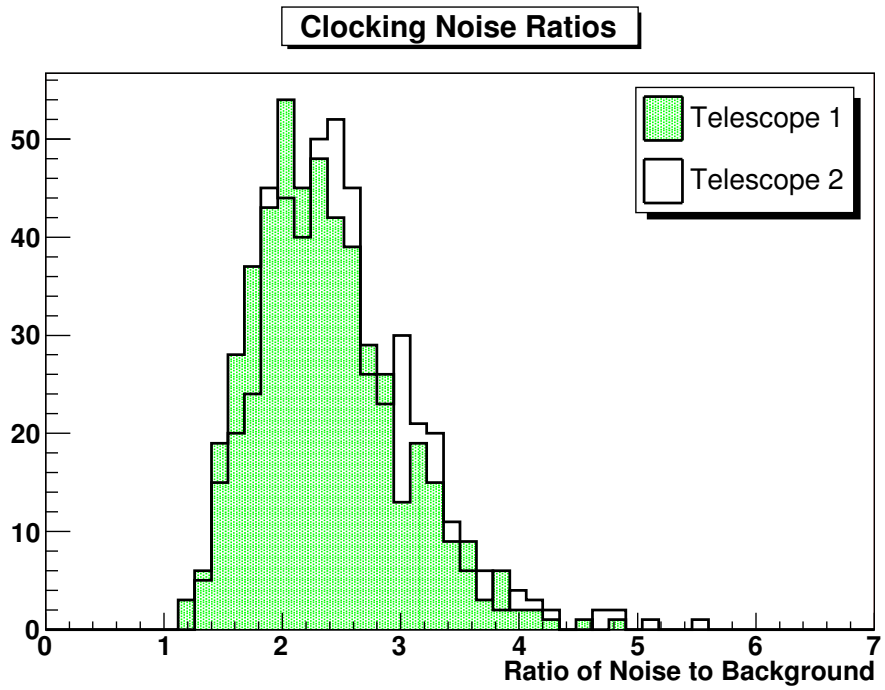

Figure 5.4: Histograms of the relative power at 125 Mhz to the average power at 146 Mhz and 104 Mhz for Telescopes 1 and 2 for all channels. This ratio can be regarded as the ratio of the power in the bin corresponding to 125 Mhz to the average power in the two adjacent bins.

given channel, this is the average difference between a specific channel's arrival time and the average arrival time of the event. The arrival time of the event T_{event} is simply the average of the arrival times of all the channels in that event and is given by

$$T_{event} = \frac{1}{n} \sum_{i=1}^{n} T_{zero} \tag{5.1}$$

where n is the number of channels. Then the time difference Δt between the i^{th} channel and that event arrival time is simply

$$\Delta T_i = T_{zero\,i} - T_{event} \tag{5.2}$$

For a large number of events m, the average relative arrival time for a single channel i is given by

$$T_{offset\,i} = \frac{1}{m} \sum_{j=0}^{j=m} \Delta T_{i_j} \tag{5.3}$$

The effect of the T_{offset} calibration can be seen by examining the average measured arrival time of each channel in a laser run after application of the T_{offset} correction. This is shown in Figure 5.7 and compared to the average arrival time prior the correction. Note that separate T_{offset} calculations are made for the high-gain and low-gain channels.

5.1.3 Relative Gain Calibration

The PMT voltages are adjusted approximately once per season such that each FADC trace gives an equivalent integrated charge. However PMT fatigue, dirt and other factors can can alter PMT response on a night to night basis. This can be corrected by taking a flat-fielding laser run each night and measuring and applying relative gains in the offline analysis. The camera is exposed to a laser flasher which illuminates the PMTs with a homogeneous light pulse. Figure 5.8 shows the distribution of the integrated charge for a single channel relative to the average integrated charge across the camera for each laser event. The mean of the distribution gives the relative gain for that channel. The width of this distribution will be shown to be dominated by the width of the photoelectron distribution (ie the distribution of the number of photoelectrons produced for a fixed number of incident photons). Assuming an equal number of photons striking the photocathode with each laser shot, and assuming a uniform PMT dynode response for each photoelectron, the width of the relative gain distribution is simply the width of the photoelectron distribution divided by the mean number of photoelectrons. To

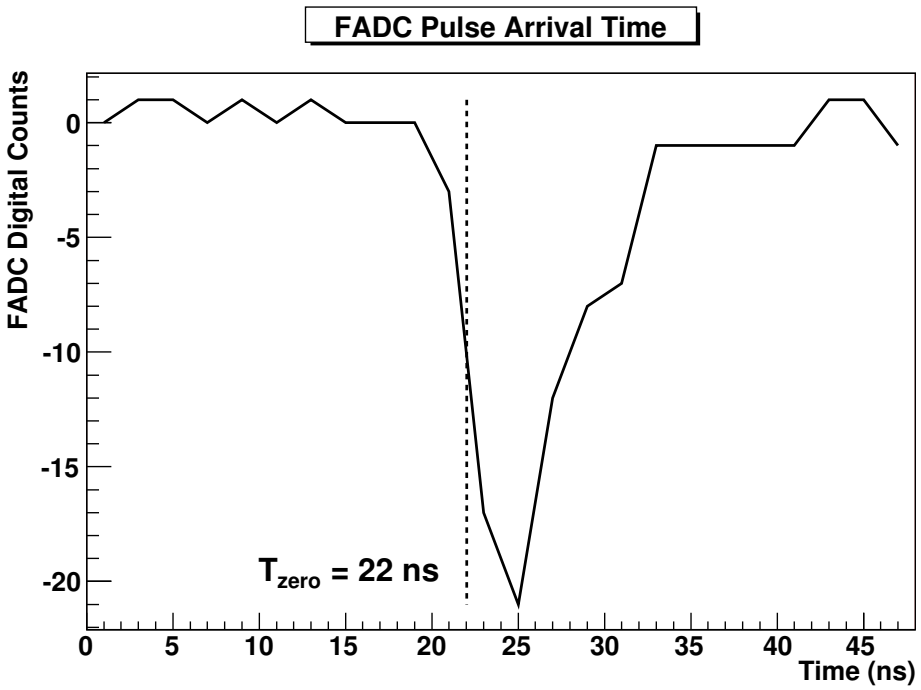

Figure 5.5: This FADC trace has 24 samples, corresponding to 48 ns. The arrival time of a single FADC trace, referred to as T_{zero} is defined as the time on the falling edge at which the trace reaches half of its maximum value after subtraction of the pedestal baseline. In this case, $T_{zero} = 22$ ns.

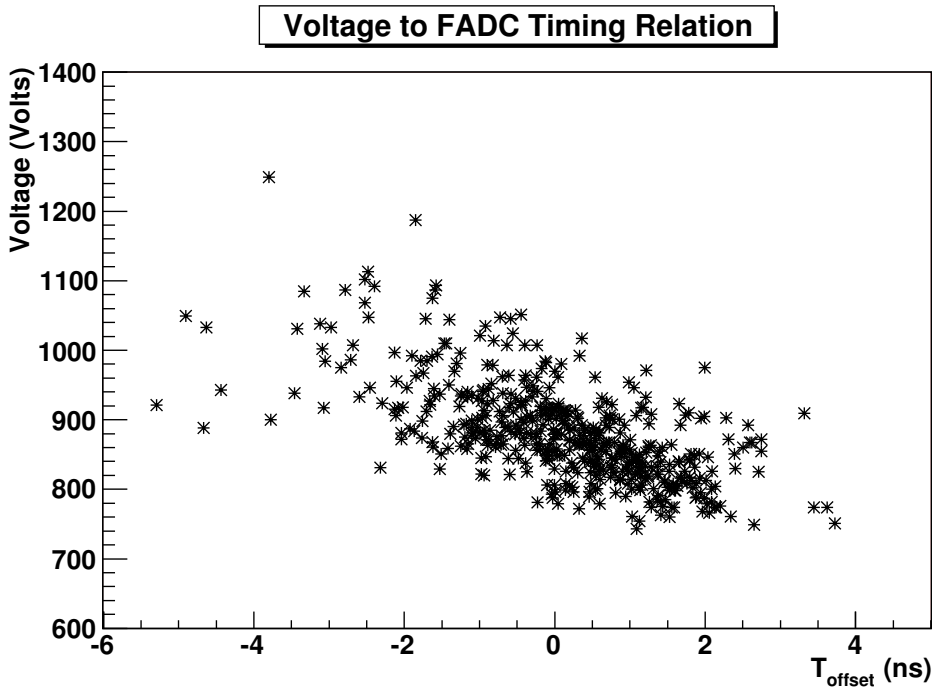

Figure 5.6: A significant contribution to the differences in arrival times of FADC traces is due to the HV. The correlation between the HV and the T_{offset} is shown.

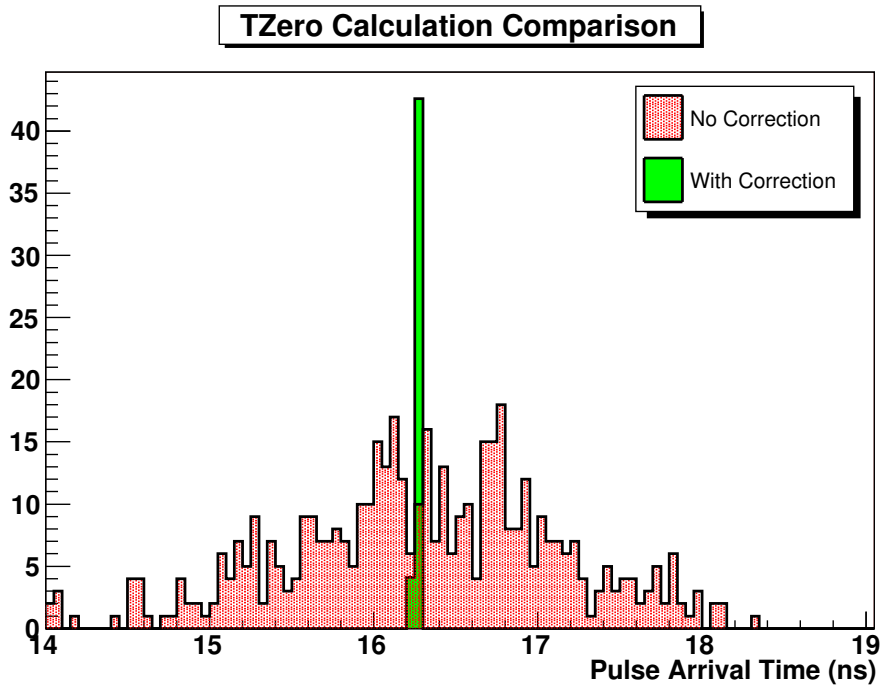

Figure 5.7: The average trace arrival time over all channels is displayed by the red distribution. After application of the T_{offset} correction, the re-calculated green distribution is tight and located at the mean of the original uncorrected distribution.

calculate the width and mean of the photoelectron distribution, the mean of the charge distribution Q can be used, along with the dc/PE (denoted R) ratio. Thus the mean number of photoelectrons, denoted P is given be $P = Q/R$, and the width of the photoelectron distribution is given by $\sqrt{P}$. Thus the theoretical width of the relative gain distribution is given by

$$\sqrt{P}/P \tag{5.4}$$

Inserting measured values of $Q = 63$ dc, $R = 5.3$ dc/PE gives the mean number of photoelectrons as $P = 11.8$, and the width of the photoelectron distribution as 3.44. Equation 5.4 gives the theoretical width of the relative gain distribution as 0.29, which is close to the measured value of 0.317 (from Figure 5.8). The remaining discrepancy can be accounted for by the assumptions which were made regarding the equal number of photons striking the photocathode with each laser shot, which is assumed to vary by $\sim 10\,\%$, and the intrinsic variation in dynode response which results in a spread (~ 0.5dc) in the measured charge per photoelectron.

The accuracy with which the relative gain is measured is determined by the number of laser flashes recorded. Figure 5.9 illustrates the accuracy of the measurement of the flat-fielding correction. As the number of flashes received increases, the error on the measurement of the relative gain decreases. After a few thousand flashes, the improvement is less than one or two parts in 10,000, however even a correction at this level is overwhelmed by the width of the photoelectron distribution.

Figure 5.10 shows the distribution of relative gains across the camera for Telescope 1. The width of this distribution indicates the quality of the flat-fielding of the High Voltage. Note that separate relative gain calculations are made for the high-gain and low-gain channels.

5.1.4 Single Photoelectron Measurement

A measurement of the system response to the input of a single photoelectron is important when reconciling Monte-Carlo simulations of extensive air showers with real data. Such a reconciliation is important given the dependence on analysis of accurate Monte-Carlo simulations in terms of shower reconstruction, gamma-hadron separation, energy estimation and spectral reconstruction. The size of the integrated single photoelectron pulse is a function of the PMT gain, preamplifier gain, cable losses, FADC gain and the analysis procedure (ie integration window size, trace analysis method etc). A method to calculate the digital count to photoelectron (dc/PE) ratio using a laser illumination of the camera is described here, although other

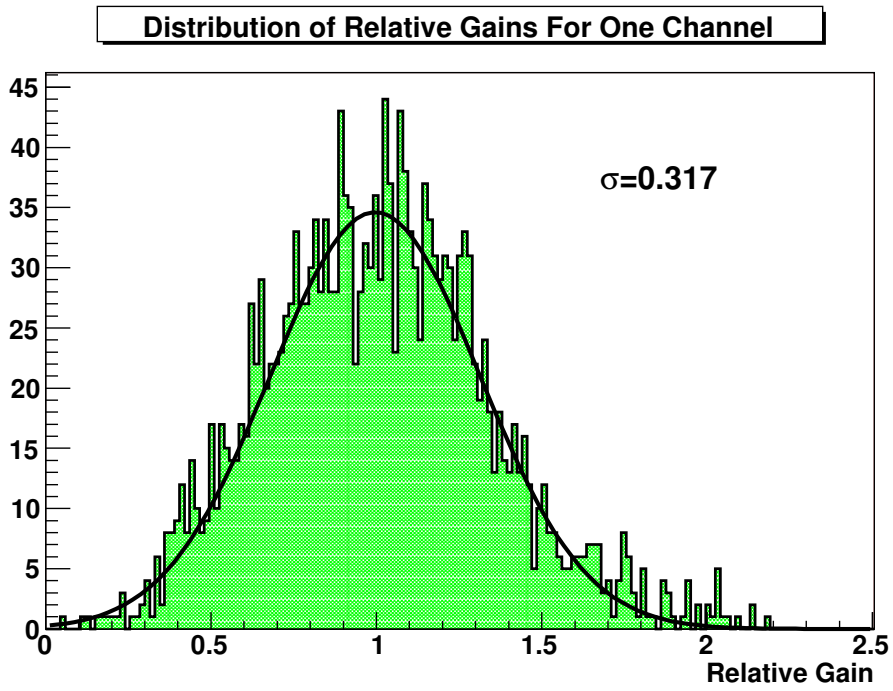

Figure 5.8: Distribution of the charge of a single channel relative to the charge for the camera for a laser-calibration run. The mean of this distribution gives the relative gain for this channel. The width, measured to be $\sigma = 0.317$, is indicative of the natural spread in photoelectron statistics (discussed in text).

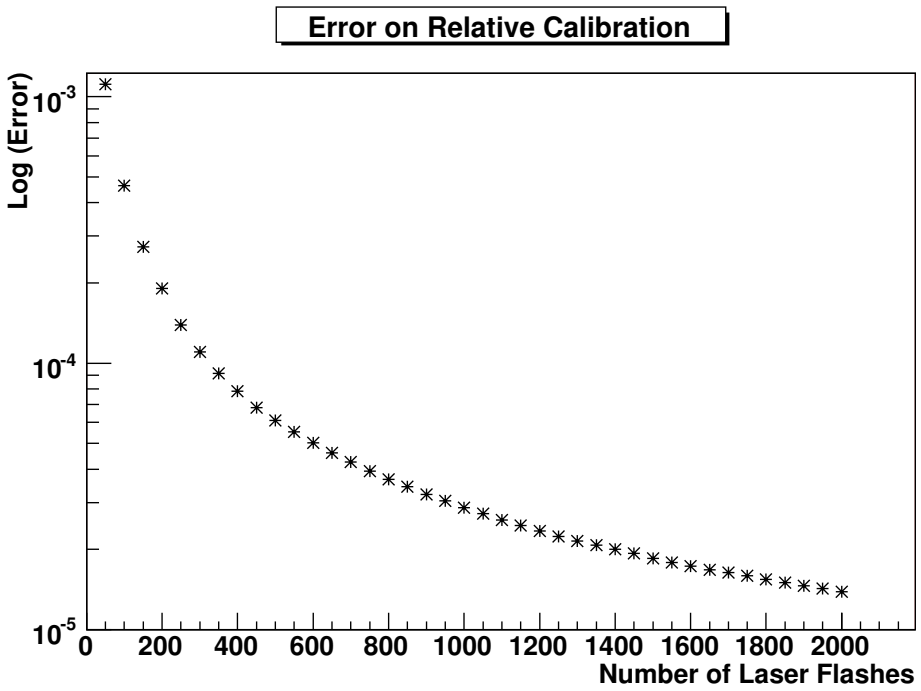

Figure 5.9: Measurement of the error in relative gain calibration as a function of the number of laser flashes used. The error (for a given channel) is given by the width of the relative gain distribution for that channel (eg Figure 5.8) divided by the square root of the number of flashes. Note the log scale on the vertical axis.

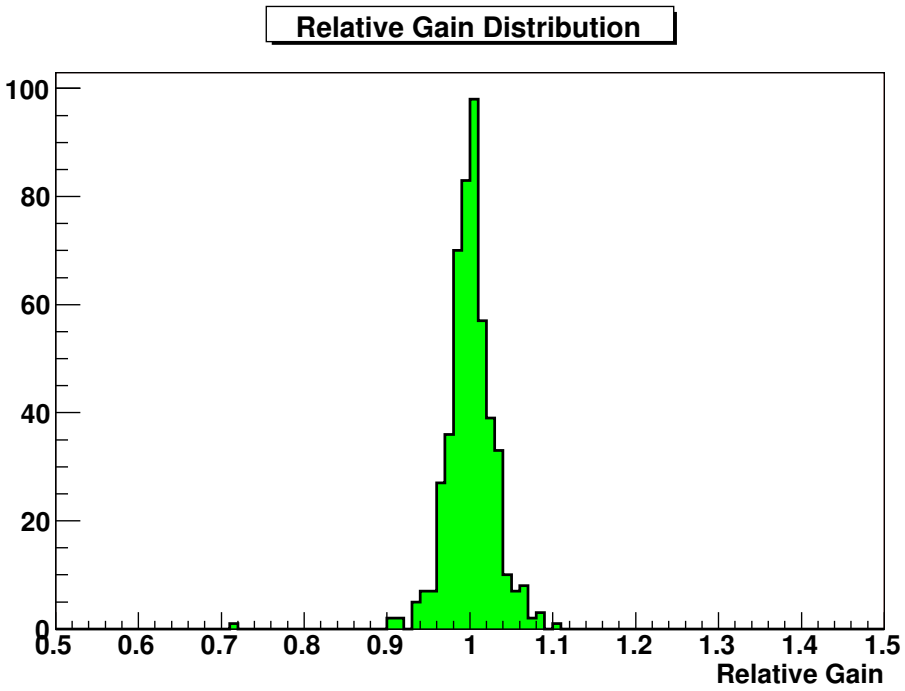

Figure 5.10: Relative gain distribution for all channels for Telescope 1.

methods using atmospheric muons (Humensky, 2005) yield similar results.

Under normal operation, the telescope triggers when 4-5 photoelectrons are produced at the photocathode. In order to record the charge from single photoelectrons, a system must be set up so that the telescope triggers when a single photoelectron strikes the photocathode, and all other background noise is eliminated. This is achieved by placing a Mylar[1] screen in front of the PMTs to exclude all background light, while illuminating the camera with the laser. The laser intensity is adjusted until single photoelectrons can be seen on an oscilloscope connected to a PMT. This may require an increase in the HV from normal operating voltages.

In order to trigger the telescope, the optical-trigger out facility of the laser system (Section 4.5) is used in conjunction with special delays and FADC lookback times. For any given trigger, photoelectrons may or may not be produced at the photocathode. The highest probability is that no photoelectrons are produced - in this scenario, the integrated charge at the FADC is equivalent to that of a pedestal event. For a single photoelectron, the integrated charge gives the dc/PE ratio. The distribution of charges for a single channel from a photoelectron laser run is shown in Figure 5.11, where the HV is set at higher than normal operating values so that the single photoelectron peak can be easily seen. Evident is the pedestal peak, with the first and subsequent photoelectron peaks at incrementally greater charges (although these are difficult to see without extremely large statistics).

The simplest way to fit the distribution is as a series of Gaussian distributions. The general equation of a Gaussian distribution is given by

$$Y(Q) = Y_0 \exp \frac{-(Q - Q_0)^2}{\sigma^2} \tag{5.5}$$

where Q_0 is the mean of the distribution, Y_0 is the height of the distribution at $Q = Q_0$ and σ is the Gaussian width of the distribution. An independent Gaussian distribution is used to fit the pedestal peak, then a series of interdependent Gaussians distributions are used to fit the photoelectron peaks. The location of each photoelectron Gaussian distribution is determined by the number of photoelectrons and is related to the location of the peak of the pedestal distribution by

$$Q_n = Q_{ped} + n\Delta Q \tag{5.6}$$

where Q_n is the location of the n^{th} photoelectron peak and ΔQ is the charge difference between each photoelectron peak and corresponds to the dc/PE ratio. Both Q_{ped} and ΔQ are free parameters in the fit. The Gaussian width

[1]Mylar is a semi-transparent polyester film

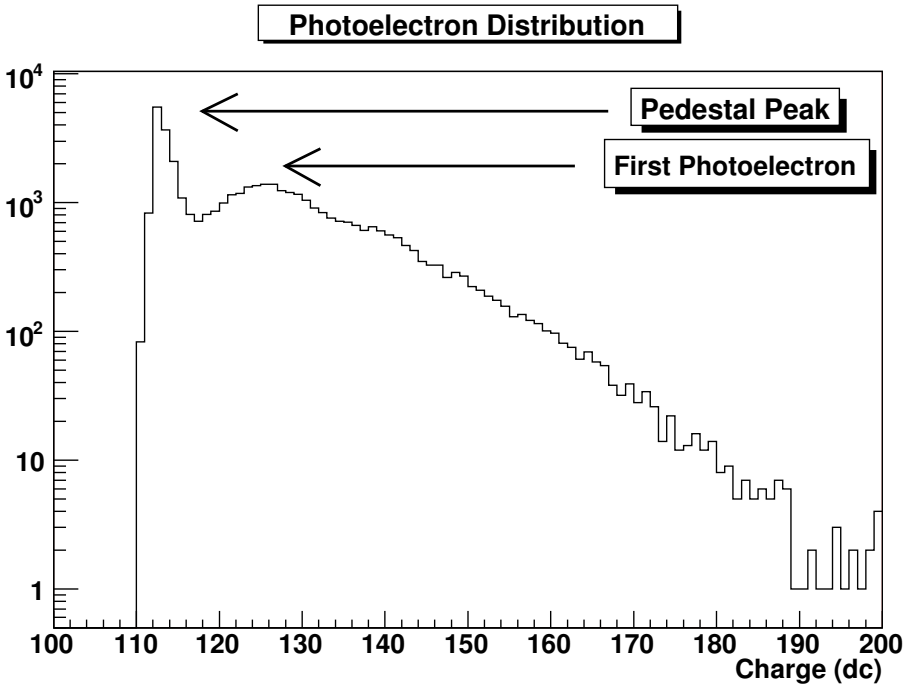

Figure 5.11: Distribution of integrated charge in dc for a single channel for a photoelectron data run.

σ_n of the n^{th} photoelectron peak is related to the Gaussian width of the first by

$$\sigma_n = \sigma_1 \sqrt{n} \tag{5.7}$$

where σ_1 is the Gaussian width of the first photoelectron peak and is a free parameter in the fit. In order to minimise the number of free parameters, a simple assumption regarding the height of each photoelectron peak can be made. Given the height of the first photoelectron peak Y_1 it is assumed that the height of each subsequent photoelectron peak is exponentially related by

$$Y_n(Q_n) = Y_1 \exp^{-\delta Q_n} \tag{5.8}$$

where δ is a decay constant relating the probability of two, three or four photoelectrons being generated relative to the number of single photoelectrons being generated and is a free parameter in the fit. The use of such an equation is entirely empirical and based on observations of the shape of the distribution.

Given the above values for Q_n, σ_n and Y_n for the Gaussian fits for each photoelectron peak, and also modelling the pedestal peak as a Gaussian distribution with Q_{ped}, Y_{ped} and σ_{ped} gives

$$Y(Q) = Y_{ped} \exp \frac{-(Q - Q_{ped})^2}{\sigma_{ped}^2} + \sum_{n=1}^{4} Y_n \exp \frac{-(Q - Q_n)^2}{\sigma_n^2} \tag{5.9}$$

The free parameters are listed in Table 5.1.

Parameter Type	Symbol	Fit Value
Parameters for	Q_{ped}	113
Pedestal	Y_{ped}	4777
	σ_{ped}	0.87
Parameters for	Y_1	1141
first Photoelectron	σ_1	5.9
Parameters for	δ	0.096
Subsequent Photoelectrons	ΔQ	10.4

Table 5.1: Free parameters for the Gaussian fit to the single photoelectron charge distribution.

A fit of the data using equation 5.9 is given in Figure 5.12(a); the quality of this fit is given by a χ^2 test yielding $\chi^2/\text{NDF} = 1286/63$ which corresponds to a reduced $\chi^2 = 20.4$. Although the fit looks relatively good by eye, such

a large reduced χ^2 is not very encouraging. A closer visual inspection of the fit indicates that the fit is not very successful in the region between the pedestal peak and the first photoelectron peak. One solution to this would be to increase σ_{ped}, however this would also increase the pedestal spread into the region to the left of the charge distribution.

An alternative function which can be used is a modified asymmetric Gaussian distribution (Equation 5.10) which can model the pedestal and single photoelectron distributions. This function is Gaussian on the left hand side of the distribution and Gaussian-like with an extended tail on the right hand side. The size of the tail is determined by the extra parameter α. The fit using this function is shown in Figure 5.12(b) and gives a $\chi^2/\text{NDF} = 127/61$ or a reduced $\chi^2 = 2.08$ which is a substantial improvement over the simple Gaussian fit. The parameters for this fit are listed in Table 5.2. This fit gives a dc/PE ratio of 11.6dc/PE. It must be noted that this particular run is taken with a greater than nominal HV, so that the first photoelectron peak can be clearly seen. There are a couple of ways that the dc/PE ratio at operating voltages can be obtained. The procedure just demonstrated can be applied to voltages at their typical operating values, however this can be a tricky approach as the first photoelectron peak may not be discernable from the pedestal peak. Alternatively the procedure can be applied at a series of large voltages to calculate the dc/PE ratio at those voltages. Then the dc/PE ratio at the operating voltage can be extrapolated. Either of these approaches yields a dc/PE ratio of 5.3 dc/PE (Holder et al., 2006).

Parameter Type	Symbol	Fit Value
Parameters for Pedestal	Q_{ped}	112.6
	Y_{ped}	5512
	σ_{ped}	0.57
	α_{ped}	0.31
Parameter for first Photoelectron	Y_1	1223
	σ_1	5.36
	α	0.8
Parameters for Subsequent Photoelectrons	δ	0.1
	ΔQ	11.6

Table 5.2: Free parameters for the asymmetric Gaussian fit to the single photoelectron charge distribution.

$$Y(Q) = \begin{cases} Y_0 \exp \frac{-(Q-Q_0)^2}{\sigma^2} & \text{for} \quad Q \leq Q_0 \\ \\ Y_0 \exp \frac{-(Q-Q_0)^2}{\sigma^2+\alpha(Q-Q_0)} & \text{for} \quad Q > Q_0 \end{cases} \tag{5.10}$$

5.2 Image Reconstruction

To calculate the energy and direction of incident gamma rays, the amount of light, and its orientation, must be accurately recorded in the camera. A multi-step event preparation process involving the calibration and cleaning of pixels and parameterisation of images is used to achieve this.

5.2.1 Pixel Cleaning

The first step in the multi-step process is to calculate the amount of residual light incident on each pixel. This is done by integrating the FADC trace with some pre-defined window. The size and location of this window should be chosen such that it provides an optimal signal-to-noise ratio which is defined as the ratio of the cleaned pixel charge to the pedvar. An example of how the window size is chosen is illustrated in Figure 5.13 which shows the (normalised) cleaned charge, pedvar and signal-to-noise ratio as a function of window size. The size and location of the window chosen depends on the algorithm used to analyse the FADC trace (see Chapter 6). Corrections are made to the start of the integration window using the T_{offset} and Crate Timing Corrections (Section 6.3). These corrections ensure that all traces are integrated in an equivalent manner. The effect of the location of the start of the integration window is demonstrated in Figure 5.14 where the signal-to-noise ratio for all windows sizes for a selection of window start locations is shown. Once the charge has been integrated, the pedestal baseline is subtracted. What remains represents the amount of light deposited in that pixel, however that representation is not uniform across the camera due to the uneven gain distribution. This is remedied by applying the relative gain constants described earlier to the charge calculated for each pixel.

Charge Padding

When running in PAIRS mode, differences in the NSB between ON and OFF fields can be a significant source of systematic error. This can be understood in terms of the cleaning of images (Section 5.2.2) which removes pixels from an image based on the charge relative to the noise. In the case of *potential*

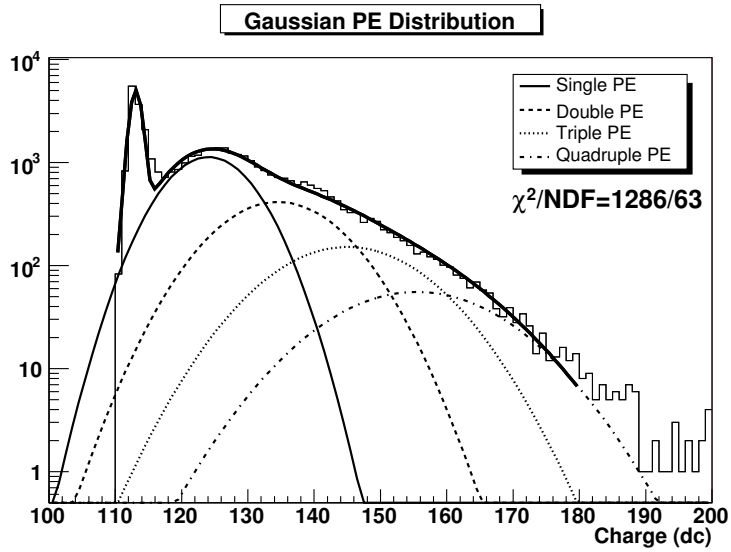

(a) Gaussian Fit

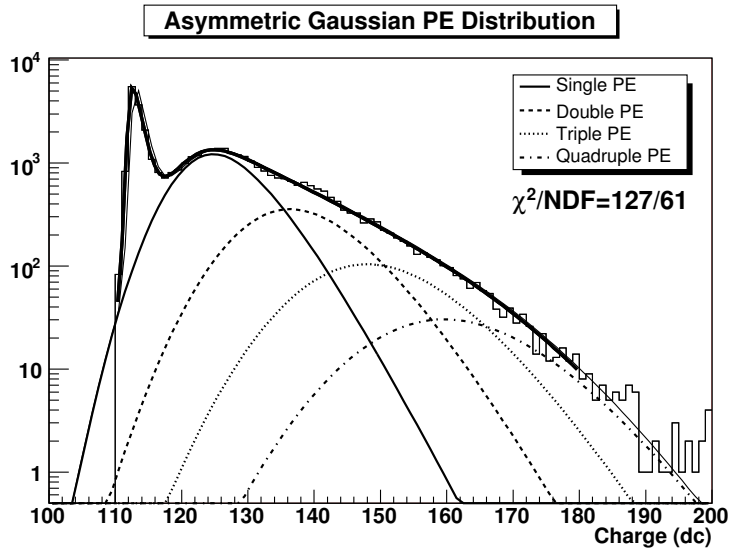

(b) Asymmetric Gaussian Fit

Figure 5.12: Fits of the charge distribution from a single photoelectron data run using a Gaussian and asymmetric Gaussian function.

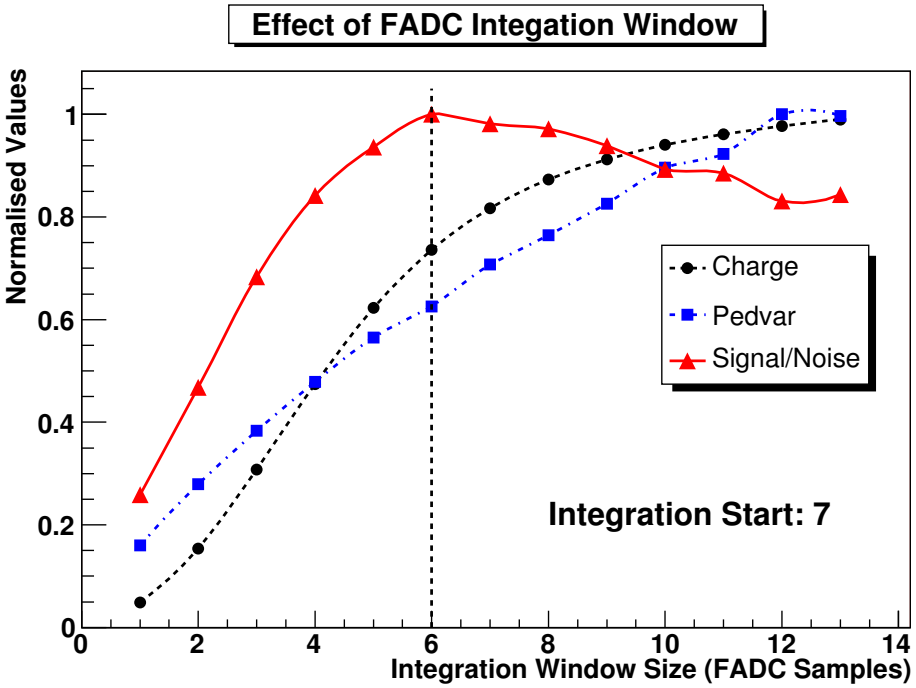

Figure 5.13: Comparison of integrated charge, pedvar and signal-to-noise (ratio of charge to pedvar) as a function of FADC window size for a single channel in one laser run. In this case the FADC integration window starts at sample 7. The integration window size for the optimum signal-to-noise ratio is indicated by the dashed line.

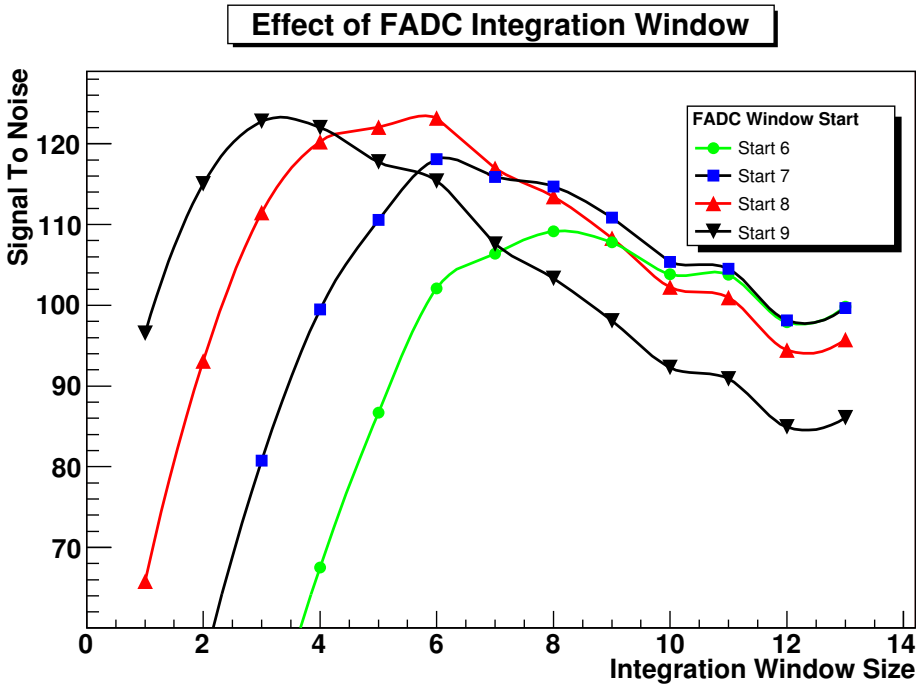

Figure 5.14: Comparison of signal-to-noise for an FADC trace as a function of window size for a selection of FADC integration window start locations.

boundary pixels, they are more likely to be removed from the image if they are especially noisy. This results in images that are narrower and more compact than they would otherwise be. This introduces a bias because these are exactly the expected characteristics of gamma-ray images. Another effect of noisy tubes is in the trigger rate. Extra background light in certain pixels in one run can promote events in that run above the hardware trigger level causing a mismatch in the trigger rate between the two runs in the pair. This can lead to a false positive or false negative detection in the offline analysis as there is an extra bias in one of the runs. In the early days of very high-energy gamma-ray astronomy, when single mirrors and single PMTs were used, padding lamps were placed in front of the PMT and the intensity adjusted until the average PMT current for the ON and OFF fields were matched. Although this method equalised the trigger rates, it becomes an impractical tool in the context of cameras which use an array of PMTs. It has the extra disadvantage of imposing a higher energy threshold, as the trigger level must be set higher because of the extra light. An alternative approach is to use a software trigger threshold in conjunction with software padding (Cawley, 1993). A software trigger threshold can be applied by cutting on the measured charge of the n^{th} brightest pixel where n is the number of pixels required by the PST. This raises the threshold, reducing the trigger rate of both runs. By padding less noisy pixels, events can be raised above the software trigger threshold so that they contribute to the effective trigger rate. It is insufficient to merely pad the less noisy run as the effective trigger rate cannot be increased above the hardware trigger rate.

The distribution of pedestal values for a typical PMT is generally Gaussian in shape (Figure 5.2). Letting P_{ON} and P_{OFF} be the pedestal values for the ON and OFF fields and σ_{ON} and σ_{OFF} be the pedvars in the ON and OFF fields, the total signal in a single pixel may be approximated as

$$ON = P_{ON} + \sigma_{ON}\text{Gauss}\,(0:1) + C_{ON} + \sqrt{(C_{ON})}\text{Gauss}\,(0:1) \qquad (5.11)$$

where C_{ON} is the Cherenkov component of the signal and $\text{Gauss}\,(0:1)$ is a Gaussian distributed random number of zero mean and unit variance. The noise component due to the night sky background is then given by

$$N_{ON} = \sigma_{ON}\text{Gauss}\,(0:1) \qquad (5.12)$$

and the noise component due to the night sky background in the OFF field is similarly given by

$$N_{OFF} = \sigma_{OFF}\text{Gauss}\,(0:1) \qquad (5.13)$$

In the case where differences in the night sky background cause N_{ON} to be greater than N_{OFF}, noise denoted by N_{add} is added to the pixel in the OFF field in quadrature such that

$$(N_{ON})^2 = (N_{OFF})^2 + (N_{add})^2 \tag{5.14}$$

giving

$$N_{add} = \sqrt{(N_{ON})^2 - (N_{OFF})^2} \tag{5.15}$$

so that the total OFF signal would be given by

$$\begin{aligned} OFF &= P_{OFF} + \sigma_{OFF}\text{Gauss}\,(0:1) + N_{add}\text{Gauss}\,(0:1) \\ &\quad + C_{OFF}\sqrt{(C_{OFF})}\,\text{Gauss}\,(0:1) \end{aligned} \tag{5.16}$$

Thus by setting the integrated charge to that given in equation 5.16, charge padding is implemented and the effect of bias between the ON and OFF regions is significantly reduced.

FADC Trace Padding

Charge padding is directly suited to telescopes equipped with Charge-Analog Digital Converters (QADC), where only the integrated charge is available. However, with the VERITAS array, FADC data are available, thus in principle a more accurate padding technique should be applied. In trace padding, noise is added directly to the FADC trace of that channel exhibiting a narrower pedestal distribution. The amplitude of the noise is related to the noise difference between the noisier and the less noisy channel. Techniques for the application of trace level padding are under development by Kenny (2006), but are not used here.

Malfunctioning Pixels

In any given data run there may be a number of pixels with an errant signal. The nature of the problem can vary from malfunctioning PMTs to bright stars in the field of view. The distribution of pedvars for a run (Figure 5.15) provides a wealth of PMT diagnostic information. Those PMTs with a very small pedvar are most likely switched off (eg due to stars) or are malfunctioning (eg due to a bad PMT/base connection or physically malfunctioning or missing PMT). These PMTs are represented by the small distribution on the left hand side of Figure 5.15. Those PMTs with a large pedvar are very noisy - this may be due to a malfunctioning PMT, or due to a bright star

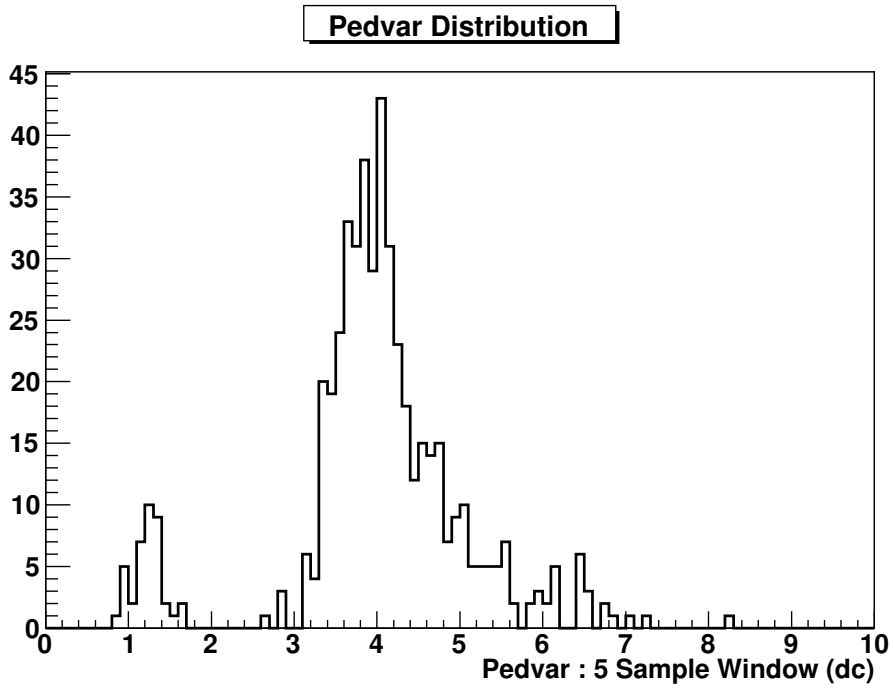

Figure 5.15: Typical distribution of pedvars for all channels in Telescope 1. The distribution clearly has two components. The dominant component corresponds to normal pedvars. The smaller component corresponds to PMTs with a low pedvar. This may be caused by a malfunctioning PMT. For a perfectly uniform field, the distribution should have a Gaussian shape, as the pedvar represents the mean number of photons striking the photocathode. Under night sky conditions, there is a significant tail to the distrubition caused by PMTs which are subjected to extra starlight. This gives the distribution a Poissonian appearance.

where the PMT was not turned off. Rather than placing simple cuts on the pedvar to remove such pixels from the image, cuts are placed on the scaled pedvar

$$\frac{pedvar - \langle pedvar \rangle}{\sigma_{pedvar}} \tag{5.17}$$

such that the pedvar cuts are in terms of the difference between that pixel's pedvar and the pedvar mean in units of the pedvar standard deviation. This allow pedvar noise cuts to be used that are consistent across different observation fields with different NSB. This scaled pedvar distribution is shown in Figure 5.16 with the lower and upper cuts indicated by the red shaded regions.

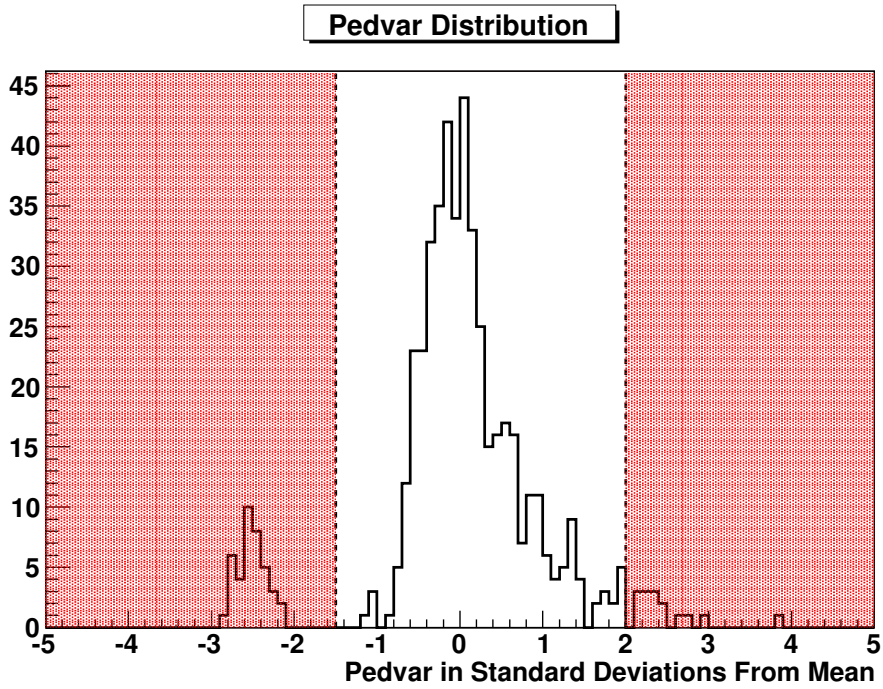

Figure 5.16: Distribution of pedvars from Figure 5.15 after rescaling them to correspond to the difference between the pedvar and mean pedvar in units of the standard deviation (Equation 5.17) . Any PMT with a scaled pedvar of less than -1.5 (indicated by the left hand red region) is excluded as the PMT is probably switched off or malfunctioning. Any PMT with a scaled pedvar greater than 2 (indicated by the right hand red region) is excluded as it is noisy (eg due to the presence of stars) and will introduce a bias into the analysis.

5.2.2 Image Cleaning

In order to proceed with parameterising the image, an algorithm is required which ensures that all pixels which contain a significant amount of Cherenkov light are included, and that all pixels which are dominated by background are excluded. It is also important that malfunctioning pixels are removed from the analysis chain. To achieve this, a two-pass cleaning method is used which depends not only on the charge deposited in each pixel on an event by event basis, but also on a measure of the noise in each pixel. This measure of noise has already been introduced as the pedvar.

In the first pass, any pixel whose charge exceeds the product of its pedvar and some fixed threshold, referred to as the *Picture Threshold*, passes the cleaning algorithm. In the second pass, any pixel which is adjacent to a pixel which passed the first criterion, and whose charge exceeds the product of its pedvar and some lower fixed threshold, referred to as the *Boundary Threshold*, passes the cleaning algorithm. Pixels which pass the first criterion are referred to as Picture Tubes, whereas pixels which pass the second criterion are referred to as Boundary Tubes. All Picture tubes and Boundary tubes are regarded as *Image* tubes and form part of the Cherenkov signal in the camera; the charge for all other tubes is set to zero. In essence this technique cuts on the Cherenkov signal in each PMT relative to the background noise in the PMT. In the two-pass approach, the second pass ensures that PMTs with a relatively small charge can still be included in the cleaned image - as it is more likely that they are genuine signals if they are adjacent to Picture tubes. Any isolated pixels which can skew the parameterisation are removed. An example of events before and after the complete cleaning process is shown in Figures 5.17 and 5.18. An alternative approach to cleaning (Bond et al. (2003)), identifies patches of Image pixels called *islands* which are surrounded by pixels with no significant signal.

5.2.3 Parameterisation

Cleaned images are characterised using a set of parameters, originally proposed by Hillas (1985) listed in Table 5.3. Further parameters listed in Table 5.4, were subsequently introduced and are also used to parameterise events. Parameterisation is achieved by fitting a set of second-order moments to the image to characterise its *width* and *length* which represent the longitudinal and lateral development of the shower. The first order moments give the image centroid, which can be used in conjunction with the primary axis of the image to give its position and orientation. Notes on the measurement and interpretation of the other parameters are given in the Tables 5.3 and

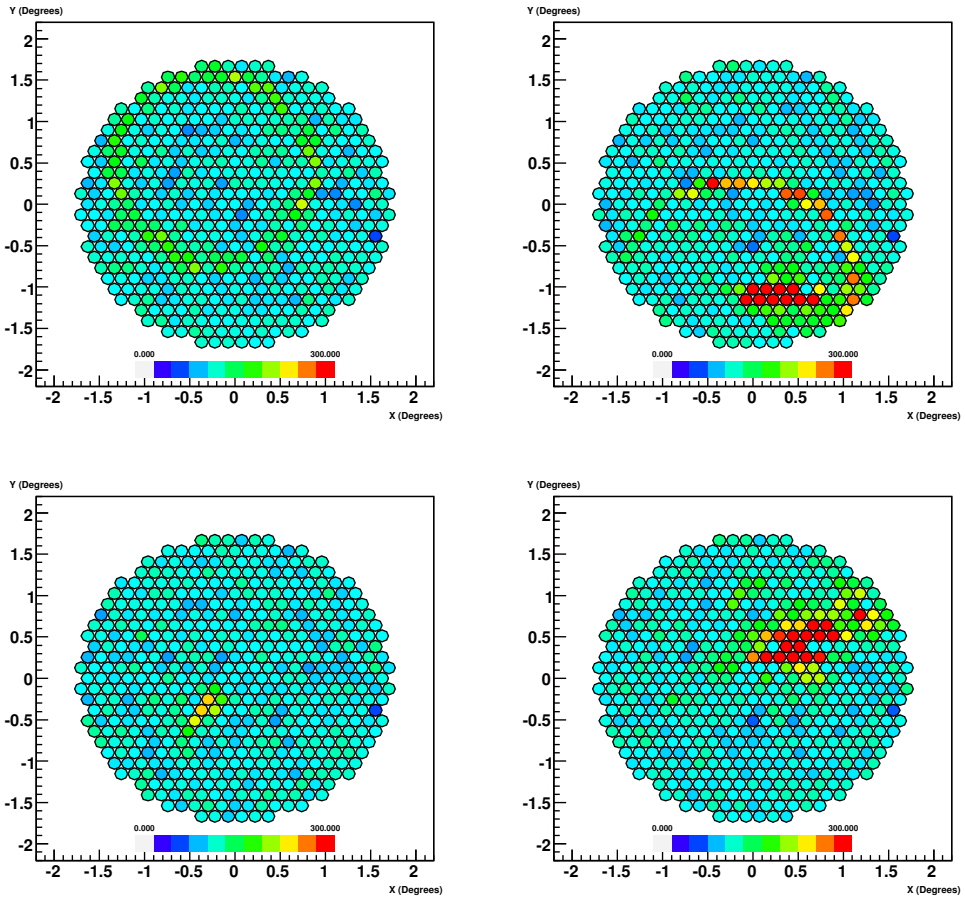

Figure 5.17: A representation of four Cherenkov shower events in a VERITAS camera. The progenitor particles are identified and the effect of cleaning is shown in Figure 5.18.

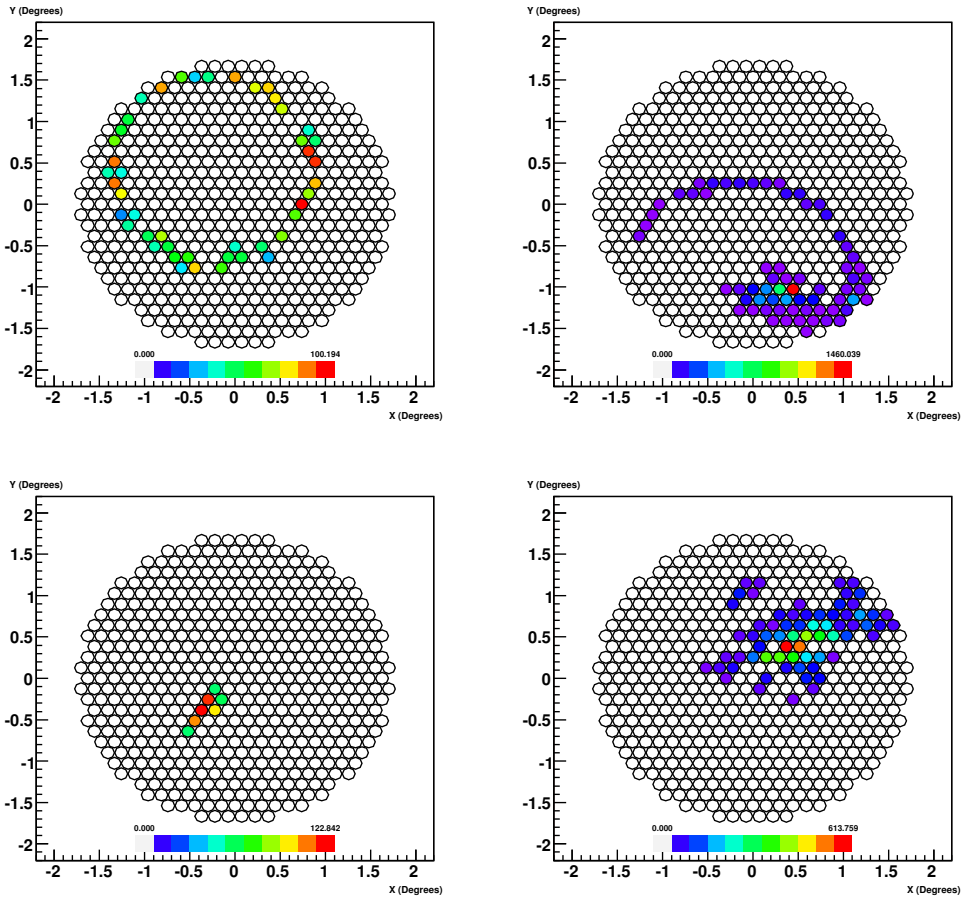

Figure 5.18: Cleaned events from Figure 5.17. Top Left : Muon Ring, Top Right : Cosmic Ray with striking muon component, Bottom Right : Cosmic Ray, Bottom Left : Gamma Ray.

Length	RMS spread of light along the major axis of the image; a measure of the vertical development of the cascade.
Frac N	Percentage of the total light content of the image contained in the N highest tubes (N=2 for original Hillas paper, subsequently used N=3 for larger cameras).
Width	RMS spread of light along the minor axis of the image; a measure of the lateral development of the cascade.
Azwidth	RMS spread of light perpendicular to the line connecting the image centroid with the centre of the field of view; a measure of the *width* as well as the pointing.
Miss	Perpendicular distance between the major axis of the image and the centre of the field of view; a measure of the shower orientation.
Distance	Distance from the centroid of the image to the centre of the field of view.

Table 5.3: Image Parameters from Hillas (1985).

5.4 and some are shown graphically in Figure 5.19.

5.3 Shower Reconstruction

A shower reconstruction method must provide the ability to identify the direction, energy and class of the shower progenitor particle. The class can be background (mostly hadrons) or gamma ray. It is necessary to identify the energy so that the source spectrum can be estimated, and it is necessary to identify the direction so that the source location can be found, and in the case of extended sources, its morphology studied. In order to examine extended sources, to search for serendipitous sources in the field of view or to perform sky surveys, it is necessary to construct a 2-dimensional sky map of events passing cuts.

The ability to reconstruct showers with single telescopes is hampered by the inherent degeneracy in determining which side of the camera field of view (FOV) the shower originated in. In a single telescope analysis, the source location is assumed to lie along the primary image axis, and the distance to it from the image centroid can be calculated according to Lessard et al. (2001). Use of multiple telescopes overcomes this degeneracy as simple intersection of lines (Figure 5.20) can be used to locate the source position. There is the added advantage that the core location on the ground can be located (Figure

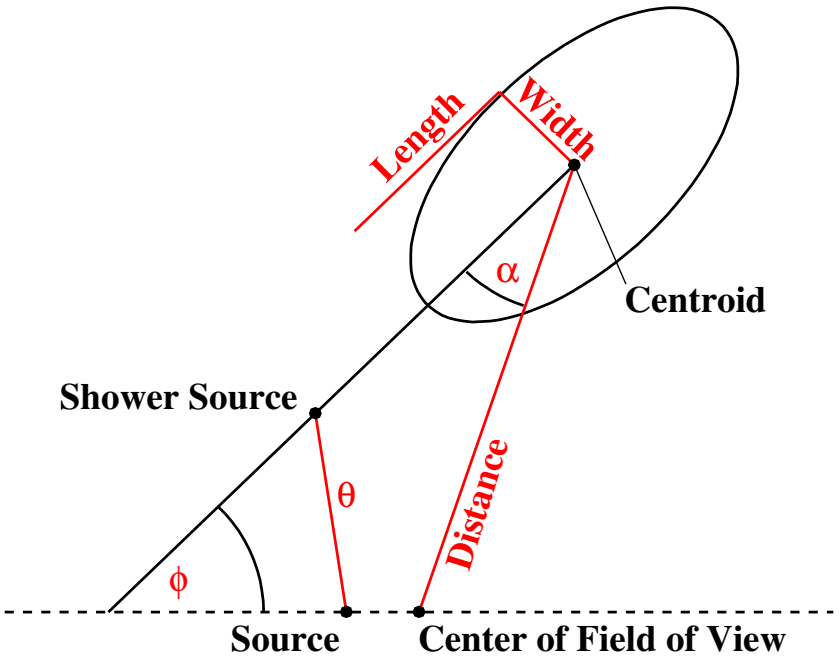

Figure 5.19: Graphical display of the elliptical form used to represent the image of a Cherenkov shower in the focal plane of a Cherenkov telescope. The angular distance θ is the distance between the reconstructed shower source in the field of view and the putative source position.

Size	Sum of the number of counts in all of the tubes; corresponding to the total light content of the image.
Length/Size	The ratio of the parameters *length* and *size*
Max N	Total amount of light in the N^{th} largest tube. This is used to apply a software trigger in the offline analysis
Alpha	Angle between the major axis of the ellipse and a line joining the centroid of the ellipse to the centre of the field of view.
Asymmetry	Measure of how asymmetric the image is. Gamma ray images should have a cometary shape with their light distributions skewed towards their source position.
Phi	Azimuthal angle of the main axis of the ellipse.

Table 5.4: Image parameters defined subsequent to Hillas (1985).

5.21), which can be used in conjunction with Monte-Carlo simulations of extensive air showers to provide a powerful background rejection technique (Section 5.4.2). A distribution of the reconstructed core positions on the ground is given in Figure 5.22.

The shower source location in the FOV is the point with a minimum weighted perpendicular distance to each image axis where the weight corresponds to the image *size* (Figure 5.20). If more than two images are available, a source location is computed for each pair of image axes. Then a weighted average of these source locations is used to determine the source location with greater accuracy. In this case, the weight (Schlenker (2005)) of each computed source location favours pairs of images with a large angular separation and image *size* over faint or circular images. The weight W for a pair of images (where the image parameters are indexed 1 and 2) is given by

$$W = \frac{\sin\left(\phi_1 - \phi_2\right)}{\left(s_1^{-1} + s_2^{-1}\right)\left(w_1/l_1 + w_2/l_2\right)} \tag{5.18}$$

where s, w and l represent the image *size* , *width* and *length* respectively, and ϕ (Table 5.4) represents the angle between the major axis of the image and the horizontal axis of the camera plane. Pairs of images with a large $\delta\phi$ are more orthogonal which provides a better geometrical reconstruction than pairs of images with a small $\delta\phi$ which are more parallel.

To account for the rotation of the sky during observations, and to combine data from multiple runs, the source location of the reconstructed shower must be transformed from camera coordinates to azimuth and elevation.

These coordinates are then derotated to RA and DEC using the event time and telescope location on the earth. The reconstructed source locations can then be binned in a 2-dimensional histogram representing the sky in a fixed RA/DEC reference frame (see Figure 7.5).

5.4 Background Rejection

The parameterised dataset is dominated by the cosmic-ray background. Highly efficient selection techniques must be employed to identify gamma-ray events in the dataset with a low false-negative probability while rejecting the cosmic-ray background with a low false-positive probability.

There are many methods available for the selection of gamma-ray images from a dataset of background dominated events. Some methods are best suited to extracting a signal, other methods are best suited to spectral analysis. Some of the commonly used techniques used are reviewed here, with more sophisticated techniques reviewed in Krawczynski et al. (2006). All the techniques rely on optimising some parameter, typically the statistical significance of the source.

5.4.1 Quality Cuts

A set of quality cuts are typically applied to datasets prior to the application of the main set of cuts. The purpose of such cuts is two-fold. Firstly they are used to exclude events which cannot be reconstructed properly. An example of such an event would be one with a very large impact parameter which suffers truncation at the edge of the camera. It is impossible to accurately reconstruct the direction of such a shower, rendering image parameters such as α and θ not only incorrect but misleading. Other images that cannot be reconstructed properly are those images which lie very close to the optic axis of one telescope - such an image is circular in shape, with similar consequences for the α and θ image parameters. In such situations, it would be common for the shower to be reconstructed without input from that telescope (assuming a stereoscopic system with more than two telescopes). A pair of images that are nearly parallel are not used to calculate the source location and impact parameter.

As Cherenkov telescopes operate as close to the noise threshold as possible, it is feasible that there may be a trigger induced bias in either the ON or OFF regions due to difference in the NSB between the ON and OFF fields. In order to eliminate such a bias, a software trigger cut may be applied (Section 5.2.1).

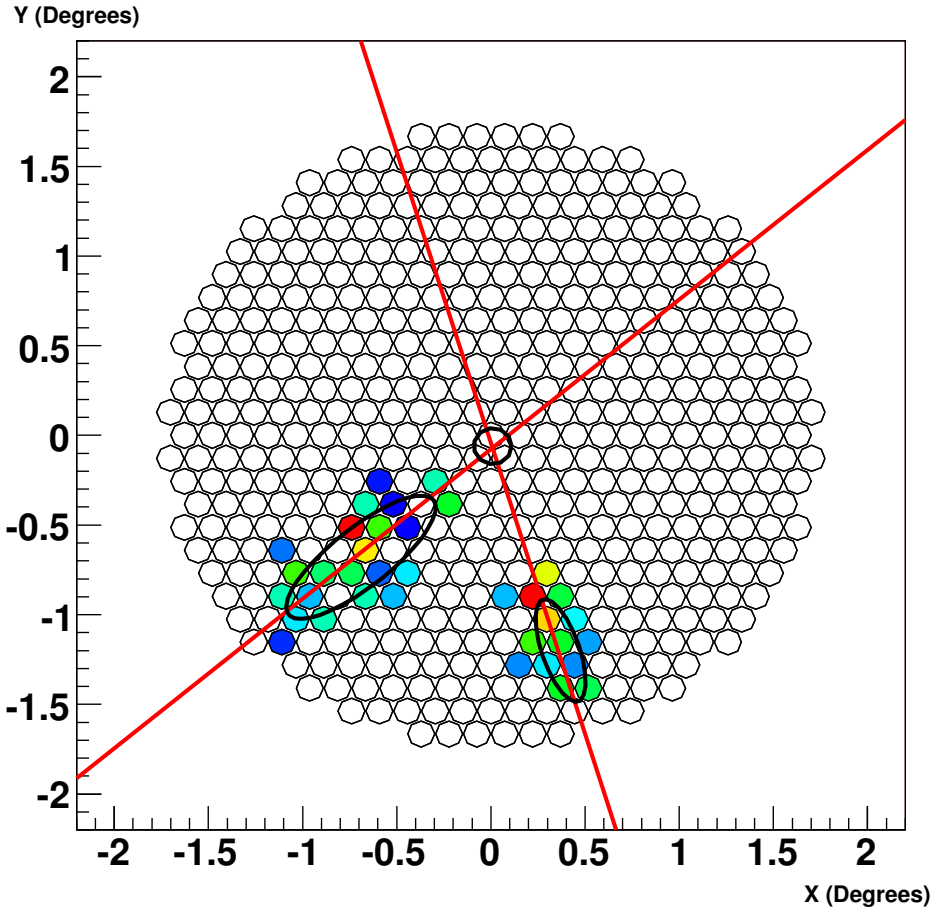

Figure 5.20: Simple source location reconstruction using intersection of lines. The Cherenkov images of the same shower as seen by two telescopes are overlayed on one camera.

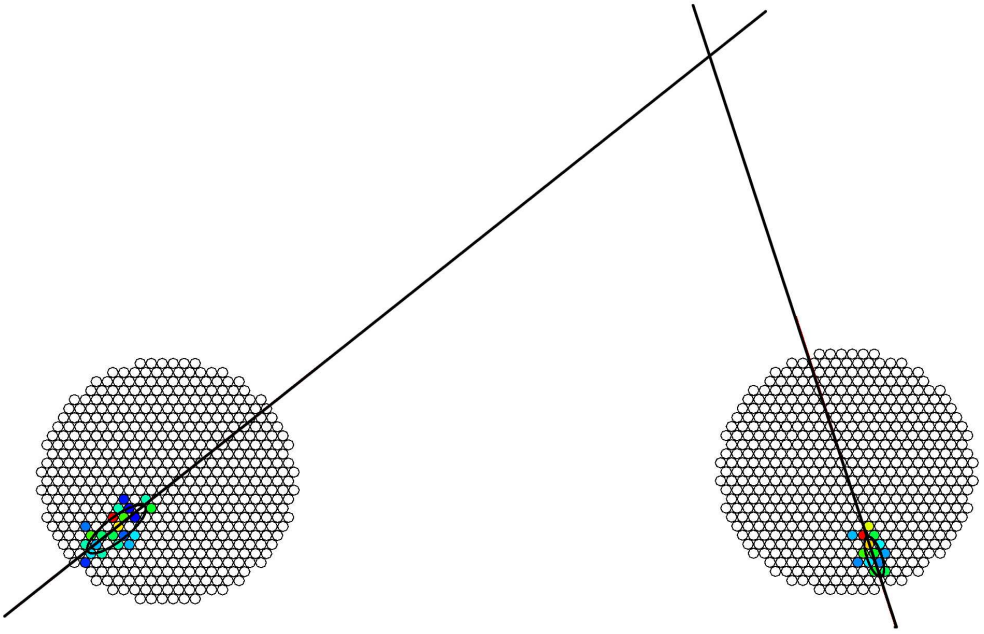

Figure 5.21: Simple core location reconstruction using intersection of lines.

In a spectral analysis, showers with reconstructed impact parameters far from the telescopes are generally excluded. This is due to the shape of the lateral distribution of Cherenkov photons which is flat out to a few hundred meters (Section 2.4) before falling away rapidly. In order to ensure the exclusion of such showers, a cut on the impact parameter can be applied.

5.4.2 Scaled Cuts

The image recorded from a shower is strongly dependent on the distance to the shower core. For instance, a shower of a given energy will be significantly brighter if the core is 100 m from the telescope rather than if the core is 300 m from the telescope. A set of cuts called *scaled cuts* is introduced in Daum et al. (1997) which addresses this problem by comparing the *width* and *length* parameters to a set of simulations. A large number of gamma rays are simulated at several discrete zenith angles, and parameterised in terms of their *width* , *length* , *size* and impact parameter (see Section 7.2 for a description of the Monte-Carlo dataset used). Given the requirement of the impact parameter, it is clear why this cut technique is only appropriate for stereoscopic observations, for which an accurate measurement of the impact

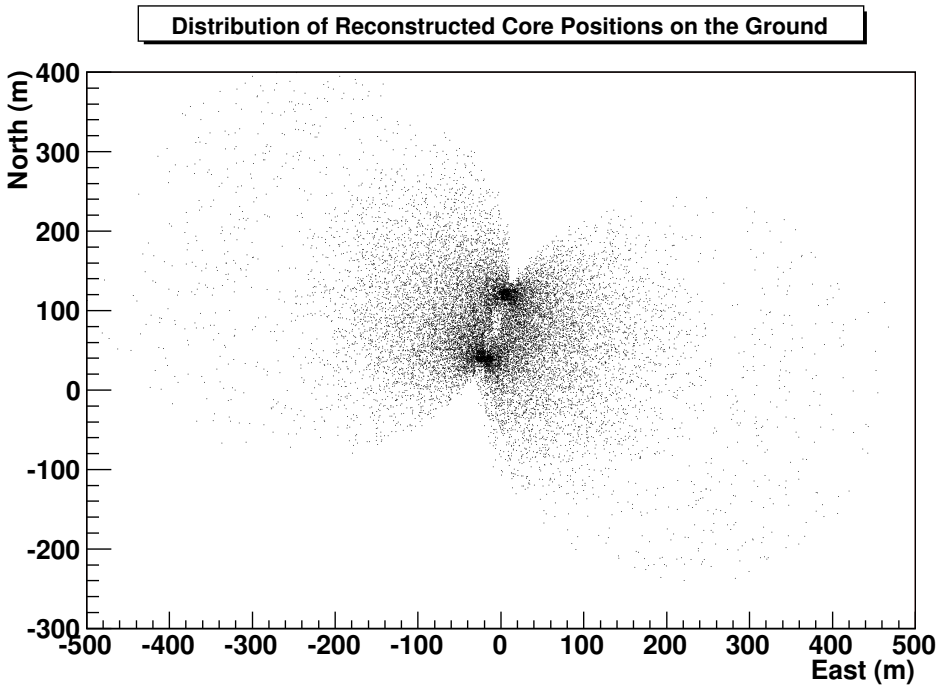

Figure 5.22: Distribution of reconstructed core positions on the ground. Some quality cuts are applied to ensure accurate reconstructions. These cuts, which include a cut on the angle between two images (Section 5.4.1), lead to the circular lobe-like features.

parameter is available. Figure 5.23 shows the lookup table used to store the calculated image *width* derived from Monte-Carlo simulations of gamma rays for a range of image *size* and impact parameters, but for a fixed zenith angle. The scaled width (SW) of a particular image is given by

$$\mathrm{SW} = \frac{w\left(S, D\right)}{\langle \hat{w}\left(S, D\right)\rangle} \tag{5.19}$$

where S is the image *size* , D is the impact parameter, $w\left(S, D\right)$ is the *width* of the image and $\langle \hat{w}\left(S, D\right)\rangle$ is the mean of the image *width* of the set of simulated gamma rays of *size* S and impact parameter D. The scaled length (SL) is similarly defined as

$$\mathrm{SL} = \frac{l\left(S, D\right)}{\left\langle \hat{l}\left(S, D\right)\right\rangle} \tag{5.20}$$

These scaled parameters can be easily combined from multiple telescopes using a simple weighted average, eg

$$\mathrm{MSW} = \frac{\sum_i^n S_i \mathrm{SW}_i}{\sum_i^n S_i} \tag{5.21}$$

and

$$\mathrm{MSL} = \frac{\sum_i^n S_i \mathrm{SL}_i}{\sum_i^n S_i} \tag{5.22}$$

where MSW is the *Mean Scaled Width* and MSL is the *Mean Scaled Length*. The MSW and MSL cuts have proven to be highly effective discriminatory parameters with stereoscopic data, however if there is any weakness it is the inherent dependence on a large database of accurate Monte-Carlo simulations.

5.4.3 Advanced Rejection Methods

Apart from the standard background rejection methods already described, there are many other rejection methods which can be used. These methods include Kernel Selection, Neural Network and Random Forest.

Kernel analysis works on the assumption that the Probability Density Function (PDF) of events in an N-dimensional parameter space (for N image parameters) can be estimated by a sum of appropriately chosen *kernel* functions. Using a sum of Gaussian kernels, the PDF of a given event can be estimated, based on a set of simulated gamma-ray events. Real background events are used in conjunction with the PDF to discriminate candidate gamma-ray events using a log-likelihood ratio.

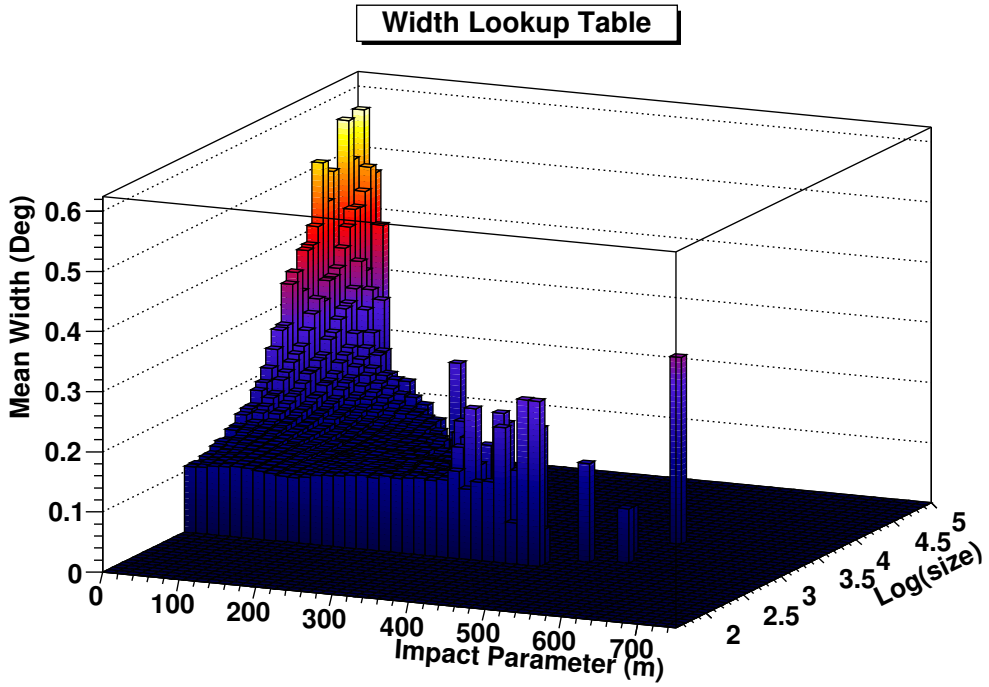

Figure 5.23: Graphical representation of the Monte-Carlo simulation derived lookup table for the *width* parameter.

A Neural Network uses a simplified model of a biological process employed in decision making in the brain (McCulloch and Pitts (1943)). In this model, a neuron is a device which sums a set of weighted inputs and returns a positive or negative result depending on some preset threshold. In order to choose the weights (Masterson (1999), Dunlea (2001)), the network must be trained using a set of inputs corresponding to image parameters from Monte-Carlo simulated gamma rays.

The Random Forest technique (Bock et al. (2004)) involves the construction of a large number of decision *trees* generated using a Monte-Carlo simulated training data set. Each node in the tree represents a binary threshold decision, with each case passing through the decision nodes until a *leaf* is reached. The leaf represents a decision corresponding to signal or background. A significant improvement to this selection strategy is to use a collection of trees, called a *forest* and to use a simple averaging or voting system to combine the results of all the trees to produce a global decision. Construction of a single tree starts with all real background and Monte-Carlo simulated gamma-ray events contained in the root node. The node is split in two using a cut on a randomly selected image parameter which maximises the decrease in average impurity of both background and simulated Monte-Carlo gamma-ray data sets. This splitting continues until the remaining data at the end of each branch has a high degree of purity - at which point a decision leaf can be assigned to that branch.

5.5 Background Estimation

In order to determine whether a signal is present in the observed sky region, the background level must be calculated. There are various methods of estimating this background, several of which are directly associated with a mode of observation (Section 2.4.10). The number of excess gamma-ray events is given by

$$N_\gamma = N_{on} - \alpha N_{off} \tag{5.23}$$

where N_{off} is the number of background counts and α is the background normalisation factor given by

$$\alpha = \frac{\int_{on} \epsilon_\gamma \left(\theta_x, \theta_y, \Theta, t\right) d\theta_x d\theta_y d\Theta \, dt}{\int_{off} \epsilon_\gamma \left(\theta_x, \theta_y, \Theta, t\right) d\theta_x d\theta_y d\Theta \, dt} \tag{5.24}$$

where ϵ_γ is the acceptance for γ-ray like showers which is a function of the source position in the camera θ_x, θ_y, the zenith angle Θ and the exposure

time t. Essentially, α is the ratio of the effective exposure integrated in time and space over the source and background regions. For a dataset of candidate gamma-ray events that have passed the MSW and MSL cuts, it is the requirement of a background model to provide values for α and N_{off}.

5.5.1 PAIRS Mode

In PAIRS mode, a region of sky offset from the source by 30 sidereal minutes in right ascension is observed and is used as the background. N_{off} is calculated simply by passing this run through the same analysis and cuts procedure as the ON source run. Calculation of α is greatly simplified since the zenith angle Θ and the camera orientation relative to the source (where the source is the background location in the sky, offset by 30 sidereal minutes) is the same for the ON and OFF regions. Therefore α is reduced to

$$\alpha_{pairs} = \frac{\int_{on} \epsilon_\gamma(t)\, dt}{\int_{off} \epsilon_\gamma(t)\, dt} \tag{5.25}$$

here $\epsilon_\gamma(t)$ is just the live time of the detector, so the calculation of α reduces to the ratio of the livetimes during observation of the ON and OFF regions.

5.5.2 Reflected Region Model

In WOBBLE (Section 2.4.10) mode, the source is offset from the center of the camera by $\pm 0.5^\circ$ or $\pm 0.3^\circ$ in right ascension or declination, thus the source rotates around the center of the camera during observations. The acceptance (See Figure 7.8) drops radially from the camera center to the edge of the field, thus α is given by

$$\alpha = \frac{\int_{on} \epsilon_\gamma(\theta_{cam})\, d\theta_{cam}}{\int_{off} \epsilon_\gamma(\theta_{cam})\, d\theta_{cam}} \tag{5.26}$$

where θ_{cam} is the angle between the shower source in the FOV and the camera center. In the reflected region background model, the locations of the backgrounds are selected such that the locus of their centers with the center of the source position traces a circle, whose radius corresponds to the WOBBLE offset, around the center of the field of view (Figure 5.24). This implies the angular acceptance for each offset background region, and for the ON source region, is identical. Therefore α is simply given by $\alpha = 1/N$ (where N is the number of reflected regions used).

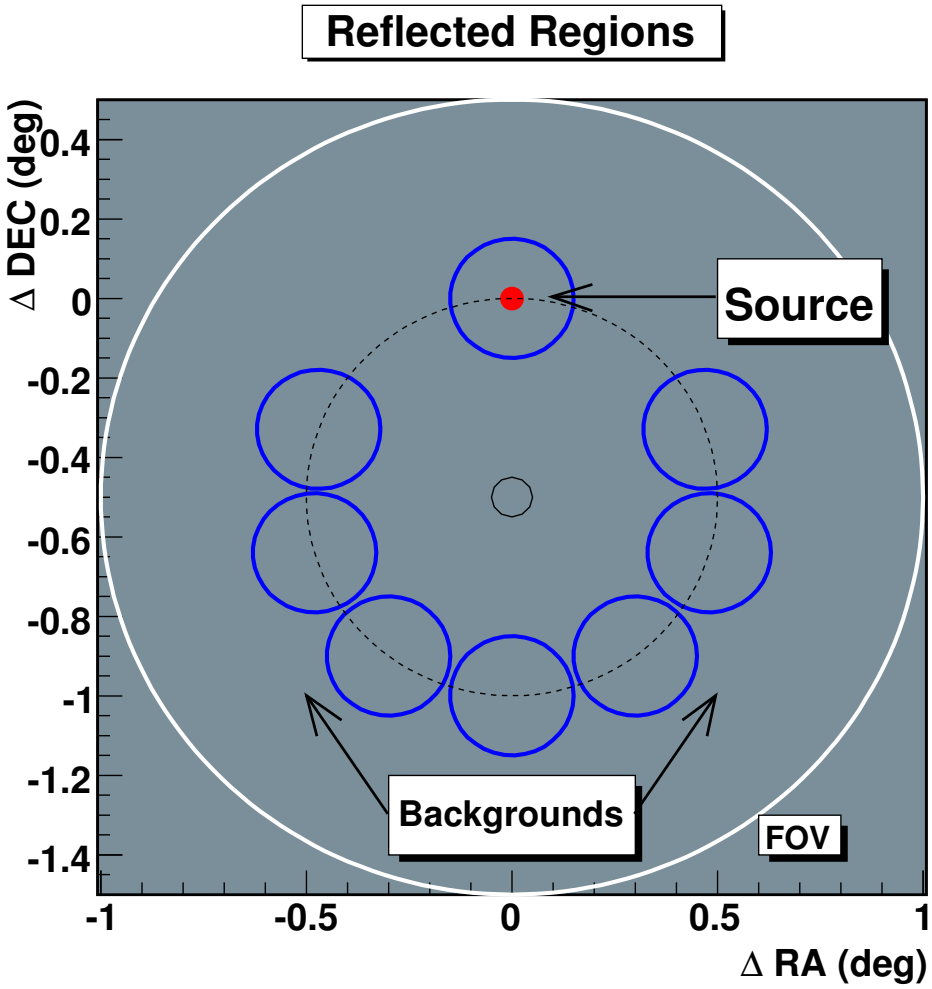

Figure 5.24: This figure indicates the location of the background regions for a WOBBLE observation using the reflected region background method. The axes are in units of Δ RA and Δ DEC where the source, marked as a red spot, is at Δ RA $= 0^\circ$ and Δ DEC $= 0^\circ$. The center of the camera, marked as a small circle, is located at Δ RA $= 0^\circ$, Δ DEC $= -0.5^\circ$ indicating that the WOBBLE is in the direction -0.5° in declination. The dashed circle indicates a contour of equal acceptance and has a radius corresponding to the WOBBLE offset. The field of view is indicated by the large white circle. The blue circle around the source indicates the signal integration region. The set of green circles, the locus of whose centers is equivalent to a contour of equal acceptance denoted by the dashed line, are used as background integration regions.

5.5.3 Ring Background

The reflected-region model is essentially a one-dimensional analysis as the number of counts is only calculated for the source region and the multiple background regions. In order to construct a 2-dimensional sky map, the excess number of counts in each grid point in the FOV must be calculated. In this model, the background region is chosen to be a ring (really an annulus) around the bin (see Figure 5.25). The center of the ring is excluded so that events from or close to the source are not considered - this exclusion region must be large enough to exclude events from extended as well as point-like sources. The primary difficulty with this method is that the acceptance across the ring is non-linear. Thus the scaling parameter α (Equation 5.27) must be expressed as the ratio of the integrated acceptance of the on-region to the integrated acceptance of the off-region for each on-region/off-region pair. The calculation of the acceptance is elaborated for the analysis of the Crab Nebula dataset in Section 7.6.4.

$$\alpha_{ring} = \frac{\int_{on} \epsilon_\gamma \left(\theta_{cam}\right) d\theta_{cam}}{\int_{off} \epsilon_\gamma \left(\theta_{cam}\right) d\theta_{cam}} \tag{5.27}$$

5.6 Spectral Analysis

In order to understand the physics behind any detected source, it is necessary to determine an energy spectrum. This energy spectrum provides a characteristic signature for the source, and is a direct link between the physical processes generating the very high-energy gamma rays and the atmospheric Cherenkov light detected by the telescope. As a full spectral analysis is not performed in this work, only an outline of the energy estimation and collection area calculation procedures is provided.

Spectral determination is dependant on an understanding of both the dataset and the telescope array (Mohanty et al., 1998; Hillas et al., 1998). For each detected gamma-ray, an energy estimate (Section 5.6.2) must be calculated, generally based on image *size* and impact parameter. The energy dependent collection area $A\left(E\right)$ for the array must be calculated from Monte-Carlo simulations (Section 5.6.1). Finally the source spectrum must be disentangled from the estimated energy distribution, collection area and livetime.

The differential flux $d\mathcal{F}/dE$ is defined as the number of particles per unit area, time and energy and is given by

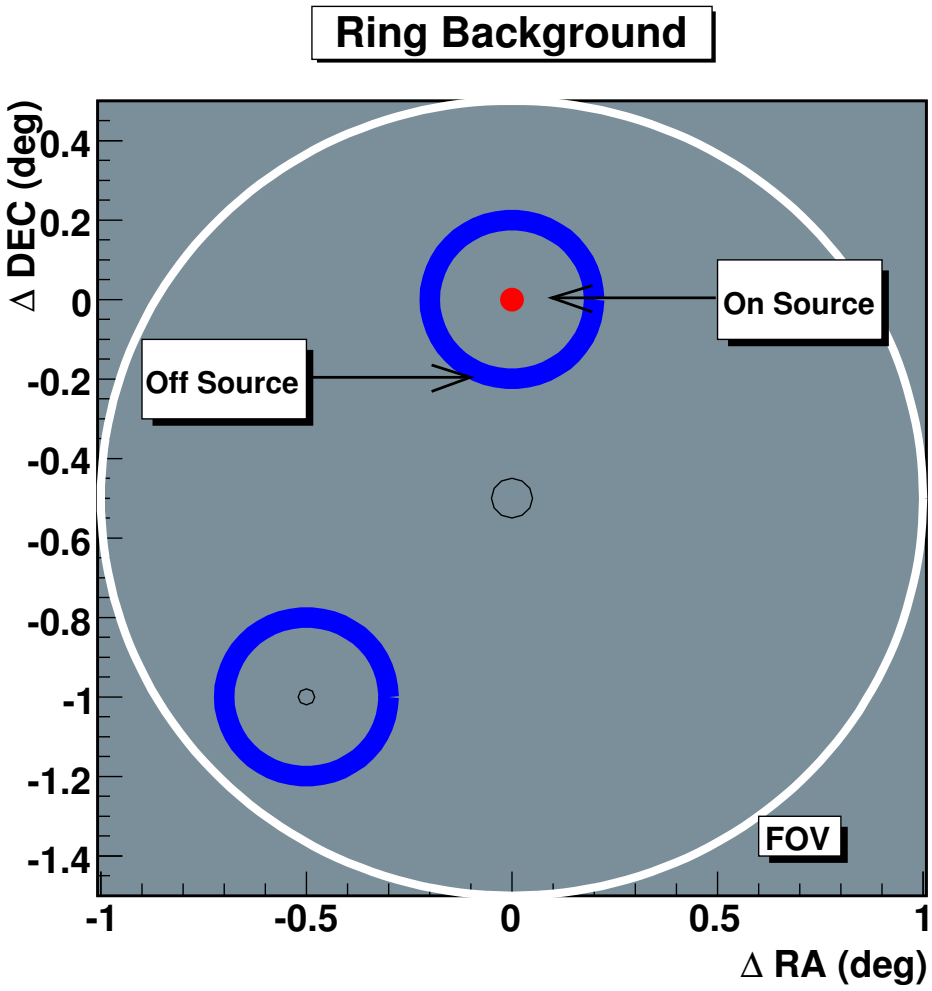

Figure 5.25: This figure assumes identical observing conditions as Figure 5.24. In this case, the number of excess points in every point in the field of view is calculated. The background used for every point corresponds to an annulus around that point. Two rings are shown. The top ring corresponds to the background region that is used for where the actual source (red point) is located. The ring in the lower left side of the FOV shows the region of background used to estimate the signal content in the small black circle within that ring. Similar rings are used at each point in the FOV to estimate the signal content everywhere.

$$\frac{d\mathcal{F}}{dE} = \frac{1}{t_{\text{live}} A\left(E\right)} \frac{dN_{\gamma}}{dE} \tag{5.28}$$

where t_{live} is the livetime of the array and N_{γ} is the number of gamma rays detected. The simplest source spectrum model is a power law of the form

$$S\left(E\right) dE = AE^{-\alpha} dE \tag{5.29}$$

where $S\left(E\right) dE$ is the number of gamma rays per unit area per unit time in the infinitesimal interval dE at an energy E, A is the flux constant and α is the spectral index of the source.

5.6.1 Collection Area

The collection area partially determines the sensitivity of the array to gamma rays at each energy and is an important aspect for deriving the source spectrum. The collection area for a system of Cherenkov telescopes cannot be determined directly from the dataset. This is because no test beam is available, ie the detector response to a beam of particles of known energy incident over a large area cannot be measured. As a result, a database of Monte-Carlo simulations must be generated and propagated through the analysis to determine the acceptance of signal as a function of energy. Gamma rays are simulated out to a maximum throw radius R_0 which defines a circular area A_0, where this area is perpendicular to the optic axis of the telescopes. R_0 is chosen such that the probability of acceptance of a gamma ray with impact parameter R is close to zero as $R \rightarrow R_0$.

The collection area is defined as

$$A\left(E\right) = A_0 \left(\frac{n_E}{N_E}\right) \tag{5.30}$$

where n_E is the number of events that triggered the detector and passed the background rejection algorithm at energy E, and N_E is the incident number of events at energy E. For very low energies, the collection area is expected to be small, as the Cherenkov light produced is insufficient to trigger a telescope. In principle, the collection area is large for high-energy showers, however such showers are often discounted by the distance quality cut. The collection area is also dependent on the zenith angle, thus simulations appropriate to the range of zenith angles used for observations must be used in approximating the collection area.

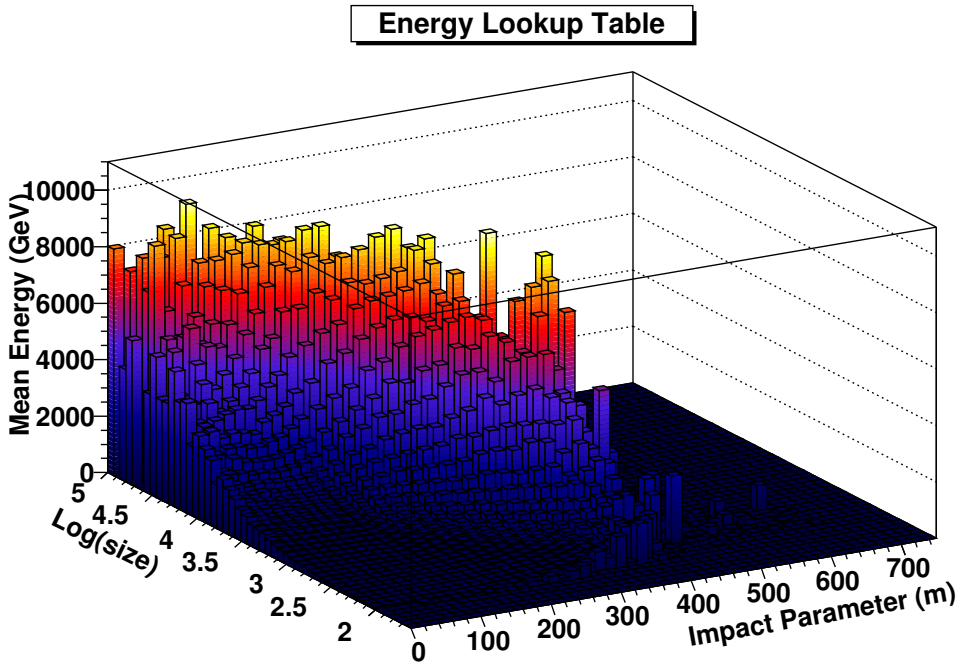

Figure 5.26: Graphical representation of the Monte-Carlo simulation derived lookup table for the energy of a gamma ray.

5.6.2 Energy Estimation

In the case of a single telescope, where an accurate measure of the impact parameter is not available, an energy estimator polynomial function is used to determine the energy of the incident particle. This function is dependent on the log of the image *size* and the parameterised distance d.

In the case of stereoscopic observations, the energy of each event is determined from the parameterised image *size* and calculated impact parameter. For each event, a lookup table generated from Monte-Carlo simulations for an appropriate zenith angle is used to determine the energy $\tilde{x}$ of a gamma ray that generates such an image *size* / impact parameter pair (see Figure 5.26). Interpolation in $\cos\Theta$ is used to cover the gaps in the discrete zenith angle simulated datasets.

5.7 Summary

The standard procedure for analysing VERITAS data has been reviewed. Particular emphasis is placed on data calibration and the preliminary analysis of FADC traces as these methods were researched and implemented as part of this thesis dissertation. Further enhancements to the analysis of FADC traces is investigated in Chapter 6. The procedures for image cleaning and parameterisation is described and the methods used for reconstructing the shower core location and origin in the field of view are outlined. Finally several background estimation and background rejection techniques are reviewed. These techniques, along with those investigated in Chapter 6 are applied to the analysis of the Crab Nebula and blazar datasets in Chapter 7.

Chapter 6

Analysis of FADC Traces

6.1 Introduction

This chapter describes a variety of techniques for analysing FADC traces, and explores mechanisms for extracting useful information from them. The Whipple 10m telescope, which was the predecessor to the VERITAS array, used QADCs rather than FADCs, thus new analysis methodologies need to be developed for the VERITAS collaboration in order to analyse FADC data. The analysis of these data, in the context of the VERITAS offline analysis software *VEGAS* , forms an integral part of this thesis dissertation.

There are many ways in which an FADC trace can be analysed. For example, the trace can be summed over a fixed window or a sliding window, or can have an assumed function fit to it; these are *trace evaluators*. Section 6.2 describes six such methods, providing theoretical background on how the evaluators are constructed. Section 6.3 deals with FADC crate jitter and an algorithm to correct it. A study to determine the optimal FADC integration window is undertaken in Section 6.4. A series of special laser calibration runs and a Crab Nebula observation run will be used to compare the pedestal, pedvars, signal-to-noise ratio, charge consistency and timing resolution achieved by the trace evaluators (Section 6.5), followed by a study of the effect of the trace evaluators on image reconstruction (Section 6.6). A study of reconstructing the low-gain FADC channel (Section 6.7) is also presented. A technique for resampling FADC traces in the time domain is introduced and used to improve the timing resolution (Section 6.8). Finally a special image parameter involving the self-consistency of FADC traces is investigated in Section 6.9 as a gamma-hadron discriminant using Monte-Carlo simulations of gamma rays and protons.

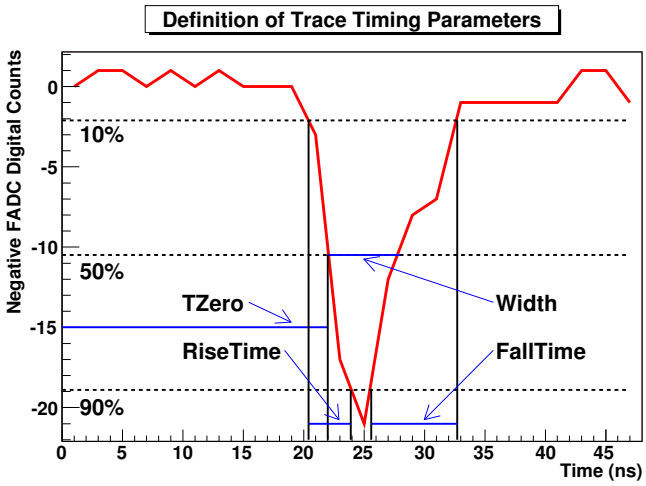

Figure 6.1: Definition of basic timing parameters that are calculated by a Trace Evaluator. The FADC trace is shown in red, with dashed black lines indicating 10%, 50% and 90% of trace maximum. The T_{zero} measurement is the time at which the trace crosses 50% of trace maximum. The risetime is the time between 10% and 90% of trace maximum, the falltime is the time between 90% and 10% of trace maximum and the width is the time between the first and second crossings of the 50% line. All actual measurements are indicated as blue lines, with the vertical black lines indicating crossing times.

Parameter	Unit
charge	Digital Counts
T_{zero}	Nanoseconds
Rise Time	Nanoseconds
Fall Time	Nanoseconds
Width	Nanoseconds
Height	Nanoseconds
Signal/Noise	none
Window Start	FADC Samples
Window Width	FADC Samples

Table 6.1: Parameters calculated by trace-evaluation algorithms.

6.2 Trace Evaluators

A trace evaluator is an algorithm which operates on an FADC trace and returns standard parameters such as the charge, rise time, fall time and width (see Table 6.1 and Figure 6.1). In this study, six trace evaluators will be examined. They are the *simple-window*, the *dynamic-window*, *linear-interpolation*, *trace fit*, *matched-filter* and *timing-gradient* trace evaluators. A simple graphic contrasting some of the methods is shown in Figure 6.2.

6.2.1 Simple Window

The *simple-window* trace evaluator use a fixed window for charge integration (Figure 6.2(a)). Corrections to the location of this window are applied using the T_{offset} correction (Section 5.1.2) on a channel-by-channel basis, and the crate jitter correction (Section 6.3) on an event by event basis. Timing parameters are only evaluated to the nearest FADC sample, with no interpolation between points. Thus, the *simple-window* trace evaluator is good for standard data analysis, so long as the location of the Cherenkov pulse in the FADC window is well established and accurate timing measurements are not required.

6.2.2 Dynamic Window

Due to the lateral development of air showers, the Cherenkov pulse arrival time may not be constant across the image. The result of this is that a fixed window may miss some of the charge for pulses that arrive late, resulting in a signal-to-noise ratio for certain channels that is lower than it could have been. Note that in this case, the signal-to-noise ratio is defined as the ratio of integrated charge over pedvar - this is the quantity that is used in image cleaning. The simplest way to overcome this is to use a window that slides across the FADC trace, and select that window which returns the maximum signal-to-noise ratio (Figure 6.2(b)). Similarly to the *simple-window* trace evaluator, the timing parameters are only calculated to the nearest FADC sample by the *dynamic-window* trace evaluator.

6.2.3 Linear Interpolation

Linear interpolation is a commonly used technique to determine a point y_n at x_n between $(x_1, y_1), (x_2, y_2)$ such that $x_1 < x_n < x_2$ (Figure 6.2(c)). In this case the y values are simply FADC samples. Using integration with the *linear-interpolation* trace evaluator, charge is calculated according to

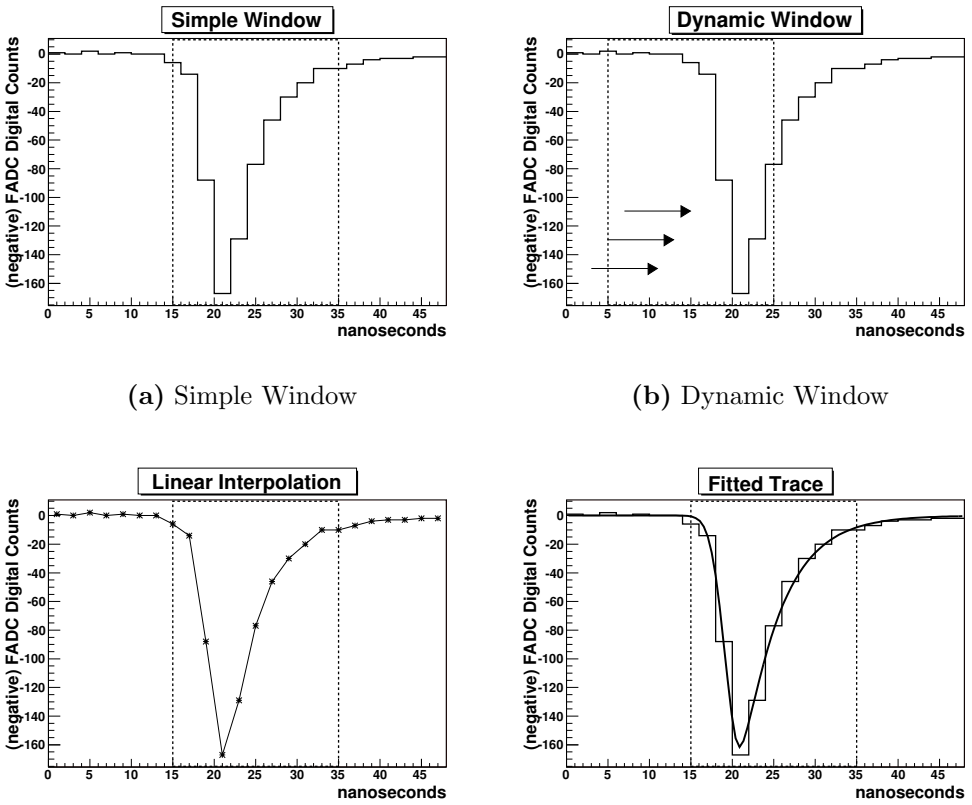

(a) Simple Window

(b) Dynamic Window

(c) Linear Interpolation

(d) Trace Fit

Figure 6.2: Figure comparing some of the Trace Evaluators. The *simple window* trace evaluator is shown in Figure 6.2(a), it places a fixed integration window over the FADC trace and calculates timing parameters to the nearest FADC sample. The *dynamic-window* trace evaluator is shown in Figure 6.2(b), it places a sliding integration window over the FADC trace and calculates timing parameters to the nearest FADC sample. The *linear-interpolation* trace evaluator is shown in Figure 6.2(c), it interpolates between samples to improve the accuracy of the timing calculation. The *trace-fit* trace evaluator is shown in Figure 6.2(c), it fits an assumed function to the trace to improve the accuracy of the timing calculation.

$$Q = \sum_{i=start}^{i=end-1} \left(Q(i) + \frac{Q(i+1) - Q(i)}{2} \right) + Q(end) \tag{6.1}$$

where $Q(i)$ is the charge in the i^{th} sample, and $Q(end)$ is the charge in the last sample. Calculation of the timing parameters requires calculating x_n for a given y_n, according to

$$x_n = x_1 + \frac{y_n - y_1}{m} \tag{6.2}$$

where m is the slope of the line between (x_1, y_1) and (x_2, y_2). For instance the parameter $\mathrm{T_{zero}}$ (corresponding to x_n in this example) is calculated by finding the pair $(x_1, y_1), (x_2, y_2)$ such that $y_1 < y_n < y_2$, where $y_n = Q/2$ and Q is the maximum height of the trace (after pedestal subtraction).

6.2.4 Trace Fit

There are many functions which can be used to fit an FADC trace, such as a Landau function or high-order polynomial. In this study an asymmetric Gaussian function, motivated by the typical shape of FADC traces, is used. The function is given by

$$q(t) = \begin{cases} q_0 \exp \frac{-(t-t_0)^2}{\sigma^2} & \text{for} \quad t \leq t_0 \\ \\ q_0 \exp \frac{-(t-t_0)^2}{\sigma^2 + \alpha(t-t_0)} & \text{for} \quad t > t_0 \end{cases} \tag{6.3}$$

where $q(t)$ is the sample charge, q_0 and t_0 are the charge and time of the trace maximum, σ is the width of the first part of the trace, and α is a parameter describing the shape of the trace beyond t_0. There is no *a priori* reason for selecting this function, however it does give a relatively good quality fit for large FADC traces such as that shown in Figure 6.2(d).

6.2.5 Matched Filter

A *matched filter* is so called because its shape is defined by the expected form of the received data (Litwin, 2001). The *matched filter*'s pulse shape is a time-reversed version of the expected pulse shape. Thus for an expected pulse shape $h(t)$, the ideal *matched-filter* $h_m(t)$ is

$$h_m(t) = h(T - t) \tag{6.4}$$

for $0 \leq t \leq T$ where T corresponds to the end of the trace. The output from a filtering application is calculated by a convolution of the input with the filter

$$y(t) = \int_0^T r(t)h_m(T-t)\,dt \tag{6.5}$$

where $y(t)$ is the output. Inserting the *matched filter* in equation 6.4 into equation 6.5 gives

$$y(t) = \int_0^T r(t)h(T-(T-t))\,dt \tag{6.6}$$

which reduces to

$$y(t) = \int_0^T r(t)h(t)\,dt \tag{6.7}$$

This is the cross correlation of $r(t)$ and $h(t)$ with zero lag.

In this case, the data which are to be filtered are that recorded by the FADC system. In order to construct the matched filter a standard laser calibration run is used. For each event, and for each channel, a subset of the laser pulse is extracted, and aligned relative to some predetermined point. This extracted pulse is summed for all events for each channel. The summed trace is normalised (Figure 6.3), and an FFT applied to it. The filter is applied to the FADC data by multiplying the FFT of the FADC trace (denoted $S(\omega)$) with the conjugate of the filter, $\overline{H}(\omega)$, and then applying an inverse Fourier transform

$$y(t) = F^{-1}\left[S(\omega) \times \overline{H}(\omega)\right] \tag{6.8}$$

which yields a cross correlation function $y(t)$. The maximum of the cross correlation is proportional to the integrated charge of the FADC trace, where the constant of proportionality is related to the integration window size. In order to establish the constant, a series of special laser calibration runs are taken with continuously increasing laser attenuation. The integrated charge as measured using the *dynamic-window* trace evaluator is compared to the output of the *matched-filter* trace evaluator and used to establish the constant. Figure 6.4 shows a plot of the average matched filter maximum correlation versus the average integrated charge for a single channel for 10 attenuation levels. A simple linear fit is applied to the data and the slope used as the constant of proportionality. This slope gives the *ratio* between the maximum correlation found by the matched filter and the charge calculated by the *dynamic-window* trace evaluator. The distribution of these ratios for

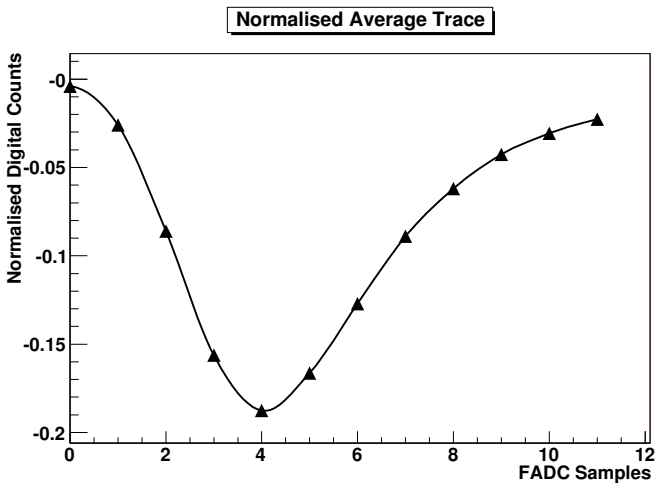

Figure 6.3: Averaged and normalised FADC trace for a single channel used in the creation of the matched filter. The fit line is only to guide the eye.

Telescopes 1 and 2 is shown in Figure 6.5. It is interesting to note that there is a clear systematic difference between the *matched-filter* ratios calculated for Telescope 1 and Telescope 2. It is difficult to understand this difference, but could be caused by factors such as different laser pulse shape or different hardware components in the camera or data acquisition system. Regardless of the reason for the discrepancy, it emphasises the need for each channel to be individually calibrated, rather than relying on a global average ratio.

When analysing data, the charge from a trace is derived by applying the *matched-filter* trace evaluator, and multiplying the output by the appropriate ratio for that channel. The arrival time is determined by the location of the maximum of the cross correlation - however, this corresponds not to the 50% of trace maximum as in the T_{zero} definition, but to the location of the trace maximum. Thus, the arrival time can only be determined to the nearest FADC sample.

6.2.6 Image Timing Gradient

One of the interesting features of data taken with FADCs is the ability to determine the arrival time of the Cherenkov pulse in each channel. In this section, it will be shown how the *timing gradient* of the shower image in the camera can be characterised, and used to determine the optimal location of the integration window.

The timing gradient parameter can be interpreted in terms of the longi-

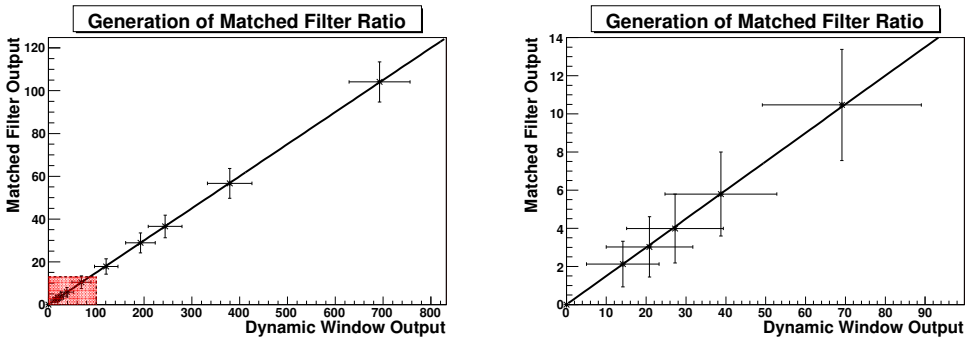

(a) Wide View **(b)** Narrow View

Figure 6.4: Left: Linear fit of the output of the *dynamic-window* trace evaluator and the raw *matched-filter* trace evaluator. Each data point is computed by fitting a Gaussian to the charge distribution for each channel. The Gaussian width is indicated by the horizontal and vertical bars (the true errors would be too small to see on the plot). The slope of this line is used to calibrate the output of the matched filter to produce a charge in digital counts. Ten laser runs were used to produce a calibration plot like this for every channel in each telescope. Right: Same plot as the left, but zoomed into the red shaded region of the left plot.

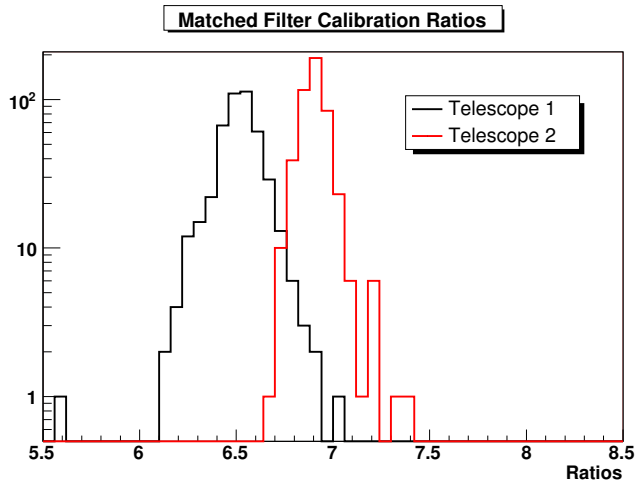

Figure 6.5: Distribution of *matched-filter* calibration ratios for Telescopes 1 and 2.

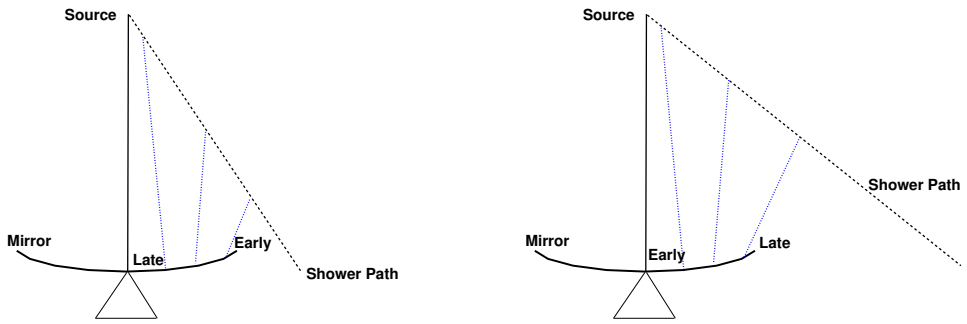

(a) Small Impact Parameter **(b)** Large Impact Parameter

Figure 6.6: This figure demonstrates the sign of the timing gradient for showers with a small and large impact parameter. For showers with a small impact parameter (left), Cherenkov photons from the bottom of the shower arrive earliest as the speed of the emitting particles dominates the distance traveled by the Cherenkov photons. For showers with a large impact parameter (right), Cherenkov photons from the bottom of the shower arrive later as the distance traveled by the Cherenkov photons dominates the speed of the emitting particles.

tudinal development of the shower and its relation to the angle of the shower relative to the telescope. Depending on the shower angle, the Cherenkov radiation from the bottom of the shower can reach the telescope before Cherenkov radiation from the top of the shower, since the particles emitting the Cherenkov radiation are traveling faster than the Cherenkov radiation emitted at the top of the shower. Thus for showers with a relatively small impact parameter, a negative timing gradient can be expected (ie the shower appears to move towards the center of the camera, see Figure 6.6(a)). However, for showers with a large impact parameter (see Figure 6.6(b)), the timing gradient is reversed as the extra distance traveled by the Cherenkov photons at the bottom of the shower compensates for the difference in speeds (Heß et al. (1999)).

Figure 6.7 shows the Cherenkov pulse arrival times of all channels on a camera face of an event showing a significant timing profile. The *timing gradient* is calculated using a linear fit of the arrival time as a function of the PMT position along the major axis of the image (Figure 6.8).

Figure 6.9 illustrates the calculation of the distance along the image axis (red line in figure, denoted A) from the centroid to the intersection between the image axis and a perpendicular line from the image axis to the PMT.

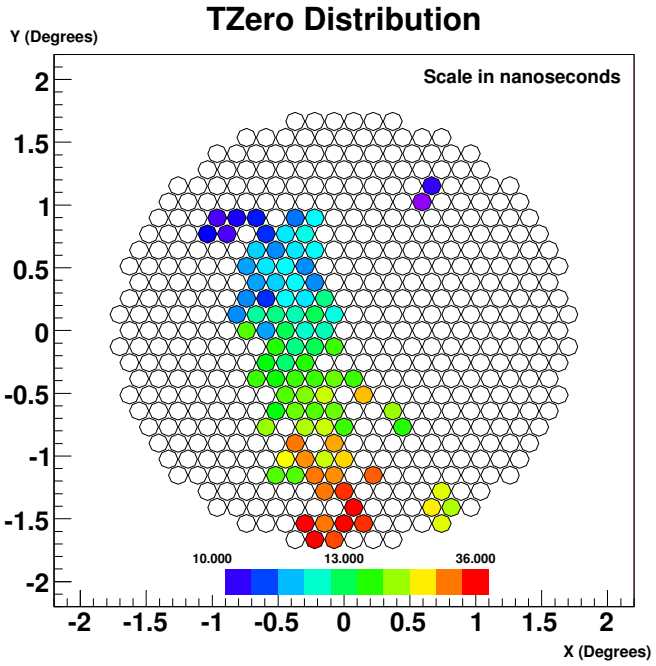

Figure 6.7: Distribution of arrival times for a cosmic ray event plotted on a camera display

The distance in the x/y plane from the PMT to the image centroid is given by

$$\begin{aligned} x &= x_{\mathrm{PMT}} - x_{\mathrm{centroid}} \\ y &= y_{\mathrm{PMT}} - y_{\mathrm{centroid}} \end{aligned} \tag{6.9}$$

where x_{PMT} and x_{centroid} are the x coordinate of the PMT and image centroid respectively (and similarly for y). To aid the calculation, A, x and y are split according to

$$\begin{aligned} A &= A_1 + A_2 \\ x &= x_1 + x_2 \\ y &= y_1 + y_2 \end{aligned} \tag{6.10}$$

The angle between the image axis and the camera x plane is given by ϕ. Prior to the calculation, x, y and ϕ are known, and A is sought. Using simple trigonometric rules, A_1 is found by

$$A_1 = \frac{y}{\sin\phi} \tag{6.11}$$

and x_2 can be found from

$$x_2 = A_1 \cos\phi \tag{6.12}$$

thus

$$x_1 = x - A_1 \cos\phi \tag{6.13}$$

now A_2 can be found from

$$A_2 = x_1 \cos\phi \tag{6.14}$$

giving

$$A = A_1 + A_2 = \frac{y}{\sin\phi} + x_1 \cos\phi \tag{6.15}$$

Expanding x_1 gives

$$A = \frac{y}{\sin\phi} + (x - A_1 \cos\phi)\cos\phi \tag{6.16}$$

expanding A_1 gives

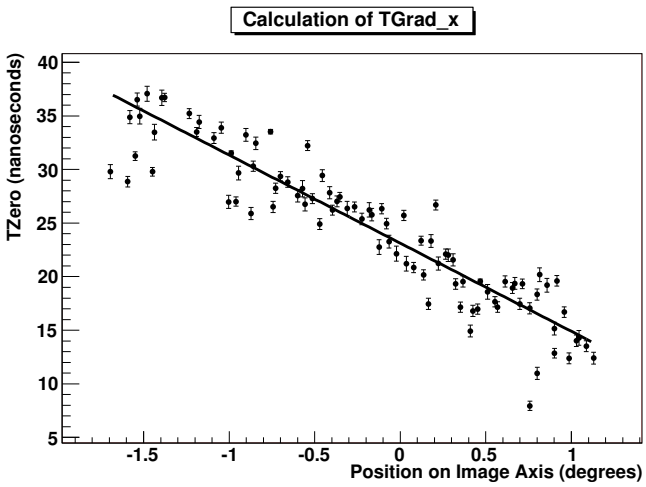

Figure 6.8: The *timing gradient* TGrad_x is determined using a simple linear fit of the Cherenkov pulse arrival time $\mathrm{T}_{\mathrm{zero}}$, against the PMT position along the primary image axis. The plot shown is the one used to calculate TGrad_x for the large cosmic-ray image in Figure 6.7.

$$A = \frac{y}{\sin\phi} + \left(x - \frac{y}{\sin\phi}\cos\phi\right)\cos\phi \tag{6.17}$$

which reduces to

$$A = \frac{y}{\sin\phi}\left(1 - \cos\phi^2\right) + x\cos\phi \tag{6.18}$$

and finally

$$A = y\sin\phi + x\cos\phi \tag{6.19}$$

A straight line is fit to the data in Figure 6.8, where the slope gives the *timing gradient* TGrad_x and the intercept gives TInt_x. In order to locate the integration window using the timing gradient, the following scheme is implemented (adopted from Holder (2005)).

- Calculate PMT charges using standard integration techniques with a large fixed window
- Apply standard Picture/Boundary cleaning
- Locate the image centroid and calculate ϕ

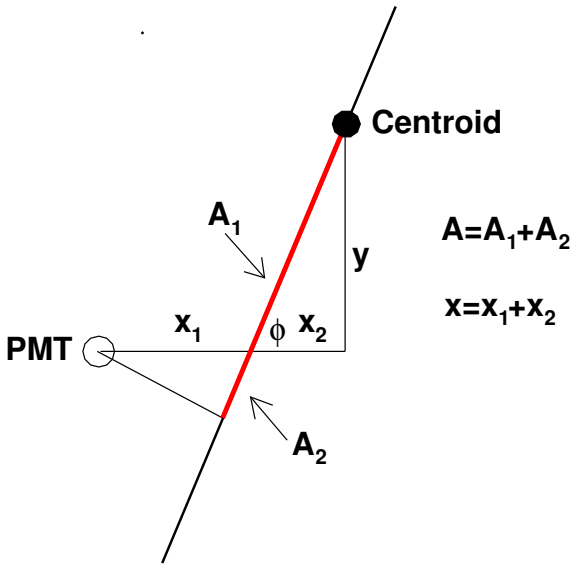

Figure 6.9: The *timing gradient* is given by the relationship between the Cherenkov pulse arrival time, and the position of the PMT along the primary image axis. The position of the PMT can be calculated using this diagram, where the primary image axis is the slanted black line, and the distance sought is overlaid in red. The angle ϕ is the angle between the primary image axis and the x-axis of the camera. The camera center and axes are not shown in this figure, rather they are replaced with the parallel axes (x,y) defined by the PMT and centroid location.

- Use the pixels that passed cleaning to calculate the timing gradient
- Use the timing gradient to set new channel-specific integration windows
- Calculate the PMT charges using the standard integration techniques with the channel-specific window

The start of the integration window for each channel is calculated according to

$$\mathrm{Win} = x \times \mathrm{TGrad}_x + \mathrm{TInt}_x \tag{6.20}$$

where as before x is given by the distance from the image centroid to the PMT. The crate jitter (Section 6.3) and $\mathrm{T}_{\mathrm{offset}}$ corrections made to the $\mathrm{T}_{\mathrm{zero}}$ calculation must be removed when the window start location is calculated as they correct the arrival time of the pulse rather than the actual location of the Cherenkov pulse in the window. The effect of integration window placement on the calculated charge using the *timing gradient* parameter is demonstrated in Figure 6.10. The measured *length* of the shower is far larger, and is a more accurate representation of the longitudinal development of the shower.

Monte-Carlo simulations of gamma-ray initiated showers are used here to study the timing gradient and confirm the understanding of the effect of shower geometry. The Monte-Carlo simulated dataset described in Section 7.2 is used for this study. The timing gradient for gamma rays is shown in Figure 6.11. The gamma-ray simulations all originate in the center of the camera, thus exhibiting the expected turnover in timing gradient.

The timing gradient has been shown by Holder (2005) to be a useful background discriminant for *single* telescope data, where the analysis energy threshold is limited by the local muon background. Images of the Cherenkov light from local muons are not expected to exhibit the timing gradient that the Cherenkov light from an extensive air shower would, as the Cherenkov photons from a local muon arrive isochronously across the camera. In the case of stereoscopic observations, the muon background is virtually eliminated, rendering cuts on the muon background such as length/size and the timing gradient cut inconsequential.

6.3 Crate Jitter

Minor clocking errors can occur in the FADC crates which causes each crate to read out the FADC boards at a slightly different time (note that the FADC boards on a given crate are still in sync - but the four crates can be slightly

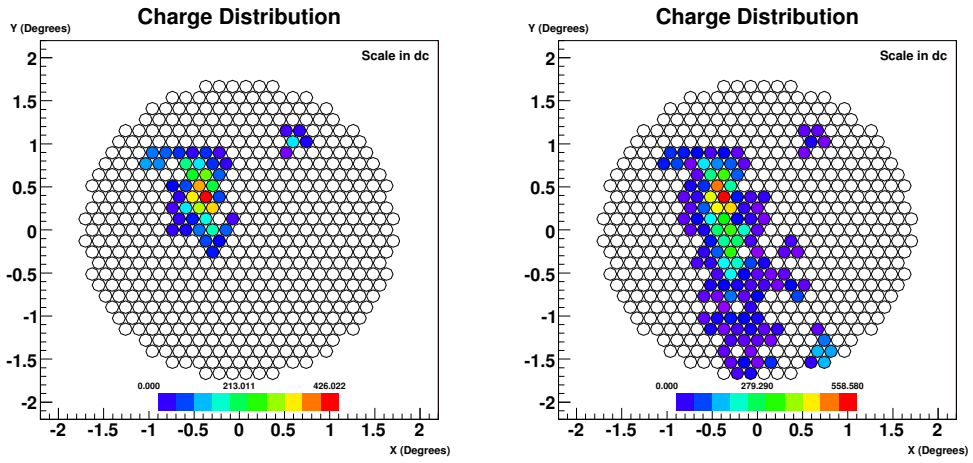

(a) Simple Window

(b) Using TGrad_x

Figure 6.10: These figures contrast the integrated charge as calculated using a *simple-window* trace evaluator, and using a window set according to the *timing gradient* trace evaluator. Standard cleaning is applied to all channels in both images. It is clear from this example, that the use of the *timing gradient* to set the integration window can have a profound effect on the calculated charge.

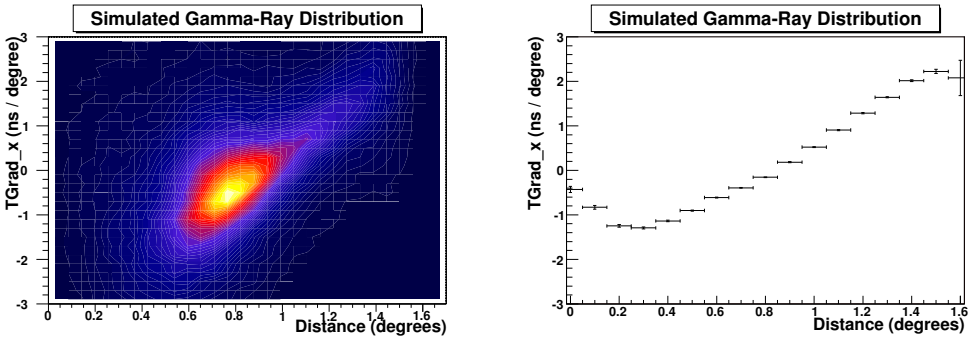

(a) **(b)**

Figure 6.11: This figure demonstrates the distribution of the timing gradient as a function of the *dist* parameter. The simulated gamma rays originate at the center of the field of view of the camera. For gamma-ray showers with small impact parameters (small values of dist), the timing gradient is negative as light from the bottom of the shower arrives first. For gamma-ray showers with large impact parameters (large values of dist), the timing gradient is positive as light from the bottom of the shower arrives later.

out of sync). This has the effect of adding a jitter to the apparent arrival time of the pulse in the FADC window. Such a jitter can be detected by piping an asynchronous copy of the Level 2 trigger signal into a spare channel in each FADC crate. The Level 2 trigger is a NIM pulse, and appears in the data stream as a large square wave (Figure 6.12). A distribution of the arrival times of the L2 pulses in the four FADC crates is shown in Figure 6.13 for one telescope for a single test run. The jitter occurrence is clear from these distributions. The difference in the arrival time of the Level 2 Trigger can be measured and used to correct the integration window of the FADC pulse in each crate and the measured arrival time of the FADC pulse in each channel.

In the algorithm used to measure the crate jitter, the arrival time of the L2 pulse for every event is measured in each crate and compared to the arrival time of the L2 pulse in the first crate. Thus the first crate is used as a reference and all other crates are aligned relative to it. However this reference itself is not fixed event to event and is dependent on the time at which crate 1 stops. It also means that no correction is applied to the channels in crate 1. However, for the calculation of the T_{offset} correction, this is irrelevant as the absolute time of the event is given by the average arrival time of all channels, and the contribution to the T_{offset} distribution is calculated relative

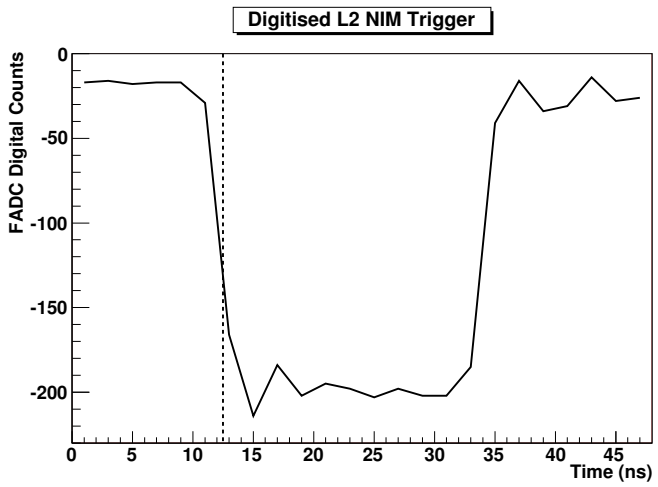

Figure 6.12: Digitised L2 NIM pulse. A copy of the Level 2 trigger pulse is piped into each FADC crate and used to ensure crate synchronisation in the offline analysis.

to that mean. The effect of the crate jitter correction on the calculation of timing resolution is shown in Figure 6.14. It can be seen that the correction improves the timing resolution by approximately 0.2 ns (note that tools for measuring and comparing the timing resolution will be introduced in the coming sections).

6.4 Optimisation of Integration Window Parameters

One of the key goals in the development of IACT telescopes is to lower the energy threshold at which events can be accurately reconstructed. One of the mechanisms for achieving this is the optimisation of the signal-to-noise ratio of the raw data. With FADC data, the signal-to-noise ratio can be optimised by varying the location and size of the integration window. With the *simple-window* trace evaluator, a laser run and a standard Crab Nebula observation run are used to compare the achieved signal-to-noise ratio as a function of window location. For each data run, a first pass is used to determine the *average* FADC trace arrival time for each camera. Two laser runs are used initially for this study, one with large FADC pulses, and one with small pulses close to the trigger threshold. The window start position is determined using a scaling factor ω such that a fraction ω of the window

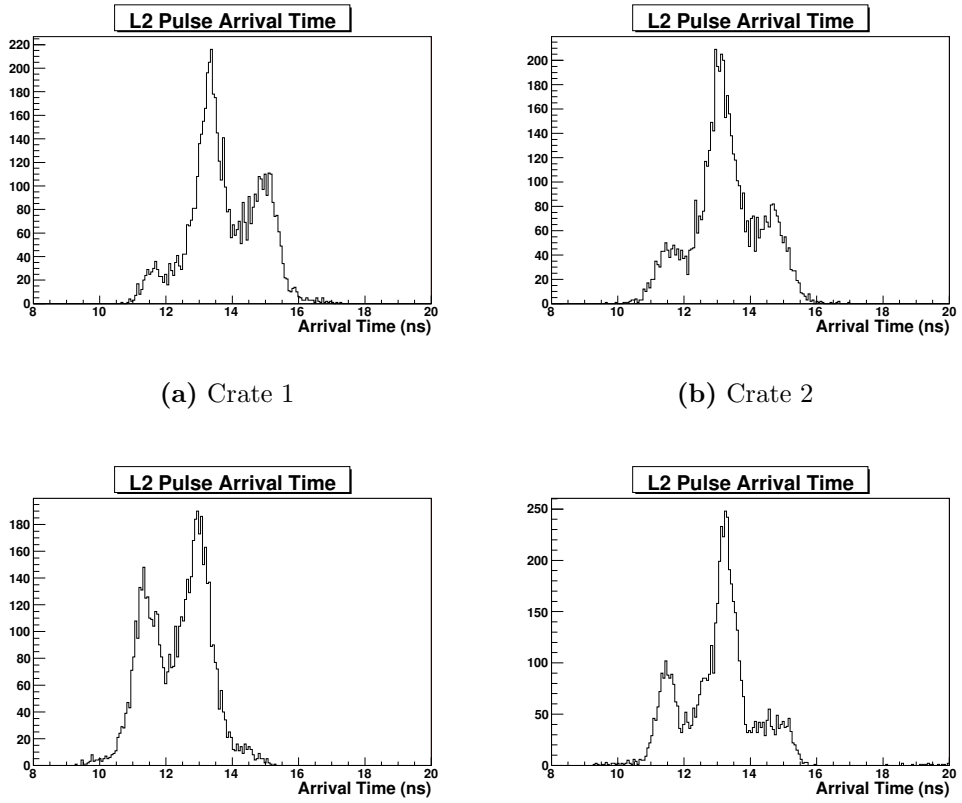

(a) Crate 1 **(b)** Crate 2

(c) Crate 3 **(d)** Crate 4

Figure 6.13: Uncorrected arrival times of the level 2 trigger pulses as recorded in the four FADC crates of one telescope. The timing jitter caused by the FADC clocking errors is evident.

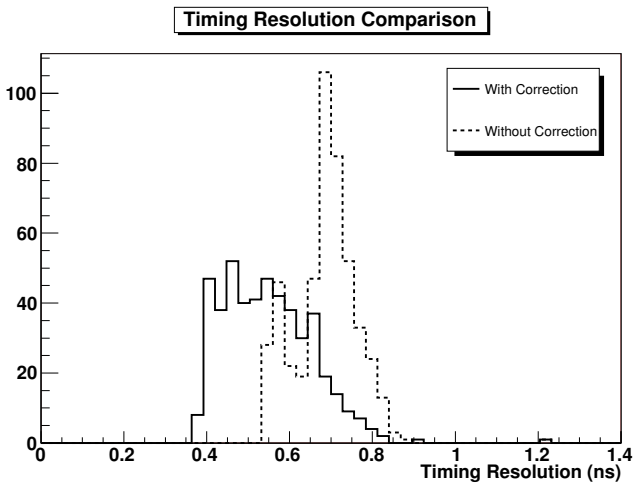

Figure 6.14: Distribution of timing resolution for each channel before and after the application of the crate jitter correction.

is located behind the average FADC T_{zero} position

$$win_{start} = \overline{T}_{zero} - \omega \times win_{width} \tag{6.21}$$

where win_{start} is the FADC window integration start location, $\overline{T}_{zero}$ is the average T_{zero} across the camera, ω is in the range $0 \rightarrow 1$ and win_{width} is the width of the FADC window. Note that the T_{offset} timing corrections as described in Section 5.1.2 and the crate jitter timing corrections as described in Section 6.3 are applied after this calculation.

For the *simple-window* trace evaluator, the signal-to-noise ratio as a function of window size, for a value of $\omega = 0.3$ is shown in Figure 6.15 for the high-intensity and low-intensity laser runs. Figure 6.16 shows the signal-to-noise ratio as a function of window size and ω in the range $0.05 \leq \omega \leq 0.95$ with step sizes of $\omega = 0.05$. This diagram indicates that the optimal combination for data without a timing gradient is $\omega = 0.05$ and window width of 6 for large pulses and 8 for small pulses. For the *dynamic-window* trace evaluator, the choice of the trace window start location is determined on a trace by trace basis, and disregards all timing corrections. The signal-to-noise ratio as a function of window size is shown for the same high-intensity and low-intensity laser runs in Figure 6.17. As expected, the signal-to-noise ratio achieved by the *dynamic-window* trace evaluator exceeds that achieved by the *simple-window* trace evaluator. However, the optimal window size for the *dynamic-window* trace evaluator is significantly smaller than the optimal window for the *simple-window* trace evaluator.

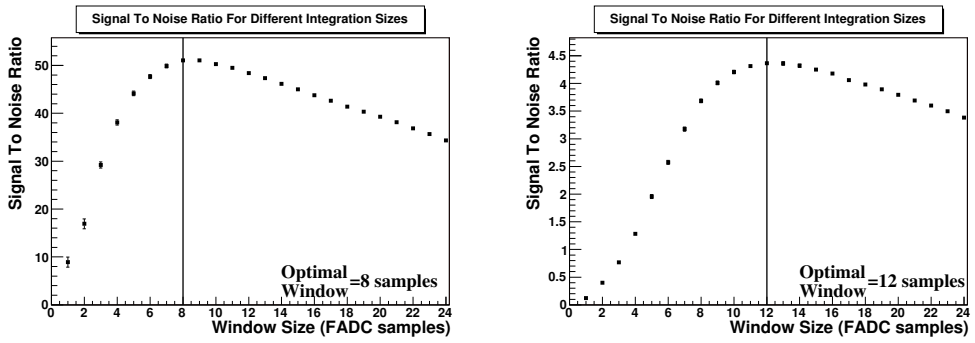

(a) Large Laser Pulse **(b)** Small Laser Pulse

Figure 6.15: Graph of the signal-to-noise ratio as a function of window size for two laser runs with large and small laser pulses. The window start is located such that 30% of the window is *before* the average T_{zero} for the camera (with T_{offset} and crate timing corrections applied).

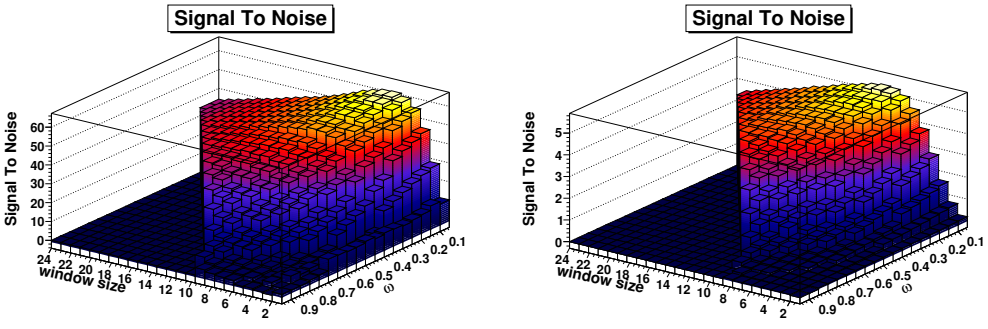

(a) Large Laser Pulse **(b)** Small Laser Pulse

Figure 6.16: Graph of the signal-to-noise ratio as a function of window size and ω for two laser runs with large and small laser pulses. The window start is located such that a fraction ω of the window is *before* the average T_{zero} for the camera (with inter-channel and crate timing corrections applied). For certain combination of ω and window size, the integration window cannot be accommodated within the confines of the FADC readout.

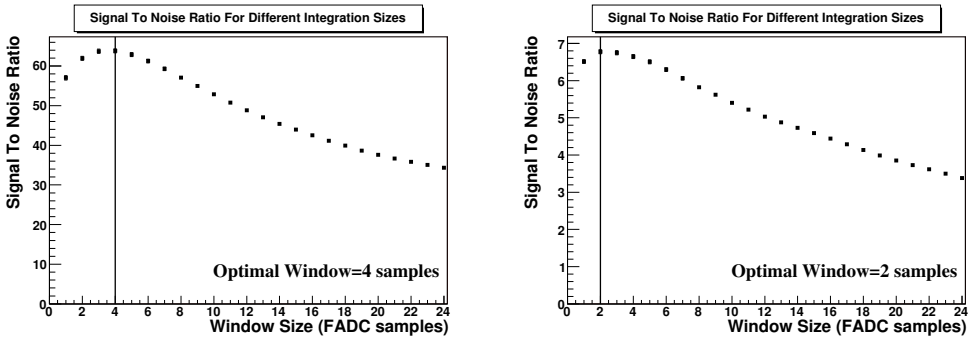

(a) Large Laser Pulse

(b) Small Laser Pulse

Figure 6.17: Graph of the signal-to-noise ratio as a function of window size for two laser runs with large and small laser pulses. The signal-to-noise ratio is evaluated using the *dynamic window* trace evaluator.

6.5 Comparisons

In this section the trace evaluators which have been described will be compared. These comparisons will be done in terms of pedestals & pedvars (Section 6.5.1), charge resolution (Section 6.5.2), signal-to-noise ratio (Section 6.5.3) and timing resolution (Section 6.5.4).

6.5.1 Pedestal and Pedvars

The first step in understanding the behaviour of each trace evaluator is to examine the calculation of charge for pedestal events (Section 5.1.1). Some of the special tools usually invoked in pedestal calculation, such as the application of multiple integration windows to a single trace (see Figure 5.1) and the randomisation of the window start are disabled for this test. The reason for this is primarily due to the *dynamic-window* trace evaluator, which would disregard the intended start position of the pedestal calculator algorithm and return the maximum possible charge. Although only the *dynamic-window* and *matched-filter* trace evaluators present this problem, the same settings are used for all evaluators to ensure consistency.

A standard Crab Nebula data run is used for the comparisons, rather than a laser run as was used for the window optimisation. The reason for this is that the Crab Nebula dataset corresponds to normal observing conditions on a region of the sky with noise variations that are frequently seen

during standard data-taking, whereas the laser runs are usually taken with the telescopes pointing at specially chosen dark regions of the sky. The series of sub-figures in Figure 6.18 shows the results of the comparisons. In all sub-figures, the distribution of pedestal and pedvars for all channels for both telescope are shown, with the *simple-window* trace evaluator show in black for comparison. The distribution of pedestals and pedvar for the *dynamic-window* trace evaluator is slightly shifted to the right. This is to be expected as this trace evaluator will always sum the largest fluctuation in the FADC trace. The *linear-interpolation* trace evaluator has very similar distributions of pedestals and pedvars to the *simple-window* trace evaluator. This is to be expected as the same window is used for each, and it would be unexpected for the linear interpolator to introduce any noise into the calculation. The *trace-fit* trace evaluator has a very similar pedestal distribution, although the pedvar distribution is shifted to the right, indicating the introduction of noise with this evaluator. This result is difficult to interpret, but could be the result of the fit function being centered on a fluctuation and overestimating the charge for certain traces. This could happen sufficiently rarely to not affect the mean of each channel's pedestal distribution (and thus not affecting the pedestal comparison), but could result in each channel's pedestal distribution being wider (thus shifting the pedvar distribution to the right). The pedestal distribution calculated by the *matched-filter* trace evaluator is essentially meaningless, as the *matched-filter* attempts to seek a portion of the trace that resembles a laser pulse - however in the case of pedestal events there are no such pulses present. It is curious that the pedvar distributions match so well, however it indicates that the pedvar as calculated by the *matched-filter* trace evaluator can be used in calculating the signal-to-noise ratio.

6.5.2 Charge Resolution and Signal-to-Noise Ratio with Laser Data

In order to compare the charge resolution of the trace evaluators, a series of laser runs is taken with progressively increasing attenuation. For a given laser shot, the trace evaluator which calculates the most consistent charge is superior. This measure is taken by applying a Gaussian fit to the charge distribution, and calculating the reduced-χ^2 value of the fit. For illustrative purposes, an example of a charge distribution with a Gaussian fit applied is shown in Figure 6.19. Such a fit is applied to all channels in the telescope for a given laser run, and a distribution of reduced-χ^2 values is shown in Figure 6.20. Whereas the reduced-χ^2 gives an indication of the quality of the fit,

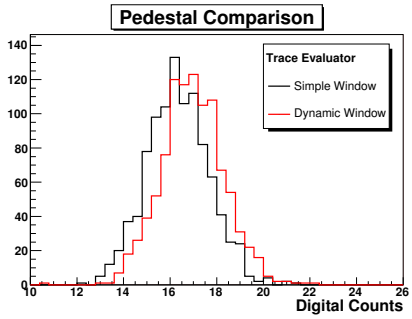

(a) Dynamic Window Pedestal

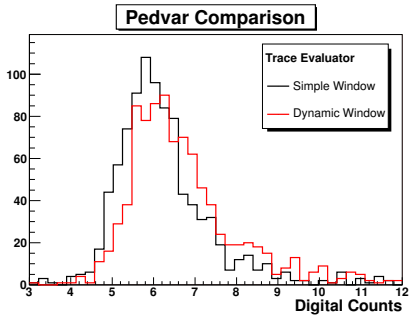

(b) Dynamic Window Pedvar

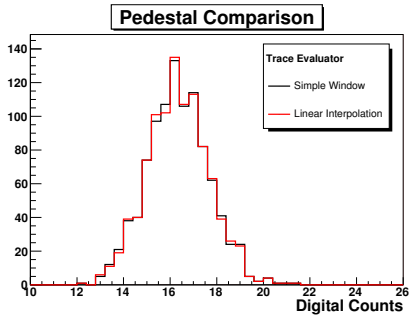

(c) Linear Interpolation Pedestal

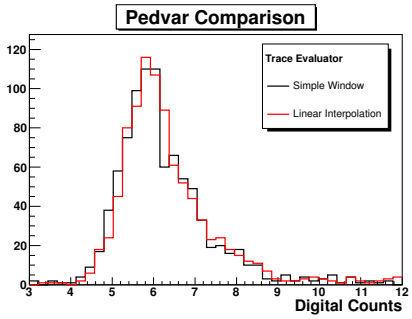

(d) Linear Interpolation Pedvar

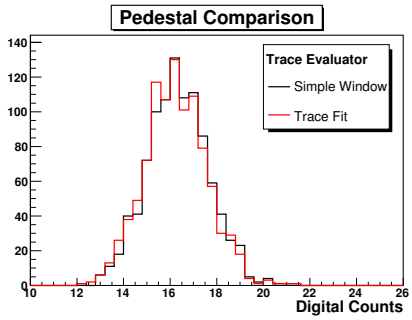

(e) Trace Fit Pedestal

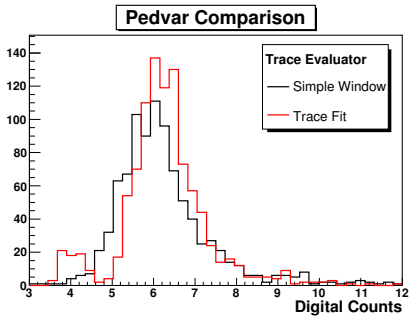

(f) Trace Fit Pedvar

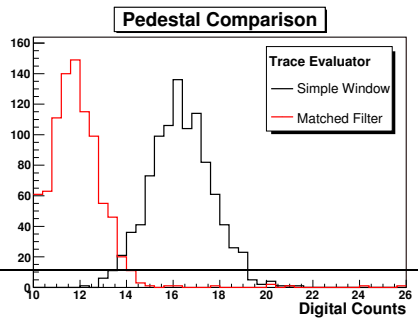

(g) Matched Filter Pedestal

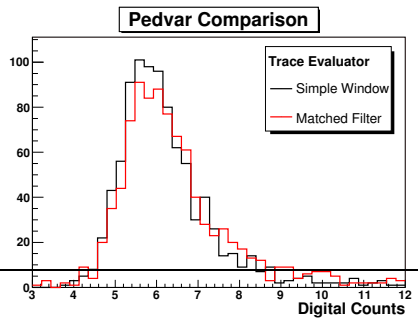

(h) Matched Filter Pedvar

Figure 6.18: Comparisons of pedestal and pedvars- see Section 6.5.1 for discussion.

the charge resolution is given by the Gaussian width (Figure 6.21).

The charge resolution is evaluated for the series of laser runs. This set of runs comprises nine two-telescope runs, with progressively decreasing laser attenuation. Due to differing laser fiber lengths and attenuation settings, the laser strength is not the same in each telescope - thus the charge resolution measurements can be made for 18 separate laser intensities. For a given laser run and telescope, the average laser intensity is calculated using the *dynamic-window* trace evaluator. This gives a good base-line measurement of the integrated charge independent of pulse location and timing corrections. The average width of a Gaussian fit as a function of the average charge is shown in Figure 6.22 and the average reduced-χ^2 as a function of the average charge is shown in Figure 6.23.

In order to perform a comparison of the trace evaluators, distributions of the Gaussian width and reduced-χ^2 for the *dynamic-window*, *linear-interpolation*, *matched-filter* and *trace-fit* trace evaluators are generated. As was the case with the pedestal distribution, for this comparison the *simple-window* trace evaluator distributions are used as a baseline comparison. In order to clearly see the difference between the *simple-window* trace evaluator distribution and the other distributions, it is easiest to plot the *difference* in the distributions. Thus Figure 6.24 shows the difference between the *simple-window* trace evaluator distribution and the other distributions for the Gaussian width and reduced-χ^2 on a fixed vertical scale. The *dynamic-window* and *matched-filter* trace evaluators show significantly narrower Gaussian widths than the *simple-window* trace evaluator. This is to be expected as their intrinsic dynamic nature ignores any remaining timing jitter that the *simple-window* and *trace-fit* evaluators are susceptible to. The *trace-fit* trace evaluator has a very large Gaussian width for small pulses, indicating that the *trace-fit* evaluator may not be good for small events. All trace evaluators have very similar reduced-χ^2 for large pulses, however there are small deviations for small pulses.

The same laser runs are used to examine the signal-to-noise ratio as a function of pulse size. For the *simple-window* trace evaluator, the signal-to-noise ratio as a function of pulse size is shown in Figure 6.25. As before, for comparison, the signal-to-noise ratio evaluated using the different trace evaluators is compared by subtracting each distribution from the distribution for the *simple-window* trace evaluator. The results, shown in Figure 6.26, indicate that the *dynamic window* and *trace-fit* trace evaluators offer superior signal-to-noise ratios for large pulses. There is no significant difference for the *linear-interpolation* and *matched-filter* trace evaluators.

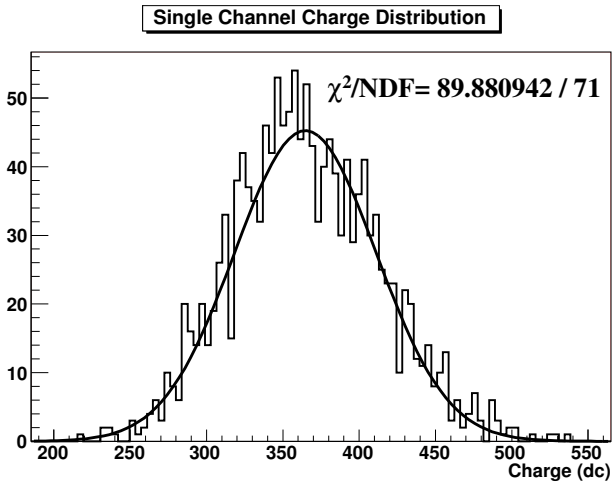

Figure 6.19: The charge resolution is determined by fitting a Gaussian function to the charge distribution and recording the χ^2/NDF for the fit. This is the charge distribution as measured using the *simple-window* trace evaluator.

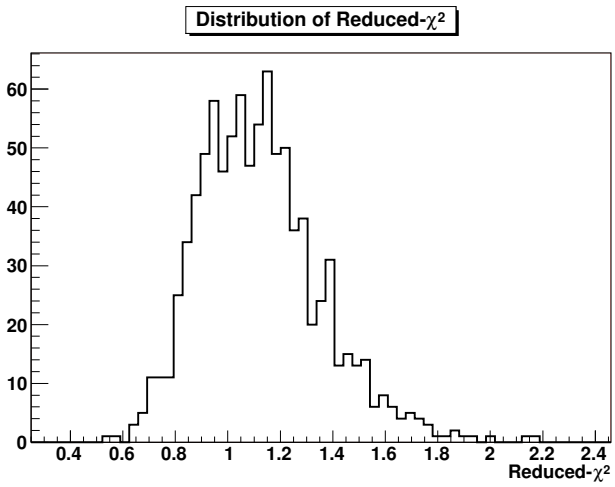

Figure 6.20: Distribution of reduced-χ^2 for a Gaussian fit to the charge distributions for a single laser run for the *simple window* trace evaluator.

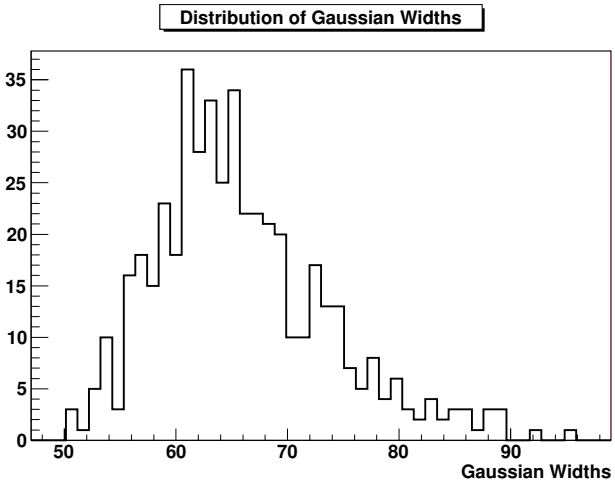

Figure 6.21: Distribution of Gaussian widths of the charge distributions for a single laser run for the *simple-window* trace evaluator.

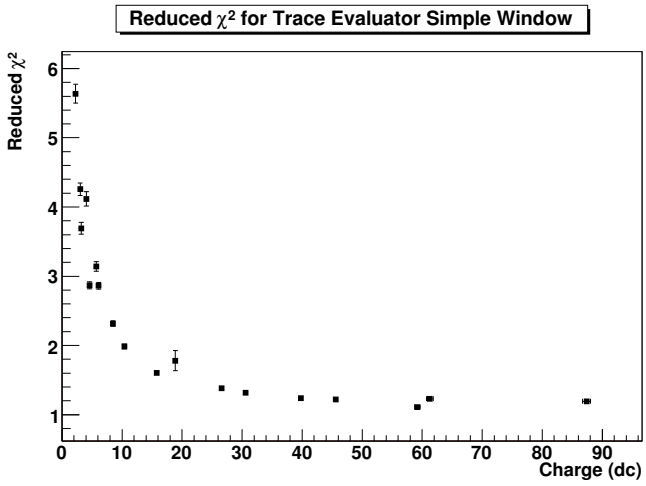

Figure 6.22: Average reduced-χ^2 of a Gaussian fit to the charge distribution of all channels for a range of laser intensities.

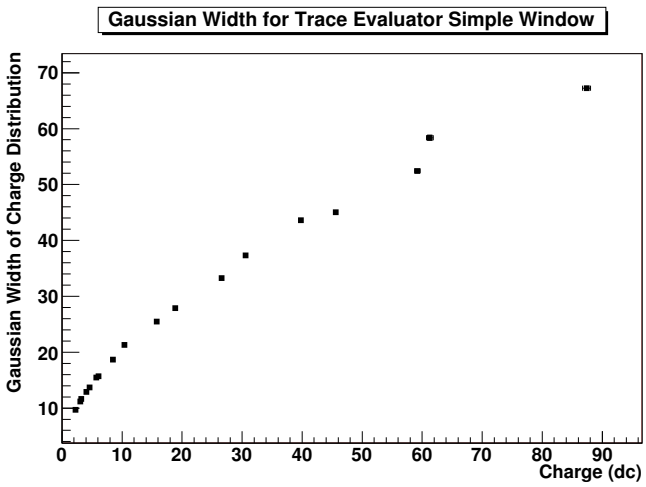

Figure 6.23: Average Gaussian width of the charge distribution of all channels for a range of laser intensities.

6.5.3 Comparison of Charge and Signal-to-Noise Ratio with Crab Nebula Data

Although the laser runs give an excellent controlled test of the performance of the trace evaluators, it is also important to test their performance using Crab Nebula data. A standard Crab Nebula observation run was taken as the test sample, with 20000 events analysed in two telescopes. The charge and signal-to-noise ratio calculated for every channel using the *simple-window* trace evaluator are shown in Figure 6.27. The charge and signal-to-noise ratio calculated using the *dynamic-window*, *linear-interpolation*, *matched-filter* and *trace fit* trace evaluators are shown in Figures 6.28 and 6.29. Each distribution also displays the *simple-window* trace evaluator distribution for comparison. As expected, the *dynamic-window* trace evaluator calculates larger charges than the *simple-window* trace evaluator, but much of the effect of this added charge is eroded by the increased pedvar resulting in a well matched signal-to-noise ratio distribution. The *linear-interpolation* trace evaluator calculates virtually identical charge and signal-to-noise ratios. The *matched-filter* trace evaluator calculates slightly higher charges for these events. This is borne out in the signal-to-noise ratio distribution, although the effect is not as clear. The *trace-fit* evaluator appears to integrate slightly larger values of the charge than the *simple-window* trace evaluator. However, this effect is canceled out by the increased pedvar of the *trace-fit* evaluator resulting in a poorer signal-to-noise ratio. Finally the *timing-gradient* trace evaluator does

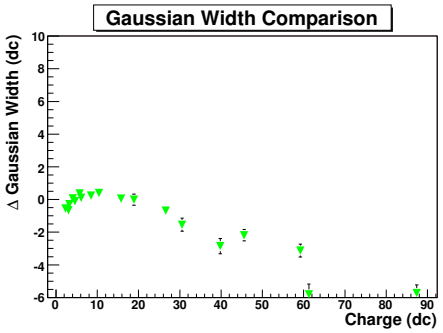

(a) Dynamic Window

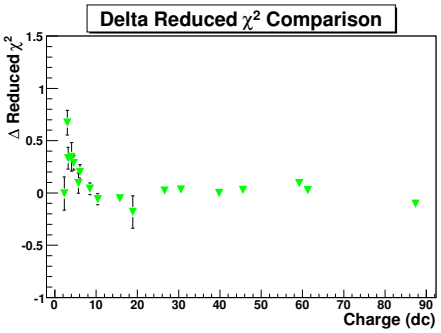

(b) Dynamic Window

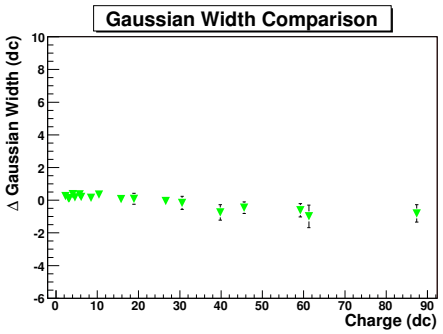

(c) Linear Interpolation

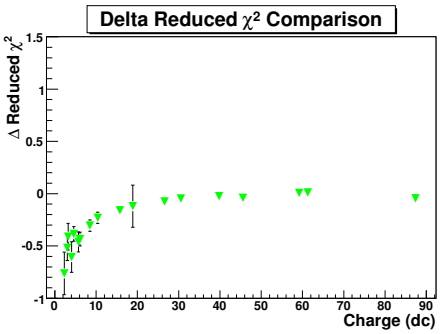

(d) Linear Interpolation

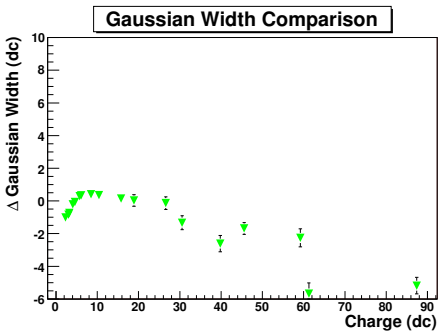

(e) Matched Filter

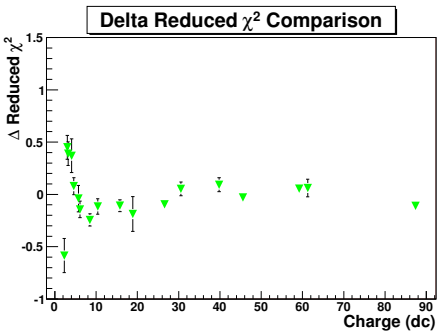

(f) Matched Filter

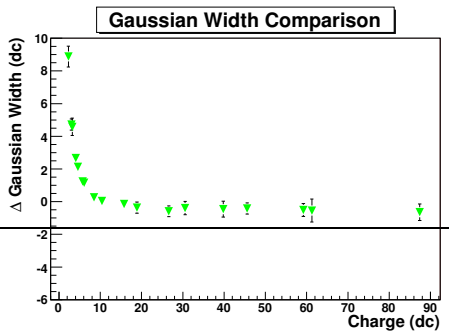

(g) Trace Fit

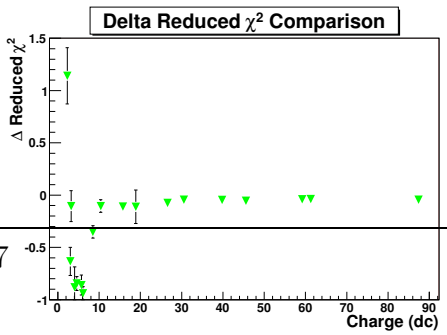

(h) Trace Fit

Figure 6.24: Study of charge resolution - see Section 6.5.2 for discussion

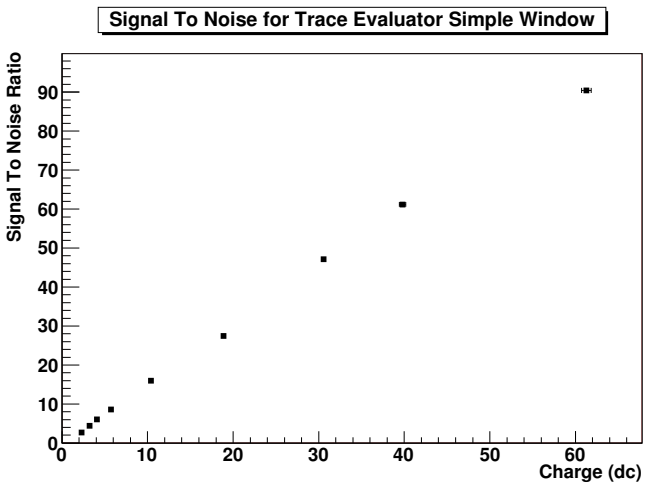

Figure 6.25: Signal-to-noise ratio as a function of trace size evaluated using the *simple-window* trace evaluator.

not appear to calculate significantly larger charges than the *simple-window* trace evaluator. This indicates that the dataset is not dominated by events exhibiting significant timing gradient along the primary image axis (events such as that in Figure 6.10).

6.5.4 Timing Resolution

In order to use the timing information provided by the FADCs, it is important to understand the timing resolution of the system. The timing resolution is determined by how well the arrival time of an asynchronous laser flash incident on the camera plane can be measured. It is important here to note that the laser pulser is placed at the cross beams of the telescope and is pointed directly at the camera face, thus bypassing the anachronicity introduced by the mirrors.

The timing resolution is defined as the width of a Gaussian function fit to the distribution of measured differences between event arrival and channel arrival time for a series of laser pulses for each channel. The event arrival time is defined as the *average* arrival time of all the channels (note this is essentially the same algorithm used in the calculation of T_{offset}). The timing resolution is dependent on the trace evaluator used to determine it, where for instance the *simple-window* trace evaluator only calculates the arrival time to the nearest 2 ns, and the *linear interpolation* trace evaluator interpolates between samples. The timing resolution as measured using the

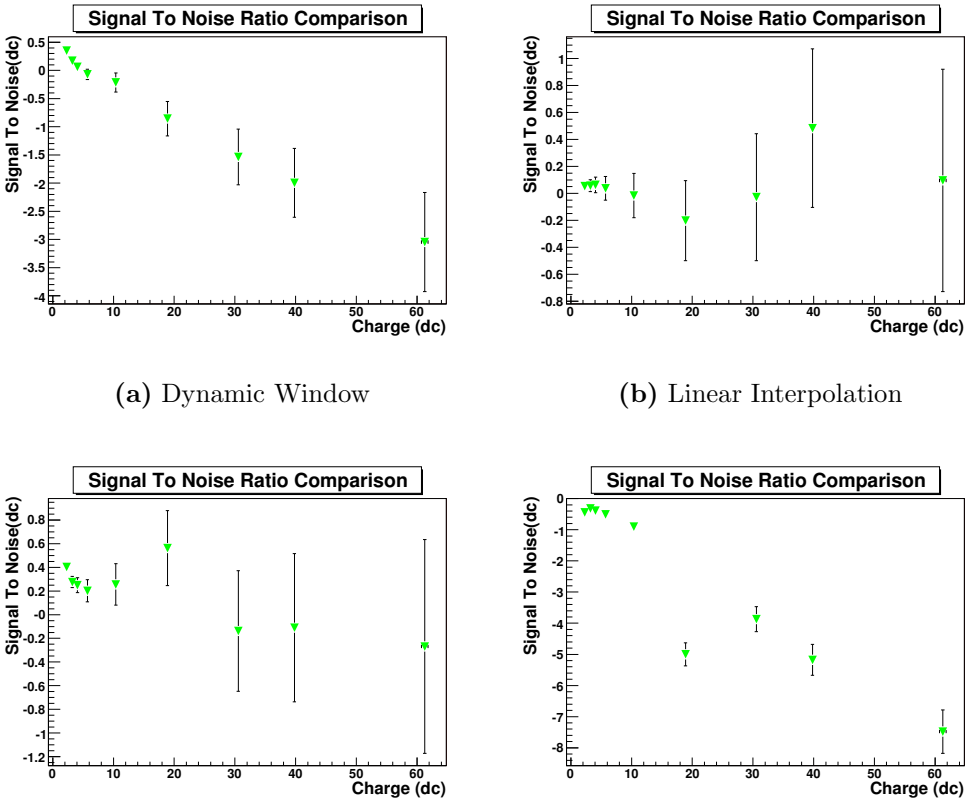

(a) Dynamic Window

(b) Linear Interpolation

(c) Matched Filter

(d) Trace Fit

Figure 6.26: Study of signal-to-noise ratio - see Section 6.5.2 for discussion.

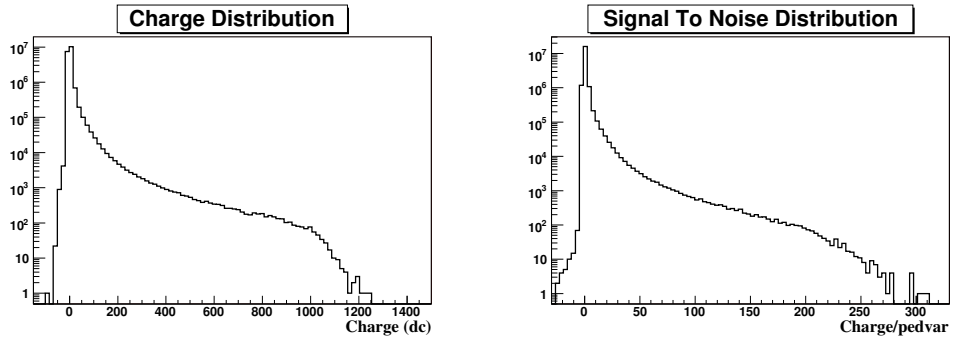

(a) Charge Distribution **(b)** Signal-To-Noise Ratio

Figure 6.27: Charge and signal-to-noise ratio for each channel for each telescope for 20,000 events of a standard Crab Nebula observation run. The charges and signal-to-noise ratios are calculated using the *simple-window* trace evaluator.

simple-window trace evaluator is shown in Figure 6.30. For small traces, there is a large spread in the arrival time, however the reconstruction is quite good for large traces. The fit is an empirically derived shape given in Equation 6.22 with the fit parameters shown in Table 6.2.

$$T_{res}(Q) = A \exp^{(B(Q+C))} + T_{res} \tag{6.22}$$

Parameter	Simp. Window	Lin. Interp.	M. Filter	Trace Fit
A	41.4	26.2	37.4	30.9
B	0.43	0.32	0.454	0.344
C	4.03	4.73	4.23	4.55
T_{res}	0.83	0.51	0.99	0.48

Table 6.2: Free parameters for the fit to the timing resolution distribution in Figures 6.30 and 6.31.

The timing resolutions as derived using the other trace evaluators are compared to that achieved with the *simple-window* trace evaluator in Figure 6.31. As expected, the *linear-interpolation* trace evaluator has superior timing resolution for all trace sizes. The *matched-filter* trace evaluator is excellent for small traces, however as trace arrival times can only be calculated to the nearest FADC sample, it is not as good for large pulses. The *trace-fit* trace evaluator has poor timing resolution for very small pulses - mirroring the

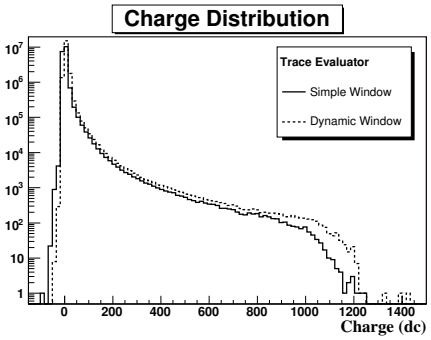

(a) Dynamic Window

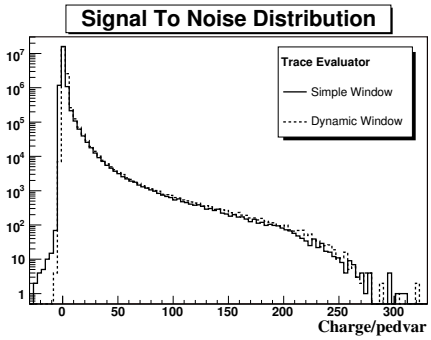

(b) Dynamic Window

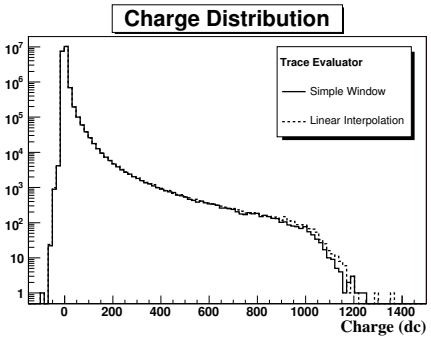

(c) Linear Interpolation

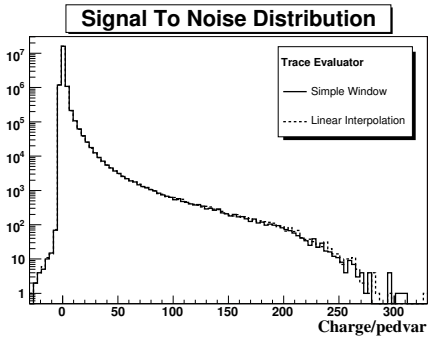

(d) Linear Interpolation

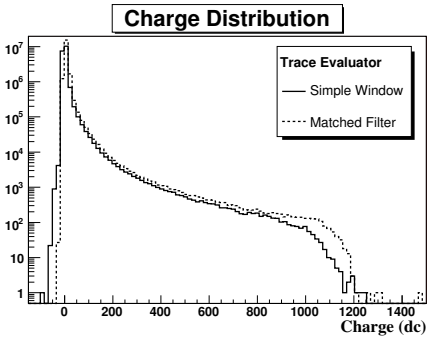

(e) Matched Filter

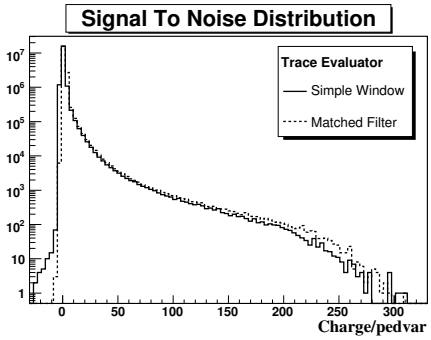

(f) Matched Filter

Figure 6.28: Part 1 of 2. Comparison of charge and signal-to-noise ratio for the Crab Nebula dataset - see Section 6.5.3 for discussion. See Figure 6.29 for part 2.

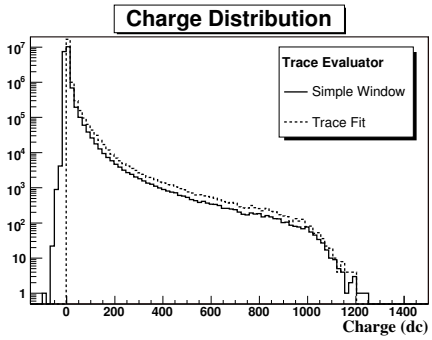

(a) Trace Fit

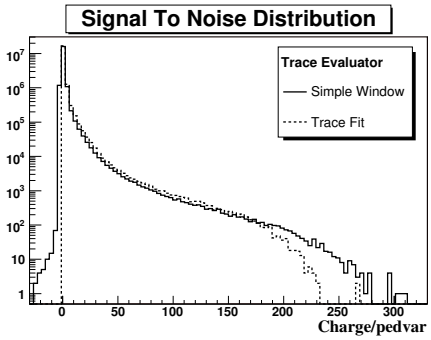

(b) Trace Fit

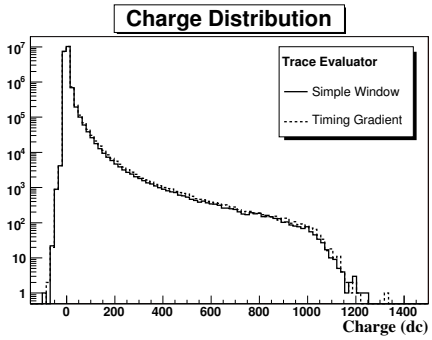

(c) Timing Gradient

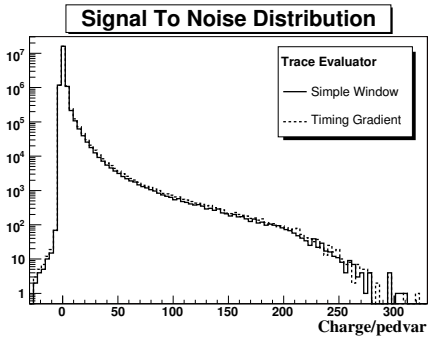

(d) Timing Gradient

Figure 6.29: Part 2 of 2. Comparison of charge and signal-to-noise ratio for the Crab Nebula dataset - see Section 6.5.3 for discussion. See Figure 6.28 for Part 1.

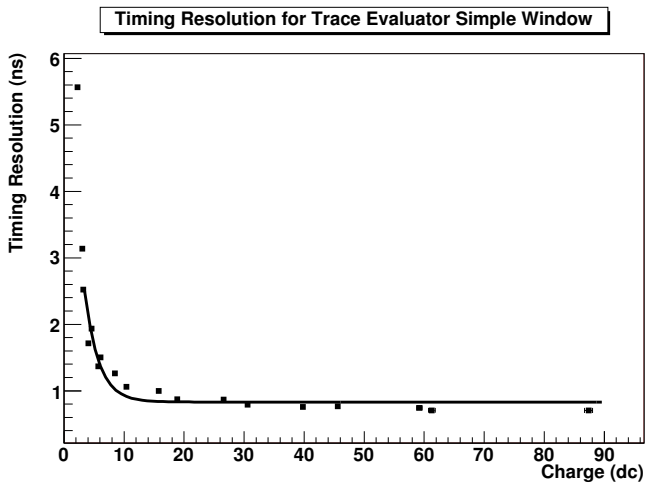

Figure 6.30: Timing resolution as a function of pulse size for the *simple-window* trace evaluator.

effect seen with the study of charge distribution, indicating that the fit function is not suited to small pulses. For large pulses the *trace-fit* evaluator has a superior resolution. The *dynamic-window* trace evaluator and *timing-gradient* trace evaluators are not shown as they use the same algorithm to find the trace arrival time as the *simple-window* trace evaluator.

6.6 Study of Image Cleaning and Reconstruction

The tests that have been performed up to now compare the trace evaluators in terms of the calculation of parameters such as charge, signal-to-noise ratio and timing. Ultimately it is the reconstruction of the image that must be optimised. It is difficult to test image reconstruction, and to define what is meant by optimal image reconstruction. Indeed the effects of the trace evaluators on image cleaning, which is an intermediary step between trace evaluation and image reconstruction, should be understood before reconstruction can occur.

One approach is to use a standard Crab Nebula dataset, apply the different trace evaluators and compare the significance of the detection. The complication with this approach is that it must be done in conjunction with an optimisation of other parameters such as Picture/Boundary cleaning thresholds, quality cuts, stereo parameter cuts etc. Thus it becomes difficult to

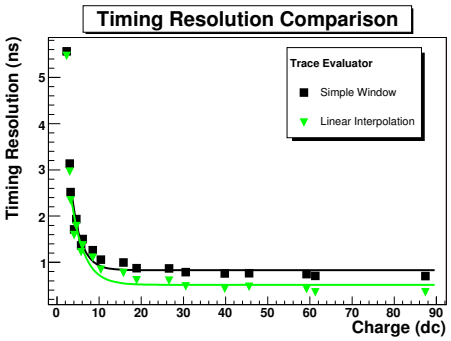

(a) Linear Interpolation

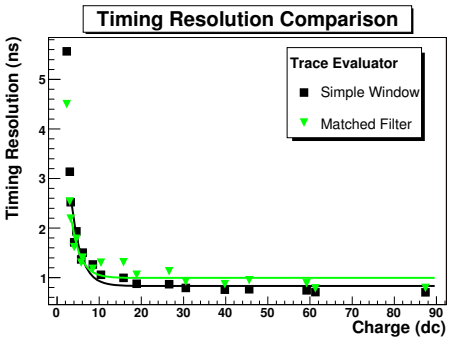

(b) Matched Filter

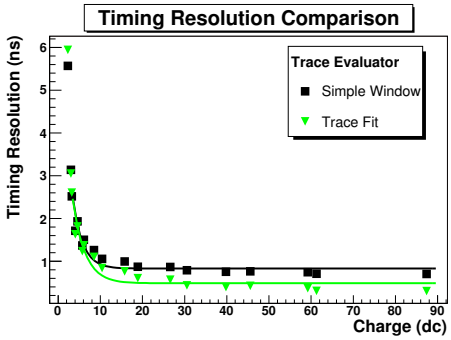

(c) Trace Fit

Figure 6.31: Timing resolution as a function of trace size compared to the *simple-window* trace evaluator for the *linear interpolation*, *matched-filter* and *trace-fit* evaluators.

tell whether any change in the calculated significance is the result of further optimisation downstream in the analysis chain, or from the original change in trace-evaluation mechanism. Nevertheless, this option is explored in greater detail in Section 7.5.

The approach adopted here is to test the quality of the image cleaning and reconstruction using the database of Monte-Carlo simulations of gamma-ray showers described in Section 7.2. The data are calibrated and parameterised using each trace evaluator. Figure 6.32 shows the distribution of the number of PMTs passing image cleaning for the dataset. In each case, the distribution from the *simple-window* trace evaluator is shown as a reference. As would be expected, the *linear interpolation* trace evaluator does not provide a larger number of image tubes. However, both the *dynamic window* and *matched filter* trace evaluators do provide larger numbers of image tubes on average per event. This occurs because both of these evaluators seek out the part of the trace containing the most significant fluctuation, regardless of whether that fluctuation is spurious. Interestingly, the *timing-gradient* trace evaluator only provides a slightly larger number of tubes. The *timing-gradient* trace evaluator is much more likely to avoid spurious fluctuations as it is designed to place the integration window at the expected location of the Cherenkov pulse.

In order to test the image reconstruction, the same Monte-Carlo dataset is used. The primary axis of each simulated gamma-ray shower image should point back towards the center of the camera. The angle (called *alpha*, Table 5.19) between the primary axis, and a line joining the image centroid and the camera center can thus be used to compare the quality of image reconstruction using the different trace evaluators. In principle, the trace evaluator with the most events constructed with alpha close to zero has achieved the best reconstruction.

The simulated gamma-ray dataset contains 315340 triggered telescope events that are used for this study. Of these triggered events, many will not have sufficient light to reconstruct the image - that is there may be no pixels which pass the Picture cleaning cut. Table 6.3 shows the number of events with enough light to reconstruct the image, the number of events with $alpha < 10$ and the percentage of the total number of events with $alpha < 10$. The comparisons indicate that the *simple-window* and *linear-interpolation* trace evaluators have very similar reconstruction efficiencies, and the *matched-filter* and *dynamic window* trace evaluators appear to be somewhat worse. This is likely due to the effect of pixels containing spurious noise that was mentioned earlier. The *timing-gradient* trace evaluator has the highest percentage of events reconstructed with $alpha < 10$. The distribution of *alpha* parameters is compared in Figure 6.33 for $alpha < 10$ for each trace

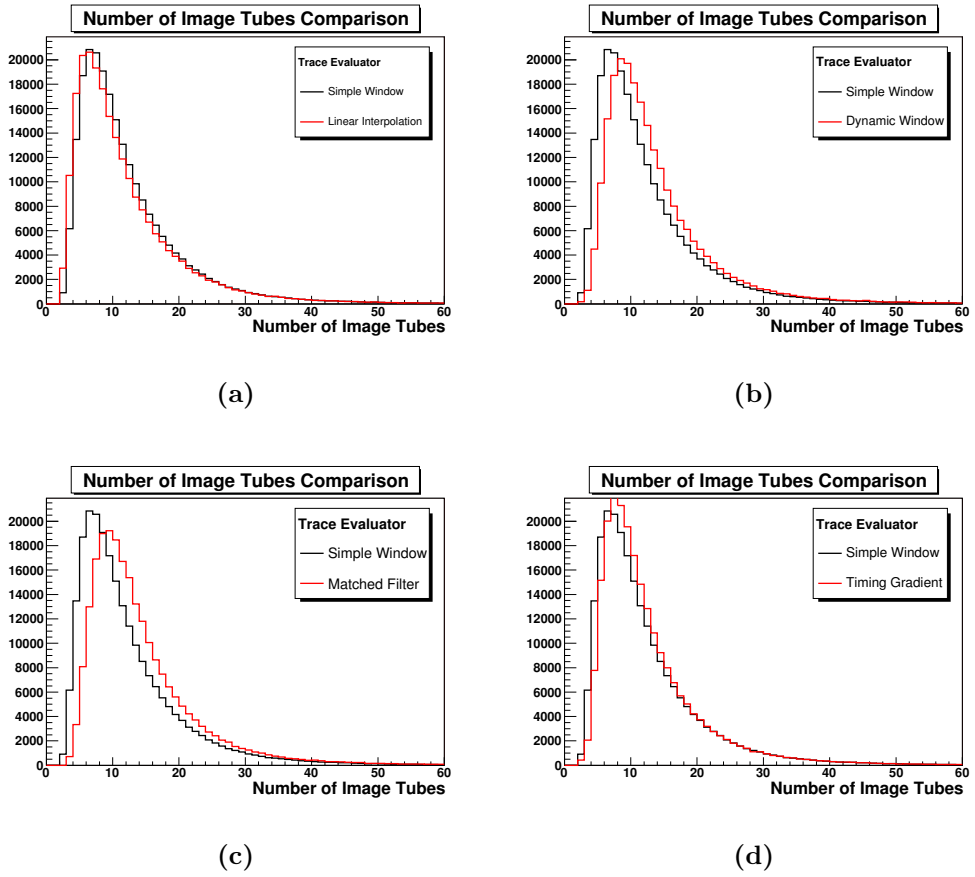

Figure 6.32: These figures demonstrate the number of tubes passing image cleaning for each trace evaluator. The standard image cleaning method and thresholds were used for each trace evaluator.

evaluator. The *alpha*-distribution for the *simple-window* trace evaluator is shown in each figure for comparison.

6.7 Low-Gain Channel Reconstruction

In order to maximise the dynamic range of the FADC system (Section 4.4.1), a secondary data acquisition readout channel with a lower FADC gain is available. The low-gain channel is used if the incoming analog signal exceeds the threshold where saturation of the 8 bit dynamic range is expected to occur. The low-gain channel has a factor of 6 less gain than the normal high-gain channel. The pedestal is added after amplification and the gain switch

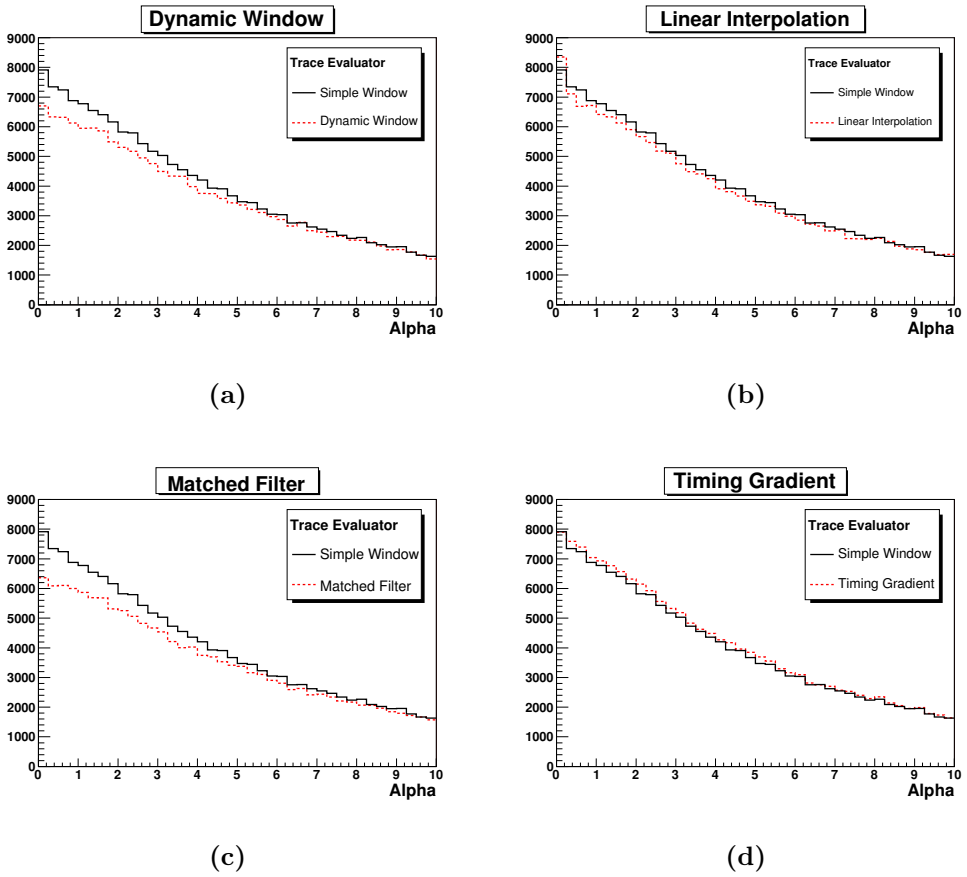

Figure 6.33: Comparison of the *alpha*-parameter distribution for *alpha* < 10 for the *dynamic-window*, *linear-interpolation*, *matched-filter* and *timing-gradient* trace evaluators. The *alpha*-parameter distribution for the *simple-window* trace evaluator is shown in each figure for comparison.

Trace Evaluator	Reconstructed	Events with $\alpha < 10$	% of all
Simple Window	234004	161200	51.12%
Linear Interpolation	231781	155710	49.38%
Dynamic Window	234704	144914	45.96%
Matched Filter	235097	148223	47.00%
Timing Gradient	234032	165377	52.44%

Table 6.3: Comparison of image reconstruction efficiency using the all the trace-evaluation algorithms. The dataset contains a total of 315340 triggered telescope events. The number of reconstructed events is different for each evaluator, as each evaluator has a different distribution of the number of tubes passing image cleaning (Figure 6.32). The criterion used to determine the best reconstruction is the image parameter α. The number of events with $\alpha < 10$ and the percentage of the total number of events with $\alpha < 10$ is shown for each evaluator.

(see Figure 4.15), so the total signal should be given by

$$charge_{corrected} = (charge_{raw} - pedestal) * 6 \tag{6.23}$$

However voltage leakage through the low-gain switch results in a shift for the high-gain and low-gain pedestal. In order to properly measure the low-gain pedestal, it is necessary to use a region of the trace following the Cherenkov pulse when the readout is still in low-gain mode. To ensure this can be done, the low-gain switch is active for $\sim$ 300 nsec, however a very long readout window is required to measure the FADC output once the Cherenkov component of the trace is gone. Under normal operations, a readout window of 24 samples (just 48 nsec) is used. Increasing the readout to 150 samples would result in an unsustainable data rate and crippling deadtime. One solution is to dynamically adjust the readout window if the low-gain switch is enabled. This would allow a determination of the low-gain pedestal from the actual data set, although the statistics would be limited by the rarity of low-gain events and the length of the run. Deadtime would also be affected, and complications in the data acquisition and offline analysis make this an unattractive approach. An alternative approach would be to take a dedicated high-intensity laser run with the readout window set to 124 samples. The detrimental effect on data rate and deadtime can be controlled by either connecting the telescope trigger to the laser sync-out, or by setting the CFD to a very high level (although in the context of this test the deadtime is irrelevant). Similarly a charge injection run can be taken to determine the low-gain pedestal in the absence of night sky background. Note that the absence of a night sky background renders the pedvar measurement irrelevant.

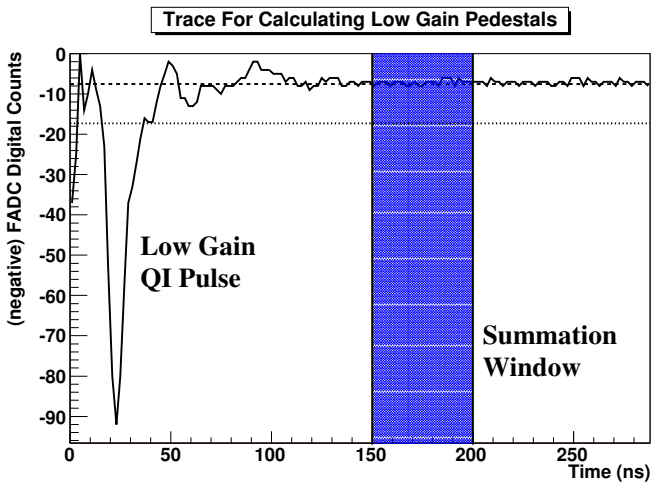

Figure 6.34: The readout used to measure the low-gain pedestal contains a large QI pulse at the start. The readout is sufficiently long that the integration window can be placed long after the QI pulse is gone. The dashed line indicates the pedestal that was measured for this channel in low-gain mode, whereas the dotted line indicates the pedestal that is measured in high-gain mode.

However, the pedvar is only used for pixel cleaning, thus the low-gain events, which will have a large charge anyway, should always pass pixel cleaning.

A special charge injection data run was taken to compare the low-gain pedestal to the high-gain pedestal. The system was run at approximately 10 Hz for 30 minutes, with large pulses injected into the PMT bases. The charges were sufficiently strong to engage the low-gain channel. AC coupling in the electronics chain results in an overshoot in the voltage to be digitised, and very large pulses (such as the one required to engage the low-gain channel) can result in ringing noise in the signal. To avoid these artefacts, a long 124 sample readout is used (see Figure 6.34). The distribution of low-gain and high-gain pedestals, shown in Figure 6.35, indicates the necessity of performing the low-gain channel calibration. If the pedestal is over-calculated by 10 digital counts for a low-gain channel event, the integrated charge could be under-calculated by 60 digital counts because of the low-gain multiplication factor.

Apart from pedestal calculation, the integration of charge for the low-gain channel can be tricky. Figure 6.36 shows the charge integration windows for three sample low-gain channel readouts using the *simple-window* and *dynamic-window* trace evaluator. Figures 6.36(a) and 6.36(b) show a rather typical low-gain readout, referred to here as a Type 1 readout. In this

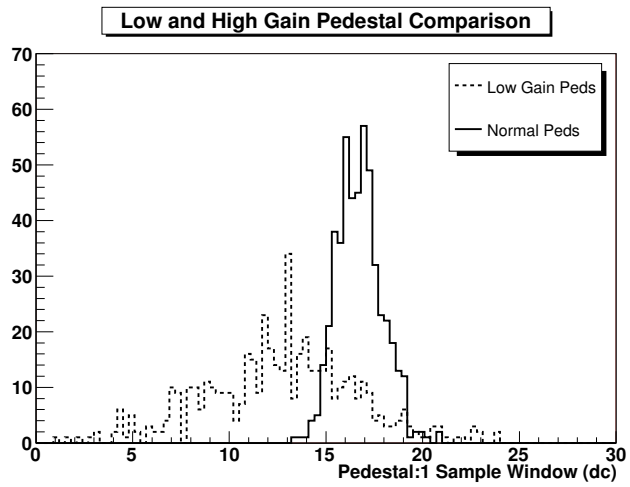

Figure 6.35: Comparison of measured pedestal for low and high-gain readout modes for all channels in Telescope 1.

case both the *simple-window* and *dynamic window* trace evaluator record charge from the same integration window (indicated by the red box) returning an equal and correct charge. A Type 2 readout is shown in Figures 6.36(c) and 6.36(d) where the low-gain pulse has come a few samples late (probably because of a timing gradient in the event). The tail end of the saturated high-gain pulse is visible at the start of the readout. In this case the *simple-window* trace evaluator records the charge incorrectly, as it has missed the relevant pulse. In rare cases, the FADC system can record on overshoot after the high-gain pulse. If the integration window is placed over the undershoot, a spurious negative charge can be calculated (if it occurs with an over-calculated pedestal). The *dynamic-window* trace evaluator has located the maximum charge correctly, resulting in the calculation of an accurate charge. A Type 3 readout is shown in Figures 6.36(e) and 6.36(f). This represents an extreme case where the low-gain pulse comes very late in the readout. This can occur for very large cosmic-ray air showers exhibiting significant timing gradient. Again the *simple-window* trace evaluator places the integration window in the wrong location. In this case the *dynamic-window* trace evaluator also places the integration window in the wrong location as the trace is dominated by the saturated component of the high-gain pulse. In order to compensate for such extreme cases, an arbitrary cut-off is placed on the range of integration windows that the *dynamic-window* trace evaluator can use by limiting the evaluator to start the sliding window at the 6^{th} sample.

Using the low-gain pedestal, and the described limited *dynamic-window* trace evaluator, the continuity between low-gain and high-gain channels can be tested. This is demonstrated in Figure 6.37, which shows good continuity between the low-gain and high-gain channels. Pile-ups are evident in both the high- and low-gain distributions due to saturation of the dynamic range. Saturation occurs where a portion of the analog pulse is cutoff in the digitisation, resulting in an underestimation of the charge (see Figure 6.38). This effect is much less noticeable in the high-gain distribution, as the low-gain channel engages before saturation can occur.

6.8 Trace Resampling

One tool commonly used in digital signal processing is *resampling* in the time domain. This is achieved by applying a Fourier transform to the trace, *zero padding* in the frequency domain, and applying an inverse Fourier transform. Zero padding in the frequency domain is achieved by simply *adding* zeros to the end of the Fourier transformed trace. This has the effect of *setting* higher frequencies to have zero amplitude. The inverse Fourier transform results in a trace which has been resampled in the time domain. Application of this algorithm to FADC data is relatively straightforward and is demonstrated in Figure 6.39. Figure 6.39(a) shows a normal FADC trace after the pedestal has been subtracted. Figure 6.39(b) shows the frequency spectrum for the same trace. Note that 500 MHz FADCs sampled 24 times provides an FFT spectrum from 0 to 250 Hz sampled 12 times. The frequency spectrum is zero padded such that it extends from 0Hz to 2GHz, sampled 96 times, (see Figure 6.39(c)). This implies a resampling ratio of 1:8, meaning that for each frequency point, seven zeroes have been added at higher frequencies. Once the inverse FFT has been taken, the trace which was previously sampled every 2 nanoseconds has been sampled every 250 picoseconds. The final resampled trace can be seen in Figure 6.39(d). Figure 6.40 compares the original and final traces (note that the resampled trace has been rescaled to match the original). The distribution of pedvars calculated using the *simple-window* trace evaluator are shown in Figure 6.41 with and without the application of the *resampling* algorithm. This comparison indicates that no significant digital noise has been introduced by the resampling algorithm.

The timing resolution achieved is compared using the *simple-window* and *linear-interpolation* trace evaluators. The trace evaluators work the same way as they do on an unprocessed trace, however in this instance, the *simple-window* trace evaluator can calculate the arrival time to the nearest 250 picoseconds. The same laser dataset is used to evaluate the timing

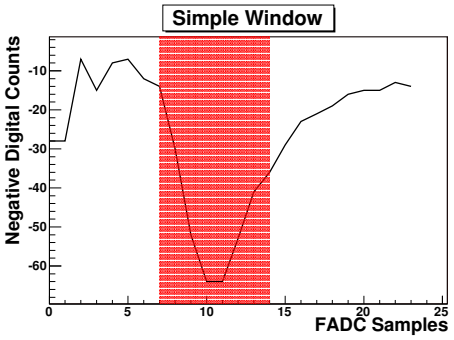

(a) Low-Gain Type 1

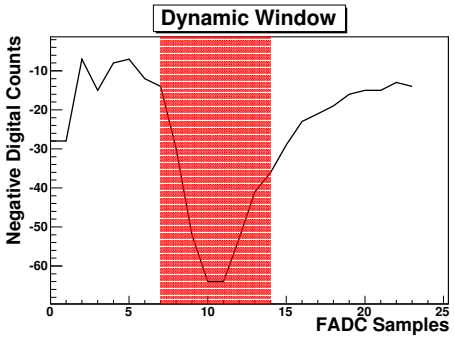

(b) Low-Gain Type 1

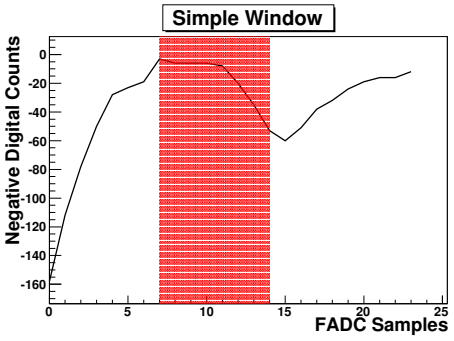

(c) Low-Gain Type 2

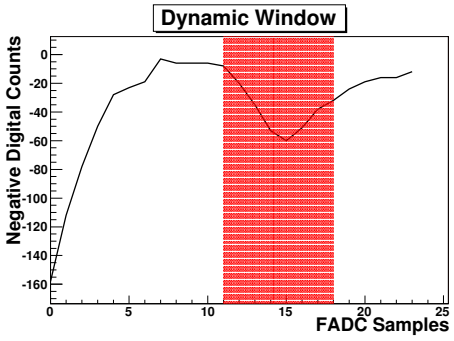

(d) Low-Gain Type 2

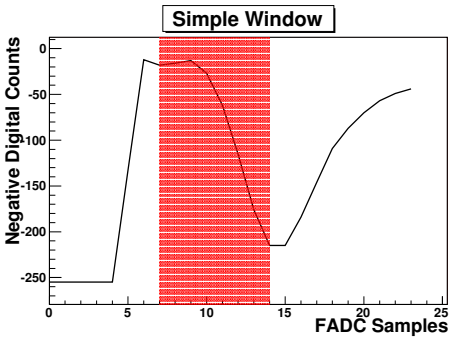

(e) Low-Gain Type 3

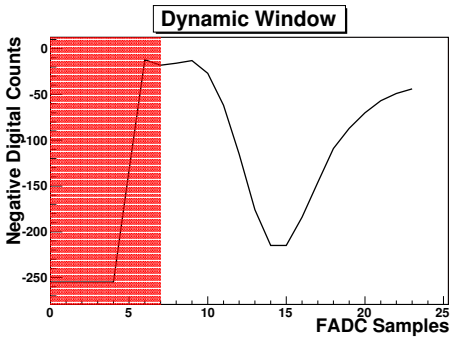

(f) Low-Gain Type 3

Figure 6.36: Three low-gain readouts analysed using the *simple-window* and *dynamic-window* trace evaluators - see Section 6.7 for discussion.

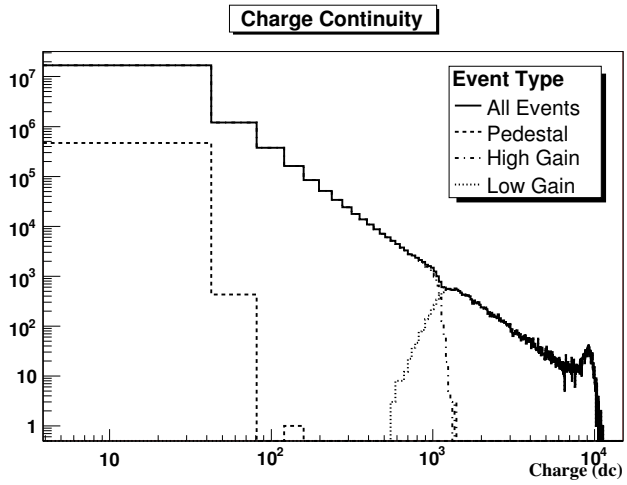

Figure 6.37: Charge distribution for a single data run. The charge calculated for pedestal, low-gain channel, high-gain channel and for all events are shown separately. The pileup at the extreme end of the spectrum is due to saturation of the low-gain channel (see Figure 6.38).

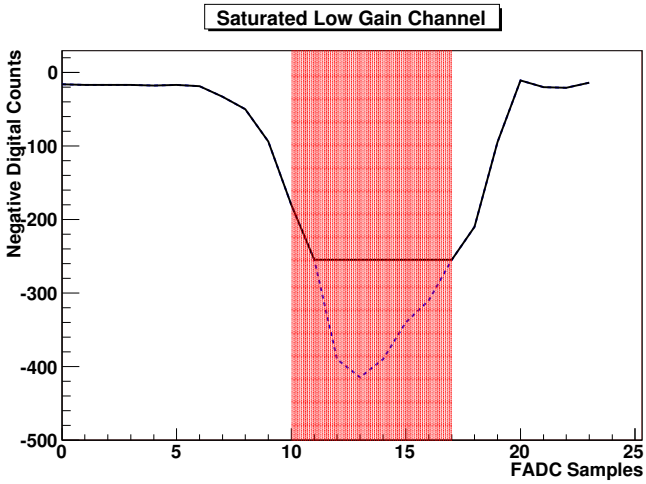

Figure 6.38: This figure shows an example of a saturated low-gain pulse. The actual recorded pulse is in black, with a clear cut off at 255 digital counts corresponding to the limit of the FADC dynamic range. The dashed blue line indicates what the original analog pulse could have looked like. What is clear is that the charge integrated using the shown window is underestimated, leading to a pileup in the charge spectrum in Figure 6.37.

resolution as was used in Section 6.5.4. The timing resolution as a function of the pulse size is shown in Figure 6.42, indicating that a substantially better timing resolution is achieved with both the *simple-window* and *linear-interpolation* trace evaluators when used in conjunction with the *resampling* algorithm. The results of the fitting are shown in Table 6.4.

Parameter	Simp. Window	Lin. Interp.
A	0.89	0.85
B	0.21	0.197
C	5.19	5.23
T_{res}	0.12	0.093

Table 6.4: Free parameters for the fit to the timing resolution distribution in Figures 6.42(a) and 6.42(b). Equation 6.22 is used in the fitting to measure the timing resolution.

6.9 The χ^2_{array} Parameter

It has been suggested by Konopelko (1991) that intrinsic shower fluctuations can be used as a gamma-hadron discriminant. Due to the multiple particle processes in hadronic showers, the temporal signatures they produce can be more irregular in form than for gamma-ray initiated showers. In this method a parameter called χ^2_{array} is calculated by measuring the statistical self-similarity of the FADC traces. Each trace passing standard Picture/Boundary cleaning is used to build up a weighted average trace, where the weight is given by the integrated charge of the trace. The weighted trace for each time slice j is given by

$$< I_j >= \sum_{i=1}^{m} \frac{A_i I_{ij}}{\sum_{i=1}^{m} A_i} \tag{6.24}$$

where $< I_j >$ is the average weight in the jth timeslice, I_{ij} is the charge in the ith pixel in the jth timeslice and A$_i$ is the summed charge for the ith pixel, where m is the number of image pixels. Now each image trace is compared to this weighted average trace using a standard χ^2 test

$$\chi^2_{\text{pixel}} = \frac{1}{n} \sum_{j=1}^{n} \frac{(I_{ij} - < I_j >)^2}{< I_j >} \tag{6.25}$$

producing a χ^2_{pixel} for each pixel, where n is the number of time slices. Typically in a χ^2 calculation, one divides by the error, in this case $< I_j >$, however

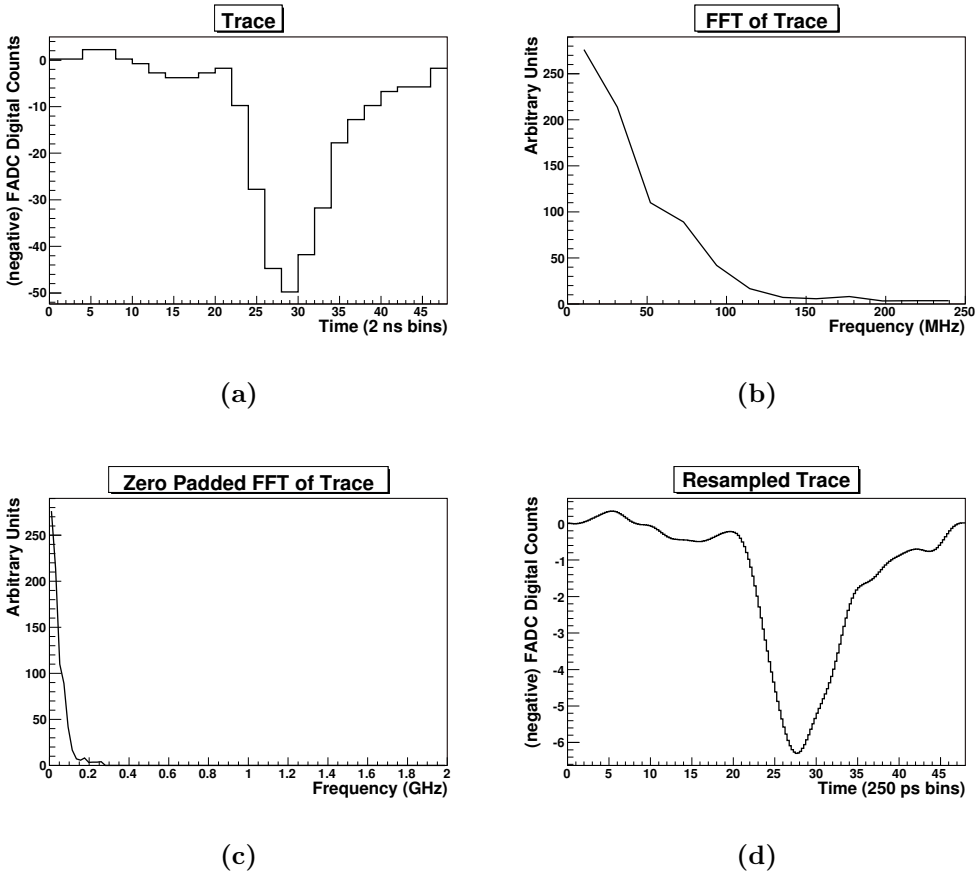

Figure 6.39: This figure demonstrates the procedure for resampling in the time domain. Figure (a) shows the trace with the pedestal subtracted. Figure (b) shows a Fourier transform of the trace in Figure (a). Figure (c) shows the Fourier Transform of the trace in Figure (b) with zero padding applied. Figure (d) shows the inverse Fourier transform of the zero padded Fourier Transform in Figure (c). Note that the total area under the pulses in Figures (a) and (d) are identical.

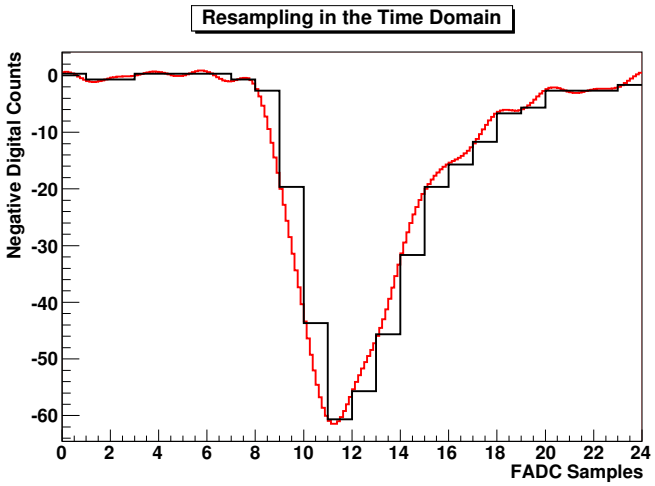

Figure 6.40: Comparison of an FADC trace before and after the application of resampling in the time domain. The resampled trace has been scaled by a factor 8 to match the size of the original trace for visual comparison.

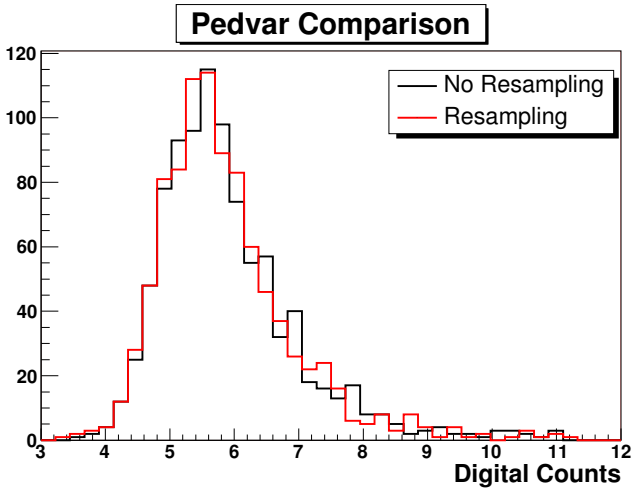

Figure 6.41: Pedvars calculated with and without the use of the *resampling* algorithm.

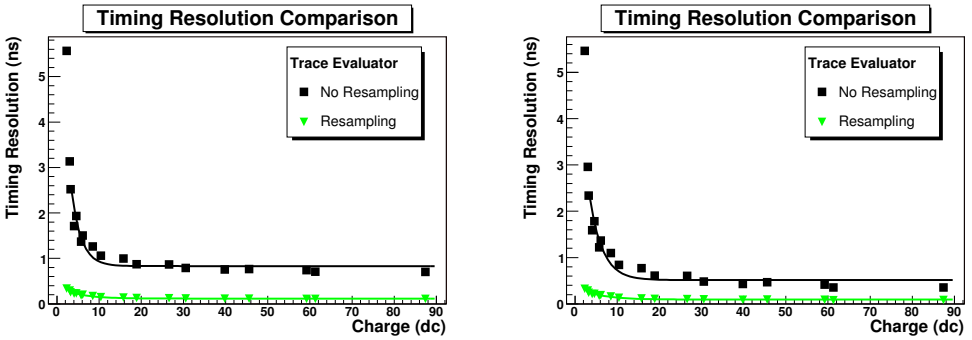

(a) **(b)**

Figure 6.42: Timing resolution as a function of pulse size using the *resampling* algorithm in conjunction with the *simple window* (left) and *linear-interpolation* (right) trace evaluators.

as shall be seen, each individual trace must be scaled so that their integrated charge matches that of the weighted average trace. This adds an additional component to the error so that the actual χ^2_{pixel} is calculated from

$$\chi^2_{\text{pixel}} = \frac{1}{n}\sum_{j=1}^{n}\frac{(I_{ij} - < I_j >)^2}{< I_j > R_i} \tag{6.26}$$

where R_i is the ratio between the integrated charges of the weighted average trace and the individual traces. The telescope event parameter χ^2_{tel} is calculated by taking the average of all χ^2_{pixel} according to

$$\chi^2_{\text{tel}} = \frac{1}{m}\sum_{i=1}^{m}\chi^2_{\text{pixel}_i} \tag{6.27}$$

where m is the number of image pixels. Finally the array event parameter χ^2_{array} is calculated by taking a weighted average over all χ^2_{tel} according to

$$\chi^2_{\text{array}} = \frac{1}{t}\left(\frac{\sum_{i=1}^{t}\chi^2_{\text{tel}_i}Q_i}{\sum_{i=1}^{t}Q_i}\right) \tag{6.28}$$

where t is the number of telescopes in the array event and Q_i is the integrated image size in the i^{th} telescope event.

Before the χ^2_{array} parameter can be calculated, preprocessing of the FADC trace must occur. Pedestals are subtracted, relative gains are factored in and Picture/Boundary cleaning is applied. A set of image pixels are collected

and any remaining bad channels are set aside. The raw FADC traces are retrieved and pedestals subtracted and relative gains factored on a sample by sample basis. The timeslice location of the trace maximum for each pixel is identified. The traces are then realigned so that all peaks coincide with the earliest peak. The traces are then trimmed at the end so they all retain the same number of samples (note that this number of samples would change on an event by event basis, depending on the spread of the trace maxima). In order to examine the Cherenkov region of the pulse, only an 8 sample window is considered, where the start of that window is again determined by passing a sliding window over the weighted average trace and choosing that window which returns the maximum charge. Rejecting the rest of the trace also means removing any remaining negative fluctuations, which are unphysical in terms of the χ^2 test (ie the χ^2 is a statistical test that two distributions match, where negative bin values are not expected). Finally the individual traces are scaled so that the integrated charge matches that of the weighted average trace. The final state of the data prior to calculation of the weighted average trace and χ^2 values consists of a set of m traces of 8 samples where the traces have been aligned according to their maxima, are pedestal and gain corrected and have been scaled such that their integrated charge matches that of the weighted average trace.

In order to test the potential of the χ^2_{array} parameter as a gamma-hadron discriminant, the gamma-ray and proton Monte-Carlo simulated dataset described in Section 7.2 is parameterised using the χ^2_{array} method. The χ^2_{array} distribution for proton and gamma-ray initiated showers shown in Figure 6.43 indicates that no significant difference between gamma-ray images and proton images have been found with this technique.

6.10 Discussion

Six trace evaluators have been investigated; these are the *simple-window*, the *dynamic-window*, *linear-interpolation*, *trace-fit*, *matched-filter* and *timing-gradient* trace evaluators. The parameters each evaluator must calculate have been defined.

Determining the size and location of the optimal FADC integration window is dependent on the trace evaluator being used. Some trace evaluators such as the *dynamic window*, *matched filter* and *timing gradient* determine their own integration window. However for the *simple-window* trace evaluator a study of the optimal integration window start location and size has shown that placing just 5% of the integration window before the average T_{zero} location, and integrating over 6 samples for large pulses and 8 samples

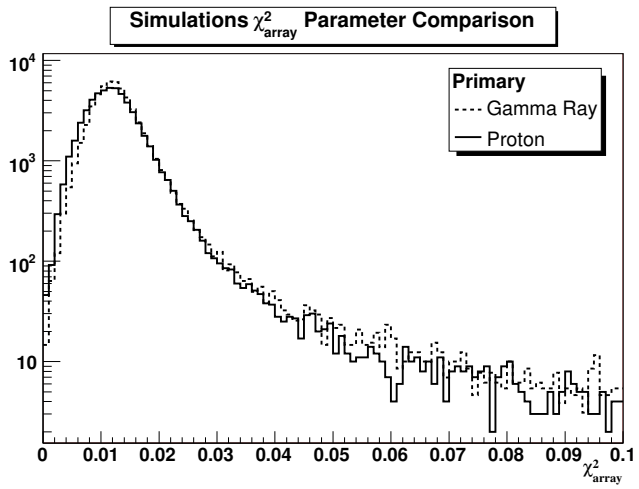

Figure 6.43: Comparison of the χ^2_{array} parameter calculated from Monte-Carlo simulations of gamma rays and protons. There is no apparent difference in the distributions, indicating that no gamma-hadron discrimination can be achieved.

for small achieves an optimal signal-to-noise ratio. It is also found that for the *dynamic-window* trace evaluator, the optimal integration window size for small pulses is 2 samples, and 4 samples for large pulses.

The primary disadvantage of a fixed integration window, is that for events with significant timing gradient, a large portion of the Cherenkov pulse can be missed (unless the integration window is very large). However, in the case of the sliding window, the charge calculated as a result of picking out the window with the maximum charge is balanced by the increased pedvar leading to a similar signal-to-noise ratio. However, if the window location can be determined *a priori* using the timing gradient to predict the location of the window, then the pedvar appropriate to the *simple-window* trace evaluator can be used.

Minor jitter in the stop time of the FADC crates can be corrected using asynchronous copied of the Level 2 trigger pulse in the FADC data stream. The arrival time of these traces is calculated and used to measure the relative jitter between crates. It has been shown that this correction improves the timing resolution by 0.3 nanoseconds.

Calculation of pedestals and pedvars for all trace evaluators have been demonstrated and, in most cases, are well understood. Although the pedestal calculation is not actually used, it is a useful sanity check. The pedvar calculations are important and are used to evaluate the signal-to-noise ratio.

The result of the charge resolution study is that the *matched-filter* and

dynamic-window trace evaluators have superior charge resolution, and that the improvement in charge resolution over the *simple-window* trace evaluator gets better with increasing pulse size. The *trace-fit* evaluator does not give good fits for small pulses, as evidenced by the large Gaussian width at small sizes. All the trace evaluators do not deviate significantly from the *simple-window* trace evaluator in terms of the reduced-χ^2 parameter, indicating the charge distributions are all equally Gaussian-like, especially for large pulses.

The *linear-interpolation*, *matched-filter* and *trace-fit* trace evaluators employ alternative methods of locating the trace T_{zero} which can provide superior timing resolution compared to the *simple-window* trace evaluator. Only the *linear-interpolation* algorithm provides superior timing resolution for all trace sizes. The *matched-filter* trace evaluator provides the best timing resolution for small pulses, but is worse even than the *simple-window* trace evaluator for large pulses. Conversely, the *trace-fit* evaluator is superior to all the trace evaluators for large pulses, but is poor for small pulses.

A Crab Nebula dataset is also used to evaluate the effect of the trace evaluators on the integrated charge and signal-to-noise ratio. The *dynamic-window* trace evaluator calculates larger charges, however this increase is undone by the increased pedvar resulting in an almost identical signal-to-noise ratio distribution as that calculated by the *simple-window* trace evaluator. Both the *matched-filter* and *trace-fit* evaluators calculate slightly larger charges than the *simple-window* trace evaluator. In the case of the *trace-fit* evaluator, the increased charge is canceled by the increased pedvar resulting in a signal-to-noise ratio which is actually lower than that for the *simple-window* trace evaluator. However, for the *matched-filter* trace evaluator, the signal-to-noise ratio is larger. The *timing-gradient* trace evaluator does not calculate noticeably larger charges.

A study of the effect of each trace evaluator on image cleaning and reconstruction was undertaken. The effect of the trace evaluators on the number of image tubes is well understood, with the use of the *dynamic-window* and *matched-filter* trace evaluators resulting in larger number of tubes passing cleaning. The primary difficulty in testing image reconstruction is that there is no *a priori* knowledge of what the image *should* look like. The approach used is to analyse a database of Monte-Carlo simulations of gamma rays using each trace evaluator, and measure the image parameter *alpha*. As images of gamma-ray initiated air showers point back towards the center of the camera, the *alpha* parameter should be small. The test showed that the *simple-window* and *timing-gradient* trace evaluators are the best candidates for accurately reconstructing gamma-ray images.

A study on reconstruction of the low-gain channel indicates the difficulties involved in extracting an accurate charge. It cannot be assumed that the

high-gain pedestal can be used in place of the low-gain pedestal. Also, events that occur in the low-gain channel tend to be from large images which tend to have significant timing gradients. The result of this is that for low-gain channels, the Cherenkov pulse can often come late in the readout, necessitating a dynamic window to accurately reconstruct the low-gain charge. However, in rare cases the dynamic window can return the charge integrated from the saturated high-gain component of the readout. In order to compensate for this a limited range dynamic window is used, resulting in good continuity in reconstructed charge between the high-gain and low-gain channels.

A method of *resampling* in the time domain by zero padding in the frequency domain has been demonstrated for FADC traces. It has been shown that the application of this simple digital signal processing tool, improves the timing resolution of both small and large pulses. A timing resolution of just 0.09 nanoseconds is achieved when the *linear-interpolation* trace evaluator is used in conjunction with the *resampling* technique. However, it should be realised that this level of timing resolution cannot be achieved on Cherenkov shower data for several reasons. The timing resolution determined by the laser system bypasses the time-spread introduced by the mirrors. This time-spread, estimated to be about 2 ns, is caused by the Davies-Cotton design of the reflector. The timing resolution is determined by building up statistics over many laser events. Such statistics are not available for a single Cherenkov pulse and the timing resolution measured here does not apply. The achievable timing resolution for single events should not exceed the intrinsic transit timespread of the PMT.

A new array parameter named χ^2_{array} has been introduced following on from the work of Konopelko (1991). This parameter measures the self-consistency of FADC traces, under the assumption that the FADC traces from gamma-ray events should be more self consistent than those for proton events. This assumption relies on the fact that proton-initiated electromagnetic cascades involve multiple-particle processes resulting in a more irregular temporal distribution of Cherenkov photons at the observation level. This assumption has not been borne out by the simulations carried out as part of this work, indicating that the technique cannot be applied to VERITAS data. However, this temporal signature may yet be uncovered if faster FADCs (such as the 2 GHz FADCs that will be used in the upcoming MAGIC upgrade) are used.

6.11 Conclusions

Several techniques for the analysis of FADC traces have been investigated in this chapter, including six separate methods for evaluating the charge in an FADC trace. In the context of the standard analysis, it is the integrated charge that is the most important parameter. The analysis presented in Section 6.5.3 indicated that there were only minor improvements in the resolution and consistency of the integrated charge using methods more sophisticated than the *simple-window* trace evaluator, so long as the integration window is correctly placed. In this case, the location of the integration window as determined by ω , is optimised on the signal-to-noise ratio. This optimisation is revisited in the next chapter where it is optimised in conjunction with Picture/Boundary cleaning thresholds on a Crab Nebula dataset.

The choice of trace evaluator in the next chapter is also influenced by the ability to reconstruct the Cherenkov image in the focal plane. Optimising this reconstruction is difficult as there is no *a-priori* information regarding what the image *should* look like. Rather, the study relies on the expected orientation of Monte-Carlo simulated gamma-ray images to determine the optimal trace evaluator. The study showed that the *simple-window* and *timing-gradient* trace evaluators reconstructed the highest number of events with $\alpha < 10^{\circ}$. Both of these trace evaluators will be applied to a Crab Nebula dataset in the next chapter.

Studies of the optimal timing resolution revealed that the optimal resolution is achieved with a combination of the trace resampling algorithm and *linear-interpolation* trace evaluator. Using this combination, an unprecedented resolution of 0.09 nanoseconds is achieved.

This chapter also covered a method to correct FADC timing jitter and a method to reconstruct the integrated charge from the low-gain FADC channel. An attempt to use the self-similarity of FADC data to discriminate hadronic background was also undertaken using Monte-Carlo simulations of gamma-ray and proton-initiated air showers.

Chapter 7

Data Analysis

7.1 Introduction

This chapter presents the final analysis carried out for this thesis dissertation. An overview of the Monte-Carlo simulation packages and settings used are presented for reference in Section 7.2. These data are used in several parts of the analysis. The VERITAS offline analysis package *VEGAS* is reviewed, with each stage of the analysis described in Section 7.3. The data analysed here were taken from September to December 2006, and the VERITAS array during this epoch is described in Section 7.4. A large Crab Nebula dataset was assembled by VERITAS during this observing epoch, and is used to optimise the analysis in Section 7.5. The *simple-window* and *timing-gradient* trace evaluators are used in the analysis of the Crab Nebula dataset, on which Picture/Boundary thresholds, shape and orientation cuts are optimised. Both one-dimensional and two-dimensional analyses are applied to the Crab Nebula dataset in Section 7.6. Three extragalactic sources, 1ES 0647+250, 1ES 0806+524 and 1ES 2344+524 were observed during the same epoch. Specific predictions for VHE emission from these objects, and previous results are discussed in Section 7.7. These data are analysed in Section 7.8 using the cuts and settings optimised on the Crab Nebula. No TeV emission is detected from any of these objects. Integral and differential flux upper limits are calculated for each object and compared to three models for predicting TeV emission. Finally x-ray data from the orbital Rossi X-Ray Timing Explorer are used to search for enhanced x-ray emission during the VERITAS observations in Section 7.9.

7.2 Simulations

Monte-Carlo simulations of gamma-ray initiated and proton-initiated air showers are used in many areas of the analysis for this dissertation. For all sections of this work requiring Monte-Carlo simulations of air showers, a single dataset was used. This dataset, and the software and parameters used to produce it are briefly described here.

Extensive air showers have been simulated using the CORSIKA[1] (Heck et al., 1998) air shower simulation package. This package uses the packages EGS4[2], QGSJet (Ostapchenko, 2004) and FLUKA[3]. The roles of these packages, and the versions used are displayed in Table 7.1. Using inputs such as spectral index, energy range and particle type, the CORSIKA package produces, for each simulated event, the distribution of Cherenkov photons on the ground (see Section 2.3 for figures displaying CORSIKA-simulated showers and the distribution of Cherenkov photons on the ground). In order to save disk space and processing time, only those Cherenkov photons which pass through the detector are recorded (in this case the detector refers to the telescope mirrors). The response of the VERITAS array is simulated using the GrISUDet[4] package. It takes as an input the Cherenkov photons striking the telescope mirror. It uses ray-tracing to back-propagate the photons to the camera, where quantum-efficiency and PMT response functions are used to generate a simulated camera output. This output is read by the trigger simulation which determines whether the telescope and subsequently the array has triggered. Finally, simulated FADC traces are produced and the data saved in the standard VBF (Section 4.4.2) data format. These data can be passed through the standard analysis chain (with special flags to disable database access etc).

Code	Package	Version
Extensive Air Showers	CORSIKA	6.2001
Electromagnetic Interactions	EGS	4
High-Energy Hadronic Interactions	QGSJet	II
Low-Energy Hadronic Interactions	FLUKA	2006.3
VERITAS Array	GrISUDet	4.1.0

Table 7.1: Monte-Carlo simulation packages used in this work.

[1] www-ik.fzk.de/corsika/
[2] www.slac.stanford.edu/egs/
[3] www.fluka.org
[4] http://www.physics.utah.edu/gammaray/GrISU

For both gamma-ray and proton-initiated extensive air showers, the primary CORSIKA configuration settings are shown in Table 7.2. The magnetic field is determined for the location of the VERITAS array using *Geomag*[5].

Setting	Value	Unit
Observation Altitude	1270	m
High-Energy / Low-Energy Cutoff	500	GeV
Magnetic Field Horizontal	25.2	μT
Magnetic Field Vertical	40.88	μT
Scatter Radius	600	m
Telescope 1 X,Y	-37.6, -23.7	m
Telescope 2 X,Y	44.1, -47.7	m
Telescope 2 X,Y	29.4, 60.1	m
Telescope 3 X,Y	-35.9, 11.3	m
Atmosphere	US Standard	

Table 7.2: Primary CORSIKA configuration settings. The High-Energy / Low-Energy cut-off describes the energy changeover between QGSJet and FLUKA.

The particular settings used for simulating the gamma-ray initiated air showers is shown in Table 7.3. The spectral index is chosen to be close to the measured spectral index of the Crab Nebula above 350 GeV (Figure 1.11). Gamma-ray showers are simulated at zenith angles of 0°, 20°, 30°, 40° and 50° in order to facilitate the calculation of lookup tables (Section 5.4.2). For both gamma-ray and proton-initiated air showers, the core location of each shower is randomised and resampled 10 times in order to increase statistics.

Setting	Value	Unit
Spectral Index	-2.5	-
Minimum Energy	50	GeV
Maximum Energy	10	TeV
Zenith Angle	0,20,30,40,50	Degrees
Number of Simulated Showers	$1.605 \times 10^6 \times 10$	-

Table 7.3: CORSIKA settings for the simulation of gamma-ray initiated air showers. For the creation of the dataset, 1.605×10^6 showers are simulated, with the core location of each shower randomised and resampled 10 times in order to increase statistics.

[5]http://www.ngdc.noaa.gov/seg/geomag/

The particular settings used for simulating the proton-initiated air showers is shown in Table 7.4. The spectral index is chosen to be close to the measured cosmic-ray spectral index in the GeV/TeV regime. A far higher quantity of cosmic-ray showers are simulated as they do not frequently trigger the detector.

Setting	Value	Unit
Spectral Index	-2.7	-
Minimum Energy	30	GeV
Maximum Energy	30	TeV
Zenith Angle	20	Degrees
Number of Simulated Showers	$7.5 \times 10^7 \times 10$	-

Table 7.4: CORSIKA settings for the simulation of proton-initiated air showers. For the creation of the dataset, 7.5×10^7 showers are simulated, with the core location of each shower randomised and resampled 10 times in order to increase statistics.

The GrISUDet simulation settings are shown in Table 7.5. Values are chosen to match the actual VERITAS settings during the September to December 2006 epoch. The same GrISUDet settings are used for both the gamma-ray and proton datasets.

Setting	Value	Unit
Diffuse Noise Level	250	photoelectrons/nanosecond
Voltage Per Digital Count	7.84	mV/dc
Pedestal	20	dc
CFD Threshold	66	mV
Pixel Multiplicity	3	-
Telescope Multiplicity	2	-
PMT Gain	2×10^5	-
Electronics Noise	3.6	mV
Triggered Gamma Rays	78835	-
Triggered Protons	60655	-

Table 7.5: Settings for the GrISUDet package which simulates the response of the VERITAS array to simulated air shower produced using CORSIKA.

7.3 Overview of *VEGAS*

The primary analysis for this work is carried out using the *VEGAS* package. All of the custom-designed trace analysis algorithms detailed and tested in Chapter 6 were implemented in *VEGAS* as part of this thesis dissertation, and are used here as part of both a standard and advanced analysis. The *VEGAS* package has six main stages summarised in Table 7.6. In Stage 1, the calibration constants pertaining to the pedestal calculation (Section 5.1.1), the T_{offset} calculation (Section 5.1.2) and the relative gain calculation (Section 5.1.3) are calculated. The VERITAS database is contacted to retrieve high voltage, PMT current, telescope tracking and source data. All results are saved into a single root[6] binary datafile. In Stage 2 (the development of which is a core part of this work), the calibration constants are combined with the raw data, and the FADC traces are analysed (see Chapter 6). For the standard analysis, the *simple-window* trace evaluator (Section 6.2.1) is used with an integration window of seven samples. Stage 2 also identifies broken pixels (Section 5.2.1) and performs interpolation between measured telescope pointing positions so that tracking data are available for each event. In Stage 3, the images are cleaned using the Picture/Boundary cleaning technique described in Section 5.2.2. Following image cleaning, the moment analysis described in Section 5.2.3 is applied. In Stage 4, the primary image axes are used to reconstruct the shower core location on the ground, and origin in the field of view (Section 5.3). The *width* and *length* parameters are compared to Monte-Carlo simulations of gamma-ray air showers to calculate the mean-scaled length and mean-scaled width parameters (Section 5.4.2) using lookup tables. Stage 4 also applies quality cuts (Section 5.4.1) such that only those showers that can be properly reconstructed are parameterised. Stage 5 applies stereo cuts to the mean-scaled width and mean-scaled length parameters such that a dataset of candidate gamma-ray events originating in all parts of the field of view is produced. Finally Stage 6 calculates the number of events in the putative source area, and in the selected background regions (Section 5.5.2), such that an excess number of events can be calculated. Distributions of the θ^2 parameter can be used to compare the number of events in the signal and background regions (for example Figure 7.4). Finally the statistical significance of any excess is calculated using Equation 17 from Li and Ma (1983) (see Section 7.6.1). In the absence of a signal, upper limits can be calculated using the method described by Helene (1983) (Section 7.8.1).

[6] http://root.cern.ch

Stage	Purpose	Input(s)	Output
1	Calib. Calculation	Raw Data	Calibration Data
2	Calib. Application	Raw + Calibration Data	Calibrated Events
3	Image Param.	Calibrated Events	Param'd Events
4	Shower Recon	Param'd Events	Recon'd Showers
5	Event Selection	Recon'd Showers	Selected Events
6	Results	Selected Events	Statistics & Figures

Table 7.6: The *VEGAS* Analysis Chain. Note that 'Calib.', 'Param'd' and 'Recon'd' are abbreviations of 'Calibration', 'Parameterised' and 'Reconstructed' respectively.

7.4 Observations

All data are taken in WOBBLE mode as described in Section 2.4.10, with WOBBLE offsets of either 0.3° or 0.5°. The telescope characteristics and trigger settings are detailed in Table 7.7. While these observations were being taken, VERITAS was still in the *engineering* phase of operations, with Telescope 3 being commissioned and Telescope 4 under construction. The Crab Nebula data and AGN data that were taken are considered engineering quality, and may possibly not be used for scientific quality publications that are expected to be made once the four-telescope data becomes available.

Level 1 Trigger Threshold	50	mV
Level 2 Trigger Adjacency	3	pixels
Level 2 Trigger Window	10-12	ns
Level 3 Trigger Multiplicity	2	Telescopes
Level 3 Trigger Window	100	ns
Run Size	1.1-1.4	GB
Data Rate	90-100	Hz

Table 7.7: VERITAS characteristics and settings September-December 2006.

7.5 Analysis of Crab Nebula Dataset

Observations of the Crab Nebula with two telescopes are used to calibrate and optimise the analysis chain. The Crab Nebula data were taken from September to December 2006, with WOBBLE offsets of 0.3° and 0.5°. Following the reduction of the dataset due to bad weather and hardware problems,

a total exposure of 1450 minutes remains in 62 data runs. Some of the runs are 20 minutes in duration and some are 28 minutes in duration. Generally when optimisation on a dataset is being carried out, the dataset is split in two and the cuts are optimised on only one dataset. The optimised cuts are then applied to the second independent dataset to determine whether an improvement in sensitivity has actually been achieved. This is not necessary here as there is no previous optimisation done to compare this optimisation with. For this analysis, it is the statistical significance of the detection of the Crab Nebula that will be used as the optimisation parameter. This parameter is chosen as it results in the optimisation of sensitivity, which is appropriate in the context of this work where new sources are sought. In other cases, where a strong signal is present, it is often preferable to allow looser cuts which results in a decrease in sensitivity but an increase in the total number of gamma rays (ie the gamma-ray *rate*) passing cuts. This would be the case where a spectral analysis is being undertaken, whereby a large database of gamma rays is desirable.

In order to ensure data integrity, quality cuts (Section 5.4.1) are applied to all data before the optimisation iteration occurs(the cuts used are listed in Table 7.8). In order to optimise the analysis of the Crab Nebula dataset, eight passes through the full *VEGAS* analysis chain are undertaken with two parameter sets adjusted (note that this initial eight-pass optimisation took approximately 48 hours to complete on a dedicated cluster of six 3 GHz Pentium processors and produced over 1TB of output). The first parameter to be varied is the ω parameter in the placement of the FADC integration window with the *simple-window* trace evaluator (Section 6.4). The second parameter to be varied is the Picture/Boundary cleaning thresholds. At the time the analysis was undertaken, lookup tables for two sets of cleaning thresholds were available. These thresholds are (Picture/Boundary) 4.25/2.25 and 5.0/3.0. The dataset is analysed for both combinations of cleaning thresholds with ω values of 0.05, 0.1, 0.2 and 0.3. This range of ω was chosen as previous tests with the *dynamic-window* trace evaluator indicate a value of ω in this range integrates the optimum charge. The results of the analysis are shown in Table 7.9, where un-optimised stereo cuts of $0.1 < \mathrm{MSW} < 1.2$ and integration ring sizes of radius $\theta = 0.22$ are used in the calculation of the number of excess counts and the statistical significance of the detection (note that it is the statistical significance of the detection that is optimised). The combination of cleaning thresholds and ω which provides the optimal sensitivity is Picture/Boundary=5/3 and $\omega = 0.1$.

The next step is to optimise the MSW and MSL cuts. This is achieved by varying MSW and MSL in the range $0.975 < \mathrm{MSW} < 1.400$ and $1.175 < \mathrm{MSL} < 1.600$ with step sizes $\Delta\mathrm{MSW} = 0.025$ and $\Delta\mathrm{MSL} = 0.025$. Again a

fixed integration ring size $\theta = 0.22$ is applied in the final calculation of the significance of the detection. The chosen combinations of MSW and MSL results in a search over a $18 \times 18 = 324$-bin parameter space. This search took 15 hours to complete on a dedicated cluster of six 3 GHz Pentium processors. The MSW/MSL combination with the optimal significance from this search is 1.050/1.425, which results in a sensitivity on the Crab Nebula corresponding to $12.7\,\sigma/\sqrt{\text{hr}}$. The statistical significance as a function of the upper MSW and MSL cuts is shown in Figure 7.1.

The final cut to be optimised is the integration ring size. This is achieved by applying the upper MSW and MSL cuts to the dataset and varying the ringsize in the range $0.068 < \text{ringsize} < 0.29$ with $\Delta\,\text{ringsize} = 0.002$. The results of this optimisation are shown in Figure 7.2, with the highest sensitivity achieved with a ringsize $= 0.152°$.

The optimum cut values are summarised in Table 7.10. The optimal sensitivity that has been achieved with this analysis is $14.42\sigma/\sqrt{\text{hour}}$. As a comparison, the Crab Nebula dataset is fully re-analysed using the *timing-gradient* technique described in Section 6.2.6. The data are processed using the same settings and cuts listed in Table 7.11, achieving a slightly lesser sensitivity of $14.05\sigma/\sqrt{\text{hour}}$. Interestingly, a slightly higher rate of 4.1 ± 0.06 gamma rays / min is achieved, which is slightly better than the 3.5 ± 0.05 gamma rays / min achieved with the previous analysis using the *simple-window* trace evaluators.

Parameter	Lower	Upper
Minimum Angle	10°	
Num Tubes	5	
Distance	0.05	1.3

Table 7.8: Quality cuts applied to Crab Nebula dataset. The Minimum Angle is the angle between the reconstructed primary axes of the two showers (note that only events for which showers from both telescopes can be reconstructed are considered). For small angles, the error on the reconstructed impact parameter is very large.

7.5.1 Data Quality Control

Observations are generally not undertaken in bad weather for a variety of reasons. Cloud cover significantly reduces the array trigger rate, rendering any background analysis, or absolute flux calculations very difficult. Generally, observations are only undertaken during cloudy weather if the array is

ω	Picture	Boundary	Signal	Background	Rate	σ	$\sigma/\sqrt{\text{hr}}$
0.05	4.25	2.25	15312	8220	4.89 ± 0.09	54.6	11.1
0.05	5	3	14420	7068	5.07 ± 0.08	59.5	12.1
0.1	4.25	2.25	16501	9212	5.08 ± 0.09	54.6	11.1
0.1	5	3	15534	7830	5.31 ± 0.09	**60**	**12.2**
0.2	4.25	2.25	18316	10455	5.42 ± 0.1	54.6	11.1
0.2	5	3	17310	9189	5.6 ± 0.09	59	12.0
0.3	4.25	2.25	19528	11581	5.48 ± 0.1	53.1	10.8
0.3	5	3	18725	10170	5.9 ± 0.1	59.5	12.1

Table 7.9: Results of optimisation of cleaning thresholds and ω parameter on the Crab Nebula dataset.

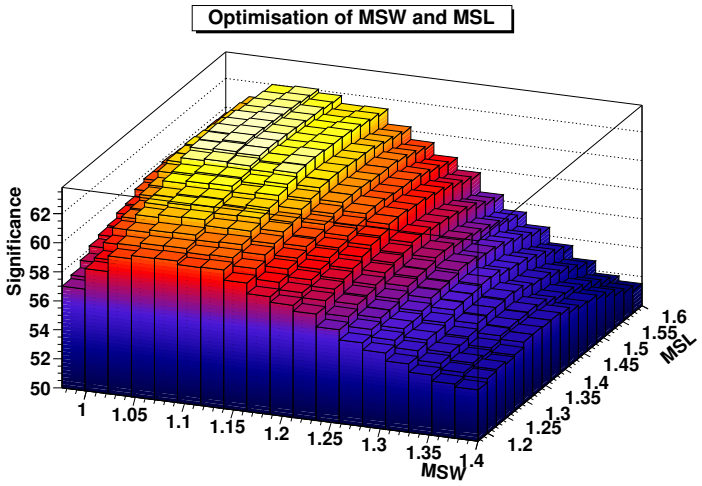

Figure 7.1: Graphical representation of the optimisation of the upper cuts on MSW and MSL using the Crab Nebula dataset.

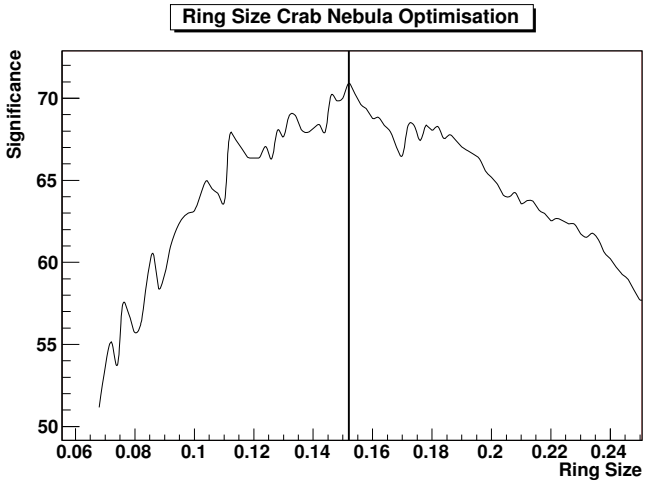

Figure 7.2: Graphical representation of the optimisation of the ring size used for the one-dimensional wobble analysis of the Crab Nebula dataset.

Parameter	Value
ω	0.1
Picture	5
Boundary	3
MSW $<$	1.05
MSL $<$	1.425
Ring Size	0.152
Signal Counts	7528
Background Counts	2399
Excess	5129
Significance	70.9σ
Rate	3.5 ± 0.05
Sensitivity	$14.42\,\sigma/\sqrt{\text{hr}}$

Table 7.10: Final settings and result for optimisation and analysis of Crab Nebula dataset.

Parameter	Value
Signal Counts	8612
Background Counts	3116
Excess	5496
Significance	69.1σ
Rate	4.1 ± 0.06
Sensitivity	$14.05\,\sigma/\sqrt{\text{hr}}$

Table 7.11: Results of analysis of the Crab Nebula dataset using the *timing gradient* trace evaluator described in Section 7.11.

partaking in a multiwavelength campaign, or AGN flare followup. The array cannot operate if it is raining or if the humidity is high as it could cause damage to the high voltage system (and surrounding systems) in the camera. Finally, observations are not undertaken in windy weather due to dangers associated with wind load on the optical support structure and telescope drive system.

Despite intentions to only run during good weather in the September-December epoch, sometimes runs are taken in moderately cloudy conditions as cloud cover can be difficult to judge at night. Thus in order to ensure data quality, each run in the Crab Nebula and AGN dataset was checked for the effects of weather variations (note that this is also important for catching trigger issues such as rate dips or spikes due to hardware or software problems). This is accomplished with a visual inspection of the trigger rate for the entirety of the run. Figure 7.3 demonstrates the array trigger rate during good and bad weather. Clouds passing in front of the field of view absorb Cherenkov radiation from extensive air showers resulting in drops in the trigger rate.

7.6 Results Extraction

The analysis of the Crab dataset is completed with graphical representations of the signal from the putative source position, and the signal from all parts of the field of view. The signal from the putative source position is determined using a one-dimensional analysis as detailed in Section 5.5.2 using the reflected region background model. The signal from all parts of the field of view is much more difficult to calculate, and involves establishing the distribution of candidate gamma-ray events in the field of view, calculating the acceptance ratio of signal and background events, and finally measuring the

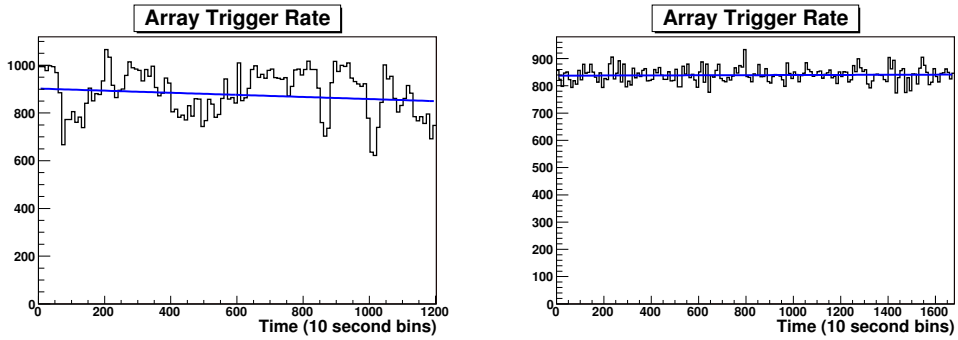

(a) Bad Weather **(b)** Good Weather

Figure 7.3: Array trigger rate for a Crab Nebula run taken during bad and good weather. In the case of bad weather, the trigger rate varies as clouds pass in front of the field of view. This run is excluded by quality control checks. The blue line is a simple flat line fit used to guide the eye. All data are visually examined.

significance at each point. This is achieved with the ring background model (Section 7.6.2).

7.6.1 One-Dimensional Analysis

This model simply counts the number of events in a region of ring size θ around the putative source position, and compares it to the number of counts in similar-sized background regions placed around the field of view equidistant from the center of the field of view. In order to ensure stability of the background, the number of counts falling within each annulus of width $\delta\theta$ around the putative source position is plotted along with the average number of counts falling within a similarly sized annulus around each background position. Figure 7.4 shows this plot for the Crab Nebula dataset. The data are plotted as a function of θ^2 as the number of counts is linearly proportional to the size of the annulus squared. The apparent excess in the background region at $0.2^\circ - 0.3^\circ$ is due to events from the Crab Nebula leaking into the background region for particular values of θ. However, this part of the background does not contribute to the statistical significance calculation. Equation 7.1, taken from Li and Ma (1983), is used in the calculation of statistical significance, where α is the acceptance ratio, N_{sig} is the number of signal counts and N_{back} is the number of background counts.

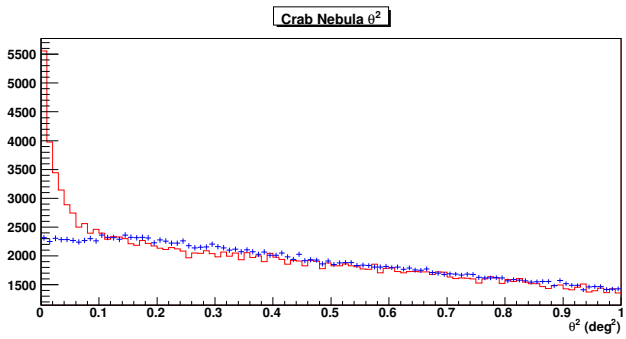

Figure 7.4: Graphical representation of the number of counts integrated in an annulus of inner radius θ^2 and outer radius $\theta^2 + 0.01$ (where 0.01 is just the bin size in the figure) using the signal and background rings as a function of ring size squared for Crab Nebula dataset.

$$\sqrt{2}\left\{N_{sig}\ln\left[\frac{1+\alpha}{\alpha}\left(\frac{N_{sig}}{N_{sig}+N_{back}}\right)\right]+N_{back}\ln\left[(1+\alpha)\left(\frac{N_{sig}}{N_{sig}+N_{back}}\right)\right]\right\}^{\frac{1}{2}} \tag{7.1}$$

7.6.2 Two-Dimensional Analysis

Two-dimensional analysis is performed using the ring background model, which was briefly described in Section 5.5.3 but will be covered in more detail here in the context of the Crab Nebula dataset. A two dimensional analysis is required to test the source location and extent in the field of view. It is used to study source morphology and has proven extremely successful in the measurement of galactic supernova-remnant morphology (Figure 1.12).

7.6.3 Calculation of Signal and Background

The first step in generating a two-dimensional map of excess counts is to generate a distribution of shower source locations in the field of view for all showers passing gamma-ray selection cuts (apart from an origin cut). Such a distribution for the Crab Nebula dataset is shown in Figure 7.5 with the data histogrammed in bins of size $0.025^\circ \times 0.025^\circ$. Figure 7.6(a) shows the signal in each grid point calculated by integrating the number of events originating within a circle of radius 0.2°. An example of such a circle is shown in the upper right quadrant of Figure 7.5 with the small square at its center

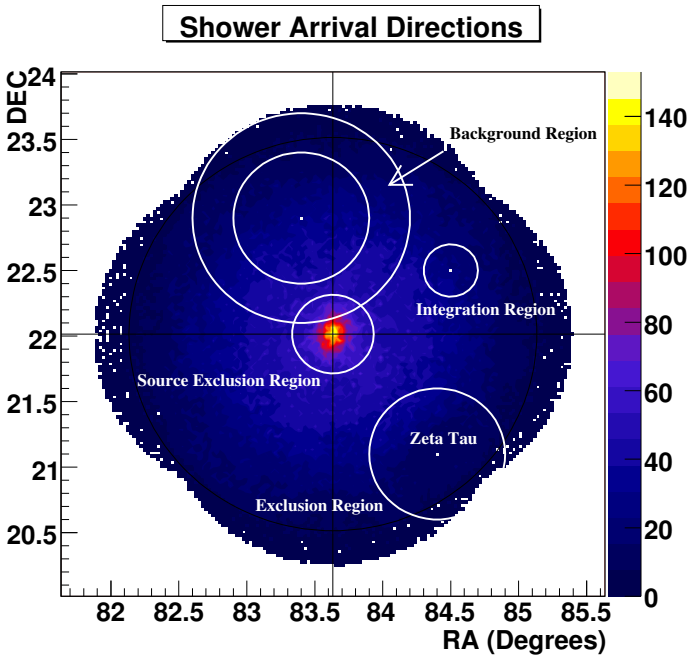

Figure 7.5: Distribution of arrival directions of candidate gamma-ray events for the Crab Nebula dataset - see text of discussion.

indicating the grid point size. Figure 7.6(b) shows the background in each grid point calculated using an annulus of inner radius 0.5° and outer radius 0.8°. An example of such an integration annulus is shown in the upper left quadrant of Figure 7.5.

The field of view of the Crab Nebula contains the bright star zeta tau, with a large number of PMTs turned off in that region. In order to reduce systematic error on the background calculation in surrounding regions, an 0.5° exclusion region is placed around the star. Events that fall within the exclusion region are not counted in the background estimation. An exclusion region is also placed around the putative position of the Crab Nebula so that events that are likely to be gamma rays are not counted in the background calculation of surrounding grid points. Both of these exclusion regions, as well as inhomogeneities in the camera response and sky brightness in the field of view strongly affects the signal acceptance. Thus an accurate measurement of the acceptance for both signal and background events must be modelled (this is covered in the next section).

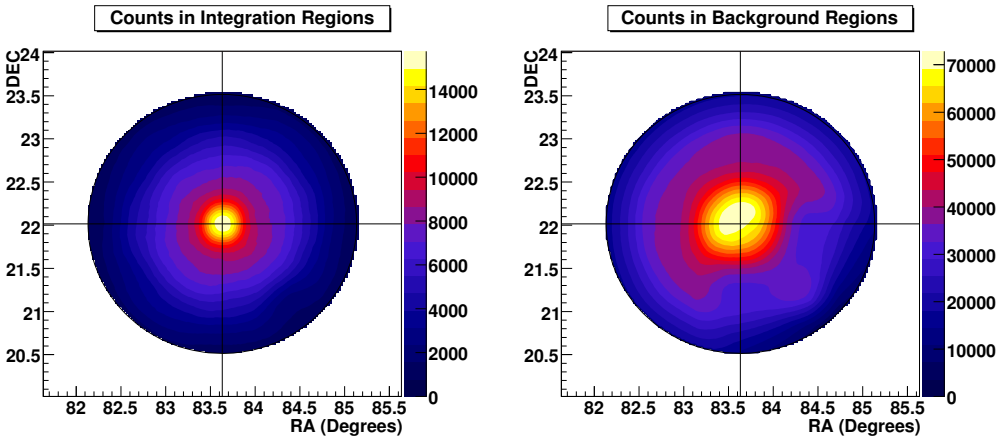

(a) **(b)**

Figure 7.6: Integrated signal and background maps using the integration circle and annulus depicted in Figure 7.5.

7.6.4 Calculation of Acceptance

In order to calculate the acceptance, the number of gamma-ray candidate events as a function of radial distance from the camera center must be accumulated (Figure 7.7(a)). The histogram is scaled according to the annular area corresponding to each bin, and normalised to the bin contents at 0.45° 7.7(b). The acceptance map is generated at each grid point in the field of view of the dataset by iterating over all runs and summing the one dimensional acceptance appropriate to the angular distance from the center of the camera for that run. A weight is applied to each entry which corresponds to the ratio of the number of candidate gamma-ray events in that run to the total number of candidate gamma-ray events in the dataset. The resultant acceptance map is shown in Figure 7.8(a) (with the centers of the cameras for the eight wobble locations shown). The same circular integration region that produced Figure 7.6(a) from Figure 7.5 is applied to Figure 7.8(a). This produces the gamma-ray acceptance at each grid point shown in Figure 7.8(b). Similarly the same annular integration region that produced Figure 7.6(b) from Figure 7.5 produces a background acceptance at each grid point. Now for each grid point a signal, signal acceptance, background and background acceptance have been calculated. It is worth noting here for clarity that the calculation of α allows a calculation of the excess number of counts in grid

points close to the exclusion region, whose background regions are smaller than other regions because of the exclusion region. The number of excess counts and significance in the exclusion region itself cannot be calculated, and the values derived (and plotted) are virtually meaningless. The number of excess counts (and hence significance) within the zeta tau exclusion region is highly negative as the derived α in that region is very large. This occurs because of the lack of background counts, which in turn is caused by the exclusion region itself.

7.6.5 Calculation of Statistical Significance

As stated in Section 5.5, the number of excess counts is given by

$$N_\gamma = N_{on} - \alpha N_{off} \tag{7.2}$$

where N_γ is the excess number of gamma-ray events, N_{on} is the number of signal events, N_{off} is the number of background events and α is the acceptance ratio between signal and background regions. For the ring background model, α is produced for every grid point (Figure 7.8(c)). The effect of the bright star zeta tau on the scaling factor is evident here.

The excess counts at each grid point is given by the number of counts in the integration regions (Figure 7.6(a)) minus the number of counts in the background regions (Figure 7.6(b)) scaled by alpha (Figure 7.8(c)). The excess number of counts at each integration region is shown in Figure 7.9(a).

The statistical significance of the excess (if any) at each grid point is calculated using Equation 7.1. The map is shown in Figure 7.9(b) and indicates that there are no statistically significant sources in the field of view of the Crab Nebula (apart from the Crab Nebula itself). The statistical significance of the Crab Nebula determined using the ring background model is consistent with that determined using the reflected region model (ie the one dimensional analysis). However, the two dimensional map has not been corrected for trials.

The distribution of significances measured using the ring background model is displayed in Figure 7.10. The excess of events on the right side of the image are due to the excess at the position of the Crab Nebula. This plot also features an excess on the left side due to apparent negative significances at the position of the star zeta tau.

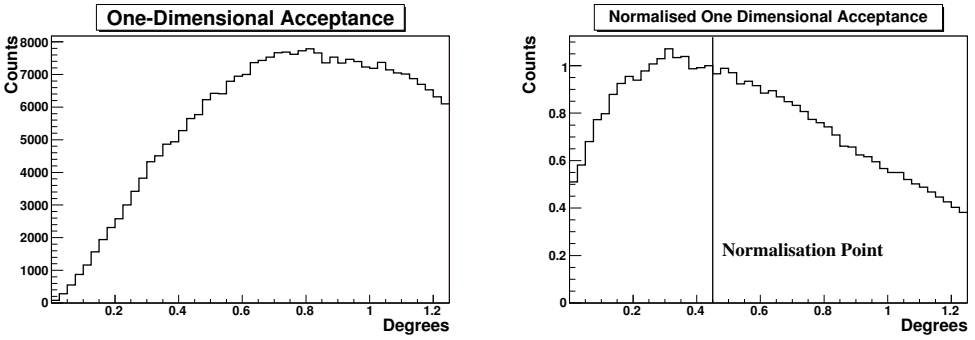

(a) **(b)**

Figure 7.7: In order to calculate the acceptance, the number of gamma-ray candidate events as a function of radial distance from the camera center must be accumulated (left Figure). The histogram is scaled according to the annular area corresponding to each bin, and normalised to the bin contents at 0.45°.

7.7 Blazar Observations

The blazars 1ES 0647+250, 1ES 0806+524 and 1ES 2344+514 have been studied as part of this work. The observations of 1ES 0647+250 and 1ES 0806+524 are motivated by the search for emission from extragalactic sources previously undetected at very-high energies. The observations of 1ES 2344+514, which has already been detected at very-high energies by Whipple, HEGRA and MAGIC, are motivated by the need for continuous monitoring of existing sources and the need to extend the measurements of the energy spectra. In the coming sections, three specific models used to predict VHE emission from blazars will be discussed and previously reported measurements and upper limits of the sources compared.

7.7.1 Models used to Predict VHE Emission

Predicting the TeV flux from blazars is fraught with difficulty. It has been shown by Böttcher et al. (2002) that the spectral fitting of blazars is subject to large uncertainties when non-contemporaneous multiwavelength data are used. Even with the best multiwavelength data, the predicted emission above 40 GeV is extremely sensitive to model parameters. This is one of the reasons why VHE observations are such a useful constraining tool for emission models.

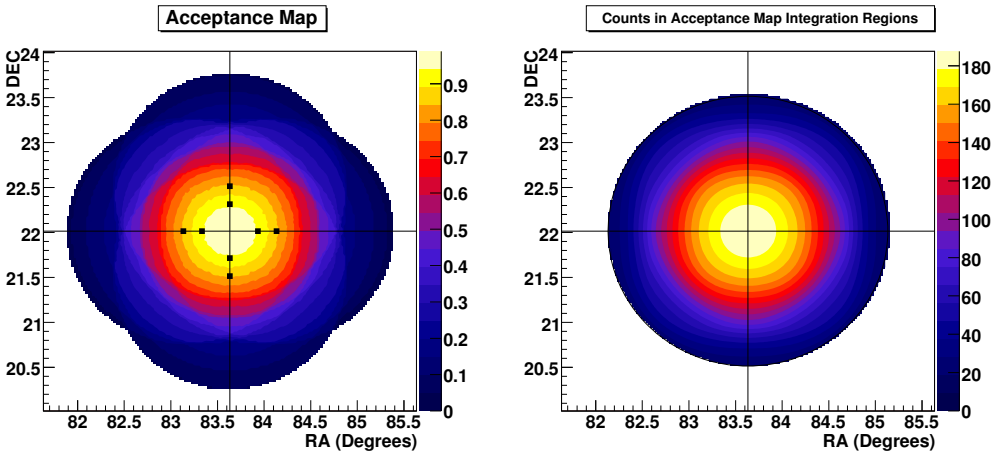

(a)

(b)

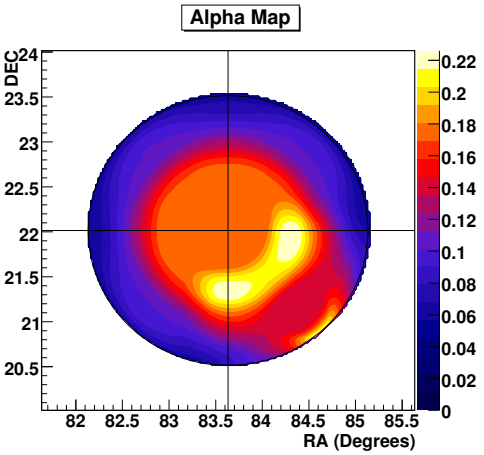

(c)

Figure 7.8: The top left figure shows the distribution of acceptance of gamma-ray events in the field of view. The top right figure shows the acceptance map with the circular signal integration region accumulating events at each grid point. The bottom figure shows the distribution of the alpha parameter which is the ratio of signal-to-background acceptances. All three figures are discussed in the text.

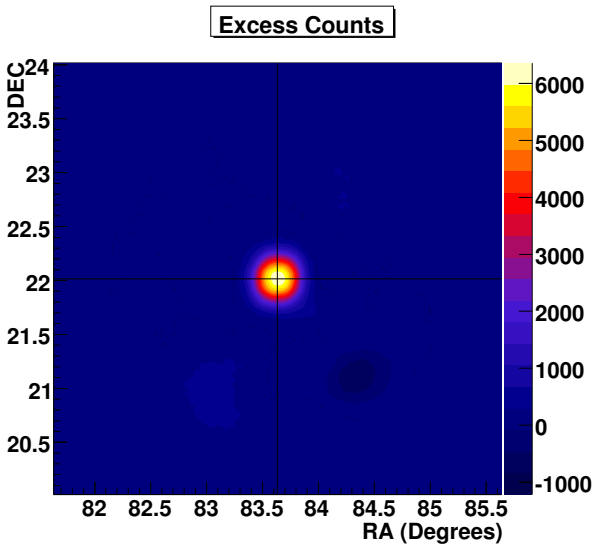

(a)

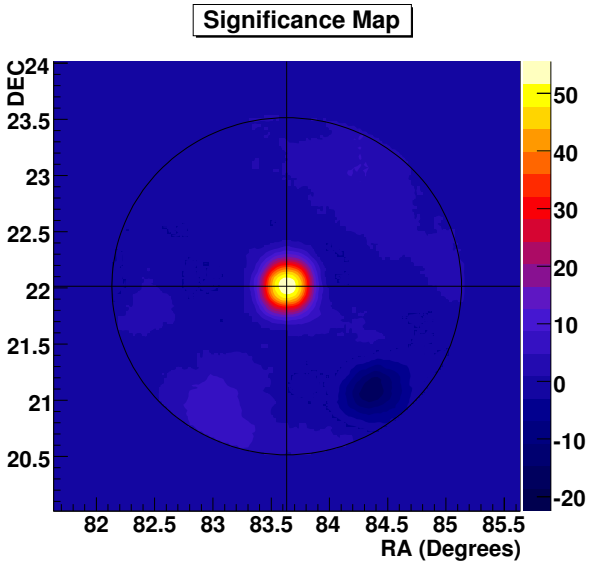

(b)

Figure 7.9: 7.9(a) shows the distribution of excess counts in the field of view, while 7.9(b) shows the statistical significance at each point in the grid.

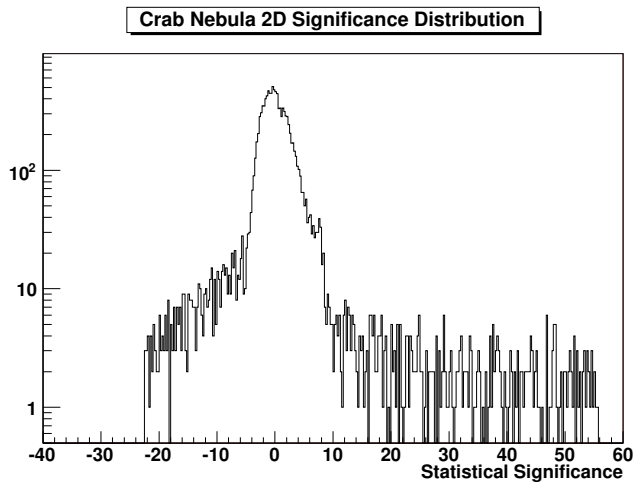

Figure 7.10: Distribution of significances from the two-dimensional significance map in Figure 7.9(b). The excess of events on the right side of the map is due to the Crab Nebula, whereas the excess of events at the left side of the plot is due to the star bright zeta tau and the exclusion region around it.

Three approaches are considered here; the scaled one-zone SSC model from Stecker et al. (1996) (hereafter *Stecker*), the Fossati et al. (1998) model modified by Donato et al. (2001) and Costamante and Ghisellini (2002) (hereafter *modified-Fossati* model) and the one-zone SSC model by Costamante and Ghisellini (2002) (hereafter *Costamante* model).

The *Stecker* model assumes a one-zone SSC model calibrated by non-contemporaneous multiwavelength data on Markarian 421. TeV fluxes are predicted by applying a scaling law to the emission spectrum of the first peak in the SED. The model assumes the luminosity and spectral shape from both the first and second peak are identical (apart from the upshift scaling). Absorption from the intergalactic background (Section 3.8) is applied by taking the average between models 1 and 2 from Stecker and de Jager (1997). The scaling law is applied to data from the Einstein Slew Survey to select VHE candidates.

In the *modified-Fossati* model, the peak frequency of the synchrotron spectrum and the relative importance of the inverse-Compton power are determined by the radio luminosity. The Donato et al. (2001) modification assumes a different relationship between the radio power, inverse-Compton power and synchrotron peak frequency, but only for objects below a radio luminosity of $10^{43}\mathrm{ergs}^{-1}$. In this modification, objects of low power are assumed to have equal luminosities in the synchrotron and self-Compton components

of their spectra. The second modification (by Costamante and Ghisellini (2002)) extends the radio range below $10^{41.2}$ erg s^{-1} by modelling Compton scattering in the Klein-Nishina regime. Costamante and Ghisellini (2002) also use a different width for the parabola representing the Compton peak, which is reduced with respect to the synchrotron peak.

In the *Costamante* model, a single zone SSC fit to multiwavelength data is used to predict fluxes in the TeV regime. The model emphasises the requirement of *both* high-energy electrons and sufficient seed photons to produce very high-energy gamma rays. In the study, a large sample of Bl Lacs were examined and the radio/optical flux and synchrotron peak frequency fit using the SSC model. The effects of absorption due to the extragalactic infrared background are not taken into account.

7.7.2 Integral Flux Scaling

Integral flux is often quoted above different energies for different experiments and for different models. In order to make comparisons between results and models, it is often useful to extrapolate the integral flux quoted above an energy E_1 to the integral flux above an energy E_2. This can be done using a simple scaling argument which is outlined here. It is important to note that the scaling assumes an unbroken power law between E_1 and E_2. The differential flux of a source exhibiting power law form is commonly expressed as

$$\frac{d\mathcal{F}}{dE} = AE^{-\alpha} \tag{7.3}$$

where $\mathcal{F}$ is the number of events with energy E in an interval dE, A is a flux constant and α is the spectral index. Thus the integral flux is

$$\mathcal{F} = A\int E^{-\alpha}\, dE = \left(\frac{A}{-\alpha+1}\right) E^{-\alpha+1} \tag{7.4}$$

Following from this the ratio of fluxes at two energies E_1 and E_2 is given by

$$\frac{\mathcal{F}_{E_1}}{\mathcal{F}_{E_2}} = \left(\frac{E_1}{E_2}\right)^{-\alpha+1} \tag{7.5}$$

For example, equation 7.5 could be used to extrapolate the integral flux above 0.74 TeV to the integral flux above 0.3 TeV according to

$$\mathcal{F}_{\mathrm{E>0.3\,TeV}} = \mathcal{F}_{\mathrm{E>0.74\,TeV}} \left(\frac{0.3}{0.74}\right)^{-\alpha+1} \tag{7.6}$$

For these studies, the spectral index $\alpha = 2.39$ corresponding to the spectral index of the Crab Nebula measured by Aharonian (2006e) will be used.

7.7.3 1ES 0647+250

The blazar 1ES 0647+250 was discovered in the MHT-Green Bank survey at 5 GHz using the NRAO 91-m transit telescope (Langston et al., 1990). X-ray emission was discovered in the Einstein Slew Survey by Elvis et al. (1992) with the synchrotron peak falling just below 10 keV. A redshift of 0.203 has been tentatively reported by Rector et al. (2003). Very Long Baseline Array (VLBA) observations do not show a distinct jet (Figure 7.11(b)) but there is some evidence for a faint, diffuse halo around the core (Rector et al., 2003). The *Costamante* model predicts a VHE flux of $\mathcal{F}_{\mathrm{E>0.3\,TeV}} = 0.59 \times 10^{-11}\,\mathrm{cm}^{-2}\,\mathrm{s}^{-1}$ with $\mathcal{F}_{\mathrm{E>0.3\,TeV}} = 0.24 \times 10^{-11}\,\mathrm{cm}^{-2}\mathrm{s}^{-1}$ predicted according to the *modified-Fossati* model. No prediction from the *Stecker* model is available. Previous observations of this source are reported by HEGRA (Aharonian et al., 2004a) with a 99 % confidence flux upper limit of $\mathcal{F}_{\mathrm{E>0.78\,TeV}} < 33.5 \times 10^{-11}\,\mathrm{cm}^{-2}\,\mathrm{s}^{-1}$ from 4.1 hours of observations. To compare this to the *Costamante* and *modified-Fossati* models, this can be extrapolated to a flux upper limit above 0.3 TeV using equation 7.5 which gives a flux upper limit of $\mathcal{F}_{\mathrm{E>0.3\,TeV}} < 126.4 \times 10^{-11}\,\mathrm{cm}^{-2}\,\mathrm{s}^{-1}$. This is well above both the predictions of the *Costamante* and *modified-Fossati* models and does not constrain either model.

7.7.4 1ES 0806+524

The blazar 1ES 0806+524 was discovered using the NRAO Green Bank 91-m telescope at 4.85 GHz (Becker et al., 1991) with x-ray emission reported in the Einstein Slew Survey (Elvis et al., 1992). The galaxy has a measured redshift of 0.138 (Bade et al., 1998). Radio imagery reported by Rector et al. (2003) shows a bright central core with a jet extending to the north (Figure 7.11(d)). Diffuse emission around the jet suggests a wide opening angle of 70°. The *Costamante* model indicates a flux of $\mathcal{F}_{\mathrm{E>0.3\,TeV}} = 1.36 \times 10^{-11}\,\mathrm{cm}^{-2}\,\mathrm{s}^{-1}$. No prediction using the *modified-Fossati* or *Stecker* models are available. Previous observations of this source are reported by Whipple and HEGRA. Whipple (Horan et al., 2004) reports a flux upper limit of $\mathcal{F}_{\mathrm{E>0.3\,TeV}} < 1.37 \times 10^{-11}\,\mathrm{cm}^{-2}\,\mathrm{s}^{-1}$ and $\mathcal{F}_{\mathrm{E>0.3\,TeV}} < 16.80 \times 10^{-11}\,\mathrm{cm}^{-2}\,\mathrm{s}^{-1}$ from two separate observing seasons and $\mathcal{F}_{\mathrm{E>0.3\,TeV}} < 1.47 \times 10^{-11}\,\mathrm{cm}^{-2}\,\mathrm{s}^{-1}$ by de la Calle Pérez et al. (2003) from 2000-2002. Upper limits are also reported by Gammell (2004) with $\mathcal{F}_{\mathrm{E>0.3\,TeV}} < 2.19 \times 10^{-11}\,\mathrm{cm}^{-2}\,\mathrm{s}^{-1}$. HEGRA reports an upper limit of $\mathcal{F}_{\mathrm{E>1.09\,TeV}} < 42.5 \times 10^{-11}\,\mathrm{cm}^{-2}\,\mathrm{s}^{-1}$ in one hour of

observation which can be extrapolated to $\mathcal{F}_{\mathrm{E>0.3\,TeV}} < 255.4 \times 10^{-11}\,\mathrm{cm}^{-2}\,\mathrm{s}^{-1}$ to compare with the Whipple result and *Costamante* prediction. Neither the Whipple nor the HEGRA results constrains the *Costamante* model (although one of the Whipple upper limits is very close).

7.7.5 1ES 2344+514

The blazar 1ES 2344+514 was discovered using the NRAO Green Bank 91-m telescope at 4.85 GHz by Becker et al. (1991) with x-ray emission reported in the Einstein Slew Survey by Elvis et al. (1992). The galaxy has a measured redshift of 0.04 (Padovani and Giommi, 1995), and is the closest of the three blazars observed in this work. Radio images with the VLBA (Rector et al., 2003) show a jet extending to the southeast. It appears to be well collimated for about 10 parsec before bending at 25° to the south and broadening into a cone with a 35° opening angle (Figure 7.11(f)). VHE emission predictions only exist for the *Stecker* model, giving $\mathcal{F}_{\mathrm{E>0.3\,TeV}} = 0.61 \times 10^{-11}\,\mathrm{cm}^{-2}\,\mathrm{s}^{-1}$. Predictions for the *Costamante* and *modified-Fossati* models are not available as TeV emission from 1ES 2344+514 had in fact been reported by Whipple (Catanese et al., 1998; Schroedter et al., 2005) by the time those predictions were published. The Whipple detection of TeV emission from 1ES 2344+514 comes mostly from an apparent flare in December 1995 with flux $\mathcal{F}_{\mathrm{E>0.35\,TeV}} = 6.6 \times 10^{-11}\,\mathrm{cm}^{-2}\,\mathrm{s}^{-1}$. Excluding the flare, observations during the rest of the 1995/1996 season resulted in a $4\,\sigma$ detection with flux $\mathcal{F}_{\mathrm{E>0.35\,TeV}} = 1.1 \times 10^{-11}\,\mathrm{cm}^{-2}\,\mathrm{s}^{-1}$ over 25 hours of observations. Further observations in the 1996/1997 season did not show any evidence of TeV emission, with a flux upper limit of $\mathcal{F}_{\mathrm{E>0.35\,TeV}} = 0.82 \times 10^{-11}\,\mathrm{cm}^{-2}\,\mathrm{s}^{-1}$ over 16 hours of observations placed on the data. This upper limit is extrapolated to 0.3 TeV giving a flux upper limit of $\mathcal{F}_{\mathrm{E>0.3\,TeV}} = 1.03 \times 10^{-11}\,\mathrm{cm}^{-2}\,\mathrm{s}^{-1}$. TeV emission from 1ES 2344+514 was confirmed by HEGRA (Aharonian et al., 2004a) with $\mathcal{F}_{\mathrm{E>0.97\,TeV}} = 0.08 \times 10^{-11}\,\mathrm{cm}^{-2}\,\mathrm{s}^{-1}$ over 72 hours of observations. This is extrapolated to $\mathcal{F}_{\mathrm{E>0.3\,TeV}} = 0.34 \times 10^{-11}\,\mathrm{cm}^{-2}\,\mathrm{s}^{-1}$ which is lower than the prediction of the *Stecker* model. Finally, the MAGIC collaboration reported a detection of 1ES 2344+514 Albert (2006b) from data taken from August 2005 and January 2006. They report an integral flux of $\mathcal{F}_{\mathrm{E>0.2\,TeV}} = 2.38 \times 10^{-11}\,\mathrm{cm}^{-2}\,\mathrm{s}^{-1}$ and fit the data with a power law of photon index $\alpha = -2.95$ between 0.14 TeV and 5.4 TeV.

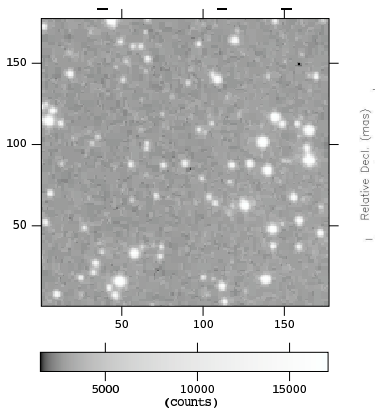

(a) 1ES 0647+250 Optical

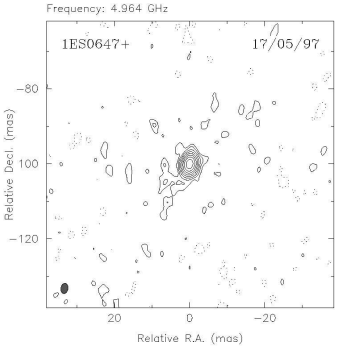

(b) 1ES 0647+250 Radio

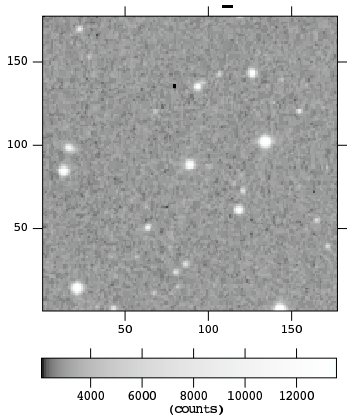

(c) 1ES 0806+524 Optical

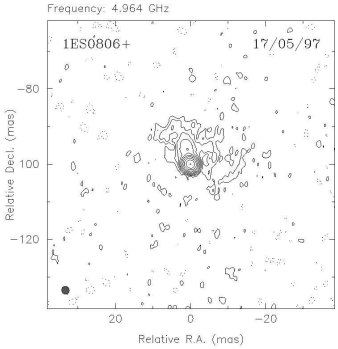

(d) 1ES 0806+524 Radio

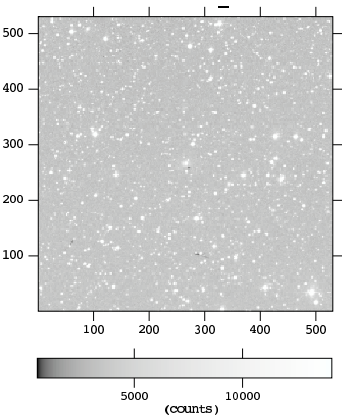

(e) 1ES 2344+514 Optical

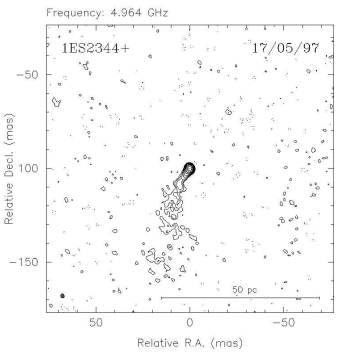

(f) 1ES 2344+514 Radio

Figure 7.11: Optical and radio images of the blazars 1ES 0674+250, 1ES 0806+524 and 1ES 2344+514. The optical data were obtained with the Palomar Schmidt 48 inch telescope. In each image, the blazar is at the center of the field of view. The radio images were taken with the VLBA - see text for discussion.

7.8 Analysis of Blazar Data

The blazar data are analysed using the settings and cuts detailed in Table 7.10. As with the Crab Nebula dataset, stringent quality control are applied to the data, with the trigger rate for each run individually examined. The results of the analysis are detailed in Table 7.12. No emission is detected from the putative source position for any of the objects observed.

Source	Exposure (mins)	Signal	Background	Excess	Significance
1ES 0647+250	781	1439	1400	39	$1.00\,\sigma$
1ES 0806+524	281	393	360	33	$1.54\,\sigma$
1ES 2344+514	412	537	530	37	$0.27\,\sigma$

Table 7.12: Results of analysis of blazar datasets.

7.8.1 Calculation of Upper Limits

Using the Crab Nebula spectrum reported by Aharonian (2006e), an upper limit on the emission of VHE gamma rays from the three observed AGN can be derived. The upper limit is found from the probability density function of the number of source counts (Helene (1983)). The excess events upper limit, C^{UL} is given by the solution of

$$\alpha\, I\left(\frac{-C}{\sigma}\right) = I\left(\frac{C^{\mathrm{UL}} - C}{\sigma}\right) \tag{7.7}$$

where α is the confidence level percentage p expressed as $1 - \frac{p}{100}$, C is the number of excess counts (signal counts - background counts), σ is given by

$$\sigma = \sqrt{(\text{signal counts}) + (\text{background counts})} \tag{7.8}$$

and the function I is given by

$$I(z) = \frac{1}{\sqrt{2\pi}} \int_z^{\infty} e^{-x^2/2}\,\mathrm{dx} \tag{7.9}$$

The energy threshold for the analysis is found using the dataset of Monte-Carlo gamma-ray simulations (Section 7.2) to be 0.19 TeV. This is demonstrated in Figure 7.15(a) which shows the number of triggered simulated gamma rays for each energy, and the number which pass cuts. In order to calculate the upper limits at 0.3 TeV, it is preferable to shift the analysis energy threshold closer to 0.3 TeV (rather than calculating the upper limits

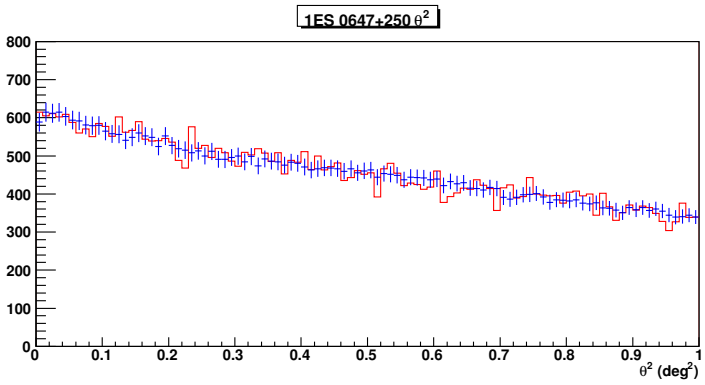

(a)

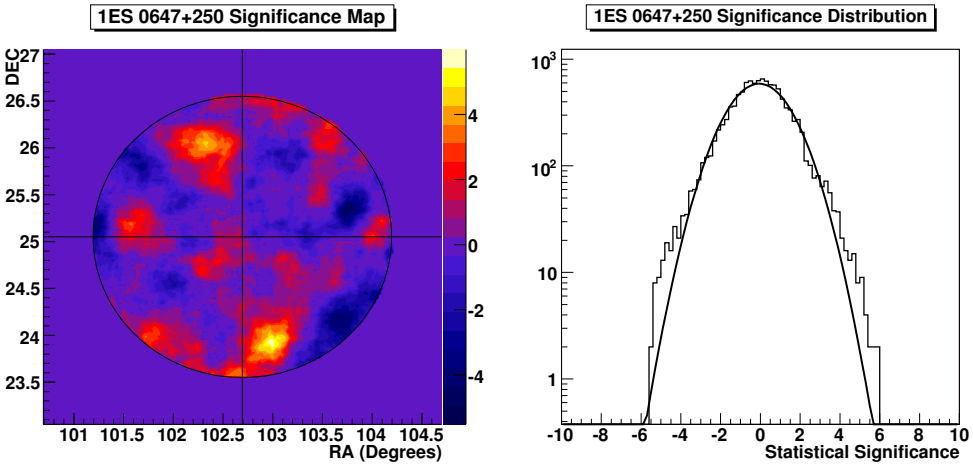

(b) **(c)**

Figure 7.12: Analysis plots for 1ES 0647+250. Figure (a) shows the θ^2 plot with no excess at the putative source position. Figure (b) shows the significance map of the region surrounding 1ES 0647+250 - although emission at the $4\,\sigma$ level appears to present - this can be discounted as there is no correction for trials, and the distribution of significances (Figure (c)) does not show an excess on the positive side.

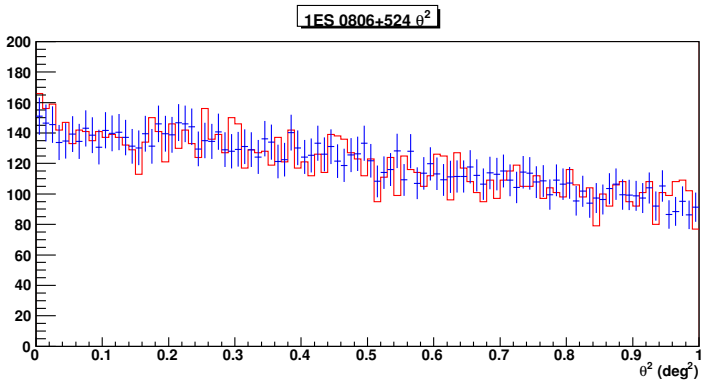

(a)

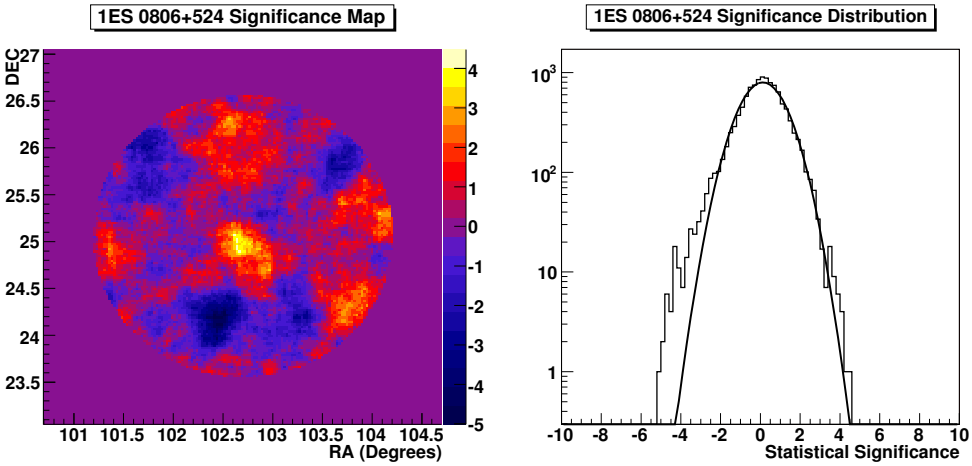

(b) (c)

Figure 7.13: Analysis plots for 1ES 0806+514. Figure (a) shows the θ^2 plot with no excess at the putative source position. Figure (b) shows the significance map of the region surrounding 1ES 0806+524 - although emission at the $4\,\sigma$ level appears to present - this can be discounted as there is no correction for trials, and the distribution of significances (Figure (c)) does not show an excess on the positive side.

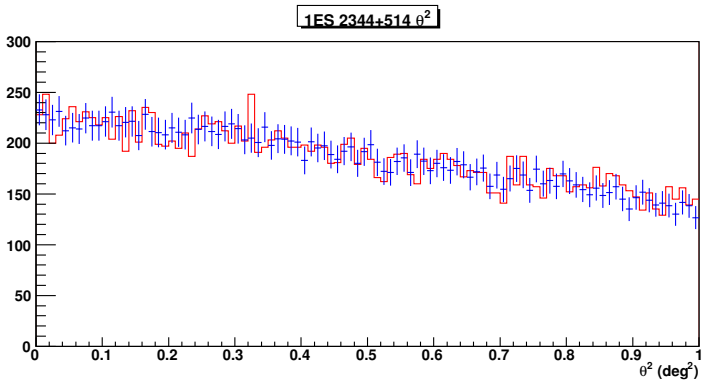

(a)

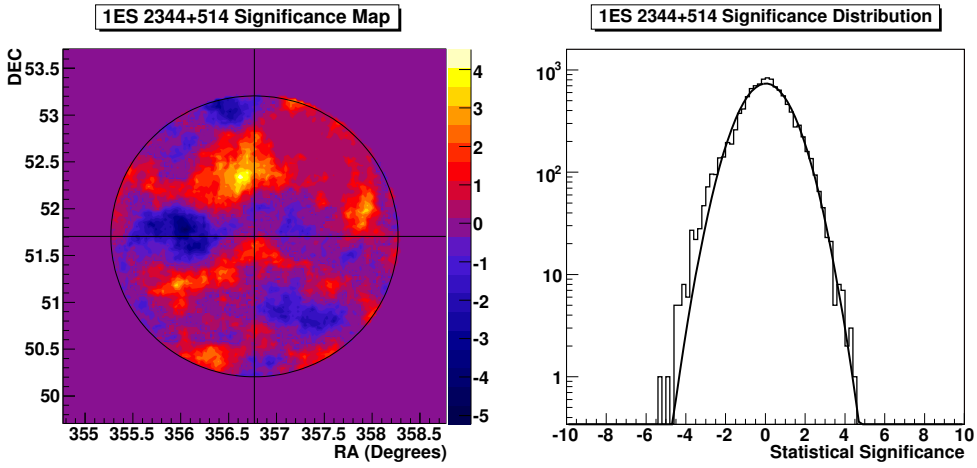

(b) (c)

Figure 7.14: Analysis plots for 1ES 2344+514. Figure (a) shows the θ^2 plot with no excess at the putative source position. Figure (b) shows the significance map of the region surrounding 1ES 2344+514 - although emission at the $4\,\sigma$ level appears to present - this can be discounted as there is no correction for trials, and the distribution of significances (Figure (c)) does not show an excess on the positive side.

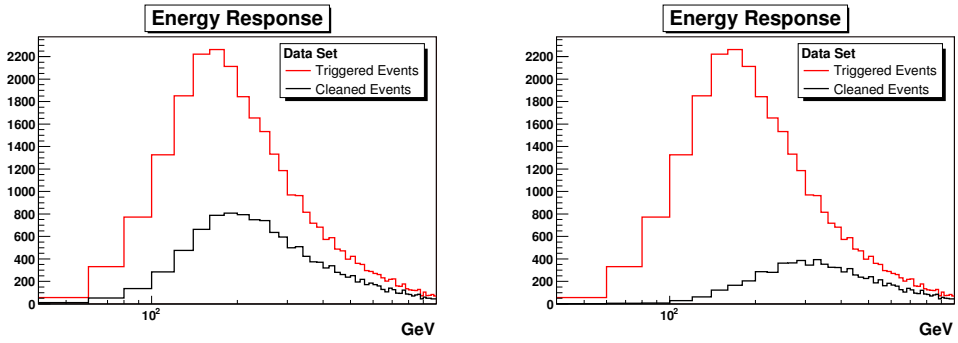

(a) Number Image Tubes>5 **(b)** Number Image Tubes>9

Figure 7.15: Energy threshold calculated using Monte-Carlo simulations of gamma rays. The energy threshold can be changed by adjusting the cut on the number of tubes in the image. The left figure has a cut of $NTubes > 5$ giving an energy threshold of 190 GeV whereas the right figure has a cut of $NTubes > 9$ giving an energy threshold of 330 GeV.

at 0.19 TeV and upscaling the limits). This is done by setting the cut on the minimum number of tubes in the image to 9. This results in an energy threshold of 0.33 TeV. Using this new cut, the Crab Nebula dataset and the three blazar datasets are reanalysed, with the results displayed in Tables 7.13 and 7.14.

Parameter	Value
Signal Counts	3821
Background Counts	550
Excess	3271
Significance	73 σ
Rate	2.25 ± 0.03

Table 7.13: Results of reanalysis of Crab Nebula dataset with a cut of $NTubes > 9$.

Using equation 7.7 with $\alpha = 0.999$ (to achieve a 99.9% confidence level), the upper limit on the number of counts and gamma-ray rate is given in Table 7.15 for an energy threshold of 0.33 TeV.

In order to convert the count upper limit into a flux upper limit, the gamma-ray rate can be compared to that of the Crab Nebula dataset. The

Source	Exposure (mins)	Signal	Background	Excess	Significance
1ES 0647+250	781	332	314	18	$0.95\,\sigma$
1ES 0806+524	281	88	70	18	$1.8\,\sigma$
1ES 2344+514	412	130	127	3	$0.21\,\sigma$

Table 7.14: Results of reanalysis of blazar datasets with a cut of $NTubes > 9$.

Source	$C^{\rm UL}_{\rm E>0.33\ TeV}$	$C^{\rm UL}_{\rm E>0.33\ TeV}$/min
1ES 0647+250	99	0.127
1ES 0806+524	57	0.203
1ES 2344+514	55	0.133

Table 7.15: Count upper limit above 0.33 TeV for the blazar datasets.

gamma-ray rate for the Crab Nebula dataset is $\gamma_{\rm Crab} = 2.25\,\gamma$ /min (from Table 7.13). Thus the flux upper limit above 0.3 TeV is given by

$$\mathcal{F}^{\rm UL}_{\rm E>0.33\ TeV} = \frac{C^{\rm UL(E>0.33\ TeV)}}{\gamma_{\rm Crab(E>0.33\ TeV)}} \times \mathcal{F}_{\rm Crab>0.33\ TeV} \tag{7.10}$$

where

$$\mathcal{F}_{\rm Crab>0.33\ TeV} = 3.76 \times 10^{-11}\ {\rm cm}^{-2}\,{\rm s}^{-1}\,{\rm TeV}^{-1} \int_{0.33}^{\infty} {\rm E}^{-2.39}\,d{\rm E} \tag{7.11}$$

Note that although the spectrum measured by Aharonian (2006e) is only given from 0.41 TeV, there is no evidence for deviation from a power law from other experiments down to 0.3 TeV (Section 1.4.1). The scaling law described in Equation 7.5 is used to convert from a flux upper limit above 0.33 TeV to a flux upper limit above 0.3 TeV. The results are shown in Table 7.16 with the predictions from the *Costamante*, *modified-Fossti* and *Stecker* models shown for comparison.
Finally, the differential flux upper limit at 0.33 TeV can be calculated from

$$\frac{d\mathcal{F}}{dE} = \frac{C^{\rm UL}_{\rm E>0.33\ TeV}}{\gamma_{\rm Crab(E>0.33\ TeV)}} \times E^{-\alpha} \tag{7.12}$$

where E = 0.33 TeV and $\alpha = 2.39$. The energy of 0.33 TeV corresponds to $\log(\nu) = 25.9$, and can be used to visually compare the flux predictions published by Costamante and Ghisellini (2002). The differential flux predictions for the three blazars are shown in Table 7.17 and Figures 7.16 and 7.17.

Source	$\mathcal{F}^{\rm UL}_{\rm E>0.33\ TeV}$	$\mathcal{F}^{\rm UL}_{\rm E>0.3\ TeV}$	*Costamante*	*modified-Fossati*	*Stecker*
1ES 0647+250	0.713	0.813	0.59	0.24	-
1ES 0806+524	1.14	1.3	1.36	-	-
1ES 2344+514	0.73	0.85	-	-	0.61

Table 7.16: Comparison of derived upper limits of the flux above 0.3 TeV with predicted flux emission from the *Stecker*, *modified-Fossati* and *Costamante* models. All data are in units of 10^{-11} cm^{-2} s^{-1}.

Source	$d\mathcal{F}^{\rm UL}/dE$ at $E = 0.33$ TeV
1ES 0647+250	4.81
1ES 0806+524	7.69
1ES 2344+514	5.04

Table 7.17: Upper limits on the differential flux at $E = 0.33$ TeV for the three blazars observed in this work. All limits are in units of 10^{-11}ergs cm^{-2} s^{-1}.

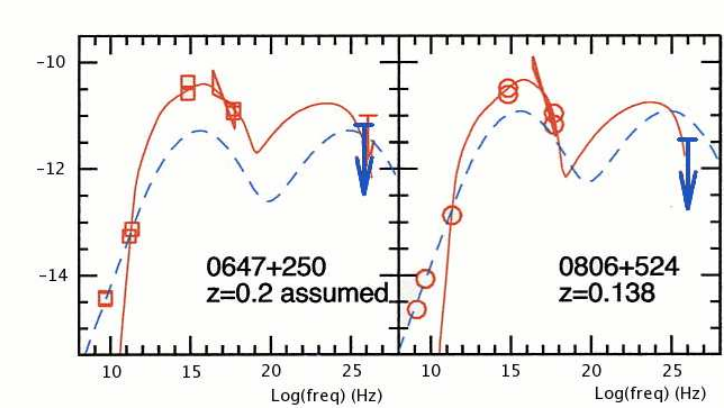

Figure 7.16: Spectral energy distribution of 1ES 0647+250 and 1ES 0806+524 from Costamante and Ghisellini (2002), with the upper limits from this work overlaid in blue. The veritical axis displays $\log \nu F_\nu$ in units of erg cm^{-2} s^{-1}.

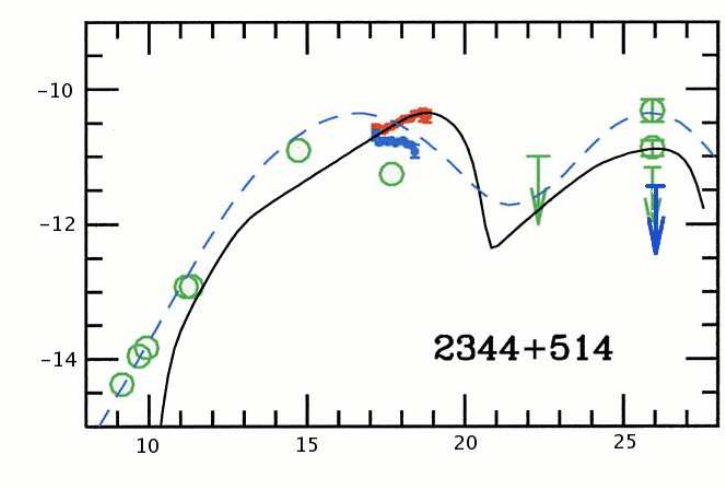

Figure 7.17: Spectral energy distribution of 1ES 2344+514 from Costamante and Ghisellini (2002), with the upper limits from this work overlaid in blue. The veritical axis displays $\log \nu F_\nu$ in units of erg cm^{-2} s^{-1}..

7.9 Comparison With X-Ray Data

As these data were taken without dedicated multiwavelength observations it is difficult to constrain emission models, beyond what has been done for the *Stecker*, *modified-Fossati* and *Costamante* scenarios. Nevertheless, as these objects are regularly monitored by the All Sky Monitor (ASM) on the Rossi X-Ray Timing Explorer (RXTE)[7] it is useful to examine the x-ray flux (in the 2-12 keV energy band) during the observing periods to determine whether an increase in TeV flux should have been expected in the context of the SSC model. As a baseline comparison, the x-ray flux from the Crab Nebula is shown in Figure 7.18 for the September to December 2006 observing period, with a simple linear fit indicating a count rate of 73.5 ± 0.1 counts per minute. Each datapoint corresponds to the daily average computed from each 90 second dwell.

The x-ray emission from 1ES 0647+250, 1ES 0806+524 and 1ES 2344+514 are shown in Figure 7.19 for the same baseline time period. The VERITAS observing windows are overlaid in red. By chance, the x-ray emission from 1ES 0647+250 appears to be in an enhanced state during one of the VERITAS observing periods. This is shown in finer detail in Figure 7.20 which indicates the individual VERITAS data runs. There is a single 90 second data point from the ASM concurrent with one VERITAS data run. The rel-

[7]ASM Quicklook data from http://xte.mit.edu/ASM_lc.html

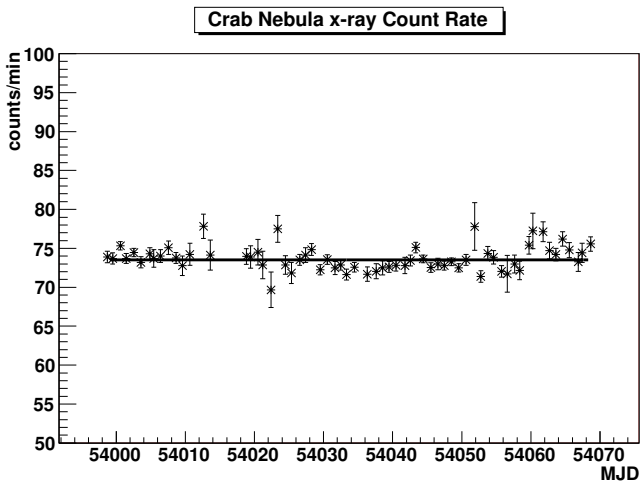

Figure 7.18: Rate of emission from the Crab Nebula measured by the All Sky Monitor onboard the Rossi X-Ray Timing Explorer. A flat line is used to measure a rate of 73.5 ± 0.1 counts/min.

evant VERITAS data run started at MJD 54058.461379 and ended at MJD 54058.475296. The ASM data was taken at 54058.468652, which is roughly in the middle of the VERITAS data run.

The VERITAS data are analysed for that single run, with the results summarised in Tables 7.18, 7.19 and 7.20. No excess of emission is found during this run, and a flux upper limit of $\mathcal{F}^{\mathrm{UL}}_{\mathrm{E>0.3\,TeV}} = 6.08 \times 10^{-11}\,\mathrm{cm}^{-2}\,\mathrm{s}^{-1}$ is placed on the emission during that phase. These results are discussed further in the next section.

Source	Exposure (mins)	Signal	Background	Excess	Significance
1ES 0647+250	20	29	42	-	-

Table 7.18: Result of the analysis of the data taken on 1ES 0647+250 during the enhanced x-ray emission on MJD 54058.

Source	C^{UL}	Exposure	C^{UL}/min
1ES 0647+250	19	20	0.95

Table 7.19: Upper limits on the count rate of the data taken on 1ES 0647+250 during the enhanced x-ray emission on MJD 54058.

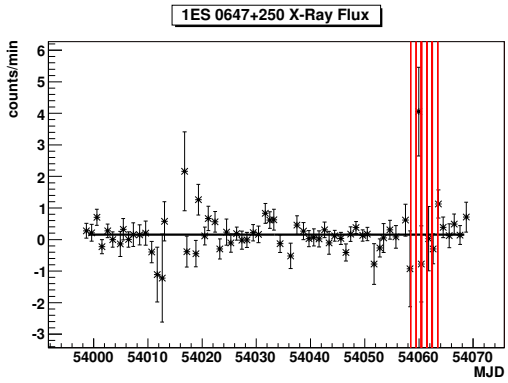

(a) 1ES 0647+250

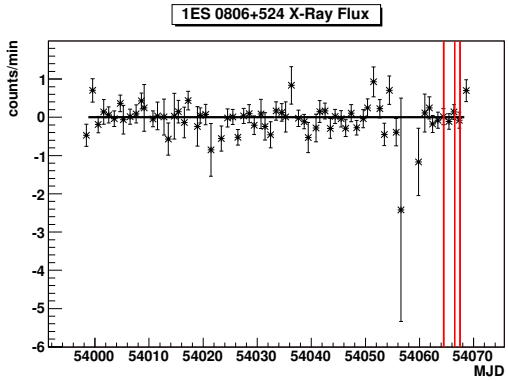

(b) 1ES 0806+524

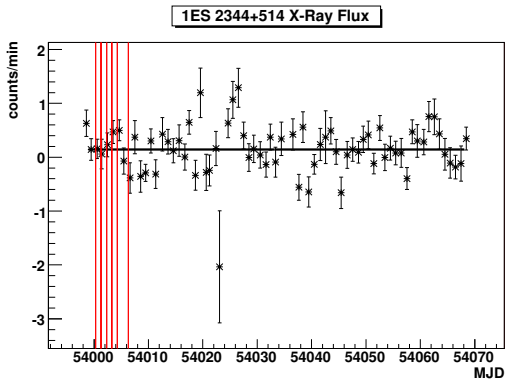

(c) 1ES 2344+514

Figure 7.19: Light curve in x-rays from the ASM on the RXTE during the observing period September-December 2006 for 1ES 0647+250, 1ES 0806+524 and 1ES 2344+514. There is no enhanced emission from any object apart from 1ES 0647+250, which is concurrent with one of the VERITAS observing runs (see Figure 7.20).

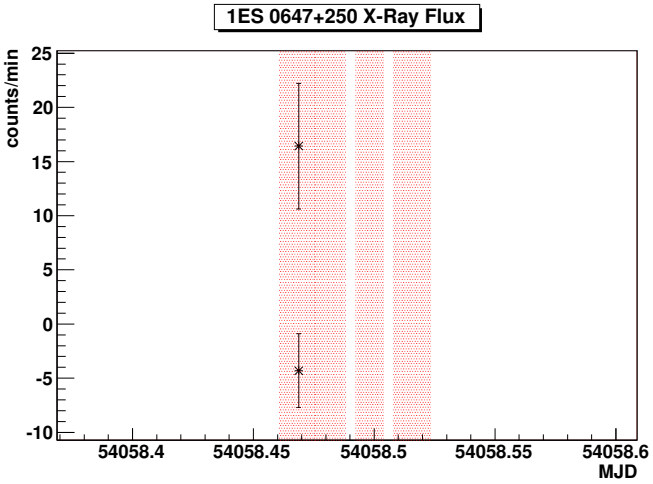

Figure 7.20: Light curve in x-rays from the ASM on the RXTE during one night of VERITAS observing of 1ES 0647+250. The VERITAS observing periods are indicated by the red shaded regions. The data points are 90 second dwells.

Source	$\mathcal{F}^{\mathrm{UL}}_{\mathrm{E>0.3\,TeV}}$	$d\mathcal{F}^{\mathrm{UL}}/dE$ at E = 0.33 TeV
1ES 0647+250	6.08	35.99

Table 7.20: Upper limits on the flux above 0.3 TeV and the differential flux at 0.33TeV of the data taken on 1ES 0647+250 during the enhanced x-ray emission on MJD 54058. The flux upper limit is in units of $10^{-11}\,\mathrm{cm}^{-2}\,\mathrm{s}^{-1}$, and the differential flux upper limit is in units of $10^{-11}\,\mathrm{erg}\,\mathrm{cm}^{-2}\,\mathrm{s}^{-1}$.

7.10 Discussion

The analysis of the blazars 1ES 0647+250, 1ES 0806+524 and 1ES 2344+514 has been covered in this chapter. Although a relatively small amount of data have been taken on these sources, interesting upper limits have been placed on their emission. These upper limits will be discussed in this section.

7.10.1 1ES 0647+250

The only upper limit in the TeV regime published to date on this source is by Aharonian et al. (2004a). After scaling (and assuming a power law spectrum with the Crab Nebula index), the upper limit corresponds to $\mathcal{F}_{\mathrm{E>0.3\,TeV}} < 126.4 \times 10^{-11}\,\mathrm{cm}^{-2}\,\mathrm{s}^{-1}$, whereas the flux upper limit reported in this work is $\mathcal{F}_{\mathrm{E>0.3\,TeV}} < 0.813 \times 10^{-11}\,\mathrm{cm}^{-2}\,\mathrm{s}^{-1}$. Although this upper limit is a significant improvement on that reported by Aharonian et al. (2004a), it falls just short of constraining the *Costamante* and *modified-Fossati* models. It is expected that when VERITAS telescopes 3 and 4 come online - these limits should be passed with just a few hours of data taking - indeed with the lower energy threshold and superior sensitivity that will be available, it is hoped that the blazar will be detected. 1ES 0647+250 is the only blazar to have displayed an excess in the RXTE ASM daily average x-ray light curve. Given the sparsity of the VERITAS sampling (Figure 7.19(a)), it is fortuitous that the 90 second dwell which revealed the enhanced x-ray emission occurred during a VERITAS observing run. Furthermore, no excess in VHE gamma rays were detected with either sets of cuts described in this chapter during the run that coincided with the ASM dwell. Although it cannot be ruled out that the a VHE excess was present below the level of detectability of the array, the detection of an orphan x-ray excess has interesting consequences for the Synchrotron Self Compton models. The relationship between x-ray and gamma-ray flux is already known to be complex, with both orphan gamma-ray, orphan x-ray and correlated gamma-ray/x-ray flares reported(see Section 3.9).

7.10.2 1ES 0806+524

Several upper limits ranging from $\mathcal{F}_{\mathrm{E>0.3\,TeV}} < 1.37 \times 10^{-11}\,\mathrm{cm}^{-2}\,\mathrm{s}^{-1}$ to $\mathcal{F}_{\mathrm{E>0.3\,TeV}} < 255.4 \times 10^{-11}\,\mathrm{cm}^{-2}\,\mathrm{s}^{-1}$ have been published on this source (Section 7.7.4). All of these limits have failed to constrain the flux prediction by Costamante and Ghisellini (2002) of $\mathcal{F}_{\mathrm{E>0.3\,TeV}} = 1.36 \times 10^{-11}\,\mathrm{cm}^{-2}\,\mathrm{s}^{-1}$. Thus, the upper limit of $\mathcal{F}_{\mathrm{E>0.3\,TeV}} < 1.3 \times 10^{-11}\,\mathrm{cm}^{-2}\,\mathrm{s}^{-1}$ reported in this work is the first to constrain the flux prediction of the *Costamante* model.

Although the prediction is broken, the implications are not necessarily severe for the SSC model. As already discussed, the prediction of TeV fluxes is extremely sensitive to small variations in model parameters such as radio and x-ray flux. The flux prediction was built from multiwavelength data on a source that is known to exhibit variability. Thus the flux at the lower energy region of the 1ES 0806+524 SED may have been different during these VERITAS observations, than it was when the multiwavelength data from which the model was built.

The blazars 1ES 0806+524 and 1ES 0647+250 will continue to be targets for northern hemisphere ground-based Cherenkov telescopes, as they are among the most promising targets according to the Costamante and Ghisellini (2002) paradigm. These predictions have already resulted in the detection of several new blazars, resulting in new constraints on emission models and the density and shape of the extragalactic infrared background.

7.10.3 1ES 2344+514

The blazar 1ES 2344+514 is the only one of the three blazars studied in this work to have been previously detected at very-high energies. The recent detection of 1ES 2344+514 by the MAGIC telescope put into context the apparent long-term variability of the source (Figure 7.21), thus it is not necessarily surprising that no detection can be reported here. The flux reported by MAGIC corresponds to 4% to 6% of the Crab Nebula flux above 0.35 TeV. The upper limit from 1ES 2344+514 reported here corresponds to 5.7% of the crab flux, assuming a crab-like spectrum above 0.35 TeV.

Variability across the spectrum on both short and long timescales is one of the key characteristics of blazars. While this variability makes them amongst the most interesting astrophysical sources, it also makes them one of the most difficult sources to study. Observations at one wavelength are virtually meaningless in the context of constraining models and understanding emission mechanisms, as models must be understood in terms of emission across the spectrum. The multiwavelength variability of 1ES 2344+514 is further evidenced by the radio measurements reported by Nieppola et al. (2006) using the Metsähovi Radio Observatory Bl Lacertae sample. In this paper, the synchrotron peak for 1ES 2344+514 is measured at $\log \nu = 16.4$, resulting in the classification of 1ES 2344+514 as an Intermediary Bl Lac (see Section 3.6). This is not necessarily in conflict with the paradigm that only HBLs emit in the TeV regime, as 1ES 2344+514 has been previously measured to have a synchrotron peak at $\log \nu = 17 - 18$ (Giommi et al., 2000), implying that this object exhibits extreme spectral variability. 1ES 2344+514 is not the only TeV blazar with such characteristics. Markarian 501, which was first

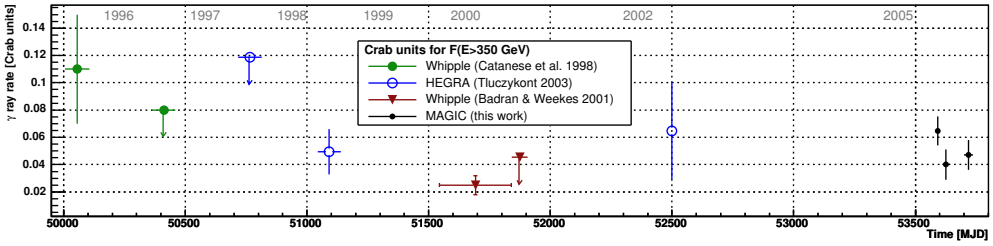

Figure 7.21: Long term variability of 1ES 2344+514 demonstrated by Albert (2006b).

detected at TeV energies by the Whipple 10m (Quinn et al., 1996, 1997) has had a synchrotron peak as high as $\log \nu = 19$ (Pian et al., 1998), but only has a synchrotron peak at $\log \nu = 16.84$ in the Nieppola et al. (2006) survey. The implications of this synchrotron spectral variability is that the radio observations carried out during one epoch, are not necessarily a good indicator of TeV emission in another. More specifically, those sources (especially so-called IBLs) that are ruled out as TeV candidates, could represent an entire catalogue of missed opportunities. Clearly a better understanding of the spectral shifting that occurs across the electromagnetic spectrum is required, before the catalogue of extragalactic VHE sources can be significantly expanded. Some progress towards this goal may already be taking place, with the recent discovery of VHE emission from PG 1553+113 (Albert, 2006a; Aharonian et al., 2006a) which is classified as an IBL by the Nieppola et al. (2006) survey and as an HBL by Giommi et al. (2000).

7.11 Conclusions

This chapter has presented a first analysis of the Crab Nebula with the VERITAS array. The sensitivity attained, after optimisation on the trace integration, Picture/Boundary thresholds and stereo cuts is almost three times that attained with the Whipple 10m. The blazars 1ES 0647+250, 1ES 0806+524 and 1ES 2344+514 were observed and analysed as part of this work. Although no emission was found from any of the sources, upper limits have been placed on TeV emission that are lower than some hitherto published upper limits on these sources, and in the case of 1ES 0806+514 is lower than the flux predicted by the *Costamante* model. The x-ray emission during the VERITAS observing periods was also examined for enhanced x-ray activity. In most cases, the x-ray activity was very low, however one of the VERITAS observing runs on 1ES 0647+524 occurred during an apparent

period of enhanced x-ray emission. No emission was detected by VERITAS during this period, and flux upper limits have been placed on the emission during that run.

Chapter 8

Conclusions and Outlook

The last twenty years has seen rapid development in the field of ground-based very high-energy gamma-ray astronomy. In 1986, the first confirmed source of very high-energy gamma rays had not yet been detected, and there was only one observatory with sufficient energy threshold and sensitivity to conceivably detect very high-energy gamma rays. In 2006, the total number of detected sources exceeds thirty, and there are four major third-generation ground-based observatories operational or nearing completion.

This thesis has concerned the development of new methodologies for analysing VERITAS data, and the analysis of the first blazar data taken while the array was being commissioned. Although telescopes one and two of the VERITAS array were essentially complete, VERITAS was still in 'engineering mode' while telescope three was being commissioned, and telescope four was being built. Despite these obstacles, a suite of analysis tools for the analysis of the raw FADC data have been developed and applied to observation of the Crab Nebula and the blazars 1ES 0647+250, 1ES 0806+524 and 1ES 2344+514.

8.1 Analysis of FADC Data

The VERITAS telescopes are equipped with 500 Mega-samples-per-second FADCs which are capable of sampling the Cherenkov light from extensive air showers every two nanoseconds. These data provide unique insight into the development of extensive air showers. A special set of tools called *trace evaluators* were developed for analysing these data. These are the *simple-window*, *dynamic-window*, *linear-interpolation*, *matched-filter*, *trace-fit* and *timing-gradient* trace evaluators.

The first study involved calculation of the optimal FADC window inte-

gration parameters for the *simple-window* and *dynamic-window* trace evaluators. It was found that placing just 10% of the integration window before the average T_{zero} location, and integrating over 6 samples for large pulses and 8 samples for small pulses achieves an optimal signal-to-noise ratio. It is also found that for the *dynamic-window* trace evaluator, the optimal integration window size for small pulses is 2 samples, and 4 samples for large pulses. It was found that the signal-to-noise ratio for the *dynamic-window* trace evaluator was superior to the *simple-window* trace evaluator.

It was found that the *matched-filter* and *dynamic-window* trace evaluators have superior charge resolution, and that the charge resolution improves as a function of pulse size when compared to the *simple-window* trace evaluator. A Gaussian fit was applied to the charge distribution calculated by each trace evaluator, and a reduced-χ^2 test used to determine whether any of the trace evaluators generated a more Gaussian-like distribution. It was found that all the evaluators produced similar results for that test.

The *linear-interpolation* trace evaluator was found to be the most robust tool for determining trace timing parameters such as the T_{zero} arrival time of the trace, achieving a timing resolution of 0.51 nanoseconds for large pulses. However, for small pulses the *matched-filter* trace evaluator had the best timing resolution, whereas for large pulses the *trace-fit* trace evaluator had the best timing resolution. As a result of these tests, the *linear-interpolation* trace evaluator was used when determining the trace timing parameters for the *timing-gradient* trace evaluator.

The charge resolution and signal-to-noise ratio inherent to each trace evaluator was studied using a series of special laser calibration runs, and a Crab Nebula observation run. It was found that the *dynamic-window*, *matched-filter* and *trace-fit* trace evaluators calculated more charge than the *simple-window* trace evaluator. However after the effect of the pedvar was taken into account by comparing the signal-to-noise ratio, it was found that the *dynamic-window* and *trace-fit* trace evaluators were no better (if not worse) than the *simple-window* trace evaluator. The signal-to-noise ratio for the *timing-gradient* evaluator was very similar to that of the *simple-window* trace evaluator. This study indicated that the use of advanced algorithms did not appear to improve the signal-to-noise ratio that could be extracted from an FADC pulse.

It is important to make an accurate calculation of the charge in each channel so that the image can be parameterised properly. The effect on image parameterisation of the charge integrated by each trace evaluator is studied by comparing the number of tubes passing image cleaning. It was found that, compared to the *simple-window* trace evaluator, the *dynamic-window* and *matched-filter* trace evaluators had, on average, more channels

passing image cleaning. It was determined that this was due to the extra charge calculated by those evaluators. However, the more relevant test of the quality of the trace evaluator is whether the reconstructed image is superior. This was tested using a database of Monte-Carlo simulations of gamma-ray initiated extensive air showers. In principle, the primary axis of the image should be oriented towards the center of the camera. By comparing *alpha*, the angle between the primary image axis and a line connecting the image centroid and the center of the field of view, the effect of image parameterisation from each trace evaluator can be studied. It was found that with more image tubes passing cleaning, the *matched-filter* and *dynamic-window* trace evaluators had less events with *alpha*$< 10^{\circ}$. This is attributed to the inclusion of spurious or noisy pixels in the image, thus degrading the image quality. In contrast the *timing-gradient* trace evaluator had the highest number of events with *alpha*$< 10^{\circ}$. Following on from these results, only the *simple-window* and *timing-gradient* trace evaluators were applied to the Crab Nebula and blazar datasets.

Methods to correct FADC timing jitter and to reconstruct the low-gain FADC channel have been successfully implemented. The FADC timing jitter is the result of minor clocking errors occurring in the synchronisation of the four FADC crates in each telescope. This effect is corrected by piping an asynchronous copy of the Level 2 trigger signal directly into the FADC crates. The effect of this correction on the timing resolution has been demonstrated. Reconstruction of the low-gain FADC channel has been shown to be a difficult operation. It has been shown that the high-gain pedestals cannot be used in the analysis of low-gain data, and that the usual integration windows used by the *simple-window* and *dynamic-window* trace evaluators cannot be employed. A method for accurately calculating the low-gain pedestals is described and implemented and a modified *dynamic-window* trace evaluator is developed and used to ensure good continuity between the low-gain and high-gain charge distributions.

A digital signal processing technique called *resampling* in the time domain is applied to the FADC data. This technique involves using Fourier transforms of the FADC data to artificially set high frequencies to have zero amplitude. This effectively allows a resampling of the FADC data with arbitrary accuracy. For this study, an accuracy corresponding to 250 picoseconds is attained. This technique is best applied to data for which highly accurate timing resolution is required. It is found that when combined with the *linear-interpolation* trace evaluator, that the resampling technique results in a timing resolution of 0.09 nanoseconds.

A new parameter termed χ^2_{array} is introduced which assesses the self-consistency of FADC traces. This technique is adopted from Konopelko

(1991) and adapted in this dissertation to stereoscopic data for the first time. The parameter was applied to a dataset of Monte-Carlo simulations of gamma-ray and proton-initiated air showers. It was found that there was no significant difference between the parameter distributions and that there was no potential to use it as a discriminant for VERITAS data. However, upcoming third generation Cherenkov telescopes such as MAGIC-II, which will employ 2 Giga-samples-per-second FADCs could use the technique to improve background rejection.

8.2 Analysis of Crab Nebula and Blazar Data

The tools that have been described have been written in C++ and implemented into the VERITAS offline analysis suite *VEGAS* . *VEGAS* is a six-stage program, with the design, development, implementation and testing of Stage 2 an integral part of this thesis dissertation. The software developed was used to optimise the analysis of Crab Nebula data using the *simple-window* and *timing-gradient* trace evaluators. Following a deep optimisation procedure requiring some 40 'computer-days' of processing, it was found that placement of the *simple-window* trace evaluator with 10 % of the integration window behind the average T_{zero} of the trace achieved optimal sensitivity. Optimisation of the Picture/Boundary thresholds, mean scaled width, mean scaled length and signal integration ring size were also performed. The result of these optimisations resulted in the achievement of a sensitivity corresponding to $14.42\,\sigma/\sqrt{\text{hour}}$ on the Crab Nebula.

The optimised analysis was applied to the observations of the blazars 1ES 0647+250, 1ES 0806+524 and 1ES 2344+514. Despite the impressive sensitivity achieved with the two-telescope stereoscopic analysis, very high-energy gamma-ray emission was not detected from these objects. Nevertheless interesting upper limits were placed on their emission above an imposed energy threshold of 0.3 TeV.

Three models used to predict very high-energy gamma-ray emission from blazars are reviewed, they are referred to as the *Costamante*, *modified-Fossati* and *Stecker* models. These predictions are compared to previous upper limits (and detections in the case of 1ES 2344+514). In this work, an upper limit of $\mathcal{F}_{\text{E}>0.3\,\text{TeV}} < 0.813 \times 10^{-11}\,\text{cm}^{-2}\,\text{s}^{-1}$ is placed on emission from 1ES 0647+250. This upper limit is far lower than any quoted in the literature, but falls just short of constraining the *Costamante* and *modified-Fossati* models. Analysis of the RXTE All Sky Monitor Quicklook data revealed an x-ray enhancement during one of the VERITAS observing periods of 1ES 0647+250. Although the ASM exposure corresponded to only 90 seconds, the implica-

tions of enhanced x-ray emission on TeV emission has been well documented. The data from the corresponding VERITAS run was analysed, however no excess emission was detected.

The analysis of the 1ES 0806+525 data produced a flux upper limit of $\mathcal{F}_{\mathrm{E>0.3\,TeV}} < 1.3 \times 10^{-11}\,\mathrm{cm}^{-2}\,\mathrm{s}^{-1}$ of VHE emission from the source, which is marginally lower than the *Costamante* flux prediction of $\mathcal{F}_{\mathrm{E>0.3\,TeV}} = 1.36 \times 10^{-11}\,\mathrm{cm}^{-2}\,\mathrm{s}^{-1}$. Although this is the first time the *Costamante* prediction has been breached for this source, it is not the first time *Costamante* predictions have been breached for candidate blazars. The implications of the upper limit are not severe in the context of the one-zone SSC model used to predict the emission. Very high-energy flux predictions are tricky to create due to the inherent sensitivity of the second peak in the SED to minor changes in the first peak. That issue compounded with the fact that the VERITAS data lacks contemporaneous multiwavelength data limits the repercussions of this result.

The recent MAGIC detection of 1ES 2344+514 confirmed the blazar as a TeV emitter. The result also confirmed the long-term variability which was already suspected from this source. In that context the non-detection of the source, with a sensitivity corresponding to 5.7% of the Crab Nebula flux from this work is not surprising. The blazar 1ES 2344+514 belongs to a growing family of blazars whose synchrotron peak frequency appears to shift from the IBL regime of $\log(\nu) = 15 - 16$ to the HBL regime of $\log(\nu) = 17 - 18$. This result indicates an underlying mechanism which profoundly effects the detectability of blazars at very-high energies. It is possible that the entire population of so-called IBLs are capable of shifting their synchrotron peaks to higher energies in an unpredictable fashion. The detection of this behaviour is only recently becoming possible and could lead to a new understanding of the intrinsic properties of blazars.

8.3 Outlook

Ground-based very high-energy gamma-ray astronomy has entered a golden age as the number of sources has blossomed beyond thirty. The global coverage by four large arrays of complete or almost complete Cherenkov telescopes promises exciting results in the coming years. The remarkable results by the H.E.S.S. collaboration in the past three years have finally revealed the true potential of ground-based gamma-ray astronomy, and provide strong motivation for continued development in the field.

The VERITAS array of telescopes has been under development for the past three years. Telescopes one and two ran stably in the September-

December 2006 epoch resulting in a reliable detection of the Crab Nebula. During that time, Telescope three was being commissioned and Telescope four was under construction. It is expected that the full array will commence operations in Spring 2007.

The scientific program of VERITAS includes a strong emphasis on the observations of Northern-Hemisphere blazars, with multiwavelength campaigns with MAGIC, H.E.S.S. and various other ground-based and space-based observatories planned. It is expected that as optimal array sensitivity is achieved, these observations will reveal a new population of very-high energy gamma-ray sources in the Northern sky.

8.4 Final Summary

The first chapter of this thesis provides an overview of the current status of very high-energy gamma-ray astronomy, with an emphasis on the variety of source categories discovered thus far. The second chapter deals with the detection of very high-energy gamma rays using the ground-based imaging atmospheric Cherenkov technique. Chapter three provides a comprehensive review of blazars, covering AGN unification and leptonic and hadronic emission models. Chapter four describes the VERITAS array. A review of the standard analysis of VERITAS data is given in chapter five, with emphasis on the calculation and application of calibration data in the early stages of the analysis.

Chapter six concerned the development of methodologies to analyse FADC data. A suite of tools have been developed and integrated into the VERITAS offline analysis suite *VEGAS* . The tools have been tested with a selection of laser-calibration data runs and Crab Nebula observations runs. The analysis determined optimal methods for extracting a gamma-ray signal from the background dominated dataset by optimising the analysis on a large Crab Nebula dataset. This optimised analysis was applied to the first VERITAS blazar observations in chapter 7, resulting in the imposition of upper limits on VHE emission from 1ES 0647+250 and 1ES 0806+524 that are significantly better than those previously reported.

Appendix A

VERITAS Specifications

Array	Ideal Spacing	85 m
	Collection Area	$> 0.1\,\mathrm{km}^2$ for E > 1 TeV
	Energy Threshold	$< 100\,\mathrm{GeV}$
	Energy Resolution	$\Delta E/E < 0.15$
	Angular Resolution	$< 0.005^\circ$
Telescopes	Number	4
	Aperture	12 m
	Max Survivable Wind Load	160 Km/hr
	Pointing Accuracy	0.1° RMS
	Pointing Readout	$< 0.00275^\circ$ RMS
	Azimuth Range	$\pm 270^\circ$ from North
	Elevation Range	$0^\circ - 88^\circ$
Cameras	Pixels	499
	Field of View	3.5°
	PMT Quantum Efficiency	20 % at 300 nm
	PMT Rise Time	< 2 ns
	HV Range	$800 - 1500$ V
	HV Resolution	1 V
	HV Ripple	10 mV
	Preamplifier Gain	6.66
	Preamplifier Bandwidth	300 MHz

Table A.1: VERITAS Specifications Table I

Mirrors	Number per Telescope	350
	Radius of Curvature	$24\text{m} \pm 1\,\%$
	Reflectance	$> 90\,\%$ at 320 nm
	Alignment	$< 0.02^\circ$
FADC	Boards Per Telescope	50
	Sampling Rate	$500\,\text{Ms/s}^*$
	Dynamic Range	~ 1200
	Jitter	2 ns
	Dead Time per Event	$100\,\mu$s
L3	Maximum Input Rate	$< 100\,\text{kHz}$
	Dead Time	$< 1\,\%$ at 1 kHz
	Coincidence Window	$10 - 100\,\text{ns}$

Table A.2: VERITAS Specifications Table II

Appendix B

Acronyms

ADC	Analogue to Digital Converter
AGN	Active Galactic Nuclei
BATSE	Burst and Transient Source Experiment
BLRG	Broad Line Radio Galaxy
CCD	Charge-Coupled Device
CFD	Constant Fraction Discriminator
CGRO	Compton Gamma-Ray Observatory
DAT	Digital Asynchronous Transceiver
DC	Digital Counts
EGRET	Energetic Gamma-Ray Experiment Telescope
FADC	Flash Analog to Digital Converter
FOV	Field of View
FPGA	Field Programmable Gate Array
FSRQ	Flat Spectrum Radio Quasar
FR I	Fanaroff-Riley type I radio galaxy
FR II	Fanaroff-Riley type II radio galaxy
GPS	Global Positioning System
GRB	Gamma-Ray Burst
HBL	High frequency peaked Bl Lacertae
HPQ	Highly Polarised Quasar
HV	High Voltage
IBL	Intermediate frequency peaked Bl Lacertae
LBL	Low frequency peaked Bl Lacertae
MSPS	Mega Samples Per Second
MSL	Mean Scaled Length
MSW	Mean Scaled Width
NELG	Narrow Emission Line X-ray Galaxy
NLRG	Narrow Line Radio Galaxy

NSB	Night Sky Background
OSS	Optical Support Structure
PAROLI	Parallel Optical Linl
PMT	Photomultiplier Tube
PSF	Point Spread Function
PST	Pattern Selection Trigger
RFB	Rate Feed-Back
QE	Quantum Effeciency
RBL	Radio BL Lac
QSO	Quasi-Stellar Object
OVV	Optically Violent Variable AGN
QADC	Charge to Digital Converter
SED	Spectral Energy Distribution
SNR	Supernova Remnant
SSRQ	Steep Spectrum Radio Quasar
VBF	VERITAS Bank Format
VHE	Very-High Energy
XBL	X-ray BL Lac
ZCD	Zero Crossing Discriminator

Bibliography

Abdo, A. A., Allen, B., Berley, D., Blaufuss, E., Casanova, S., Chen, C., Coyne, D. G., Delay, R. S., Dingus, B. L., Ellsworth, R. W., Fleysher, L., Fleysher, R., Gonzalez, M. M., Goodman, J. A., Hays, E., Hoffman, C. M., Kolterman, B. E., Kelley, L. A., Lansdell, C. P., Linnemann, J. T., McEnery, J. E., Mincer, A. I., Moskalenko, I. V., Nemethy, P., Noyes, D., Ryan, J. M., Samuelson, F. W., Saz Parkinson, P. M., Schneider, M., Shoup, A., Sinnis, G., Smith, A. J., Strong, A. W., Sullivan, G. W., Vasileiou, V., Walker, G. P., Williams, D. A., Xu, X. W., and Yodh, G. B.: 2006, *ArXiv Astrophysics e-prints*

Aharonian, F.: 2005a, *ArXiv Astrophysics e-prints*

Aharonian, F.: 2005b, *ArXiv Astrophysics e-prints*

Aharonian, F.: 2006a, *ArXiv Astrophysics e-prints*

Aharonian, F.: 2006b, *ArXiv Astrophysics e-prints*

Aharonian, F.: 2006c, *ArXiv Astrophysics e-prints*

Aharonian, F.: 2006d, *ArXiv Astrophysics e-prints*

Aharonian, F.: 2006e, *ArXiv Astrophysics e-prints*

Aharonian, F., Akhperjanian, A., Barrio, J., Bernlöhr, K., Börst, H., Bojahr, H., Bolz, O., Contreras, J., Cortina, J., Denninghoff, S., Fonseca, V., Gonzalez, J., Götting, N., Heinzelmann, G., Hermann, G., Heusler, A., Hofmann, W., Horns, D., Ibarra, A., Iserlohe, C., Jung, I., Kankanyan, R., Kestel, M., Kettler, J., Kohnle, A., Konopelko, A., Kornmeyer, H., Kranich, D., Krawczynski, H., Lampeitl, H., Lopez, M., Lorenz, E., Lucarelli, F., Magnussen, N., Mang, O., Meyer, H., Mirzoyan, R., Moralejo, A., Ona, E., Padilla, L., Panter, M., Plaga, R., Plyasheshnikov, A., Prahl, J., Pühlhofer, G., Rauterberg, G., Röhring, A., Rhode, W., Rowell, G. P., Sahakian, V., Samorski, M., Schilling, M., Schröder, F., Siems, M., Stamm,

W., Tluczykont, M., Völk, H. J., Wiedner, C. A., and Wittek, W.: 2001, A&A **370**, 112

Aharonian, F., Akhperjanian, A., Beilicke, M., Bernlöhr, K., Börst, H., Bojahr, H., Bolz, O., Coarasa, T., Contreras, J., Cortina, J., Denninghoff, S., Fonseca, V., Girma, M., Götting, N., Heinzelmann, G., Hermann, G., Heusler, A., Hofmann, W., Horns, D., Jung, I., Kankanyan, R., Kestel, M., Kettler, J., Kohnle, A., Konopelko, A., Kornmeyer, H., Kranich, D., Krawczynski, H., Lampeitl, H., Lopez, M., Lorenz, E., Lucarelli, F., Magnussen, N., Mang, O., Meyer, H., Milite, M., Mirzoyan, R., Moralejo, A., Ona, E., Panter, M., Plyasheshnikov, A., Prahl, J., Pühlhofer, G., Rauterberg, G., Reyes, R., Rhode, W., Ripken, J., Röhring, A., Rowell, G. P., Sahakian, V., Samorski, M., Schilling, M., Schröder, F., Siems, M., Sobzynska, D., Stamm, W., Tluczykont, M., Völk, H. J., Wiedner, C. A., Wittek, W., Uchiyama, Y., Takahashi, T., and HEGRA Collaboration: 2002, A&A **393**, L37

Aharonian, F., Akhperjanian, A., Beilicke, M., Bernlöhr, K., Börst, H.-G., Bojahr, H., Bolz, O., Coarasa, T., Contreras, J., Cortina, J., Denninghoff, S., Fonseca, V., Girma, M., Götting, N., Heinzelmann, G., Hermann, G., Heusler, A., Hofmann, W., Horns, D., Jung, I., Kankanyan, R., Kestel, M., Kohnle, A., Konopelko, A., Kranich, D., Lampeitl, H., Lopez, M., Lorenz, E., Lucarelli, F., Mang, O., Mazin, D., Meyer, H., Mirzoyan, R., Moralejo, A., Oña-Wilhelmi, E., Panter, M., Plyasheshnikov, A., Pühlhofer, G., de los Reyes, R., Rhode, W., Ripken, J., Rowell, G. P., Sahakian, V., Samorski, M., Schilling, M., Siems, M., Sobzynska, D., Stamm, W., Tluczykont, M., Vitale, V., Völk, H. J., Wiedner, C. A., and Wittek, W.: 2005a, A&A **431**, 197

Aharonian, F., Akhperjanian, A., Beilicke, M., Bernlöhr, K., Börst, H.-G., Bojahr, H., Bolz, O., Coarasa, T., Contreras, J. L., Cortina, J., Denninghoff, S., Fonseca, M. V., Girma, M., Götting, N., Heinzelmann, G., Hermann, G., Heusler, A., Hofmann, W., Horns, D., Jung, I., Kankanyan, R., Kestel, M., Kohnle, A., Konopelko, A., Kornmeyer, H., Kranich, D., Lampeitl, H., Lopez, M., Lorenz, E., Lucarelli, F., Mang, O., Meyer, H., Mirzoyan, R., Moralejo, A., Ona-Wilhelmi, E., Panter, M., Plyasheshnikov, A., Pühlhofer, G., de los Reyes, R., Rhode, W., Ripken, J., Rowell, G., Sahakian, V., Samorski, M., Schilling, M., Siems, M., Sobzynska, D., Stamm, W., Tluczykont, M., Vitale, V., Völk, H. J., Wiedner, C. A., and Wittek, W.: 2003, A&A **403**, L1

Aharonian, F., Akhperjanian, A., Beilicke, M., Bernlöhr, K., Börst, H.-G., Bojahr, H., Bolz, O., Coarasa, T., Contreras, J. L., Cortina, J., Denninghoff, S., Fonseca, V., Girma, M., Götting, N., Heinzelmann, G., Hermann, G., Heusler, A., Hofmann, W., Horns, D., Jung, I., Kankanyan, R., Kestel, M., Konopelko, A., Kornmeyer, H., Kranich, D., Lampeitl, H., Lopez, M., Lorenz, E., Lucarelli, F., Mang, O., Mazin, D., Meyer, H., Mirzoyan, R., Moralejo, A., Ona-Wilhelmi, E., Panter, M., Plyasheshnikov, A., Pühlhofer, G., de los Reyes, R., Rhode, W., Ripken, J., Rowell, G., Sahakian, V., Samorski, M., Schilling, M., Siems, M., Sobzynska, D., Stamm, W., Tluczykont, M., Vitale, V., Völk, H. J., Wiedner, C. A., and Wittek, W.: 2004a, A&A **421**, 529

Aharonian, F., Akhperjanian, A. G., Aye, K.-M., Bazer-Bachi, A. R., Beilicke, M., Benbow, W., Berge, D., Berghaus, P., Bernlöhr, K., Boisson, C., Bolz, O., Borrel, V., Braun, I., Breitling, F., Brown, A. M., Gordo, J. B., Chadwick, P. M., Chounet, L.-M., Cornils, R., Costamante, L., Degrange, B., Dickinson, H. J., Djannati-Ataï, A., Drury, L. O., Dubus, G., Emmanoulopoulos, D., Espigat, P., Feinstein, F., Fleury, P., Fontaine, G., Fuchs, Y., Funk, S., Gallant, Y. A., Giebels, B., Gillessen, S., Glicenstein, J. F., Goret, P., Hadjichristidis, C., Hauser, M., Heinzelmann, G., Henri, G., Hermann, G., Hinton, J. A., Hofmann, W., Holleran, M., Horns, D., Jacholkowska, A., de Jager, O. C., Khélifi, B., Komin, N., Konopelko, A., Latham, I. J., Le Gallou, R., Lemière, A., Lemoine-Goumard, M., Leroy, N., Lohse, T., Marcowith, A., Martin, J.-M., Martineau-Huynh, O., Masterson, C., McComb, T. J. L., de Naurois, M., Nolan, S. J., Noutsos, A., Orford, K. J., Osborne, J. L., Ouchrif, M., Panter, M., Pelletier, G., Pita, S., Pühlhofer, G., Punch, M., Raubenheimer, B. C., Raue, M., Raux, J., Rayner, S. M., Reimer, A., Reimer, O., Ripken, J., Rob, L., Rolland, L., Rowell, G., Sahakian, V., Saugé, L., Schlenker, S., Schlickeiser, R., Schuster, C., Schwanke, U., Siewert, M., Sol, H., Spangler, D., Steenkamp, R., Stegmann, C., Tavernet, J.-P., Terrier, R., Théoret, C. G., Tluczykont, M., Vasileiadis, G., Venter, C., Vincent, P., Völk, H. J., and Wagner, S. J.: 2005b, *Science* **309**, 746

Aharonian, F., Akhperjanian, A. G., Aye, K.-M., Bazer-Bachi, A. R., Beilicke, M., Benbow, W., Berge, D., Berghaus, P., Bernlöhr, K., Boisson, C., Bolz, O., Braun, I., Breitling, F., Brown, A. M., Bussons Gordo, J., Chadwick, P. M., Chounet, L.-M., Cornils, R., Costamante, L., Degrange, B., Djannati-Ataï, A., O'C. Drury, L., Dubus, G., Emmanoulopoulos, D., Espigat, P., Feinstein, F., Fleury, P., Fontaine, G., Fuchs, Y., Funk, S., Gallant, Y. A., Giebels, B., Gillessen, S., Glicenstein, J. F., Goret, P.,

Hadjichristidis, C., Hauser, M., Heinzelmann, G., Henri, G., Hermann, G., Hinton, J. A., Hofmann, W., Holleran, M., Horns, D., de Jager, O. C., Khélifi, B., Komin, N., Konopelko, A., Latham, I. J., Le Gallou, R., Lemière, A., Lemoine-Goumard, M., Leroy, N., Lohse, T., Martineau-Huynh, O., Marcowith, A., Masterson, C., McComb, T. J. L., de Naurois, M., Nolan, S. J., Noutsos, A., Orford, K. J., Osborne, J. L., Ouchrif, M., Panter, M., Pelletier, G., Pita, S., Pühlhofer, G., Punch, M., Raubenheimer, B. C., Raue, M., Raux, J., Rayner, S. M., Redondo, I., Reimer, A., Reimer, O., Ripken, J., Rob, L., Rolland, L., Rowell, G., Sahakian, V., Saugé, L., Schlenker, S., Schlickeiser, R., Schuster, C., Schwanke, U., Siewert, M., Sol, H., Steenkamp, R., Stegmann, C., Tavernet, J.-P., Terrier, R., Théoret, C. G., Tluczykont, M., van der Walt, D. J., Vasileiadis, G., Venter, C., Vincent, P., Völk, H. J., and Wagner, S. J.: 2005c, A&A **439**, 1013

Aharonian, F., Akhperjanian, A. G., Aye, K.-M., Bazer-Bachi, A. R., Beilicke, M., Benbow, W., Berge, D., Berghaus, P., Bernlöhr, K., Boisson, C., Bolz, O., Braun, I., Breitling, F., Brown, A. M., Bussons Gordo, J., Chadwick, P. M., Chounet, L.-M., Cornils, R., Costamante, L., Degrange, B., Djannati-Ataï, A., O'C. Drury, L., Dubus, G., Emmanoulopoulos, D., Espigat, P., Feinstein, F., Fleury, P., Fontaine, G., Fuchs, Y., Funk, S., Gallant, Y. A., Giebels, B., Gillessen, S., Glicenstein, J. F., Goret, P., Hadjichristidis, C., Hauser, M., Heinzelmann, G., Henri, G., Hermann, G., Hinton, J. A., Hofmann, W., Holleran, M., Horns, D., de Jager, O. C., Khélifi, B., Komin, N., Konopelko, A., Latham, I. J., Le Gallou, R., Lemière, A., Lemoine, M., Leroy, N., Lohse, T., Marcowith, A., Masterson, C., McComb, T. J. L., de Naurois, M., Nolan, S. J., Noutsos, A., Orford, K. J., Osborne, J. L., Ouchrif, M., Panter, M., Pelletier, G., Pita, S., Pühlhofer, G., Punch, M., Raubenheimer, B. C., Raue, M., Raux, J., Rayner, S. M., Redondo, I., Reimer, A., Reimer, O., Ripken, J., Rob, L., Rolland, L., Rowell, G., Sahakian, V., Saugé, L., Schlenker, S., Schlickeiser, R., Schuster, C., Schwanke, U., Siewert, M., Sol, H., Steenkamp, R., Stegmann, C., Tavernet, J.-P., Terrier, R., Théoret, C. G., Tluczykont, M., Vasileiadis, G., Venter, C., Vincent, P., Völk, H. J., and Wagner, S. J.: 2005d, A&A **437**, 95

Aharonian, F., Akhperjanian, A. G., Aye, K.-M., Bazer-Bachi, A. R., Beilicke, M., Benbow, W., Berge, D., Berghaus, P., Bernlöhr, K., Bolz, O., Boisson, C., Borgmeier, C., Breitling, F., Brown, A. M., Bussons Gordo, J., Chadwick, P. M., Chitnis, V. R., Chounet, L.-M., Cornils, R., Costamante, L., Degrange, B., Djannati-Ataï, A., O'C. Drury, L., Ergin, T.,

Espigat, P., Feinstein, F., Fleury, P., Fontaine, G., Funk, S., Gallant, Y., Giebels, B., Gillessen, S., Goret, P., Guy, J., Hadjichristidis, C., Hauser, M., Heinzelmann, G., Henri, G., Hermann, G., Hinton, J. A., Hofmann, W., Holleran, M., Horns, D., de Jager, O. C., Jung, I., Khélifi, B., Komin, N., Konopelko, A., Latham, I. J., Le Gallou, R., Lemoine, M., Lemière, A., Leroy, N., Lohse, T., Marcowith, A., Masterson, C., McComb, T. J. L., de Naurois, M., Nolan, S. J., Noutsos, A., Orford, K. J., Osborne, J. L., Ouchrif, M., Panter, M., Pelletier, G., Pita, S., Pohl, M., Pühlhofer, G., Punch, M., Raubenheimer, B. C., Raue, M., Raux, J., Rayner, S. M., Redondo, I., Reimer, A., Reimer, O., Ripken, J., Rivoal, M., Rob, L., Rolland, L., Rowell, G., Sahakian, V., Saugé, L., Schlenker, S., Schlickeiser, R., Schuster, C., Schwanke, U., Siewert, M., Sol, H., Steenkamp, R., Stegmann, C., Tavernet, J.-P., Théoret, C. G., Tluczykont, M., van der Walt, D. J., Vasileiadis, G., Vincent, P., Visser, B., Völk, H. J., and Wagner, S. J.: 2004b, A&A **425**, L13

Aharonian, F., Akhperjanian, A. G., Bazer-Bachi, A. R., Beilicke, M., Benbow, W., Berge, D., Bernlöhr, K., Boisson, C., Bolz, O., Borrel, V., Braun, I., Breitling, F., Brown, A. M., Bühler, R., Carrigan, S., Chadwick, P. M., Chounet, L.-M., Cornils, R., Costamante, L., Degrange, B., Dickinson, H. J., Djannati-Ataï, A., O'C. Drury, L., Dubus, G., Egberts, K., Emmanoulopoulos, D., Espigat, P., Feinstein, F., Fontaine, G., Funk, S., Gallant, Y. A., Giebels, B., Glicenstein, J. F., Goret, P., Hadjichristidis, C., Hauser, D., Hauser, M., Heinzelmann, G., Henri, G., Hermann, G., Hinton, J. A., Hofmann, W., Holleran, M., Horns, D., Jacholkowska, A., de Jager, O. C., Khélifi, B., Komin, N., Konopelko, A., Latham, I. J., Le Gallou, R., Lemière, A., Lemoine-Goumard, M., Lohse, T., Martin, J. M., Martineau-Huynh, O., Marcowith, A., Masterson, C., McComb, T. J. L., de Naurois, M., Nedbal, D., Nolan, S. J., Noutsos, A., Orford, K. J., Osborne, J. L., Ouchrif, M., Panter, M., Pelletier, G., Pita, S., Pühlhofer, G., Punch, M., Raubenheimer, B. C., Raue, M., Rayner, S. M., Reimer, A., Reimer, O., Ripken, J., Rob, L., Rolland, L., Rowell, G., Sahakian, V., Saugé, L., Schlenker, S., Schlickeiser, R., Schuster, C., Schwanke, U., Siewert, M., Sol, H., Spangler, D., Steenkamp, R., Stegmann, C., Superina, G., Tavernet, J.-P., Terrier, R., Théoret, C. G., Tluczykont, M., van Eldik, C., Vasileiadis, G., Venter, C., Vincent, P., Völk, H. J., Wagner, S. J., and Ward, M.: 2006a, A&A **448**, L19

Aharonian, F., Akhperjanian, A. G., Bazer-Bachi, A. R., Beilicke, M., Benbow, W., Berge, D., Bernlöhr, K., Boisson, C., Bolz, O., Borrel, V., Braun, I., Breitling, F., Brown, A. M., Chadwick, P. M., Chounet, L.-M., Cornils,

R., Costamante, L., Degrange, B., Dickinson, H. J., Djannati-Ataï, A., Drury, L. O., Dubus, G., Emmanoulopoulos, D., Espigat, P., Feinstein, F., Fontaine, G., Fuchs, Y., Funk, S., Gallant, Y. A., Giebels, B., Gillessen, S., Glicenstein, J. F., Goret, P., Hadjichristidis, C., Hauser, D., Hauser, M., Heinzelmann, G., Henri, G., Hermann, G., Hinton, J. A., Hofmann, W., Holleran, M., Horns, D., Jacholkowska, A., de Jager, O. C., Khélifi, B., Klages, S., Komin, N., Konopelko, A., Latham, I. J., Le Gallou, R., Lemière, A., Lemoine-Goumard, M., Leroy, N., Lohse, T., Martin, J. M., Martineau-Huynh, O., Marcowith, A., Masterson, C., McComb, T. J. L., de Naurois, M., Nolan, S. J., Noutsos, A., Orford, K. J., Osborne, J. L., Ouchrif, M., Panter, M., Pelletier, G., Pita, S., Pühlhofer, G., Punch, M., Raubenheimer, B. C., Raue, M., Raux, J., Rayner, S. M., Reimer, A., Reimer, O., Ripken, J., Rob, L., Rolland, L., Rowell, G., Sahakian, V., Saugé, L., Schlenker, S., Schlickeiser, R., Schuster, C., Schwanke, U., Siewert, M., Sol, H., Spangler, D., Steenkamp, R., Stegmann, C., Tavernet, J.-P., Terrier, R., Théoret, C. G., Tluczykont, M., van Eldik, C., Vasileiadis, G., Venter, C., Vincent, P., Völk, H. J., and Wagner, S. J.: 2006b, Nature **440**, 1018

Aharonian, F., Akhperjanian, A. G., Bazer-Bachi, A. R., Beilicke, M., Benbow, W., Berge, D., Bernlöhr, K., Boisson, C., Bolz, O., Borrel, V., Braun, I., Breitling, F., Brown, A. M., Chadwick, P. M., Chounet, L.-M., Cornils, R., Costamante, L., Degrange, B., Dickinson, H. J., Djannati-Ataï, A., O'C. Drury, L., Dubus, G., Emmanoulopoulos, D., Espigat, P., Feinstein, F., Fontaine, G., Fuchs, Y., Funk, S., Gallant, Y. A., Giebels, B., Gillessen, S., Glicenstein, J. F., Goret, P., Hadjichristidis, C., Hauser, M., Heinzelmann, G., Henri, G., Hermann, G., Hinton, J. A., Hofmann, W., Holleran, M., Horns, D., Jacholkowska, A., de Jager, O. C., Khélifi, B., Komin, N., Konopelko, A., Latham, I. J., Le Gallou, R., Lemière, A., Lemoine-Goumard, M., Leroy, N., Lohse, T., Martin, J. M., Martineau-Huynh, O., Marcowith, A., Masterson, C., McComb, T. J. L., de Naurois, M., Nolan, S. J., Noutsos, A., Orford, K. J., Osborne, J. L., Ouchrif, M., Panter, M., Pelletier, G., Pita, S., Pühlhofer, G., Punch, M., Raubenheimer, B. C., Raue, M., Raux, J., Rayner, S. M., Reimer, A., Reimer, O., Ripken, J., Rob, L., Rolland, L., Rowell, G., Sahakian, V., Saugé, L., Schlenker, S., Schlickeiser, R., Schuster, C., Schwanke, U., Siewert, M., Sol, H., Spangler, D., Steenkamp, R., Stegmann, C., Tavernet, J.-P., Terrier, R., Théoret, C. G., Tluczykont, M., Vasileiadis, G., Venter, C., Vincent, P., Völk, H. J., and Wagner, S. J.: 2005e, A&A **442**, 177

Aharonian, F., Akhperjanian, A. G., Bazer-Bachi, A. R., Beilicke, M., Ben-

bow, W., Berge, D., Bernlöhr, K., Boisson, C., Bolz, O., Borrel, V., Braun, I., Breitling, F., Brown, A. M., Chadwick, P. M., Chounet, L.-M., Cornils, R., Costamante, L., Degrange, B., Dickinson, H. J., Djannati-Ataï, A., Drury, L. O., Dubus, G., Emmanoulopoulos, D., Espigat, P., Feinstein, F., Fontaine, G., Fuchs, Y., Funk, S., Gallant, Y. A., Giebels, B., Gillessen, S., Glicenstein, J. F., Goret, P., Hadjichristidis, C., Hauser, M., Heinzelmann, G., Henri, G., Hermann, G., Hinton, J. A., Hofmann, W., Holleran, M., Horns, D., Jacholkowska, A., de Jager, O. C., Khélifi, B., Komin, N., Konopelko, A., Latham, I. J., Le Gallou, R., Lemière, A., Lemoine-Goumard, M., Leroy, N., Lohse, T., Martin, J. M., Martineau-Huynh, O., Marcowith, A., Masterson, C., McComb, T. J. L., de Naurois, M., Nolan, S. J., Noutsos, A., Orford, K. J., Osborne, J. L., Ouchrif, M., Panter, M., Pelletier, G., Pita, S., Pühlhofer, G., Punch, M., Raubenheimer, B. C., Raue, M., Raux, J., Rayner, S. M., Reimer, A., Reimer, O., Ripken, J., Rob, L., Rolland, L., Rowell, G., Sahakian, V., Saugé, L., Schlenker, S., Schlickeiser, R., Schuster, C., Schwanke, U., Siewert, M., Sol, H., Spangler, D., Steenkamp, R., Stegmann, C., Tavernet, J.-P., Terrier, R., Théoret, C. G., Tluczykont, M., Vasileiadis, G., Venter, C., Vincent, P., Völk, H. J., and Wagner, S. J.: 2006c, ApJ **636**, 777

Aharonian, F. A.: 2000, *New Astronomy* **5**, 377

Aharonian, F. A. e.: 1991, in *International Cosmic Ray Conference*, pp 468–+

Albert, J.: 2006a, *ArXiv Astrophysics e-prints*

Albert, J.: 2006b, *ArXiv Astrophysics e-prints*

Albert, J., Aliu, E., Anderhub, H., Antoranz, P., Armada, A., Asensio, M., Baixeras, C., Barrio, J. A., Bartelt, M., Bartko, H., Bastieri, D., Bavikadi, S. R., Bednarek, W., Berger, K., Bigongiari, C., Biland, A., Bisesi, E., Bock, R. K., Bordas, P., Bosch-Ramon, V., Bretz, T., Britvitch, I., Camara, M., Carmona, E., Chilingarian, A., Ciprini, S., Coarasa, J. A., Commichau, S., Contreras, J. L., Cortina, J., Curtef, V., Danielyan, V., Dazzi, F., De Angelis, A., de los Reyes, R., De Lotto, B., Domingo-Santamaría, E., Dorner, D., Doro, M., Errando, M., Fagiolini, M., Ferenc, D., Fernández, E., Firpo, R., Flix, J., Fonseca, M. V., Font, L., Fuchs, M., Galante, N., Garczarczyk, M., Gaug, M., Giller, M., Goebel, F., Hakobyan, D., Hayashida, M., Hengstebeck, T., Höhne, D., Hose, J., Hsu, C. C., Isar, P. G., Jacon, P., Kalekin, O., Kosyra, R., Kranich, D., Laatiaoui, M., Laille, A., Lenisa, T., Liebing, P., Lindfors, E., Lombardi, S., Longo, F.,

López, J., López, M., Lorenz, E., Lucarelli, F., Majumdar, P., Maneva, G., Mannheim, K., Mansutti, O., Mariotti, M., Martínez, M., Mase, K., Mazin, D., Merck, C., Meucci, M., Meyer, M., Miranda, J. M., Mirzoyan, R., Mizobuchi, S., Moralejo, A., Nilsson, K., Oña-Wilhelmi, E., Orduña, R., Otte, N., Oya, I., Paneque, D., Paoletti, R., Paredes, J. M., Pasanen, M., Pascoli, D., Pauss, F., Pavel, N., Pegna, R., Persic, M., Peruzzo, L., Piccioli, A., Poller, M., Pooley, G., Prandini, E., Raymers, A., Rhode, W., Ribó, M., Rico, J., Riegel, B., Rissi, M., Robert, A., Romero, G. E., Rügamer, S., Saggion, A., Sánchez, A., Sartori, P., Scalzotto, V., Scapin, V., Schmitt, R., Schweizer, T., Shayduk, M., Shinozaki, K., Shore, S. N., Sidro, N., Sillanpää, A., Sobczynska, D., Stamerra, A., Stark, L. S., Takalo, L., Temnikov, P., Tescaro, D., Teshima, M., Tonello, N., Torres, A., Torres, D. F., Turini, N., Vankov, H., Vitale, V., Wagner, R. M., Wibig, T., Wittek, W., Zanin, R., and Zapatero, J.: 2006a, *Science* **312**, 1771

Albert, J., Aliu, E., Anderhub, H., Antoranz, P., Armada, A., Asensio, M., Baixeras, C., Barrio, J. A., Bartelt, M., Bartko, H., Bastieri, D., Bavikadi, S. R., Bednarek, W., Berger, K., Bigongiari, C., Biland, A., Bisesi, E., Bock, R. K., Bordas, P., Bosch-Ramon, V., Bretz, T., Britvitch, I., Camara, M., Carmona, E., Chilingarian, A., Ciprini, S., Coarasa, J. A., Commichau, S., Contreras, J. L., Cortina, J., Curtef, V., Danielyan, V., Dazzi, F., De Angelis, A., de los Reyes, R., De Lotto, B., Domingo-Santamaría, E., Dorner, D., Doro, M., Errando, M., Fagiolini, M., Ferenc, D., Fernández, E., Firpo, R., Flix, J., Fonseca, M. V., Font, L., Fuchs, M., Galante, N., Garczarczyk, M., Gaug, M., Giller, M., Goebel, F., Hakobyan, D., Hayashida, M., Hengstebeck, T., Höhne, D., Hose, J., Hsu, C. C., Isar, P. G., Jacon, P., Kalekin, O., Kosyra, R., Kranich, D., Laatiaoui, M., Laille, A., Lenisa, T., Liebing, P., Lindfors, E., Lombardi, S., Longo, F., López, J., López, M., Lorenz, E., Lucarelli, F., Majumdar, P., Maneva, G., Mannheim, K., Mansutti, O., Mariotti, M., Martínez, M., Mase, K., Mazin, D., Merck, C., Meucci, M., Meyer, M., Miranda, J. M., Mirzoyan, R., Mizobuchi, S., Moralejo, A., Nilsson, K., Oña-Wilhelmi, E., Orduña, R., Otte, N., Oya, I., Paneque, D., Paoletti, R., Paredes, J. M., Pasanen, M., Pascoli, D., Pauss, F., Pavel, N., Pegna, R., Persic, M., Peruzzo, L., Piccioli, A., Poller, M., Pooley, G., Prandini, E., Raymers, A., Rhode, W., Ribó, M., Rico, J., Riegel, B., Rissi, M., Robert, A., Romero, G. E., Rügamer, S., Saggion, A., Sánchez, A., Sartori, P., Scalzotto, V., Scapin, V., Schmitt, R., Schweizer, T., Shayduk, M., Shinozaki, K., Shore, S. N., Sidro, N., Sillanpää, A., Sobczynska, D., Stamerra, A., Stark, L. S., Takalo, L., Temnikov, P., Tescaro, D., Teshima, M., Tonello, N., Torres, A., Torres, D. F., Turini, N., Vankov, H., Vitale, V., Wagner, R. M., Wibig, T.,

Wittek, W., Zanin, R., and Zapatero, J.: 2006b, ApJ **0**, 0, in press

Amenomori, M., Cao, Z., Ding, L. K., Feng, Z. Y., Hibino, K., Hotta, N., Huang, Q., Huo, A. X., Jia, H. Y., and Jiang, G. Z.: 1992, *Physical Review Letters* **69**, 2468

Armstrong, P., Chadwick, P. M., Cottle, P. J., Dickinson, J. E., Dickinson, M. R., Dipper, N. A., Hilton, S. E., Hogg, W., Holder, J., Kendall, T. R., McComb, T. J. L., Moore, C. M., Orford, K. J., Rayner, S. M., Roberts, I. D., Roberts, M. D., Robertshaw, M., Shaw, S. E., Tindale, K., Tummey, S. P., and Turver, K. E.: 1999, *Experimental Astronomy* **9**, 51

Arqueros, F., Ballestrin, J., Borque, D. M., Diaz Trigo, M., Enriquez, R., Gebauer, H.-J., and Plaga, R.: 2001, in *International Cosmic Ray Conference*, pp 2399–+

Bacci, C., Bao, K. Z., Barone, F., Bartoli, B., Bastieri, D., Bernardini, P., Buonomo, R., Bussino, S., Calloni, E., Cao, B. Y., Cardarelli, R., Catalanotti, S., Cavaliere, A., Cesaroni, F., Creti, P., Danzengluobu, D'Ettorre Piazzoli, B., de Vincenzi, M., di Girolamo, T., di Sciascio, G., Feng, Z. Y., Fu, Y., Gao, X. Y., Geng, Q. X., Guo, H. W., He, H. H., He, M., Huang, Q., Iacovacci, M., Iucci, N., Jai, H. Y., Kong, F. M., Kuang, H. H., Labaciren, Li, B., Li, J. Y., Liu, Z. Q., Lu, H., Ma, X. H., Mancarella, G., Mari, S. M., Marsella, G., Martello, D., Mei, D. M., Meng, X. R., Milano, L., Morselli, A., Mu, J., Oliviero, M., Padovani, P., Panareo, M., Parisi, M., Pellizzoni, G., Peng, Z. R., Pistilli, P., Santonico, R., Sartori, G., Sbarra, C., Severino, G., Shen, P. R., Sparvoli, R., Stanescu, C., Su, J., Sun, L. R., Sun, S. C., Surdo, A., Tan, Y. H., Vernetto, S., Vietri, M., Wang, C. R., Wang, H., Wang, H. Y., Wei, Y. N., Yang, H. T., Yao, Q. K., Yu, G. C., Yue, X. D., Yuan, A. F., Zhang, H. M., Zhang, J. L., Zhang, N. J., Zhang, T. J., Zhang, X. Y., Zhaxisangzhu, Zhaxiciren, and Zhu, Q. Q.: 1999, A&AS **138**, 597

Bade, N., Beckmann, V., Douglas, N. G., Barthel, P. D., Engels, D., Cordis, L., Nass, P., and Voges, W.: 1998, A&A **334**, 459

Badran, H. M. and Weekes, T. C.: 2001, in *International Cosmic Ray Conference*, pp 2892–+

Baixeras, C. e.: 2005, in *International Cosmic Ray Conference*, pp 227–+

Baldwin, J., Boksenberg, A., Carswell, R., Burbidge, G., Cowsik, R., Perry, J., and Wolfe, A.: 1977, A&A **61**, 165

Barrau, J. et al.: 1998, *Nuclear Instruments and Methods A* **416**, 278

Bartko, H. e.: 2005, in *International Cosmic Ray Conference*, pp 167–+

Bastieri, D., Galante, N., Gaug, M., Garczarczyk, M., Longo, F., Mizobuchi, S., Peruzzo, L., and The MAGIC Collaboration: 2005, *Nuovo Cimento C Geophysics Space Physics C* **28**, 711

Becker, R. H., White, R. L., and Edwards, A. L.: 1991, ApJS **75**, 1

Bednarek, W.: 1998, A&A **336**, 123

Bergström, L., Bringmann, T., Eriksson, M., and Gustafsson, M.: 2005, *Physical Review Letters* **94(13)**, 131301

Bernlöhr, K., Carrol, O., Cornils, R., Elfahem, S., Espigat, P., Gillessen, S., Heinzelmann, G., Hermann, G., Hofmann, W., Horns, D., Jung, I., Kankanyan, R., Katona, A., Khelifi, B., Krawczynski, H., Panter, M., Punch, M., Rayner, S., Rowell, G., Tluczykont, M., and van Staa, R.: 2003, *Astroparticle Physics* **20**, 111

Bhattacharya, D., Chantell, M. C., Coppi, P., Covault, C. E., Dragovan, M., Gregorich, D. T., Hanna, D. S., Mukherjee, R., Ong, R. A., Oser, S., Ragan, K., Tumer, O. T., and Williams, D. A.: 1997, in *AIP Conf. Proc. 410: Proceedings of the Fourth Compton Symposium*, p. 1626

Blackett, P.: 1948, *Physical Society Gassiot Committee Report* 34

Blandford, R. D. and Levinson, A.: 1995, ApJ **441**, 79

Błażejowski, M., Blaylock, G., Bond, I. H., Bradbury, S. M., Buckley, J. H., Carter-Lewis, D. A., Celik, O., Cogan, P., Cui, W., Daniel, M., Duke, C., Falcone, A., Fegan, D. J., Fegan, S. J., Finley, J. P., Fortson, L., Gammell, S., Gibbs, K., Gillanders, G. G., Grube, J., Gutierrez, K., Hall, J., Hanna, D., Holder, J., Horan, D., Humensky, B., Kenny, G., Kertzman, M., Kieda, D., Kildea, J., Knapp, J., Kosack, K., Krawczynski, H., Krennrich, F., Lang, M., LeBohec, S., Linton, E., Lloyd-Evans, J., Maier, G., Mendoza, D., Milovanovic, A., Moriarty, P., Nagai, T. N., Ong, R. A., Power-Mooney, B., Quinn, J., Quinn, M., Ragan, K., Reynolds, P. T., Rebillot, P., Rose, H. J., Schroedter, M., Sembroski, G. H., Swordy, S. P., Syson, A., Valcarel, L., Vassiliev, V. V., Wakely, S. P., Walker, G., Weekes, T. C., White, R., Zweerink, J., Mochejska, B., Smith, B., Aller, M., Aller, H., Teräsranta, H., Boltwood, P., Sadun, A., Stanek, K., Adams, E., Foster, J., Hartman, J., Lai, K., Böttcher, M., Reimer, A., and Jung, I.: 2005, ApJ **630**, 130

Bloom, S. D. and Marscher, A. P.: 1996, ApJ **461**, 657+

Bock, R. K., Chilingarian, A., Gaug, M., Hakl, F., Hengstebeck, T., Jiřina, M., Klaschka, J., Kotrč, E., Savický, P., Towers, S., Vaiciulis, A., and Wittek, W.: 2004, *Nuclear Instruments and Methods in Physics Research A* **516**, 511

Bond, I. H., Hillas, A. M., and Bradbury, S. M.: 2003, *Astroparticle Physics* **20**, 311

Borione, A. e.: 1993, in L. Jones (ed.), *AIP Conf. Proc. 276: Very High Energy Cosmic-Ray Interactions*, pp 207–+

Böttcher, M.: 2005, ApJ **621**, 176

Böttcher, M.: 2006, ApJ **641**, 1233

Bottcher, M. and Dermer, C. D.: 1998, in *Abstracts of the 19th Texas Symposium on Relativistic Astrophysics and Cosmology, held in Paris, France, Dec. 14-18, 1998. Eds.: J. Paul, T. Montmerle, and E. Aubourg (CEA Saclay).*

Böttcher, M., Mukherjee, R., and Reimer, A.: 2002, ApJ **581**, 143

Bradbury, S.: 1999, in *International Cosmic Ray Conference*, pp 263–+

Buckley, J. H. e.: 1998, in J. Paul, T. Montmerle, and E. Aubourg (eds.), *Abstracts of the 19th Texas Symposium on Relativistic Astrophysics and Cosmology, held in Paris, France, Dec. 14-18, 1998. Eds.: J. Paul, T. Montmerle, and E. Aubourg (CEA Saclay), meeting abstract.*

Butt, Y. M., Combi, J. A., Drake, J., Finley, J. P., Konopelko, A., Lister, M., and Rodriguez, J.: 2006, *ArXiv Astrophysics e-prints*

Catanese, M., Akerlof, C. W., Badran, H. M., Biller, S. D., Bond, I. H., Boyle, P. J., Bradbury, S. M., Buckley, J. H., Burdett, A. M., Bussons Gordo, J., Carter-Lewis, D. A., Cawley, M. F., Connaughton, V., Fegan, D. J., Finley, J. P., Gaidos, J. A., Hall, T., Hillas, A. M., Krennrich, F., Lamb, R. C., Lessard, R. W., Masterson, C., McEnery, J. E., Mohanty, G., Quinn, J., Rodgers, A. J., Rose, H. J., Samuelson, F. W., Schubnell, M. S., Sembroski, G. H., Srinivasan, R., Weekes, T. C., Wilson, C. W., and Zweerink, J.: 1998, ApJ **501**, 616

Cawley, M.: 1993, in R. Lamb (ed.), *Workshop Towards a Major Cherenkov Detector (Calgary)*, p. 176

Chitnis, V. R. e.: 2005, in *International Cosmic Ray Conference*, pp 235–+

Cogan, P.: 2004, *FADC Clocking Noise*, Internal VERITAS Memo

Connaughton, V., Akerlof, C. W., Biller, S., Boyle, P., Buckley, J., Carter-Lewis, D. A., Catanese, M., Cawley, M. F., Fegan, D. J., Finley, J., Gaidos, J., Hillas, A. M., Lamb, R. C., Lessard, R., McEnery, J., Mohanty, G., Porter, N. A., Quinn, J., Rose, H. J., Schubnell, M. S., Sembroski, G., Srinivasan, R., Weekes, T. C., Wilson, C., and Zweerink, J.: 1998, *Astroparticle Physics* **8**, 179

Coppi, P. S. and Aharonian, F. A.: 1999, ApJ **521**, L33

Cornils, R., Gillessen, S., Jung, I., Hofmann, W., Beilicke, M., Bernlöhr, K., Carrol, O., Elfahem, S., Heinzelmann, G., Hermann, G., Horns, D., Kankanyan, R., Katona, A., Krawczynski, H., Panter, M., Rayner, S., Rowell, G., Tluczykont, M., and van Staa, R.: 2003, *Astroparticle Physics* **20**, 129

Cortina, J. e.: 2005, in *International Cosmic Ray Conference*, pp 359–+

Costa, E., Frontera, F., Heise, J., Feroci, M., in 't Zand, J., Fiore, F., Cinti, M. N., dal Fiume, D., Nicastro, L., Orlandini, M., Palazzi, E., Rapisarda, M., Zavattini, G., Jager, R., Parmar, A., Owens, A., Molendi, S., Cusumano, G., Maccarone, M. C., Giarrusso, S., Coletta, A., Antonelli, L. A., Giommi, P., Muller, J. M., Piro, L., and Butler, R. C.: 1997, Nature **387**, 783

Costamante, L. and Ghisellini, G.: 2002, A&A **384**, 56

Daniel, M. K., Badran, H. M., Bond, I. H., Boyle, P. J., Bradbury, S. M., Buckley, J. H., Carter-Lewis, D. A., Catanese, M., Celik, O., Cogan, P., Cui, W., D'Vali, M., de la Calle Perez, I., Duke, C., Falcone, A., Fegan, D. J., Fegan, S. J., Finley, J. P., Fortson, L. F., Gaidos, J. A., Gammell, S., Gibbs, K., Gillanders, G. H., Grube, J., Hall, J., Hall, T. A., Hanna, D., Hillas, A. M., Holder, J., Horan, D., Humensky, T. B., Jarvis, A., Jordan, M., Kenny, G. E., Kertzman, M., Kieda, D., Kildea, J., Knapp, J., Kosack, K., Krawczynski, H., Krennrich, F., Lang, M. J., Le Bohec, S., Linton, E., Lloyd-Evans, J., Milovanovic, A., Moriarty, P., Müller, D., Nagai, T., Nolan, S., Ong, R. A., Pallassini, R., Petry, D., Power-Mooney, B., Quinn, J., Quinn, M., Ragan, K., Rebillot, P., Reynolds, P. T., Rose, H. J., Schroedter, M., Sembroski, G. H., Swordy, S. P., Syson, A., Vassiliev, V. V., Wakely, S. P., Walker, G., Weekes, T. C., and Zweerink, J.: 2005, ApJ **621**, 181

Dar, A. and Laor, A.: 1997, ApJ **478**, L5

Daum, A., Hermann, G., Hess, M., Hofmann, W., Lampeitl, H., Pühlhofer, G., Aharonian, F., Akhperjanian, A. G., Barrio, J. A., Beglarian, A. S., Bernlöhr, K., Beteta, J. J. G., Bradbury, S. M., Contreras, J. L., Cortina, J., Deckers, T., Feigl, E., Fernandez, J., Fonseca, V., Frass, A., Funk, B., Gonzalez, J. C., Heinzelmann, G., Hemberger, M., Heusler, A., Holl, I., Horns, D., Kankanyan, R., Kirstein, O., Köhler, C., Konopelko, A., Kranich, D., Krawczynski, H., Kornmayer, H., Lindner, A., Lorenz, E., Magnussen, N., Meyer, H., Mirzoyan, R., Möller, H., Moralejo, A., Padilla, L., Panter, M., Petry, D., Plaga, R., Prahl, J., Prosch, C., Rauterberg, G., Rhode, W., Röhring, A., Sahakian, V., Samorski, M., Sanchez, J. A., Schmele, D., Stamm, W., Ulrich, M., Völk, H. J., Westerhoff, S., Wiebel-Sooth, B., Wiedner, C. A., Willmer, M., and Wirth, H.: 1997, *Astroparticle Physics* **8**, 1

Davies, J. and Cotton, E.: 1957, *Journal of Solar Energy* **1**, 16

de la Calle Perez, I.: 2003, *Ph.D. thesis*, University of Leeds

de la Calle Pérez, I., Bond, I. H., Boyle, P. J., Bradbury, S. M., Buckley, J. H., Carter-Lewis, D. A., Celik, O., Cui, W., Dowdall, C., Duke, C., Falcone, A., Fegan, D. J., Fegan, S. J., Finley, J. P., Fortson, L., Gaidos, J. A., Gibbs, K., Gammell, S., Hall, J., Hall, T. A., Hillas, A. M., Holder, J., Horan, D., Jordan, M., Kertzman, M., Kieda, D., Kildea, J., Knapp, J., Kosack, K., Krawczynski, H., Krennrich, F., LeBohec, S., Linton, E. T., Lloyd-Evans, J., Moriarty, P., Müller, D., Nagai, T. N., Ong, R. A., Page, M., Pallassini, R., Petry, D., Power-Mooney, B., Quinn, J., Rebillot, P., Reynolds, P. T., Rose, H. J., Schroedter, M., Sembroski, G. H., Swordy, S. P., Vassiliev, V. V., Wakely, S. P., Walker, G., and Weekes, T. C.: 2003, ApJ **599**, 909

Dermer, C. D. and Schlickeiser, R.: 1993, ApJ **416**, 458

Dermer, C. D., Schlickeiser, R., and Mastichiadis, A.: 1992, A&A **256**, L27

Donato, D., Ghisellini, G., Tagliaferri, G., and Fossati, G.: 2001, A&A **375**, 739

Dunlea, S.: 2001, *Ph.D. thesis*, National University of Ireland

Dwek, E. and Krennrich, F.: 2005, ApJ **618**, 657

Elvis, M., Plummer, D., Schachter, J., and Fabbiano, G.: 1992, ApJS **80**, 257

Enomoto, R., Tsuchiya, K., Adachi, Y., Kabuki, S., Edwards, P. G., Asahara, A., Bicknell, G. V., Clay, R. W., Doi, Y., Gunji, S., Hara, S., Hara, T., Hattori, T., Hayashi, S., Higashi, Y., Inoue, R., Itoh, C., Kajino, F., Katagiri, H., Kawachi, A., Kawasaki, S., Kifune, T., Kiuchi, R., Konno, K., Ksenofontov, L. T., Kubo, H., Kushida, J., Matsubara, Y., Mizumoto, Y., Mori, M., Muraishi, H., Muraki, Y., Naito, T., Nakamori, T., Nishida, D., Nishijima, K., Ohishi, M., Patterson, J. R., Protheroe, R. J., Sakamoto, Y., Sato, M., Suzuki, S., Suzuki, T., Swaby, D. L., Tanimori, T., Tanimura, H., Thornton, G. J., Watanabe, S., Yamaoka, T., Yamazaki, M., Yanagita, S., Yoshida, T., Yoshikoshi, T., Yuasa, M., and Yukawa, Y.: 2006, ApJ **638**, 397

Fossati, G., Maraschi, L., Celotti, A., Comastri, A., and Ghisellini, G.: 1998, MNRAS **299**, 433

Funk, S., Hermann, G., Hinton, J., Berge, D., Bernlöhr, K., Hofmann, W., Nayman, P., Toussenel, F., and Vincent, P.: 2004, *Astroparticle Physics* **22**, 285

Gaidos, J. A., Akerlof, C. W., Biller, S. D., Boyle, P. J., Breslin, A. C., Buckley, J. H., Carter-Lewis, D. A., Catanese, M., Cawley, M. F., Fegan, D. J., Finley, J. P., Hillas, A. M., Krennrich, F., Lamb, R. C., Lessard, R., McEnery, J., Mohanty, G., Moriarty, P., Quinn, J., Rodgers, A., Rose, H. J., Samuelson, F., Schubnell, M. S., Sembroski, G., Srinivasan, R., Weekes, T. C., Wilson, C. L., and Zweerink, J.: 1996, Nature **383**, 319

Galbraith, W. and Jelley, J.: 1955, *Journal of Atmospheric and Terrestrial Physics* **6**, 250

Gammell, S.: 2004, *Ph.D. thesis*, University College Dublin

Georganopoulos, M. and Kazanas, D.: 2003, ApJ **594**, L27

Ghisellini, G. and Madau, P.: 1996, MNRAS **280**, 67

Ghisellini, G., Maraschi, M., and Treves, A.: 1985, *Astronomy and Astrophysics* **146**, 204

Ghisellini, G., Tavecchio, F., and Chiaberge, M.: 2005, A&A **432**, 401

Gibbs, K. e.: 2003, in *International Cosmic Ray Conference*, pp 2823–+

Giommi, P., Padovani, P., and Perlman, E.: 2000, MNRAS **317**, 743

Giroletti, M., Giovannini, G., Feretti, L., Cotton, W. D., Edwards, P. G., Lara, L., Marscher, A. P., Mattox, J. R., Piner, B. G., and Venturi, T.: 2004, ApJ **600**, 127

Gould, R. J. and Schréder, G.: 1966, *Physical Review Letters* **16**, 252

Halzen, F. and Hooper, D.: 2005, *Astroparticle Physics* **23**, 537

Hartman, R. C., Bertsch, D. L., Bloom, S. D., Chen, A. W., Deines-Jones, P., Esposito, J. A., Fichtel, C. E., Friedlander, D. P., Hunter, S. D., McDonald, L. M., Sreekumar, P., Thompson, D. J., Jones, B. B., Lin, Y. C., Michelson, P. F., Nolan, P. L., Tompkins, W. F., Kanbach, G., Mayer-Hasselwander, H. A., Mücke, A., Pohl, M., Reimer, O., Kniffen, D. A., Schneid, E. J., Von Montigny, C., Mukherjee, R., and Dingus, B. L.: 1999, ApJS **123**, 79

Hawking, S. W.: 1974, Nature **248**, 30

Hayashi, Y.: 2005, in *International Cosmic Ray Conference*, pp 243–+

Heck, D., Knapp, J., Capdevielle, G., Schatz, G., and Thouw, T.: 1998, *Forschungszentrum Karlsruhe Report FZKA* 6019

Helene, O.: 1983, *Nuclear Instruments and Methods* **212**, 319

Heß, M., Bernlöhr, K., Daum, A., Hemberger, M., Hermann, G., Hofmann, W., Lampeitl, H., Aharonian, F. A., Akhperjanian, A. G., Barrio, J. A., Beteta, J. J. G., Contreras, J. L., Cortina, J., Deckers, T., Fernandez, J., Fonseca, V., Gonzalez, J. C., Heinzelmann, G., Heusler, A., Hohl, H., Holl, I., Horns, D., Kankanyan, R., Kestel, M., Kirstein, O., Köhler, C., Konopelko, A., Kornmayer, H., Kranich, D., Krawczynski, H., Lindner, A., Lorenz, E., Magnussen, N., Meyer, H., Mirzoyan, R., Moralejo, A., Padilla, L., Panter, M., Petry, D., Plaga, R., Prahl, J., Prosch, C., Pühlhofer, G., Rauterberg, G., Rhode, W., Röhring, A., Samorski, M., Sanchez, J. A., Schmele, D., Schröder, F., Stamm, W., Völk, H. J., Wiebel-Sooth, B., Wiedner, C. A., and Willmer, M.: 1999, *Astroparticle Physics* **11**, 363

Hillas, A.: 1985, in *Proc. 19th I.C.R.C. (La Jolla)*, Vol. 3, p. 445

Hillas, A. M., Akerlof, C. W., Biller, S. D., Buckley, J. H., Carter-Lewis, D. A., Catanese, M., Cawley, M. F., Fegan, D. J., Finley, J. P., Gaidos, J. A., Krennrich, F., Lamb, R. C., Lang, M. J., Mohanty, G., Punch,

M., Reynolds, P. T., Rodgers, A. J., Rose, H. J., Rovero, A. C., Schubnell, M. S., Sembroski, G. H., Vacanti, G., Weekes, T. C., West, M., and Zweerink, J.: 1998, ApJ **503**, 744

Holder, J.: 2005, in *International Cosmic Ray Conference*, pp 383–+

Holder, J., Atkins, R. W., Badran, H. M., Blaylock, G., Bradbury, S. M., Buckley, J. H., Byrum, K. L., Carter-Lewis, D. A., Celik, O., Chow, Y. C. K., Cogan, P., Cui, W., Daniel, M. K., de La Calle Perez, I., Dowdall, C., Dowkontt, P., Duke, C., Falcone, A. D., Fegan, S. J., Finley, J. P., Fortin, P., Fortson, L. F., Gibbs, K., Gillanders, G., Glidewell, O. J., Grube, J., Gutierrez, K. J., Gyuk, G., Hall, J., Hanna, D., Hays, E., Horan, D., Hughes, S. B., Humensky, T. B., Imran, A., Jung, I., Kaaret, P., Kenny, G. E., Kieda, D., Kildea, J., Knapp, J., Krawczynski, H., Krennrich, F., Lang, M. J., Lebohec, S., Linton, E., Little, E. K., Maier, G., Manseri, H., Milovanovic, A., Moriarty, P., Mukherjee, R., Ogden, P. A., Ong, R. A., Petry, D., Perkins, J. S., Pizlo, F., Pohl, M., Quinn, J., Ragan, K., Reynolds, P. T., Roache, E. T., Rose, H. J., Schroedter, M., Sembroski, G. H., Sleege, G., Steele, D., Swordy, S. P., Syson, A., Toner, J. A., Valcarcel, L., Vassiliev, V. V., Wakely, S. P., Weekes, T. C., White, R. J., Williams, D. A., and Wagner, R.: 2006, *Astroparticle Physics* **25**, 391

Horan, D., Badran, H. M., Bond, I. H., Boyle, P. J., Bradbury, S. M., Buckley, J. H., Carter-Lewis, D. A., Catanese, M., Celik, O., Cui, W., Daniel, M., D'Vali, M., de la Calle Perez, I., Duke, C., Falcone, A., Fegan, D. J., Fegan, S. J., Finley, J. P., Fortson, L. F., Gaidos, J. A., Gammell, S., Gibbs, K., Gillanders, G. H., Grube, J., Hall, J., Hall, T. A., Hanna, D., Hillas, A. M., Holder, J., Jarvis, A., Jordan, M., Kenny, G. E., Kertzman, M., Kieda, D., Kildea, J., Knapp, J., Kosack, K., Krawczynski, H., Krennrich, F., Lang, M. J., Le Bohec, S., Linton, E., Lloyd-Evans, J., Milovanovic, A., Moriarty, P., Muller, D., Nagai, T., Nolan, S., Ong, R. A., Pallassini, R., Petry, D., Power-Mooney, B., Quinn, J., Quinn, M., Ragan, K., Rebillot, P., Reynolds, P. T., Rose, H. J., Schroedter, M., Sembroski, G. H., Swordy, S. P., Syson, A., Vassiliev, V. V., Wakely, S. P., Walker, G., Weekes, T. C., and Zweerink, J.: 2004, ApJ **603**, 51

Horan, D., Badran, H. M., Bond, I. H., Bradbury, S. M., Buckley, J. H., Carson, M. J., Carter-Lewis, D. A., Catanese, M., Cui, W., Dunlea, S., Das, D., de la Calle Perez, I., D'Vali, M., Fegan, D. J., Fegan, S. J., Finley, J. P., Gaidos, J. A., Gibbs, K., Gillanders, G. H., Hall, T. A., Hillas, A. M., Holder, J., Jordan, M., Kertzman, M., Kieda, D., Kildea, J., Knapp, J.,

Kosack, K., Krennrich, F., Lang, M. J., LeBohec, S., Lessard, R., Lloyd-Evans, J., McKernan, B., Moriarty, P., Muller, D., Ong, R., Pallassini, R., Petry, D., Quinn, J., Reay, N. W., Reynolds, P. T., Rose, H. J., Sembroski, G. H., Sidwell, R., Stanton, N., Swordy, S. P., Vassiliev, V. V., Wakely, S. P., and Weekes, T. C.: 2002, ApJ **571**, 753

Horan, D. and Weekes, T. C.: 2004, *New Astronomy Review* **48**, 527

Horns, D.: 2003, in L. O. Takalo and E. Valtaoja (eds.), *ASP Conf. Ser. 299: High Energy Blazar Astronomy*, pp 13–+

Humensky, B.: 2005, in *International Cosmic Ray Conference*

Itoh, C., Enomoto, R., Yanagita, S., Yoshida, T., Asahara, A., Bicknell, G. V., Clay, R. W., Edwards, P. G., Gunji, S., Hara, S., Hara, T., Hattori, T., Hayashi, S., Hayashi, S., Kabuki, S., Kajino, F., Katagiri, H., Kawachi, A., Kifune, T., Kubo, H., Kushida, J., Matsubara, Y., Mizumoto, Y., Mori, M., Moro, H., Muraishi, H., Muraki, Y., Naito, T., Nakase, T., Nishida, D., Nishijima, K., Okumura, K., Ohishi, M., Patterson, J. R., Protheroe, R. J., Sakurazawa, K., Swaby, D. L., Tanimori, T., Tokanai, F., Tsuchiya, K., Tsunoo, H., Uchida, T., Watanabe, A., Watanabe, S., and Yoshikoshi, T.: 2002, A&A **396**, L1

Jelley, J.: 1958, *BLABLA Radiation and its Applications*, Pergamon Press, Oxford

Jelley, J.: 1967, *Progress in Elementary Particles and Cosmic Ray Physics*, Vol. 9, p. 41, North Holland

Jelley, J. and Galbraith, W.: 1955, *Journal of Atmospheric and Terrestrial Physics* **6**, 304

Jelley, J. V.: 1966, *Physical Review Letters* **16**, 479

Jones, T.: 1979, *Astrophysical Journal* **233**, 796

Kabuki, S.: 2003, in *International Cosmic Ray Conference*, pp 2859–+

Kazanas, D. and Georganopoulos, M.: 2006, in H. R. Miller, K. Marshall, J. R. Webb, and M. F. Aller (eds.), *Astronomical Society of the Pacific Conference Series*, pp 124–+

Kenny, J.: 2006, *M.Sc. thesis in preparation*, National University of Ireland

Kieda, D. B.: 2003a, in *International Cosmic Ray Conference*, pp 2831–+

Kieda, D. B.: 2003b, in *International Cosmic Ray Conference*, pp 2835–+

Kildea, J. e.: 2005, in *International Cosmic Ray Conference*, pp 135–+

Kildea, J. e. a.: 2006, *The Whipple 10 meter Gamma-Ray Telescope, 1997-2006*, in preparation

Kirk, J. G. and Mastichiadis, A.: 1999, *Astroparticle Physics* **11**, 45

Klebesadel, R. W., Strong, I. B., and Olson, R. A.: 1973, ApJ **182**, L85+

Koide, S., Shibata, K., and Kudoh, T.: 1999, in S. M. Miyama, K. Tomisaka, and T. Hanawa (eds.), *ASSL Vol. 240: Numerical Astrophysics*, pp 215–+

Konopelko, A.: 1991, in *Proceedings of the 22nd International Cosmic Ray Conference (Dublin)*, Vol. 1, p. 484

Konopelko, A., Atkins, R. W., Blaylock, G., Buckley, J. H., Butt, Y., Carter-Lewis, D. A., Celik, O., Cogan, P., Chow, Y. C. K., Cui, W., Dowdall, C., Ergin, T., Falcone, A. D., Fegan, D. J., Fegan, S. J., Finley, J. P., Fortin, P., Gillanders, G. H., Gutierrez, K. J., Hall, J., Hanna, D., Horan, D., Hughes, S. B., Humensky, T. B., Imran, A., Jung, I., Kaaret, P., Kenny, G. E., Kertzman, M., Kieda, D. B., Kildea, J., Knapp, J., Kosack, K., Krawczynski, H., Krennrich, F., Lang, M. J., LeBohec, S., Moriarty, P., Mukherjee, R., Nagai, T., Ong, R. A., Perkins, J. S., Pohl, M., Ragan, K., Reynolds, P. T., Rose, H. J., Sembroski, G. H., Schroedter, M., Smith, A. W., Steele, D., Syson, A., Swordy, S. P., Toner, J. A., Valcarcel, L., Vassiliev, V. V., Wagner, R. G., Wakely, S. P., Weekes, T. C., White, R. J., Williams, D. A., and Zitzer, B.: 2006, *ArXiv Astrophysics e-prints*

Konopelko, A. K., Mastichiadis, A., Kirk, J., de Jager, O. C., and Stecker, F. W.: 2003, in *International Cosmic Ray Conference*, pp 2611–+

Kosack, K., Badran, H. M., Bond, I. H., Boyle, P. J., Bradbury, S. M., Buckley, J. H., Carter-Lewis, D. A., Celik, O., Connaughton, V., Cui, W., Daniel, M., D'Vali, M., de la Calle Perez, I., Duke, C., Falcone, A., Fegan, D. J., Fegan, S. J., Finley, J. P., Fortson, L. F., Gaidos, J. A., Gammell, S., Gibbs, K., Gillanders, G. H., Grube, J., Gutierrez, K., Hall, J., Hall, T. A., Hanna, D., Hillas, A. M., Holder, J., Horan, D., Jarvis, A., Jordan, M., Kenny, G. E., Kertzman, M., Kieda, D., Kildea, J., Knapp, J., Krawczynski, H., Krennrich, F., Lang, M. J., Le Bohec, S., Linton, E., Lloyd-Evans, J., Milovanovic, A., McEnery, J., Moriarty, P., Muller, D., Nagai, T., Nolan, S., Ong, R. A., Pallassini, R., Petry, D., Power-Mooney, B., Quinn, J., Quinn, M., Ragan, K., Rebillot, P., Reynolds, P. T., Rose,

H. J., Schroedter, M., Sembroski, G. H., Swordy, S. P., Syson, A., Vassiliev, V. V., Wakely, S. P., Walker, G., Weekes, T. C., and Zweerink, J.: 2004, ApJ **608**, L97

Krawczynski, H., Carter-Lewis, D. A., Duke, C., Holder, J., Maier, G., Le Bohec, S., and Sembroski, G.: 2006, *Astroparticle Physics* **25**, 380

Krawczynski, H., Coppi, P. S., and Aharonian, F.: 2002, MNRAS **336**, 721

Krawczynski, H., Hughes, S. B., Horan, D., Aharonian, F., Aller, M. F., Aller, H., Boltwood, P., Buckley, J., Coppi, P., Fossati, G., Götting, N., Holder, J., Horns, D., Kurtanidze, O. M., Marscher, A. P., Nikolashvili, M., Remillard, R. A., Sadun, A., and Schröder, M.: 2004, ApJ **601**, 151

Krawczynski, H., Sambruna, R., Kohnle, A., Coppi, P. S., Aharonian, F., Akhperjanian, A., Barrio, J., Bernlöhr, K., Börst, H., Bojahr, H., Bolz, O., Contreras, J., Cortina, J., Denninghoff, S., Fonseca, V., Gonzalez, J., Götting, N., Heinzelmann, G., Hermann, G., Heusler, A., Hofmann, W., Horns, D., Ibarra, A., Jung, I., Kankanyan, R., Kestel, M., Kettler, J., Konopelko, A., Kornmeyer, H., Kranich, D., Lampeitl, H., Lorenz, E., Lucarelli, F., Magnussen, N., Mang, O., Meyer, H., Mirzoyan, R., Moralejo, A., Padilla, L., Panter, M., Plaga, R., Plyasheshnikov, A., Pühlhofer, G., Rauterberg, G., Röhring, A., Rhode, W., Rowell, G., Sahakian, V., Samorski, M., Schilling, M., Schröder, F., Siems, M., Stamm, W., Tluczykont, M., Völk, H. J., Wiedner, C. A., and Wittek, W.: 2001, ApJ **559**, 187

Krennrich, F., Bond, I. H., Bradbury, S. M., Buckley, J. H., Carter-Lewis, D. A., Cui, W., de la Calle Perez, I., Fegan, D. J., Fegan, S. J., Finley, J. P., Gaidos, J. A., Gibbs, K., Gillanders, G. H., Hall, T. A., Hillas, A. M., Holder, J., Horan, D., Jordan, M., Kertzman, M., Kieda, D., Kildea, J., Knapp, J., Kosack, K., Lang, M. J., LeBohec, S., Moriarty, P., Müller, D., Ong, R. A., Pallassini, R., Petry, D., Quinn, J., Reay, N. W., Reynolds, P. T., Rose, H. J., Sembroski, G. H., Sidwell, R., Stanton, N., Swordy, S. P., Vassiliev, V. V., Wakely, S. P., and Weekes, T. C.: 2002, ApJ **575**, L9

Kusunose, M. and Takahara, F.: 2006, *ArXiv Astrophysics e-prints*

Laing, R. A., Parma, P., de Ruiter, H. R., and Fanti, R.: 1999, MNRAS **306**, 513

Lang, M. J., Carter-Lewis, D. A., Fegan, D. J., Fegan, S. J., Hillas, A. M., Lamb, R. C., Punch, M., Reynolds, P. T., and Weekes, T. C.: 2005, Ap&SS **297**, 345

Langston, G. I., Heflin, M. B., Conner, S. R., Lehar, J., Carrilli, C. L., and Burke, B. F.: 1990, ApJS **72**, 621

Lessard, R. W., Buckley, J. H., Connaughton, V., and Le Bohec, S.: 2001, *Astroparticle Physics* **15**, 1

Li, T.-P. and Ma, Y.-Q.: 1983, ApJ **272**, 317

Lindfors, E. J., Valtaoja, E., and Türler, M.: 2005, A&A **440**, 845

Linton, E. T., Atkins, R. W., Badran, H. M., Blaylock, G., Boyle, P. J., Buckley, J. H., Byrum, K. L., Carter-Lewis, D. A., Celik, O., Chow, Y. C. K., Cogan, P., Daniel, M. K., Dowdall, C., Falcone, A. D., Fegan, D. J., Fegan, S. J., Finley, J. P., Fortin, P., Guiterrez, K. J., Hall, J., Hanna, D., Holder, J., Horan, D., Hughes, S. B., Humensky, T. B., Jung, I., Kenny, G. E., Kertzman, M., Kieda, D. B., Kildea, J., Knapp, J., Krawczynski, H., Lang, M. J., LeBohec, S., Maier, G., Moriarty, P., Ong, R. A., Perkins, J. S., Pizlo, F., Pohl, M., Quinn, J., Ragan, K., Rebillot, P. F., Reynolds, P. T., Sembroski, G. H., Steele, D., Swordy, S. P., Valcarcel, L., Wakely, S. P., Weekes, T. C., and White, R. J.: 2006, *Journal of Cosmology and Astro-Particle Physics* **1**, 13

Litwin, L.: 2001, *RF Time and Frequency* p. 32

Mannheim, K.: 1993, A&A **269**, 67

Maraschi, L., Ghisellini, G., and Celotti, A.: 1992, ApJ **397**, L5

Marscher, A. P.: 1999, *Astroparticle Physics* **11**, 19

Masterson, C. P.: 1999, *Ph.D. thesis*, National University of Ireland

Mattox, J. R., Michelson, P. F., Nolan, P. L., Willis, T. D., Lin, Y. C., Jones, B., Tompkins, B., Twiggs, B., Yearian, M., Bloom, E. D., Atwood, W. B., Godfrey, G. L., Luebke, A., Shabad, G., Engavotov, D., Broeder, J., Ballam, J., Taylor, R. E., Wood, K. S., Johnson, W. N., Grove, J. E., Hertz, P. L., Lovellette, M., Suson, D., Oreglia, M., Ong, R., Mayer-Hasselwander, H. A., Merck, M., Scargle, J. D., Colavita, A., Barbiellini, G., Morselli, A., Vacchi, A., Kamae, T., Kasahara, K., Nakano, G., Burnett, T., Johnson, R., and Cominsky, L. R.: 1996, *Memorie della Societa Astronomica Italiana* **67**, 607

McCulloch, W. S. and Pitts, W.: 1943, *Bulletin of Mathematical Biophysics* **5**, 115

Mirzoyan, R., Garczarczyk, M., Merck, M., Danielyan, V., Lorenz, E., Mirzoyan, R., and Laille, A.: 2003, in *International Cosmic Ray Conference*, pp 2935–+

Mirzoyan, R., Sobczynska, D., Lorenz, E., and Teshima, M.: 2006, *Astroparticle Physics* **25**, 342

Mohanty, G., Biller, S., Carter-Lewis, D. A., Fegan, D. J., Hillas, A. M., Lamb, R. C., Weekes, T. C., West, M., and Zweerink, J.: 1998, *Astroparticle Physics* **9**, 15

Morselli, A.: 2003, *Chinese Journal of Astronony and Astrophysics* **3**, 523

Mücke, A., Protheroe, R. J., Engel, R., Rachen, J. P., and Stanev, T.: 2003, *Astroparticle Physics* **18**, 593

Nagai, T.: 2005, *Ph.D. Thesis*

Neshpor, Y. et al.: 1995, in *Proc. 24th I.C.R.C. (Rome)*

Nieppola, E., Tornikoski, M., and Valtaoja, E.: 2006, A&A **445**, 441

Nikishov, A.: 1962, *Journal of Experimental and Theoretical Physics* **14**, 393

Nishiyama, T., Chikawa, M., Hayashi, Y., Hibino, K., Honda, K., Inoue, N., Ito, N., Kajino, F., Kakizawa, S., Kawasaki, Y., Kitamura, H., Kusano, E., Loh, E. C., Matsuyama, T., Morizane, Y., Nishikawa, D., Nishizawa, M., Ohoka, H., Osone, S., Sakaki, N., Sasano, M., Shiomi, A., Takahashi, T., Taylor, F., Teshima, M., Tsukiji, M., Yamamoto, T., Yasui, K., Yoshii, H., and Yuda, Y.: 1999, in *Proceedings of the 26th International Cosmic Ray Conference (Salt Lake City)*, Vol. 3, p. 370

Ostapchenko, S.: 2004, *ArXiv Astrophysics e-prints*

Padovani, P.: 2006, *ArXiv Astrophysics e-prints*

Padovani, P. and Giommi, P.: 1995, MNRAS **277**, 1477

Paneque, D., Gebauer, H. J., Lorenz, E., and Mirzoyan, R.: 2004, *Nuclear Instruments and Methods in Physics Research A* **518**, 619

Paredes, J. M., Marti, J., Ishwara Chandra C., H., and Bosch-Ramon, V.: 2006, *ArXiv Astrophysics e-prints*

Penzias, A. A. and Wilson, R. W.: 1965, ApJ **142**, 419

Perkins, J. S., Badran, H. M., Blaylock, G., Bradbury, S. M., Cogan, P., Chow, Y. C. K., Cui, W., Daniel, M. K., Falcone, A. D., Fegan, S. J., Finley, J. P., Fortin, P., Fortson, L. F., Gillanders, G. H., Gutierrez, K. J., Grube, J., Hall, J., Hanna, D., Holder, J., Horan, D., Hughes, S. B., Humensky, T. B., Kenny, G. E., Kertzman, M., Kieda, D. B., Kildea, J., Kosack, K., Krawczynski, H., Krennrich, F., Lang, M. J., LeBohec, S., Maier, G., Moriarty, P., Ong, R. A., Pohl, M., Ragan, K., Rebillot, P. F., Sembroski, G. H., Steele, D., Swordy, S. P., Valcarcel, L., Vassiliev, V. V., Wakely, S. P., Weekes, T. C., and Williams, D. A.: 2006, ApJ **644**, 148

PHILIPS: 1994, *Photomultiplier Tubes, Principles & Applications*, Cambridge University Press

Pian, E., Vacanti, G., Tagliaferri, G., Ghisellini, G., Maraschi, L., Treves, A., Urry, M., Fiore, F., Giommi, P., Palazzi, E., Chiappetti, L., and Sambruna, R. M.: 1998, ApJ **492**, L17

Pohl, M. and Schlickeiser, R.: 2000, A&A **354**, 395

Porter, N. A. and Weekes, T. C.: 1979, Nature **277**, 199

Pühlhofer, G., Bolz, O., Götting, N., Heusler, A., Horns, D., Kohnle, A., Lampeitl, H., Panter, M., Tluczykont, M., Aharonian, F., Akhperjanian, A., Beilicke, M., Bernlöhr, K., Börst, H., Bojahr, H., Coarasa, T., Contreras, J. L., Cortina, J., Denninghoff, S., Fonseca, M. V., Girma, M., Heinzelmann, G., Hermann, G., Hofmann, W., Jung, I., Kankanyan, R., Kestel, M., Konopelko, A., Kornmeyer, H., Kranich, D., Lopez, M., Lorenz, E., Lucarelli, F., Mang, O., Meyer, H., Mirzoyan, R., Moralejo, A., Ona-Wilhelmi, E., Plyasheshnikov, A., de Los Reyes, R., Rhode, W., Ripken, J., Rowell, G., Sahakian, V., Samorski, M., Schilling, M., Siems, M., Sobzynska, D., Stamm, W., Vitale, V., Völk, H. J., Wiedner, C. A., and Wittek, W.: 2003, *Astroparticle Physics* **20**, 267

Punch, M., Akerlof, C. W., Cawley, M. F., Chantell, M., Fegan, D. J., Fennell, S., Gaidos, J. A., Hagan, J., Hillas, A. M., Jiang, Y. K., A. D., Lamb, R. C., Lawrence, M. A., Lewis, D. A., Meyer, D. I., Mohanty, G., O'Flaherty, K. S., Reynolds, P. T., Rovero, A. C., Schubnell, M. S., Sembroski, G., Weekes, T. C., and Wilson, C.: 1992, Nature **358**, 477

Quinn, J., Akerlof, C. W., Biller, S., Buckley, J., Carter-Lewis, D. A., Cawley, M. F., Catanese, M., Connaughton, V., Fegan, D. J., Finley, J. P., Gaidos,

J., Hillas, A. M., Lamb, R. C., Krennrich, F., Lessard, R., McEnery, J. E., Meyer, D. I., Mohanty, G., Rodgers, A. J., Rose, H. J., Sembroski, G., Schubnell, M. S., Weekes, T. C., Wilson, C., and Zweerink, J.: 1996, ApJ **456**, L83

Quinn, J., Bond, I. H., Boyle, P. J., Buckley, J. H., Bradbury, S. M., Breslin, A. C., Burdett, A. M., Bussons Gordo, J., Carter-Lewis, D. A., Catanese, M., Cawley, M. F., Fegan, D. J., Finley, J. P., Gaidos, J. A., Hall, A., Hillas, A. M., Krennrich, F., Lamb, R. C., Lessard, R., Masterson, C., McEnery, J. E., Mohanty, G., Moriarty, P., Rodgers, A. J., Rose, H. J., Samuelson, F. W., Sembroski, G. H., Srinivasan, R., Weekes, T. C., and Zweerink, J.: 1997, *Proceedings of the 25th International Cosmic Ray Conference (Durban, South Africa)* **25**, 249

Quinn, J., Buckley, J., Weekes, T. C., Catanese, M., Carter-Lewis, D. A., Krennrich, F., Lamb, R. C., Zweerink, J., Akerlof, C. W., Meyer, D., Schubnell, M., Gaidos, J., Sembroski, G., Wilson, C., Fegan, D. J., Lessard, R., McEnery, J., Cawley, M. F., Biller, S., Hillas, A. M., Rodgers, A., and Rose, J.: 1995, IAU Circ. **6178**, 1

Rector, T. A., Gabuzda, D. C., and Stocke, J. T.: 2003, AJ **125**, 1060

Reimer, A., Böttcher, M., and Postnikov, S.: 2005, ApJ **630**, 186

Robson, I.: 1996, *Active Galactic Nuclei*, Wiley

Rolland, L. e.: 2005, in *International Cosmic Ray Conference*, pp 109–+

Rybicki, G. B. and Lightman, A.: 2004, *Radiative Processes in Astrophysics*, Wiley-VCH

Sapru, M. L. e.: 2005, in *International Cosmic Ray Conference*, pp 263–+

Schlenker, S.: 2005, *Ph.D. thesis*, Humboldt University Berlin

Schödel, R., Ott, T., Genzel, R., Hofmann, R., Lehnert, M., Eckart, A., Mouawad, N., Alexander, T., Reid, M. J., Lenzen, R., Hartung, M., Lacombe, F., Rouan, D., Gendron, E., Rousset, G., Lagrange, A.-M., Brandner, W., Ageorges, N., Lidman, C., Moorwood, A. F. M., Spyromilio, J., Hubin, N., and Menten, K. M.: 2002, Nature **419**, 694

Schroedter, M., Badran, H. M., Buckley, J. H., Bussons Gordo, J., Carter-Lewis, D. A., Duke, C., Fegan, D. J., Fegan, S. F., Finley, J. P., Gillanders, G. H., Grube, J., Horan, D., Kenny, G. E., Kertzman, M., Kosack, K.,

Krennrich, F., Kieda, D. B., Kildea, J., Lang, M. J., Lee, K., Moriarty, P., Quinn, J., Quinn, M., Power-Mooney, B., Sembroski, G. H., Wakely, S. P., Vassiliev, V. V., Weekes, T. C., and Zweerink, J.: 2005, ApJ **634**, 947

Sikora, M., Begelman, M. C., and Rees, M. J.: 1994, ApJ **421**, 153

Sikora, M. and Madejski, G.: 2001, *AIP Conf. Proc. 599: X-ray Astronomy: Stellar Endpoints, AGN, and the Diffuse X-ray Background* **599**, 935

Sinitsyna, V. G.: 1993, in R. C. Lamb (ed.), *Towards a Major Atmospheric Cherenkov Detector – II for TeV Astro/Particle Physics*, pp 91–+

Sinnis, G.: 2005, in F. A. Aharonian, H. J. Völk, and D. Horns (eds.), *AIP Conf. Proc. 745: High Energy Gamma-Ray Astronomy*, pp 234–245

Smith, A. J.: 2005, in *International Cosmic Ray Conference*, pp 227–+

Smith, D. A., Bergeret, H., Cordier, A., Dumora, D., Eschstruth, P., Espigat, P., Fabre, B., Fleury, P., Giebels, B., Merkel, B., Meynadier, C., Paré, E., Procureur, J., Québert, J., Rob, L., Roy, P., Salamon, M. H., Schovanek, P., and Vrana, J.: 1997, *Nuclear Physics B Proceedings Supplements* **54**, 362

Stecker, F. W. and de Jager, O. C.: 1997, ApJ **476**, 712

Stecker, F. W., de Jager, O. C., and Salamon, M. H.: 1992, ApJ **390**, L49

Stecker, F. W., de Jager, O. C., and Salamon, M. H.: 1996, ApJ **473**, L75+

Tavecchio, F., Maraschi, L., Pian, E., Chiappetti, L., Celotti, A., Fossati, G., Ghisellini, G., Palazzi, E., Raiteri, C. M., Sambruna, R. M., Treves, A., Urry, C. M., Villata, M., and Djannati-Ataï, A.: 2001, ApJ **554**, 725

Tsuchiya, K., Enomoto, R., Ksenofontov, L. T., Mori, M., Naito, T., Asahara, A., Bicknell, G. V., Clay, R. W., Doi, Y., Edwards, P. G., Gunji, S., Hara, S., Hara, T., Hattori, T., Hayashi, S., Itoh, C., Kabuki, S., Kajino, F., Katagiri, H., Kawachi, A., Kifune, T., Kubo, H., Kurihara, T., Kurosaka, R., Kushida, J., Matsubara, Y., Miyashita, Y., Mizumoto, Y., Moro, H., Muraishi, H., Muraki, Y., Nakase, T., Nishida, D., Nishijima, K., Ohishi, M., Okumura, K., Patterson, J. R., Protheroe, R. J., Sakamoto, N., Sakurazawa, K., Swaby, D. L., Tanimori, T., Tanimura, H., Thornton, G., Tokanai, F., Uchida, T., Watanabe, S., Yamaoka, T., Yanagita, S., Yoshida, T., and Yoshikoshi, T.: 2004, ApJ **606**, L115

Urry, C.: 2004, in G. T. Richards and P. B. Hall (eds.), *ASP Conf. Ser. 311: AGN Physics with the Sloan Digital Sky Survey*, pp 49–+

Urry, C. M. and Padovani, P.: 1995, PASP **107**, 803+

Vassiliev, V. V.: 2003, in *International Cosmic Ray Conference*, pp 2851–+

Vincent, P.: 2005, in *International Cosmic Ray Conference*, pp 163–+

Vincent, P., Denanca, J.-P., Huppert, J.-F., Manigot, P., de Naurois, M., Nayman, P., Tavernet, J.-P., Toussenel, F., Chounet, L.-M., Degrange, B., Espigat, P., Fonraine, G., Guy, J., Hermann, G., Kohnle, A., Masterson, C., Punch, M., Rivoal, M., Rolland, L., and Saitoh, T.: 2003, in *International Cosmic Ray Conference*, pp 2887–+

Vladimirsky, B. M., Zyskin, Y. L., Neshpor, Y. I., Stepanian, A. A., Fomin, V. P., and Shitov, V. G.: 1989, in A. A. Stepanian, D. J. Fegan, and M. F. Cawley (eds.), *Very High Energy Gamma Ray Astronomy*, pp 21–+

W. Galbraith, J. J.: 1953, *Nature* **171**, 349

Weekes, T.: 2003, *Very High Energy Gamma-Ray Astronomy*, Institure of Physics, Bristol

Weekes, T. C.: 2006, in *Proceedings of the International Workshop on "Energy Budget in the High Energy Universe", Kashiwa, Japan*

Weekes, T. C., Cawley, M. F., Fegan, D. J., Gibbs, K. G., Hillas, A. M., Kowk, P. W., Lamb, R. C., Lewis, D. A., Macomb, D., Porter, N. A., Reynolds, P. T., and Vacanti, G.: 1989, ApJ **342**, 379

White, R. J.: 2005, in *AIP Conf. Proc. 745: High Energy Gamma-Ray Astronomy*, pp 797–802

Winkler, C., Courvoisier, T. J.-L., Di Cocco, G., Gehrels, N., Giménez, A., Grebenev, S., Hermsen, W., Mas-Hesse, J. M., Lebrun, F., Lund, N., Palumbo, G. G. C., Paul, J., Roques, J.-P., Schnopper, H., Schönfelder, V., Sunyaev, R., Teegarden, B., Ubertini, P., Vedrenne, G., and Dean, A. J.: 2003, A&A **411**, L1

Yadav, K. K., Koul, R., Kanda, A., Kaul, S. R., Tickoo, A. K., Rannot, R. C., Chandra, P., Bhatt, N., Chouhan, N., Venugopal, K., Kothari, M., Goyal, H. C., Dhar, V. K., and Kaul, S. K.: 2004, *Nuclear Instruments and Methods in Physics Research A* **527**, 411

Yamamoto, T., Chamoto, N., Chikawa, M., Hayashi, S., Hayashi, Y., Hayashida, N., Hibino, K., Hirasawa, H., Honda, K., Hotta, N., Inoue, N., Ishikawa, F., Ito, N., Kabe, S., Kajino, F., Kashiwagi, T., Kakizawa, S., Kawakami, S., Kawasaki, Y., Kawasumi, N., Kitamura, H., Kuramochi, K., Kusano, E., Loh, E. C., Mase, K., Matsuyama, T., Mizutani, K., Morizane, Y., Nishikawa, D., Nagano, M., Nishimura, J., Nishiyama, T., Nishizawa, M., Ouchi, T., Ohoka, H., Ohnishi, M., Osone, S., Saito, T., Sakaki, N., Sakata, M., Sasano, M., Shimodaira, H., Shiomi, A., Sokolsky, P., Takahashi, T., Taylor, S. F., Takeda, M., Teshima, M., Torii, R., Tsukiji, M., Uchihori, Y., Yamamoto, Y., Yasui, K., Yoshida, S., Yoshii, H., and Yuda, T.: 1999, in *International Cosmic Ray Conference*, pp 275–+

Zweerink, J., Bhattacharya, D., Mohanty, G., Mohideen, U., Radu, A., Rieben, R., Sushkov, V. V., Tom, H. W., and Tumer, T. O.: 1999, in O. H. Siegmund and K. A. Flanagan (eds.), *Proc. SPIE Vol. 3765, p. 524-529, EUV, X-Ray, and Gamma-Ray Instrumentation for Astronomy X, Oswald H. Siegmund; Kathryn A. Flanagan; Eds.*, pp 524–529